Phase Shifting Surface (PSS) and Phase and Amplitude Shifting Surface (PASS) for Microwave Applications

Nicolas Gagnon

Thesis submitted to the
Faculty of Graduate and Postdoctoral Studies
In partial fulfillment of the requirements
For the PhD degree in Electrical and Computer Engineering

School of Information Technology and Engineering
Faculty of Engineering
University of Ottawa

ABSTRACT

This thesis describes an electrically thin surface used for electromagnetic applications in the microwave regime. The surface is free-standing and its primary purpose is to modify the phase distribution, or the phase and amplitude distribution of electromagnetic fields propagating through it: it is called phase shifting surface (PSS) in the first case, and phase and amplitude shifting surface (PASS) in the second case. For practical applications, the surface typically comprises three or four layers of metallic patterns spaced by dielectric layers. The patterns of the metallic layers are designed to locally alter the phase (and amplitude in the case of the PASS) of an incoming wave to a prescribed set of desired values for the outgoing wave. The PSS/PASS takes advantage of the reactive coupling by closely spacing of the metallic layers, which results in a larger phase shift range while keeping the structure significantly thin.

The PSS concept is used to design components such as gratings and lens antennas which are presented in this document. The components are designed for an operating frequency of 30 GHz. The PSS phase grating gives high diffraction efficiency, even higher than a dielectric phase grating. Several types of lens antennas are also presented, which show comparable performance to that of a conventional dielectric plano-hyperbolic lens antenna with similar parameters. The PASS concept is used in a beam shaping application in which a flat-topped beam antenna is designed.

This work demonstrates the potential for realising thin, lightweight and low-cost antennas at Ka band, in particular for substituting higher-gain antenna technologies such as conventional dielectric shaped lens antennas.

RÉSUMÉ

La présente thèse décrit une surface électriquement mince servant pour des applications électromagnétiques en hyperfréquences. La surface est autoporteuse dans l'espace libre et sa fonction principale consiste à modifier la distribution de phase, ou la distribution de phase et d'amplitude des champs électromagnétiques qui la traversent : dans le premier cas, on l'appelle surface à changement de phase; dans le second, on l'appelle surface à changement de phase et d'amplitude. Pour des applications pratiques, la surface est normalement constituée d'éléments métalliques variables gravés sur trois ou quatre couches, lesquels sont séparées par des couches de matériaux diélectriques. Les éléments variables des couches métalliques sont ajustés partout sur la surface dans le but de modifier la phase (et l'amplitude, le cas échéant) du front d'ondes incident pour obtenir le front d'ondes émanent désiré. En utilisant des couches diélectriques très minces par rapport à la longueur d'onde, ces surfaces tirent profit du couplage réactif entre les différentes couches de métallisation, lequel permet d'obtenir à la fois une large plage de changement de phase et une structure très mince.

Dans le présent document, le concept de surface à changement de phase est utilisé dans le but de concevoir des réseaux de diffraction en phase et des antennes à lentille à la fréquence de 30 GHz. Le réseau de diffraction obtenu à partir d'une surface à changement de phase présente une efficacité de diffraction très élevée, même plus élevée que celle d'un réseau de diffraction diélectrique. Plusieurs antennes à lentille réalisées à partir de ce concept sont aussi proposées, lesquelles présentent des performances comparables à celles d'une antenne à lentille diélectrique plano-hyperbolique ayant des paramètres similaires. De son côté, le concept de surface à changement de phase et d'amplitude est utilisé dans

une application de formation de faisceau dans lequel une antenne ayant un faisceau principal plat est réalisée.

Ce travail démontre la possibilité de concevoir des antennes en bande Ka très pratiques puisqu’elles sont minces, légères et peu coûteuses, surtout si elles sont utilisées en remplacement d’antennes à gain élevé telles que des antennes à lentille diélectrique conventionnelle.

ACKNOWLEDGEMENTS

I would like to take the opportunity to thank all the people who helped me during my PhD work and research.

First of all I would like to thank my supervisor, Prof. Derek McNamara, for his helpful guidance during the course of this work. I am also grateful to my colleague Dr. Aldo Petosa from the Communications Research Centre (CRC) Canada for his help, support and patience.

This thesis would not have been possible without the support of Mr. Michel Cuhaci, manager of the Advanced Antenna Technology (RAAT) group at CRC, who gave me the opportunity to complete my thesis project at CRC.

I am grateful for the following people, whose help has been essential to the completion of this thesis:

- Mr. David Lee of CRC for his continuous dedication. Mr. Lee has always been available to provide technical assistance, in particular for conducting the near-field measurements presented in this thesis.
- Ms. Bonnie Todd of CRC for the good work on fabricating the multiple prototypes presented in this thesis, and making available some of her laboratory equipment.
- Mr. John Brebner of CRC for taking numerous pictures of the prototypes presented in this thesis.
- Ms. Xiangjun (Jane) Meng of the University of Ottawa for providing assistance with the synthesis of the flat-topped beam distribution.
- Mr. E’qab Almajali of the University of Ottawa for providing assistance with simulating the feed horn used for the flat-topped beam antenna.

Finally, I wish to express my gratitude to my colleagues who helped and encouraged me throughout this work. In particular, I would like to thank former office mate Ms. Sara Stout-Grandy for providing me part of the motivation to start working on a PhD degree.

REMERCIEMENTS

J’aimerais prendre le temps de remercier tous ceux et celles qui m’ont aidé de près ou de loin à mener à bien cette thèse.

Tout d’abord j’aimerais remercier ma conjointe, Véronique, sans qui ce travail n’aurait pas été possible. Merci pour ton soutien, ta patience, ta compréhension. Plus particulièrement, merci pour la révision et l’édition de la thèse ainsi que pour l’aide précieuse dans l’écriture de scripts de programmation pour la manipulation de ma colossale base de données. J’aimerais aussi remercier ma fille Sophie pour sa patience et sa présence.

Un merci spécial à Mme Louise Casavant du Service de création visuelle au Centre de recherches sur les communications (CRC) Canada pour l’aide apportée à l’impression de ce document.

Merci à ma famille et à mes amis qui m’ont encouragé dans ce projet. Finalement, j’aimerais remercier l’Université d’Ottawa pour le soutien financier.

TABLE OF CONTENTS

LIST OF FIGURES

LIST OF TABLES

LIST OF SYMBOLS

a	magnitude of the desired wavefront
A	magnitude of the reference wavefront
A, A'	physical region delimiters
a_i	patch size or strip width on layer i or amplitude of diffracted beam i
a_m	patch size or strip width on layer i or amplitude of diffracted beam i
$\hat{a}_x$	unit vector along the x-axis
$\hat{a}_y$	unit vector along the y-axis
b	threshold
C	capacitance
d	thickness of a dielectric layer or sheet
D	diameter (generally of a lens)
$\bar{E}$	electric field (vector)
E	electric field
E_x	electric field component along the x-axis
E_y	electric field component along the y-axis
E_z	electric field component along the z-axis
E_{inc}	incident electric field
E_{trans}	transmitted electric field
f	phase profile
F	focal length or radiation pattern
F_e	radiation pattern of an element
g_i	gap size on layer i
h	height or thickness of a structure
H	magnetic field
i	layer number or zone number or general identifier
I	interference
j	imaginary number
k_0	free-space wave number
k	wave number

L	inductance
m	diffracted beam order or general identifier
M	number of grating transitions
n	integer number
N_x	number of subdivisions along x
N_y	number of subdivisions along y
P	number of corrections within a wavelength
q	width factor
r_i	radius of the zone i
R	distance from the focal point to the lens surface
s	unit cell size or unit cell height or step thickness in a phase-correcting FZP
t	thickness of a lens
t_0	backing thickness of some types of lens
T	transmittance or transmission coefficient
T_x	transmission coefficient along the x-axis
T_y	transmission coefficient along the y-axis
T_B	binary transmittance
U_C	reconstructed wavefront
U_D	desired wavefront
U_R	reference wavefront
U_i	i^{th} order diffracted beam
x	rectangular coordinate
x_m	position along x of the m^{th} element
y	rectangular coordinate
y_m	position along y of the m^{th} element
z	rectangular or cylindrical coordinate
α	spatial frequency
α_m	amplitude of the m^{th} element
Δx	subdivision dimension along the x-axis
Δy	subdivision dimension along the y-axis
ε_r	relative permittivity (dielectric constant)

θ	radiation angle <u>or</u> grating phase shift
θ_{max}	maximum scan angle
η_0	impedance of free-space
λ	wavelength
λ_0	free-space wavelength
λ_g	guided wavelength
Λ	grating period
μ	permeability
μ_0	free-space permeability
μ_r	relative permeability
ϕ	phase of the desired wavefront <u>or</u> required phase correction
ϕ_0	required phase correction in the middle of the lens
Φ	output angle
τ	roll angle
ψ	phase of the reference wavefront
ψ_m	phase of the m^{th} element
ζ	error

LIST OF ACRONYMS

CAD	computer-aided design
CPU	central processing unit
CRC	Communications Research Centre
DPHLA	dielectric plano-hyperbolic lens antenna
FDTD	finite-difference time-domain
FEM	finite-element method
FR4	Flame Resistant 4
FSS	frequency selective surface
FZP	Fresnel zone plate
FZPA	Fresnel zone plate antenna
MoM	method of moments
PASS	phase and amplitude shifting surface
PC-FZPA	phase-correcting Fresnel zone plate antenna
PEC	perfect electric conductor
PMC	perfect magnetic conductor
PSS	phase shifting surface
RAM	random access memory

LIST OF PUBLICATIONS

N. Gagnon, A. Petosa, D. McNamara, “Phase Hologram Composed of Square Patches on a Thin Dielectric Sheet,” in *Proceedings of the International Symposium on Antennas and Propagation (ISAP 2008)*, Taipei, Taiwan, pp. 678-681, October 2008 *(digital format)*.[1]

N. Gagnon, A. Petosa, D.A. McNamara, “Comparison between Conventional Lenses and an Electrically Thin Lens Made Using a Phase Shifting Surface (PSS) at Ka Band,” in *Loughborough Antennas & Propagation Conference (LAPC 2009)*, Loughborough, UK, pp. 117-120, November 2009.[2]

N. Gagnon, A. Petosa and D.A. McNamara, "Thin Microwave Phase-Shifting Surface (PSS) Lens Antenna Made of Square Elements," *IET Electronics Letters*, vol. 46, no. 5, pp. 327-329, March 2010.

N. Gagnon, A. Petosa, D.A. McNamara, “Thin Microwave Quasi-Transparent Phase-Shifting Surface (PSS),” *IEEE Transactions on Antennas and Propagation*, vol. 58, no. 4, pp. 1193-1201, April 2010.

N. Gagnon, A. Petosa and D.A. McNamara, “Phase-Correcting Lens Antennas Made Using a Three-Layer Phase Shifting Surface (PSS) at Ka Band,” in the *14th International Symposium on Antenna Technology and Applied Electromagnetics (ANTEM 2010)*, Ottawa, Canada, July 2010 *(digital format)*.

N. Gagnon, D.A. McNamara and A. Petosa, “Performance Comparison of Lens Antennas Realized Using a Thin Free-Standing Transmissive Phase-Shifting Surface (PSS),” in *IEEE AP-S International Symposium*, Toronto, Canada, July 2010 *(digital format)*.

[1] Finalist for Best Paper Competition.
[2] Winner of one of the two Best Student Paper Prizes.

N. Gagnon, A. Petosa and D.A. McNamara, “A Phase Element for Introducing a Phase Shift Pattern into an Electromagnetic Wave,” Patent Pending (Application number 2,674,785 for Canada; File number 10354 for USA), filed August 2, 2009.

CHAPTER 1 Introduction

1.1 Problem Statement

Free-standing phase-correcting and/or amplitude-correcting structures are useful devices for antenna applications. They are usually used to modify the incoming beam from a feed antenna and transform it to obtain gain enhancement, beam shaping or beam splitting. They are commonly used in antenna applications.

The antenna gain is proportional to the aperture size of the antenna. For gain enhancement, it is usually required to increase the aperture size. This is usually done by introducing a device of size larger than the feed antenna to be used for phase correction. The best known application is the reflector antenna, for which the parabolic shape results in uniform phase a given distance away from its surface. Lens antennas are another example, operating like a reflector but in transmission. The resulting shape of the lens antenna is a hyperbola.

Another way of increasing the gain of an antenna is by using multiple antenna elements in an array configuration. Again phasing is important and maximum broadside gain is achieved with uniform phasing. When such a control is possible, a uniform amplitude as well as a uniform phase will ensure a maximum antenna gain. However, if the beam is to be shaped to achieve some specifications, the amplitude and phase can be varied at the price of a gain penalty. For example, a non-uniform amplitude weighting such as binomial or Dolph-Chebyshev allow for sidelobes improvements. A linear phase progression in an array results in beam tilting. Phased arrays are an example of a device combining phase and amplitude correction for beam shaping and beam tilting; however because they are integrating numerous active devices (typically one phase shifter and one attenuator per element), their implementation is very high cost and, for that reason, their deployment is limited.

This thesis focuses on free-standing phase correcting devices of the transmissive type. The most common are lenses, Fresnel lenses and phase-correcting Fresnel zone plates which, although they look physically different, have the same operation principle of correcting phase of electromagnetic waves propagating through them. Other types of free-standing phase correcting devices include phase gratings, which are commonly used as a beam-splitting device. All the above-mentioned are usually made by machining of thick dielectric slabs for microwave and millimetre-wave frequency applications. As a result, they are difficult and expensive to fabricate, thick, heavy and bulky. For these reasons they are not attractive and alternative technologies are commonly used. Lensing devices could be useful for high-gain applications, but reflectors, reflectarrays or arrays of low-gain elements are usually preferred for practical reasons even though lensing devices have useful advantages over reflecting structures such as no feed blockage and higher fabrication tolerances, and lower losses than arrays. The afore-mentioned practical problems also arise with phase gratings and phase holograms, and therefore their deployment is marginal. Amplitude gratings and amplitude holograms, which are significantly lighter, thinner and lower-cost, are usually preferred, despite their poor performance [IIZU75], [LÉVI01], [HIRV97].

Consequently, free-standing phase correcting devices suffer from a tradeoff between performance and practicality, as highlighted in [GAGN10b]. The typical phase correcting devices present good performance but low practicality, whereas the amplitude approach could be used as an alternative to the phase approach, offering high practicality but poor performance. This will be discussed in more details in Chapter 2.

1.2 Motivation

The ultimate goal would be to obtain a free-standing device for use at microwave, millimetre wave or sub-millimetre wave frequencies having most of the advantages of the traditional phase-correcting and amplitude-correcting devices yet few or none of their disadvantages.

The idea of generating different phase shifts over the aperture of a free-standing device from a thin flat dielectric sheet covered with conducting shapes comes from the analogy with newspaper printing, where the grey tones are obtained using small black dots of different sizes in a predetermined array [WATE66a]. The ink on the paper in the newspaper printing process corresponds to the metal on dielectric in this potential microwave, millimetre wave or sub-millimetre wave phase-correcting concept.

1.3 Proposed Concept

In order to achieve phase shifting in a thin flat configuration as briefly described in Section 1.2, a novel concept called *phase shifting surface* (PSS) is introduced in this thesis. This concept has the physical advantages of amplitude-correcting free-standing devices [GUO02]: it is thin, flat, lightweight and low-cost. Yet its phase-correcting parameter can be varied over a significant range while keeping the transmission amplitude high, resulting in a good operational bandwidth. It is shown in this work that the performance of such

PSS-based free-standing devices could be as high as conventional devices that are bulkier, heavier and more expensive.

A more generalised version of the PSS is the phase and amplitude shifting surface (PASS), where both the transmission amplitude and transmission phase are varied over the aperture of the free-standing structure. This concept can be used for beam shaping where both the amplitude and phase need to be changed over the aperture surface. In that sense, the PASS concept goes beyond the traditional concept of phase correction being separated from the amplitude correction, and therefore it shows that such a device, along with its PSS version, can be used for many different types of applications.

1.4 Thesis Objectives

The main objective of this thesis is to present the novel concept of a phase-shifting surface (PSS) and its extension to a phase and amplitude shifting surface (PASS), as well as proofs of concepts and comparison with existing technologies. The prototypes are compared to conventional technologies in order to demonstrate the usefulness of the PSS approach. Basic design rules are introduced. Limitations, essentially only of a bandwidth nature compared to similar technologies, are investigated.

1.5 Thesis Organisation

This thesis is organised in eight chapters that are thoroughly described in this section.

Chapter 2 sets the background of the present study. It presents a literature review of the transmissive free-space phase shifting technologies as well as previously proposed concepts to realise thin lenses.

Chapter 3 presents the PSS/PASS concept. It describes the approach used for obtaining the desired behaviour. It presents the different unit cells used as well as the simulation work involved.

Chapter 4 presents the first proof of concept based on a PSS, which consists in a linear phase grating. This confirms the possibility of producing computer-generated structures based on holography principles at microwave, millimetre wave and sub-millimetre wave frequencies using a low-cost, mature and efficient fabrication process that leads to a thin and lightweight structure.

Chapter 5 presents the first lensing proof of concept, which consists in a cylindrical phase-correcting Fresnel zone plate antenna.

In Chapter 6, the PSS concept is applied to full (as opposed to just cylindrical) lensing devices: in this case phase-correcting Fresnel zone plate antennas and Fresnel lens antennas. A comparison with conventional lens technologies at Ka band is conducted. The comparison reveals that the PSS-based lensing devices offer good performance with the advantage of being low-cost, thin and lightweight.

Chapter 7 presents the first proof of concept of a PASS, which consists in a flat-topped beam antenna.

The last chapter summarises the work, provides a general conclusion, describes future work to be performed and lists the contributions of this thesis.

CHAPTER 2 Background

2.1 Introduction

This chapter presents some useful background information related to the novel concepts of a phase shifting surface (PSS), a phase and amplitude shifting surface (PASS) and some of their applications. Conventional lens antennas are presented in Section 2.2 whereas alternatives to conventional lens antennas are presented in Section 2.3. Section 2.4 focuses on microwave holography. The chapter is concluded in Section 2.5.

2.2 Conventional Lens Antenna Technologies

Traditionally, high-gain antennas designed for microwave applications have consisted of reflectors, lenses, or planar arrays of low-gain elements. Each technology has its strengths and weaknesses, and the requirements of the application will usually dictate the type of antenna to be selected. A lens is a device that transforms an incoming phasefront into some desired outgoing phasefront, usually from a spherical to a planar one when used as a transmitting device, or the other way around as a receiving device. Conventional dielectric lenses are shaped, generally leading to a plano-hyperbolic profile which introduces the required phase delay for phase transformation and consequently obtaining the desired output phasefront. The background of such lenses is given in Appendix B.

Dielectric lens antennas, like reflector antennas, generally have a high radiation efficiency and, for fixed-beam applications, have good electrical performance; however, both types suffer from having a large volume. Lenses offer certain advantages over reflectors, such as the elimination of aperture blockage by the feed antenna and reduced sensitivity to manufacturing tolerances, both of which are important for higher frequency designs. However, microwave lenses have the major disadvantage of occupying a large volume because of their large thickness (especially for designs with small ratios of focal length F to diameter D, commonly denoted as F/D ratios) and therefore they are bulky and heavy.

2.3 Transmissive Free-Standing Phase Correcting Antennas

This section presents a survey of free-standing phase correcting lens antennas that have been proposed for use in the microwave regime.

2.3.1 Shaped dielectric lens

The most common type of transmissive free-standing phase correcting device is the dielectric plano-hyperbolic lens antenna (DPHLA) reviewed in Appendix B. It consists of a shaped lens with no step function having a hyperbolic profile generally made out from machining or moulding. At microwave frequencies, such lenses have a large electrical thickness, especially for small F/D values. Figure 2.3-1 presents a shaped lens. The aperture efficiency of a shaped dielectric lens is typically around 50%.

2.3.2 Fresnel lens and Fresnel zone plates

The overall lens thickness can be reduced by removing certain portions of the dielectric based on a zoning technique. The resultant lens is known as a Fresnel lens or a

Figure 2.3-1: Dielectric plano-hyperbolic lens antenna (courtesy of CRC).

phase-correcting Fresnel zone plate. Fresnel lenses and phase-correcting Fresnel zone plate antennas (PC-FZPA) are also reviewed in Appendix B. Although these lenses are thinner than the corresponding DPHLA, they suffer from a reduced bandwidth and in many cases a lower aperture efficiency resulting from a reduction of the phase correction efficiency. Traditionally, PC-FZPAs are realised by concentric grooves in a material with uniform dielectric constant. A PC-FZPA is shown in Figure 2.3-2.

Figure 2.3-2: Phase-correcting Fresnel zone plate antenna (courtesy of CRC).

A Fresnel zone plate antenna (FZPA), also reviewed in Appendix B, is another alternative. It is not a phase correcting structure but rather an amplitude correcting one. It can be made extremely thin, but its aperture efficiency is significantly reduced compared to the phase-correcting lenses [HRIS00]. Typically, the aperture efficiency of an FZPA is between 10% and 15%. An FZPA is presented in Figure 2.3-3.

2.3.3 Metallic waveguide lens

In the middle of the twentieth century, Kock introduced metallic waveguide lens antennas [KOCK46] consisting of parallel conducting plates used as hollow waveguides to control the phase velocity of the electromagnetic waves propagating through the plates. They can be regarded as an early transmitarray concept, which will be discussed in Section 2.3.6. In this configuration, the wave passing through the plate has a higher phase velocity than free-space, which is opposite to that of dielectric materials for which the phase velocity is lower than in free-space. The motivation behind the use of metallic

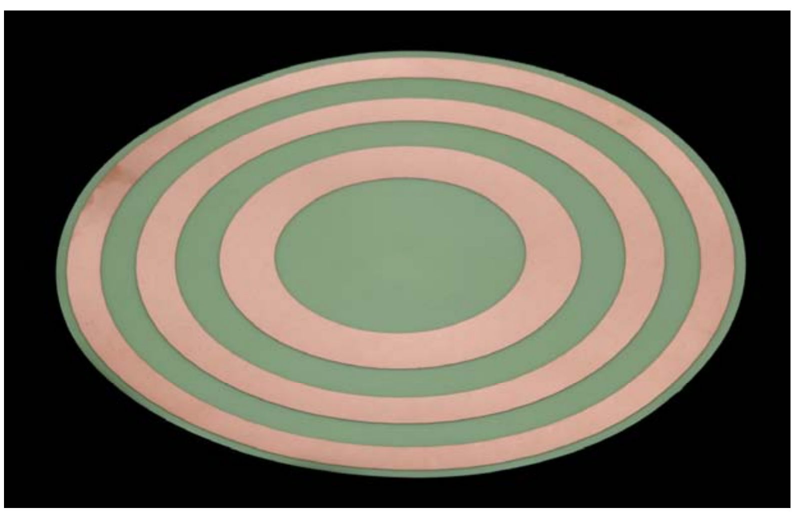

Figure 2.3-3: Fresnel zone plate antenna.

waveguides is to reduce the weight of microwave lenses. However, they suffer from thickness issues, bandwidth limitations and polarisation sensitivity. A prototype is shown in Figure 1 of [KOCK48].

2.3.4 Artificial dielectric lens

Another notable study by Kock is that of artificial dielectric lenses [KOCK48]. The concept of an artificial dielectric has been well documented by Cohn in [COHN54] and will only be briefly explained here; for additional information on artificial dielectrics, the reader can refer to [THOU60] and [COLL91]. Artificial dielectrics consist of a series of thin, parallel dielectric layers containing two-dimensional arrays of small metallic implants whose size and spacing are small compared to the wavelength. The size of the metallic implants and their spacing is designed to achieve a desired effective dielectric constant. A lens designed using this concept typically requires many dielectric layers. It is not thinner than a dielectric lens of equivalent dielectric constant, but can be designed of light-weight material and can thus be lighter than a solid dielectric.

Kock's idea was to reproduce the relative permittivity of a higher dielectric material by inserting metallic implants (thin strips or disks) within a dielectric host of lower relative permittivity, in this case foam ($\varepsilon_r \approx 1$). The phase correction is achieved by shaping the thick artificial dielectric the same way a dielectric material is shaped to traditionally form a lens. Since foam is a fairly light material, the advantage is a significant weight reduction, although the thickness is not reduced since the lens remains shaped, as mentioned above. (The foam slabs can be made all of the same size, leading to a flat lens; on the other hand, the strip distribution must ensure that the correct effective permittivity profile is achieved.) Figure 12 in [KOCK48] presents a prototype of an artificial dielectric lens.

In [ABEL93], an artificial dielectric which presents variable metallic implants throughout the aperture of the lens is used to design a lens. Since a single layer was not enough to allow for sufficient phase correction, many layers were inserted in cascade, spaced by thick layers of low dielectric constant. Although this results in a flat lens, the thickness remains particularly high. Figure 2.3-4 depicts this artificial dielectric lens.

In [PETO03b], a uniformly thick PC-FZPA designed from artificial dielectric principles is reported, in which the artificial dielectric constant is varied over the aperture of the lensing device to achieve the desired phase correction. In this case, there are no metallic implants to increase the dielectric constant; instead, the artificial dielectric is obtained from perforation of the dielectric material and results in lower dielectric constant in the perforated regions compared to the dielectric constant of the host material. The

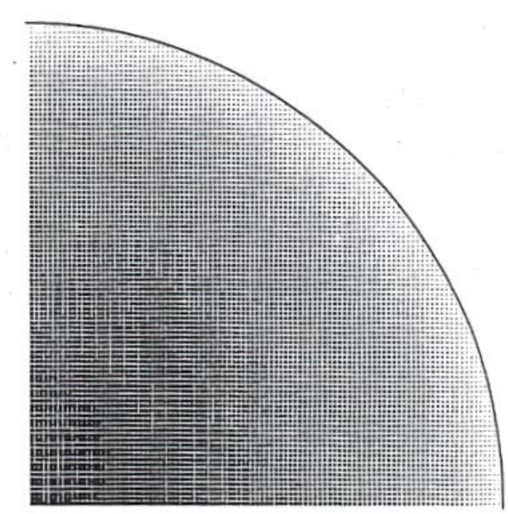

Figure 2.3-4: Portion of an artificial dielectric lens antenna. Reprinted with permission from [ABEL93]. © European Microwave Association, EuMA.

fabrication process thus involves numerous perforations requiring different diameters, is rather complicated and time-consuming. Furthermore, there is really no additional thickness reduction obtained compared to a traditional grooved PC-FZPA. Figure 2.3-5 shows a photograph of a perforated dielectric lens prototype.

2.3.5 Flat lens antenna using microstrip patches

A limited amount of research has been carried out to significantly reduce the thickness of phase-correcting lenses at microwave frequencies. The first true thin, flat phase-correcting free-standing device was introduced in the mid 1980's by McGrath [McGR86] and was revisited in the mid 1990's by Pozar [POZA96]. The concept makes use of front and back layers of resonant microstrip patch antennas connected by varying lengths of transmission lines. The length of the transmission lines is carefully adjusted at every location on the surface in order to perform an overall lens function, i.e. to obtain the

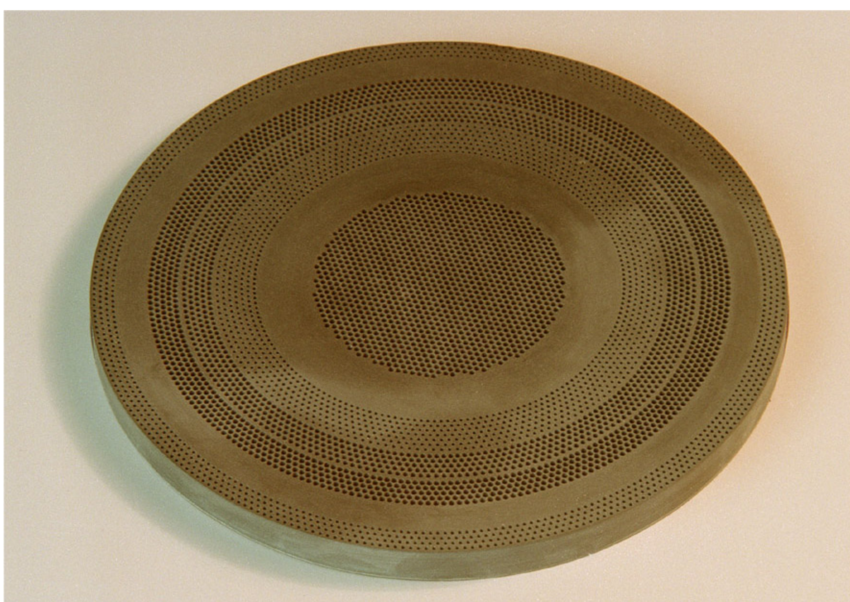

Figure 2.3-5: Perforated dielectric lens prototype (courtesy of CRC).

desired phase transformation between the incoming and outgoing wavefronts. The prototype is a thin, single-piece free-standing device that uses the mature photolithographic (wet chemical) etching process. However, it suffers from two major drawbacks: increased complexity of fabrication, resulting either from the use of vias [McGR86] or a large number of layers [POZA96], and quantisation error due to the fact that a single patch antenna occupies a significant area of the lens aperture. Note that the microstrip patch sizes are on the order of half a guided wavelength, and the separation between patches has to be less than half a free-space wavelength to avoid grating lobes. This quantisation error reduces the overall aperture efficiency of the lens. The reflection loss, transmission line loss and bandwidth limitation are also of concern. An interesting point in [POZA96] is that the author provides valuable explanations on the problem of using an FSS as a lensing device, namely limited bandwidth and reduced phase shift range. The design element for realising a flat lens antenna using microstrip patches introduced by McGrath is presented in Figure 2.3-6.

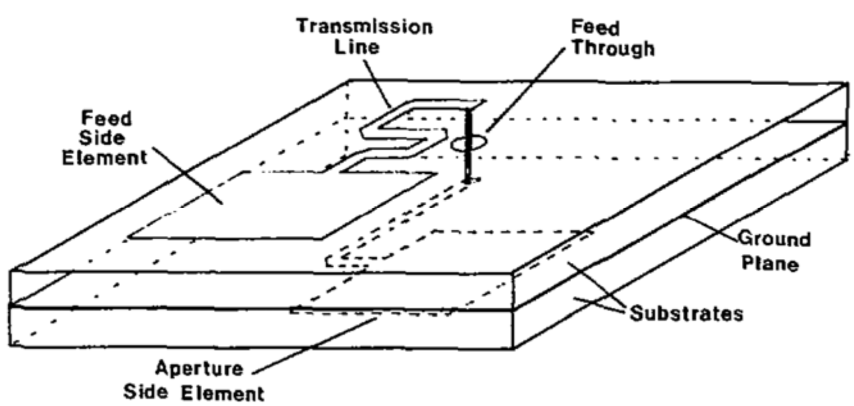

Figure 2.3-6: Design element for realising a flat lens antenna using microstrip patches. Reprinted with permission from [McGR86]. © 1986 IEEE.

2.3.6 Transmitarray

A transmitarray is a free-standing structure that is composed of an array of multiple discrete elements used as a transmitting device. The name is inspired from the reflectarray, but is used as a transmitting surface rather than a reflective surface. When made out of printed metallic elements, both the reflectarray and the transmitarray are flat. As a reflectarray can replace a conventional reflector, a transmitarray can replace a conventional lens. However, a single layer is not enough to realise a significant phase shift; as a result, many layers need to be cascaded to realise a good antenna operation.

Prototype transmitarrays consisting of a few dielectric sheets were demonstrated in [CHAH06], [CHAH07] and [RYAN10] for single-band and dual-band, where the constitutive layers are inspired by frequency-selective surface (FSS) elements. Figure 2.3-7 presents a four layer circularly polarised transmitarray operating at 30 GHz. Although thinner than a traditional dielectric lens, one drawback with current transmitarray designs is the requirement for an air gap between dielectric layers in order to maximize gain. This increases the mechanical complexity of the design and does not allow for achieving an optimum thickness reduction. In the cases mentioned above, the resulting structure is fairly light and the thickness is reduced, but not to a point where it could be considered to be a significantly small fraction of a wavelength.

2.4 Development and Application of Microwave Holography

A literature review relevant to the work presented in this thesis would not be complete without mentioning some of the milestone work performed on holography since

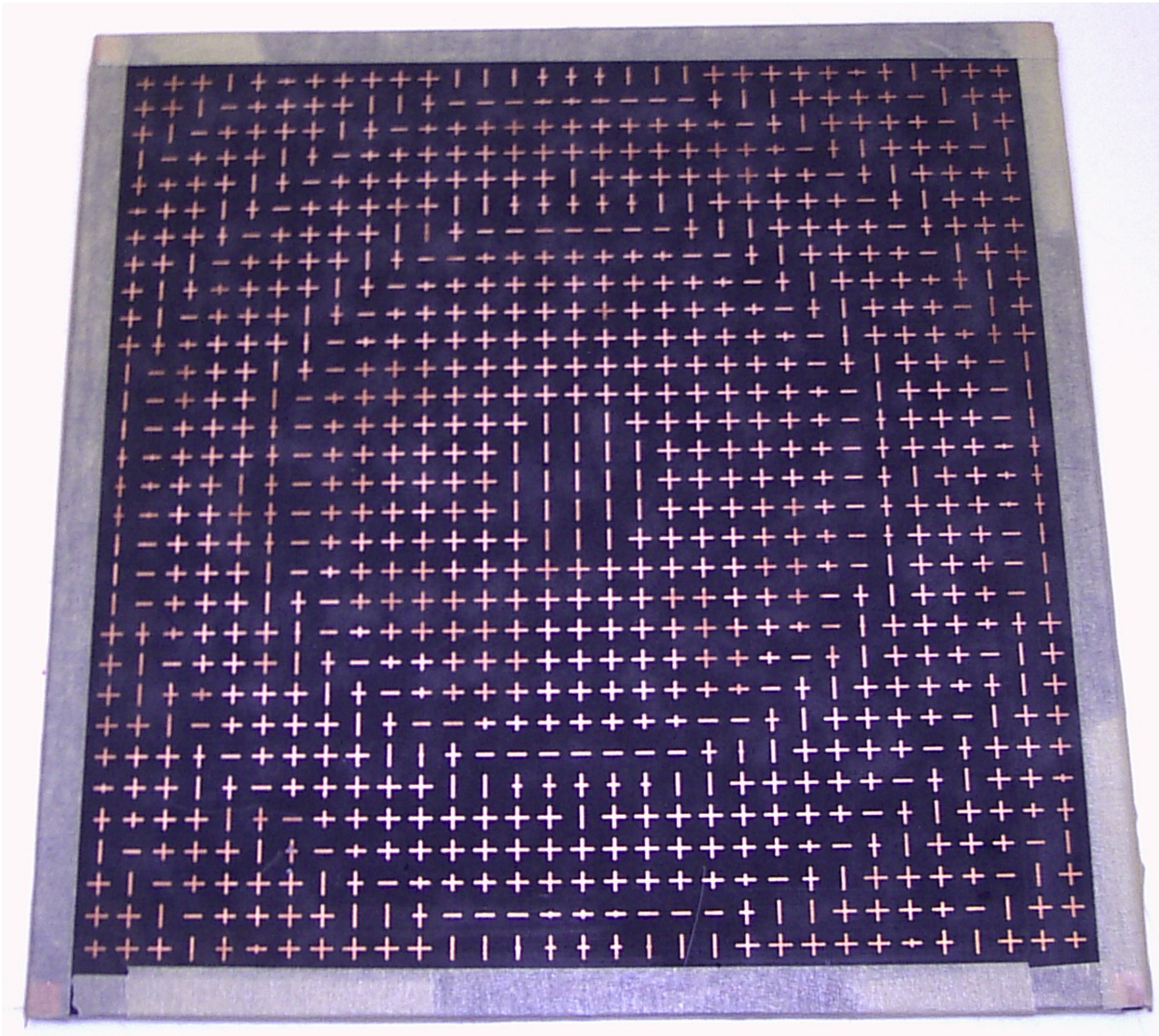

Figure 2.3-7: Four layer circularly polarised transmitarray antenna operating at 30 GHz (courtesy of CRC).

the 1960's. Free-standing structures used at microwave frequencies for introducing a desired phase shift profile are of great importance not only in lens antenna research but also in microwave holography. In this section, the pioneering work on microwave holography in general and microwave holography applied to the design of antennas are addressed.

2.4.1 Microwave holography and *computer-generated* holograms

In the 1960's and early 1970's, many papers on holograms were published, including the milestone papers by Kock [KOCK68] and Goodman [GOOD71]. Even though Kock's paper [KOCK68] is one of the first on microwave holography, the foundations for practical microwave holograms was introduced by Brown and Lohmann [BROW69]. The latter reference describes computer-generated holograms which, unlike conventional holograms, do not require the use of recording media and the interference of beams for generating them, but rather numerical data. The concept was demonstrated at optical wavelengths but is also easily applicable to non-optical wavelengths such as microwave frequencies. This result is of significant importance for realising microwave holograms since the absence of efficient sensitive recording media in the microwave regime makes it difficult to generate holograms by interference means. Computer-generated holograms are still widely used nowadays. The term *computer-generated* may appear obsolete, but has been kept over the years [GOOD96] and, consequently, it will be used in this thesis.

2.4.2 Kinoform and *detour phase* concept

In the late 1960's and early 1970's, some work was carried out to control the phase of microwaves, although with only limited success and a high degree of complexity. Nevertheless, it is worth mentioning the work performed on the so-called *detour phase* concept, in which the phase is controlled by means of moving the position of lines or slits within a hologram grating [TRIC70], [BROW66]. The other relevant concept is that of the so-called *kinoform*, which is similar to a hologram but operates only on the phase (assuming a constant amplitude) [LESE69]. However, both the *detour phase* devices and kinoforms suffer from a lack of practicality due to the complexity for implementing the phase shifting.

2.4.3 Antennas realised using holographic principles

Since it was difficult to implement phase holograms at microwaves, the research in microwave holography rapidly focused on amplitude holograms. Although amplitude holograms are much less efficient than phase holograms, binary versions of such holograms turn out to be more efficient than the holograms with a continuous range of amplitude transmittance [BROW69]. This result discouraged the development of holograms with a full range of control of the amplitude; instead the research focused on binary holograms. This is true for both optical and non-optical wavelengths, including microwaves, in which regime the realisation of binary holograms could be easily achieved by means of a photolithographic (wet chemical) etching process; the presence of metallisation corresponds to null transmittance and the absence of metallisation corresponds to total transmittance. Work on the realisation of antennas using holographic principles in the microwave regime is presented in [IIZU75], [LÉVI01], [HIRV97] and [ELSH04]. Figure 2.4-1 presents an antenna realised using the holographic principles.

2.5 Conclusions

In this chapter, background information relevant to the work on a phase shifting surface (PSS) and a phase and amplitude shifting surface (PASS) was reported. In particular, the work on alternative lens antenna technologies, including the work on

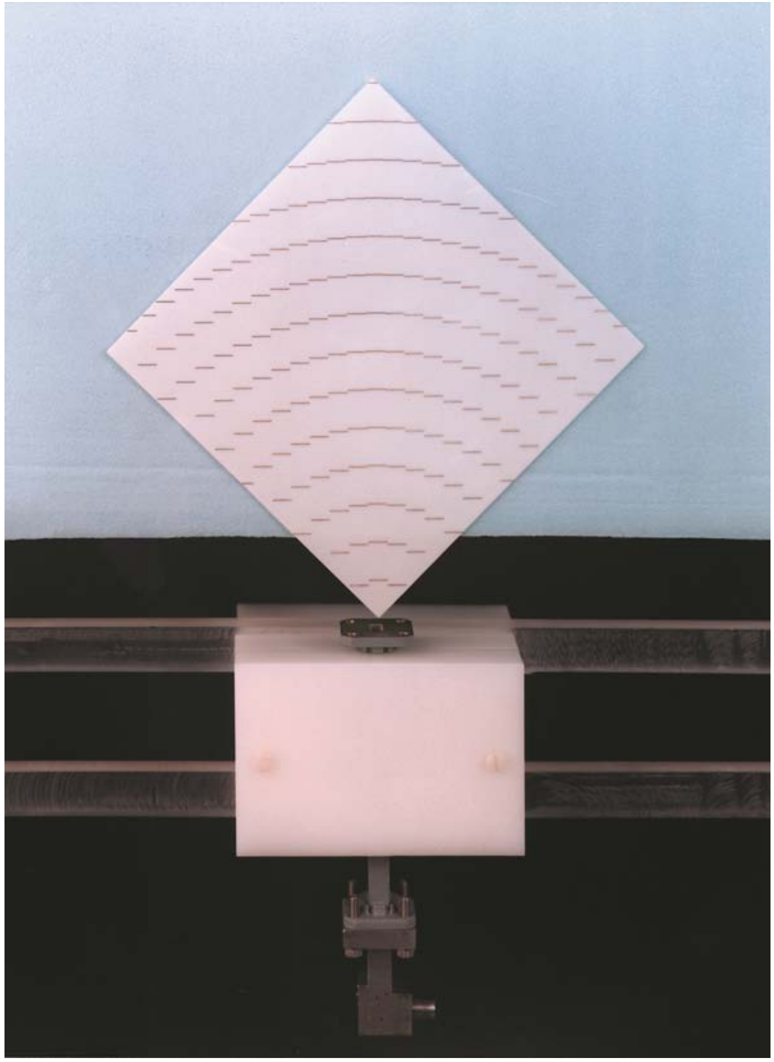

Figure 2.4-1: Antenna realised using the holographic principles (courtesy of CRC).

artificial dielectric lenses, lenses made with microstrip patches, and transmitarrays. In addition, some work on microwave holography was reviewed, including that on *detour-phase*, kinoform and antennas based on amplitude holograms.

In the next chapter, the PSS/PASS concept will be described in detail. It will be shown that this concept is applicable to the design of phase-correcting devices. These designs are presented in Chapters 4 to 7.

CHAPTER 3 PSS/PASS Concept

3.1 Introduction

This chapter presents the concept of the phase shifting surface (PSS), and the phase and amplitude shifting surface (PASS). The PSS/PASS concept constitutes the major contribution of the thesis. This chapter describes practical considerations for realising the PSS/PASS, explains how the PSS/PASS operates and provides meaningful information regarding the modelling.

The basic concept is presented in Section 3.2. The description of the unit cell – the fundamental constituent of the PSS/PASS – is presented in Section 3.3. Two specific types of unit cells – namely the strip and the square – are specifically described in Sections 3.4 and 3.5, respectively. The equivalent circuit model of the PSS/PASS unit cell is introduced in Section 3.6. The PSS/PASS is discussed in Section 3.7. The chapter is concluded in Section 3.8.

3.2 Basic Concept

As its name suggests, the phase shifting surface (PSS) is a free-standing surface or screen that allows for controlled changing of the phase of an electromagnetic wave propagating through it. The phase and amplitude shifting surface (PASS) acts in a similar fashion, but in addition to providing a prescribed amount of phase shift, it also controls the amplitude. In order to transform a radiated beam from a feed antenna to achieve certain characteristics such as antenna gain enhancement or beam shaping, the PSS/PASS is made non-uniform over its transverse cross-section, since every location on its surface has to provide different phase (and/or amplitude) shifts. In fact, the PSS/PASS surface is divided into a rectangular lattice of unit cells, with each cell designed to provide a predetermined amplitude weighting and phase shift. For this reason, the unit cell physical parameters are of crucial importance since the combination of these physical parameters leads to different phase (and/or amplitude) shift. The different unit cells are analysed independently by electromagnetic simulations; the process is described in more detail in Section 3.3.1. The combination of many different unit cells results in a final PSS/PASS design.

In traditional phase shifting designs, such as lenses or phase gratings, the phase shifting is achieved by varying the thickness of a dielectric slab over the aperture of the device, as outlined in Appendix B. In the optical regime, the wavelengths are short and this traditional approach results in physically compact designs. It is well known that the physical size needed to achieve a given phase shift is proportional to the wavelength, assuming that the dielectric constant or index of refraction is unchanged. Consequently, as the wavelength is increased, the physical size of the phase shifting structure will increase proportionally, leading to bulky designs at microwave and millimetre wavelengths.

For the reason stated above, conventional lens antennas are still only marginally practical in these wavelengths since they are thick, heavy and bulky. Furthermore, conventional lens antennas require machining or moulding, which are expensive fabrication processes when compared to other types of fabrication techniques in these frequency bands, such as etching thin and flat conductor-clad sheets of dielectric material through photolithographic (wet chemical) etching, mechanical etching, laser etching, or conductive pattern printing using conductive ink on unclad thin and flat dielectric sheets. Consequently, the idea would be to use the low-cost approach traditionally used in microwave engineering in order to design lens antennas. The lens would then be flat, with a constant thickness. The dielectric constant of each layer of dielectric material could be the same or could be different, although in the work presented hereafter it is the same throughout. If multiple layers are to be used, their number would have to be limited in order to reduce the complexity of fabrication, the thickness of the surface and the overall weight. As a result, the material composition and thickness does not vary over the transverse cross-sectional area of the free-standing device; what varies is the conductive pattern, which locally (i.e. at the unit cell level) introduces an amplitude and phase change to the transmission coefficient. This concept is different from the usual concept of a device introducing a phase shift, although some previous alternative technologies, such as the ones reported in Section 2.3, were based on a similar approach.

The idea of generating different phase shifts from a thin and flat dielectric sheet and a photolithographic (wet chemical) conductor etching process is devised by analogy to newspaper printing, where the grey tones are obtained from different size of small black dots [WATE66a] in a given, predetermined array. The ink on paper in the newspaper printing process then becomes the metal on dielectric in the microwave PSS/PASS structure developed in this thesis.

3.3 Unit Cell Design

This section describes the unit cell of the phase shifting surface (PSS) or phase and amplitude shifting surface (PASS). The unit cell is the fundamental constituent of the PSS/PASS. The analysis of the unit cells is of great importance: the dimensions of the conducting elements of the unit cell are varied in order to obtain different results of transmission amplitude and phase. The arrangement of different unit cell elements over the area of the PSS/PASS results in a free-standing device that is used to perform the desired function.

Each unit cell has unique physical dimensions of conductor printed on the different layers; these unique physical dimensions lead to a unique amplitude and phase for the transmission coefficient. Different physical dimensions of conductors are used within a unit cell to locally accomplish a given transformation of the electromagnetic wave. The transverse cross-sectional location in the *xy*-plane of the PSS/PASS of the different unit cells allows for achieving a given operation on the beam, such as gain enhancement or beam shaping.

The different unit cells used in a PSS/PASS are analysed in the context of a periodic structure, similar to the one shown in Figure 3.3-1. A periodic structure analysis allows for significant reduction in computer resources and time, while leading to a good comprehension of the local behaviour of the structure. This will be explained in further detail in Section 3.3.1. From these unique electromagnetic properties, the different possible types of unit cells allow for designing a complete structure such as a PSS or a PASS without having to perform simulations or computations of the complete structure, which would be extremely computer-intensive and time-consuming. This is why the analysis of unit cells is of primary importance and constitutes the initial step in the design of PSS/PASS structures.

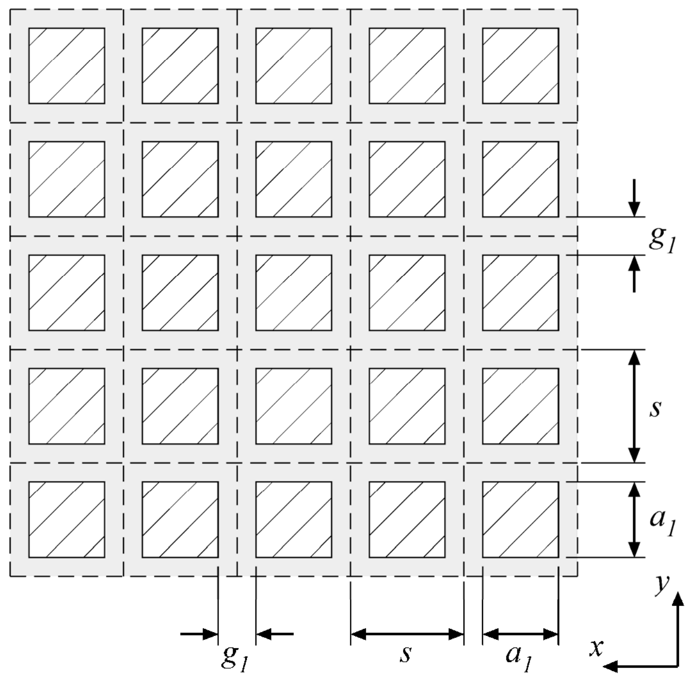

Figure 3.3-1: Front view of the square uniform periodic structure composed of square unit cells with square metallic patches (the dielectric is shown in grey and the metal is shown as hatched).

3.3.1 Case characterisation and periodic structure approach

The conductive elements on the different dielectric sheets constituting the PSS/PASS have to be selected carefully. As a preliminary study, the first electromagnetic simulations were conducted on square unit cells partially covered with centred square patches [GAGN08], similar to those shown in Figure 3.3-1. To perform such an analysis, it is assumed that the structure is infinitely periodic since it constitutes a good way for obtaining a behaviour of the unit cell. This kind of analysis assumes that the neighbouring cells are identical to the single cell being studied; consequently there is no unpredictable influence of the neighbouring cells. Of course, the result obtained constitutes an ideal case where all cells are identical, which is not what occurs in a practical case since, in order for the local amplitude and phase to be different at every location on the surface (that is, for different *xy*-locations), the PSS/PASS is designed to be constituted of unit cells with different physical size of conductor. Since the PSS/PASS surface is electrically large, it is impractical to analyze the full structure using numerical methods due to the large memory storage and computational time requirements. Instead, the structure is analyzed using a similar approach to the analysis of reflectarrays [HUAN07]. Each unit cell is analyzed within an infinite periodic lattice of identical unit cells, which can be modelled through the use of appropriate boundary conditions, described below. Such an analysis approach is computationally more efficient and can be used to fairly accurately predict the result of the actual PSS/PASS structure. In practice, the PSS/PASS is not an infinite array of identical unit cells, and there will be some differences in the results. These differences will be addressed later.

In terms of analysis, it is clearly not possible to consider an infinite structure in the simulations. To overcome this problem, a special technique is used, such as that addressed in the next paragraph. It is true that the infinite size of the periodic structure can be truncated to a finite size containing a large number of cells. However, there will be an error associated with the size of truncation. The number of cells required for a valid analysis could be determined by convergence studies. Nevertheless, even though this approach may lead to a marginal error for many unit cell elements, the size of the problem that has to be analysed will be substantial and potentially reaches limits beyond the available memory capacity of modern computers. Furthermore, for such sizable problems, the simulation time may be of significant length.

Instead, from periodic structure theory [CWIK08], it is well known that it is not required to simulate a complete infinite periodic structure, or even substantial part of it, in order to obtain its electromagnetic behaviour. Using the differential equation-based electromagnetic simulation methods to be used in this thesis, the behaviour may be obtained by simply using appropriate electromagnetic boundary conditions around a single unit cell from which the infinite periodic structure is constituted, as long as the following rule is respected:

$$s < \frac{\lambda_0}{1 + |\sin \theta_{\max}|} \tag{3.3-1}$$

where s is the unit cell size, λ_0 is the free-space wavelength and $\theta_{\max}$ is the maximum angle of the incident wave measured normal to the surface, i.e. from the z-axis. For a normal-incident plane wave, $\theta_{\max} = 0°$ and s < λ_0; in the worst case, $\theta_{\max} = 90°$ and s < $\lambda_0/2$. This is the condition where a single main beam is allowed in visible space.

In the electromagnetic simulations discussed in this chapter, the PSS/PASS is positioned in the xy-plane, the electromagnetic waves incident on the structure are assumed to be plane waves propagating in the +z-direction, the incident electric field is selected to be polarised along the y-axis and the incident magnetic field is selected to be polarised along the x-axis. The assumption of a normally incident plane wave constitutes an approximation since, for most antenna applications, the incoming wave onto the structure made of PSS/PASS is not plane and the angle of incidence is not necessarily normal. This point will be addressed in Section 3.7.4. Nevertheless, the plane wave assumption in the simulations is found to lead to good results, as will later be shown.

The simulations conducted on the structure were performed using a commercially-available full-wave simulation package employing the finite-difference time-domain

(FDTD) technique. The commercial package is called EMPIRE XCcel™ and is developed by IMST GmbH [EMPI07]. This software package was used for its short simulation time, broadband response and affordability. In the FDTD simulations conducted on the structure, a single unit cell is simulated by placing perfect electric conductors parallel to the *x*-axis and perfect magnetic conductors parallel to the *y*-axis at the unit cell boundaries, as shown in Figure 3.3-2(a). This enforces normal-incidence plane-wave propagation and an electric field polarisation along the *y*-direction. The unit cell size has to be electrically small, i.e. less than a free-space wavelength for normal incidence and less than half a free-space wavelength for any incidence angle, for such a configuration to be able to mimic the infinite periodic structure shown in Figure 3.3-1 without the problem of generating propagating higher-order Floquet modes. Consequently, these simulations allow for

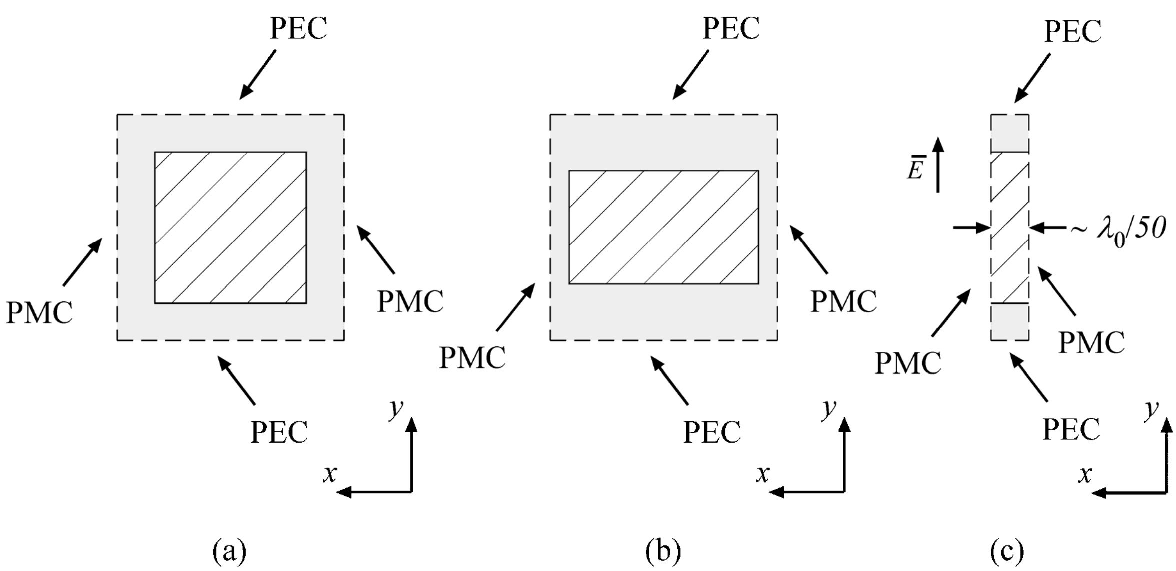

Figure 3.3-2: Front view of the unit cell with boundary conditions as used in the simulations; (a) square two-dimensional unit cell with square conductive element, (b) square two-dimensional unit cell with rectangular conductive element, (c) one-dimensional unit cell with strip conductive element (the dielectric is shown in grey and the metal is shown as hatched).

obtaining the amplitude and phase of the transmission coefficient under the assumption of an infinite periodic structure. In the most general case of a non-periodic structure, such as for the current usage of the PSS/PASS, the infinite periodic assumption can be used to translate the results to a local region of the multi unit cell structure corresponding to the same unit cell dimensions. Proceeding in such a way usually leads to accurate results.

The parameters to be tuned in the unit cell simulations are shown in Figure 3.3-1. In the simulations of the PSS/PASS unit cell, the unit cell size s was fixed while the patch size a_1 was varied according to the range $0 \leq a_1 < s$, where $a_1 = 0$ corresponds to the case of the bare sample. This is the simplest form of PSS/PASS unit cell. More elaborate unit cells, albeit based on this simple design, will be presented in Sections 3.4 and 3.5.

3.3.2 Choice of basic parameters

The parameters for which the present study was conducted are presented in the following sections.

3.3.2.1 Frequency of operation

In order for the PSS/PASS concept to be practical, one must select a frequency band at which PSS/PASS designs can show significant improvement in terms of size, weight and cost compared to conventional technologies. Therefore, it was decided to use a frequency of operation of 30 GHz, at which frequency the free-space wavelength λ_0 is approximately equal to 10 mm. This operating frequency is in the Ka band, which is a practical band for prototyping because of the size being neither too big nor too small, cost being a good trade-off between lower material cost but higher miscellaneous parts cost, mature photolithographic (wet chemical) etching process for the targeted frequency band,

and adequate facilities for measurement. Furthermore, the Ka band includes the multimedia satellite band, for which potential applications could be developed for the PSS/PASS.

It is worth mentioning though that the above selection does not mean that the PSS/PASS concept is strictly limited to this frequency band. In fact, the PSS/PASS could potentially be scaled to be used at higher and lower frequencies for other types of applications. This will be addressed in Section 3.7.2.

3.3.2.2 Unit cell size

Initially, s was selected to be equal to 1 mm, which is one tenth of a free-space wavelength, λ_0 [GAGN08]. This number was selected to minimise as much as possible the quantisation error which occurs when s is large with respect to λ_0. However, it was found that, for such a small s, the tolerance of the photolithographic (wet chemical) etching process used to fabricate the structure could not allow for small enough gaps g_1 (see Figure 3.3-1) between the patches to obtain a wide range of phases. It was then decided to increase the value of s in order to overcome this problem, and therefore s was set equal to 3 mm. This value still meets the requirement of (3.3-1) regarding the propagation of higher-order Floquet modes in the fast-wave region.

One of the problems arising with s = 3 mm is that the unit cell size is large with respect to the required discretisation in the FDTD-based electromagnetic simulation [EMPI07] since a high density mesh is required in some areas of the unit cells where the electromagnetic fields are strong. Consequently, the number of unknowns in the simulation problem is high and the simulations require a large amount of memory (RAM) and a high computer processor (CPU) speed, resulting in practical issues due to computer memory limitations and long simulation times. Since the simulations have to be repeated for many different cases of patch size a_1, the overall simulation time becomes huge. In Section 3.3.3.2, a means of reducing the computation time by changing the unit cell etching pattern is presented.

3.3.2.3 Relative permittivity and thickness

The thickness and relative permittivity of a dielectric sheet are crucial parameters that need to be selected carefully while designing the PSS/PASS. For the PSS, the thickness and relative permittivity must be chosen to assure that the amplitude of the transmission coefficient is high when the sample is bare and also to ensure that the amplitude of the transmission coefficient will remain high for the large range of patch sizes needed to provide the required range of phase shifts. Choosing the thickness and relative permittivity of the bare sample that produce an amplitude transmission coefficient that is low will lead to sub-optimal cases for PSS applications. Surface plots of the amplitude and phase in the thickness versus relative permittivity space, as shown in Fig. 3.3-3, may be helpful in the selection of these parameters.

The addition of metallic elements onto and/or into (for the multilayer cases to be discussed in Section 3.4) an initially bare dielectric sheet or slab will change its transmission behaviour. It is reasonable to consider the infinitesimally small metallic elements as resulting in similar behaviour as the bare sample. As the metallic elements increase in size and/or density, the behaviour of the resulting structure will differ more and more from that of the initially bare dielectric slab. Consequently, the bare case constitutes

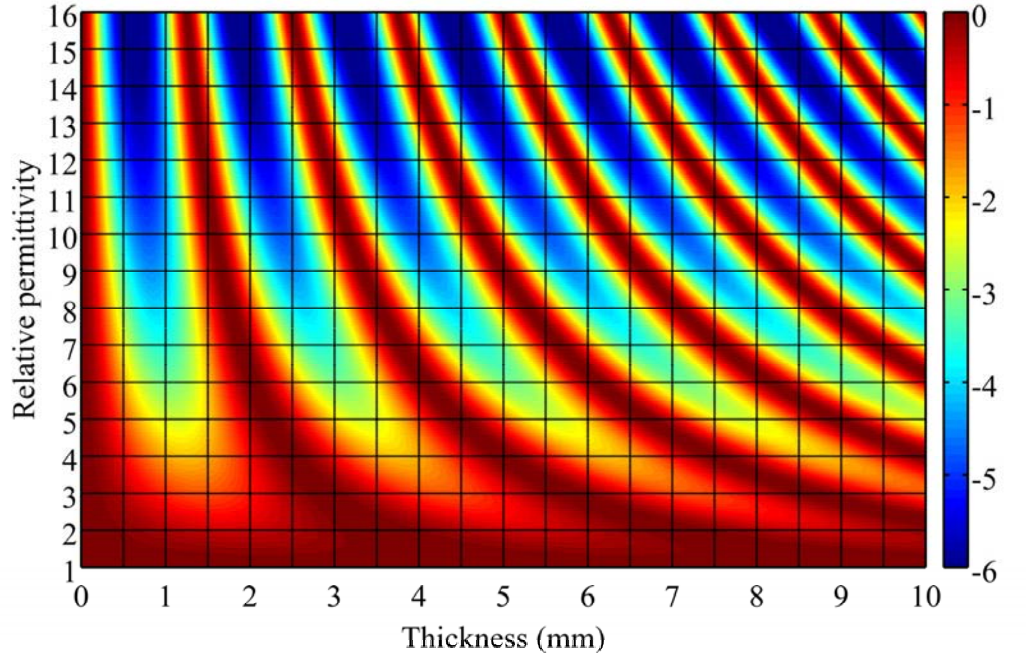

(a)

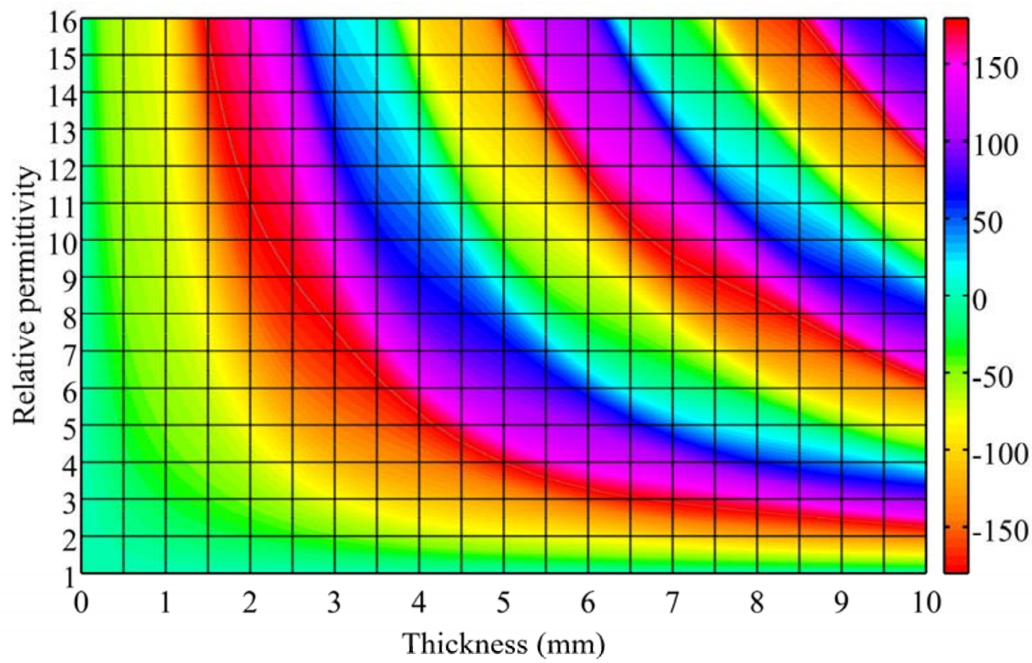

(b)

Figure 3.3-3: Transmission coefficient in the thickness vs relative permittivity space for a frequency of 30 GHz; (a) Amplitude (in dB), (b) Normalised phase (in degrees).

the starting point of the phase shift range that can be obtained from a dielectric slab with metallic elements. Intuitively, one may want to choose the dielectric constant and thickness in a region where the amplitude of the transmission coefficient is high (and remains high), and the phase of the transmission coefficient varies significantly. From Figure 3.3-3, cases with high thickness seem to have the potential for obtaining a large phase shift range while maintaining a high amplitude transmission coefficient. However, large thickness cases are not recommended because they are bulky, heavy and, since more material is required, more expensive. Consequently, a compromise must be reached.

The thinner the structure, the more attractive it is in terms of weight and material cost. However, if the structure is too thin, it will be difficult to obtain a good phase shift range. Similarly, the dielectric constant of the structure must be wisely selected. A low dielectric constant will not lead to a broad phase shift range while a high dielectric constant will lead to a small practical phase shift range due to the low amplitude of the transmission coefficient, either when bare or with conducting elements. After some preliminary studies, the dielectric constant was selected to be 2.2 and the thickness between 1 mm and 1.5 mm. From Figure 3.3-3, such values correspond to a region where the amplitude of the transmission coefficient is high. Sections 3.4 and 3.5 will reveal that selecting a dielectric material with the above mentioned parameters is not a problem for obtaining an acceptable phase shift range.

The choice of thickness and relative permittivity has been presented here mostly from an essentially qualitative point of view. In Section 3.6, more quantitative insight is given for the selection of these parameters.

3.3.3 Unit cell etching pattern

As previously mentioned, the initial unit cell etching pattern studied was that of a square conductive patch within a square unit cell. In this section, this approach is revisited and a new etching pattern based on a conductive strip is introduced.

3.3.3.1 Conductive square patch

The conductive square patch in a square unit cell lattice as shown in Figure 3.3-2(a) is a logical choice since, due to their symmetry, square elements can be used to support orthogonal polarisations. Furthermore, it will be shown in Section 3.5 that this configuration is almost perfectly polarisation-independent; this is also confirmed from the far-field measurement of a phase-correcting Fresnel zone plate antenna based on this unit cell design and presented in Section 6.8.

The conductive square patch can be easily modified into a conductive rectangular patch, as shown in Figure 3.3-2(b), while keeping the unit cell square. Such a configuration would support orthogonal polarisations, but the amplitude and phase of the transmission coefficient would be different for the two polarisations. This is an interesting concept that can bring polarisation-dependent behaviour, such as different focal point in a lens design or different beam shaping. This will be further addressed in Section 8.4.4.

Using square conductive patches in a square lattice, it is not possible to obtain a significant phase shift range from a single layer of conductive pattern [GAGN08]. Moreover, each case selected to provide a specific phase is at once also associated with resultant amplitude; the phase and amplitude response are dependent. In order to improve the phase shifting performance, a second layer of identical square conductive patches in the same square lattice is added on the back of the dielectric sheet; no additional dielectric is added. This results in a more significant phase shift range. However, square element unit cells require full three-dimensional simulation capabilities, which make them computer-intensive, requiring a high memory (RAM) capability and a long computation time.

3.3.3.2 Conductive strip

In order to reduce the simulation time as well as the computer memory (RAM) requirement, horizontal conductive strip elements rather than conductive patch elements are used, although the square patch elements will be revisited in Section 3.5. Unlike patch elements, strip elements extend to the boundary of the unit cell, on the left and right sides, as shown in Figure 3.3-2(c). Since there is no variation of the incident field or the geometry along the *x*-axis, the result is a one-dimensional unit cell rather than a two-dimensional unit cell as it repeats itself along the *y*-axis only. In principle, this allows for eliminating one dimension in the simulation and running the problem as a two-dimensional one. To analyse the structure, a commercial finite-difference time-domain (FDTD) simulation package [EMPI07] is used. Since the simulation package is a three-dimensional solver, it is not possible to run the problem as being intrinsically two-dimensional. However, the structure can be assumed to be periodic along the *x*-axis as well. Since the length of the strip equals that of the unit cell this simulates an infinitely long strip. This permits one to exploit the commercial code's periodic structure capability and the resulting computational simplicity of being able to determine the fields on a single unit cell. This is only a computational trick that produces useful results as it allows for significantly reducing the length along the *x*-axis. Consequently, the results obtained will be independent of the length of the unit cell along the *x*-direction. This has been confirmed by simulating the same case with different values for the unit cell width along the *x*-axis and obtaining the same results. To reduce the computation time, a very small value (roughly $\lambda_0/50$) was used for the unit cell along the *x*-axis. Another possibility to further reduce the simulation time is to implement an in-house code specifically written for this particular problem. Alternatively, a different numerical method could be used, such as the finite-element method (FEM) or the method of moments (MoM). This will be discussed further in Section 8.4.1.

When the strip element used for the unit cell in Figure 3.3-2(c) is transposed into its equivalent infinite periodic structure, the resulting structure is represented in Figure 3.3-4. Assuming a structure that varies along the *x*-axis only, such as a linear grating or a

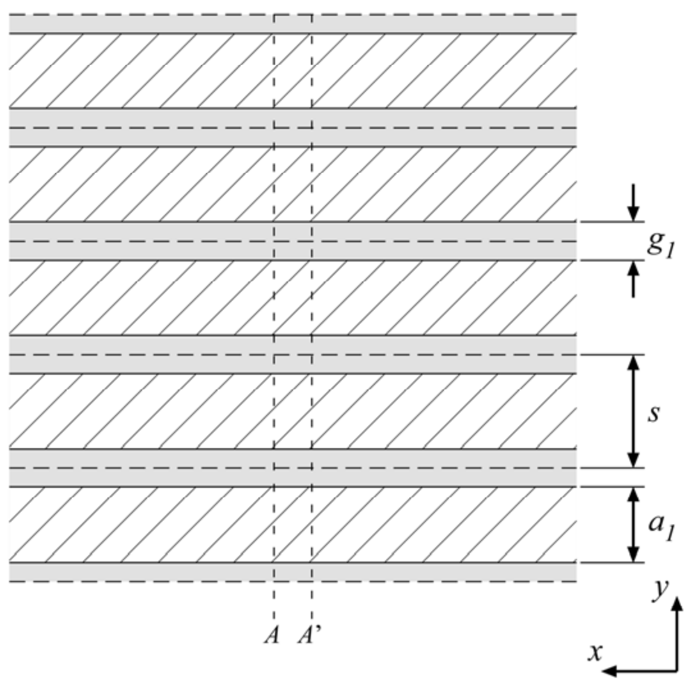

Figure 3.3-4: Front view of the uniform periodic structure composed of strip elements (the dielectric is shown in grey and the metal is shown as hatched).

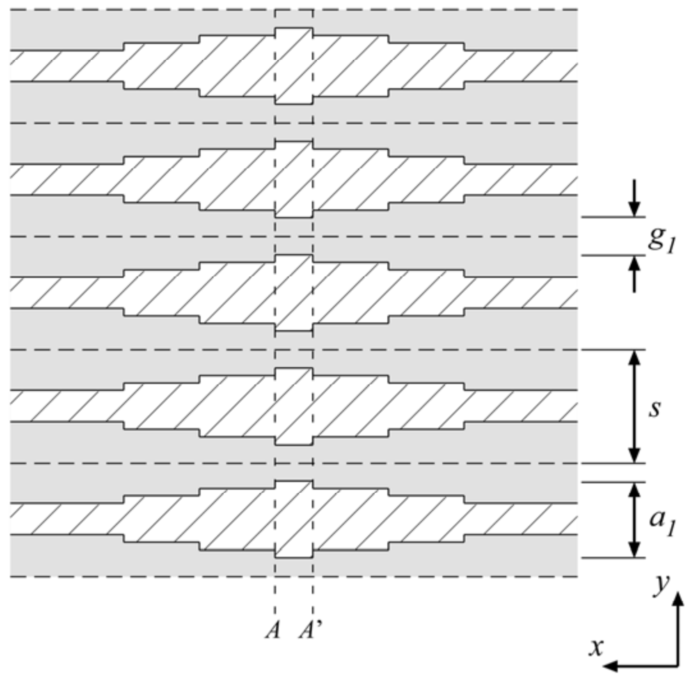

Figure 3.3-5: Front view of a non-periodic structure composed of strip elements (the dielectric is shown in grey and the metal is shown as hatched).

cylindrical lens, a region of the periodic structure, say from *A* to *A*', can be selected and transposed into a non-periodic structure like the one shown in Figure 3.3-5. In the design, the transmission coefficient result for the region from *A* to *A*' is then considered locally in the non-periodic structure of Figure 3.3-5. In other words, the result obtained with Figure 3.3-4 can be transposed into the region from *A* to *A*' of Figure 3.3-5. Even though a structure varying only along the *x*-axis is being considered and explained here, this is merely being done to generate design data, and the periodicity along the *y*-axis is not retained when using such data in lens design. This will be demonstrated in the design of full lenses in Chapter 6 and the concept will be demonstrated experimentally.

As mentioned earlier, the strip approach does present significant advantages over the square approach in terms of simulations, which directly translates into faster designs.

But it is not the only advantage of using such a configuration. The fact that the strip constitutes a continuously varying shape along the *x*-axis – as opposed to the square, which is quantised in both *x*- and *y*-axis – leads to less quantisation error. Furthermore, as previously reported [SIEV08], the bandwidth is increased when the fields more uniformly fill the volume of a unit cell, as is the case for a continuous strip compared to a discrete patch. In Section 6.9, experimental results on full lenses confirm the bandwidth advantage of the strip compared to the patch. Finally, because the element is strongly dependent on the orientation of the polarisation, it potentially allows for a reduction of the cross-polarisation level, but at the cost of a single-polarisation capability.

3.4 Strip Unit Cell

The following sections present the different cases that were studied in FDTD simulations [EMPI07] for the strip elements with a unit cell size of s = 3 mm using a dielectric constant of ε_r = 2.2. In the simulations, the conductive layers were assumed infinitesimally thin and perfectly conducting while the dielectric material was assumed to be lossless. The normalised phase assumes that a bare case, i.e. a case with dielectric layer only without any strips (strip width a_i = 0 mm, where i is the layer number unless otherwise specified), produces a phase shift of 0°. The frequency of simulation is 30 GHz.

3.4.1 Single layer

The simplest configuration consists of metallic strips on a single layer. In the present case, the arrangement is similar to Figure 3.3-2(c) with strips on the front layer only, as shown in Figure 3.4-1(a). In the simulation, the strips are assumed to be etched on a dielectric sheet of thickness h = 1 mm and relative permittivity of ε_r = 2.2. The width of the strip takes different values in the simulations, covering the range $0 \leq a_1 < 2.85$ mm, which corresponds to a gap of g_1 = 0.15 mm, the minimum achievable by the etching process used, since

$$g_i = s - a_i \tag{3.4-1}$$

where i corresponds to the layer number corresponding to Figure 3.4-1, unless otherwise specified. Figure 3.4-2 shows the simulated results of the transmission amplitude and phase using three different graphical representations. Of particular interest is the

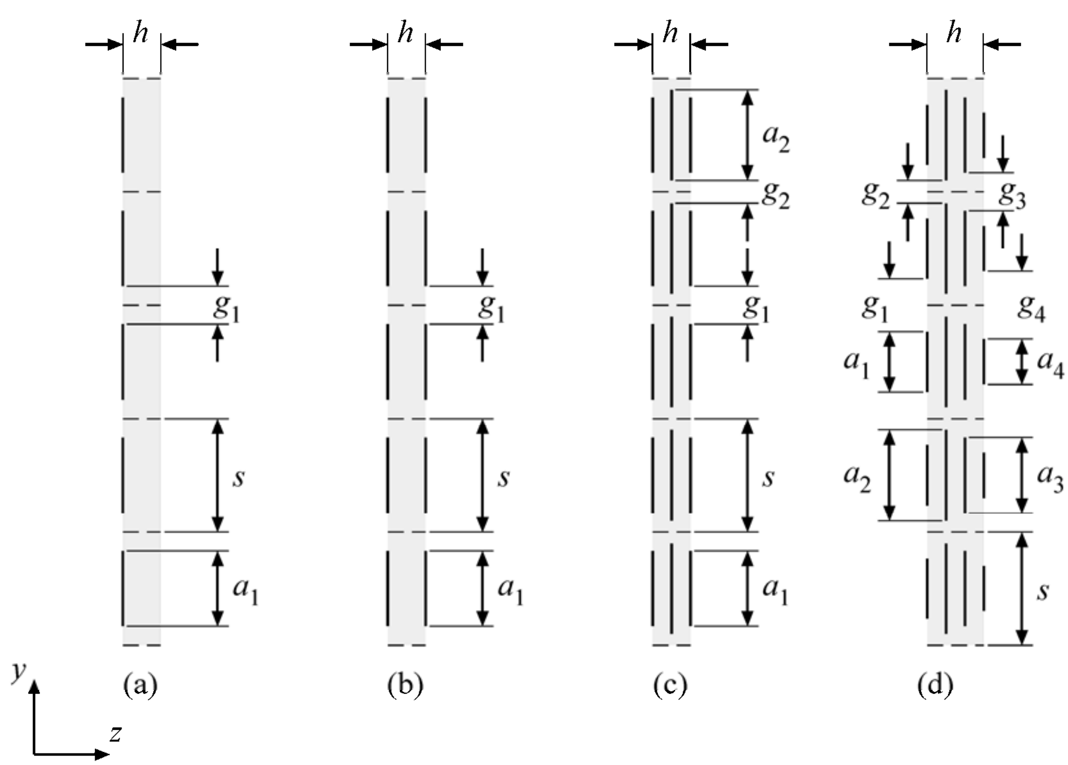

Figure 3.4-1: Side views of different configurations of periodic structures composed of strip elements; (a) single layer, (b) symmetrical double layer, (c) symmetrical three independent layers, (d) four fully independent layers. The dielectric is shown in grey and the metal is shown in black.

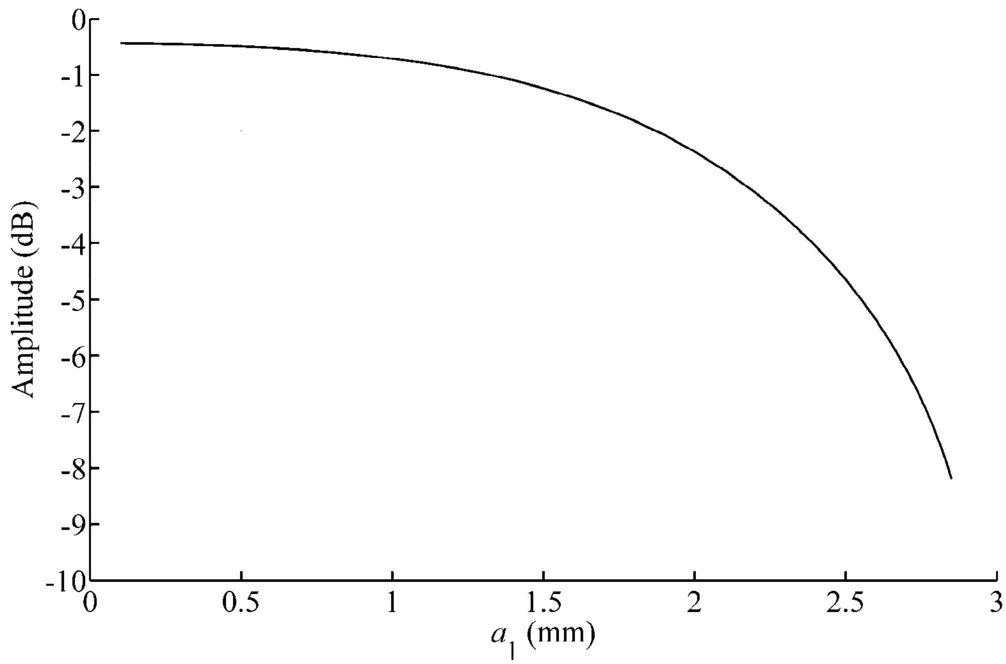

(a)

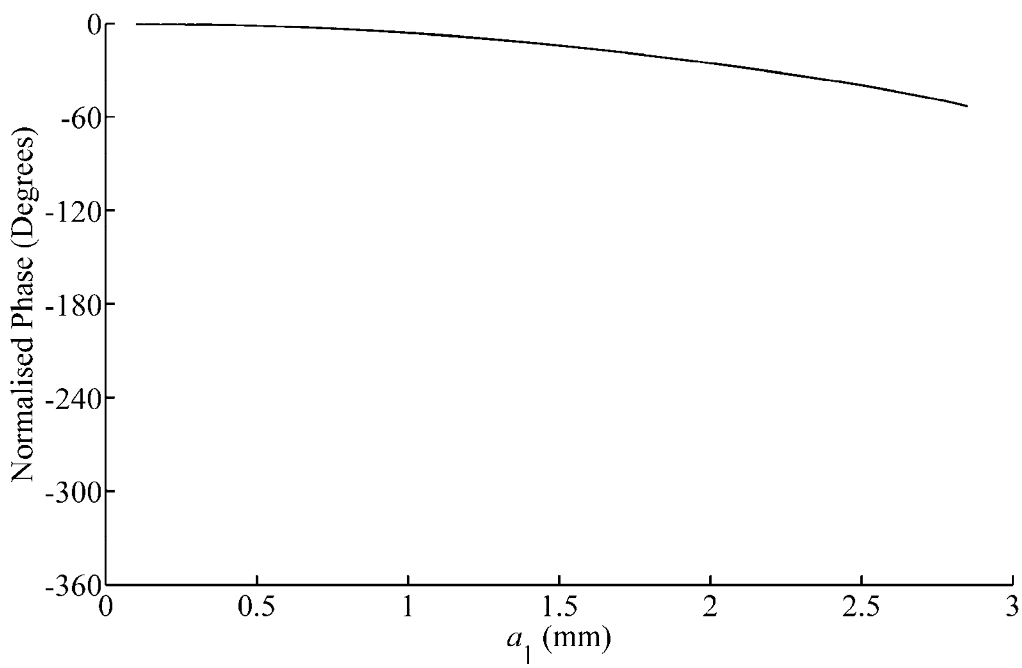

(b)

Figure 3.4-2: Simulated transmission results for single layer with s = 3 mm, h = 1 mm and ε_r = 2.2 at 30 GHz; (a) amplitude versus strip width, (b) normalised phase versus strip width.

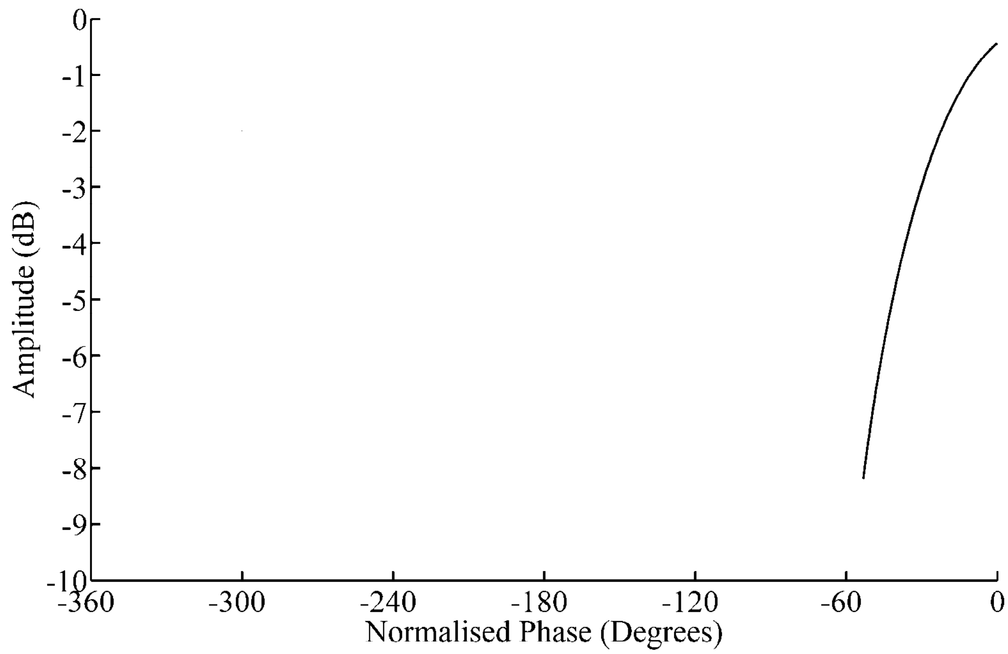

(c)

Figure 3.4-2 (continued): (c) amplitude versus normalised phase.

representation of Figure 3.4-2(c), where the strip width a_1 is not shown, but only the two parameters of the transmission coefficient, i.e. the phase and the amplitude, respectively along x and y. This view will turn out to be very useful when more than one physical parameter is used as it allows for visualising the essential information in a single succinct plot. The parameter information, i.e. the values of a_i's, is still known even if not shown.

Analysis of Figure 3.4-2 reveals that the amplitude and phase cannot be adjusted independently. This is expected since there is only one physical variable parameter, i.e. a_1. Furthermore, the phase shift range obtained is quite marginal as less than 60° is achieved for the complete strip width range, while the transmission amplitude is less than -3 dB for phase shifts greater than 30°.

3.4.2 Double layer

It is of course possible to etch layers of metallic strips on the front and back side of a single dielectric sheet, as shown in Figure 3.4-1(b). As for the single layer case, the strips are assumed to be etched on a dielectric sheet of thickness h = 1 mm and relative permittivity of ε_r = 2.2. Figure 3.4-3 presents in the same format as Figure 3.4-2 the simulated results of the transmission amplitude and phase. As for the previous single layer case, the amplitude and phase cannot be tuned independently since the front and back layers were assumed to take the same value of strip width. The phase shift range obtained is significantly better than for the single layer case, but it is still not sufficient to cover the desired range of 360° while still maintaining a high amplitude of transmission coefficient since the available phase shift range is only 135° if the transmission amplitude must be higher than -3 dB.

3.4.3 Symmetrical three independent layers

By bonding multiple dielectric sheets together, it is possible to obtain layers of conductive strips not only on the front and back side, but also between the bonded dielectric sheets, as shown in Figure 3.4-1(c). The dielectric sheets each have a thickness of d = 0.5 mm, taking into account the bonding film, leading to a final single piece arrangement of thickness h = 1 mm. It is also assumed that the front and back layers have the same strip width of a_1 and that the middle strips have a width of a_2.

Figure 3.4-4 shows the simulated results for the symmetrical three independent layers. Having two physical parameters allows for a representation of the results using two

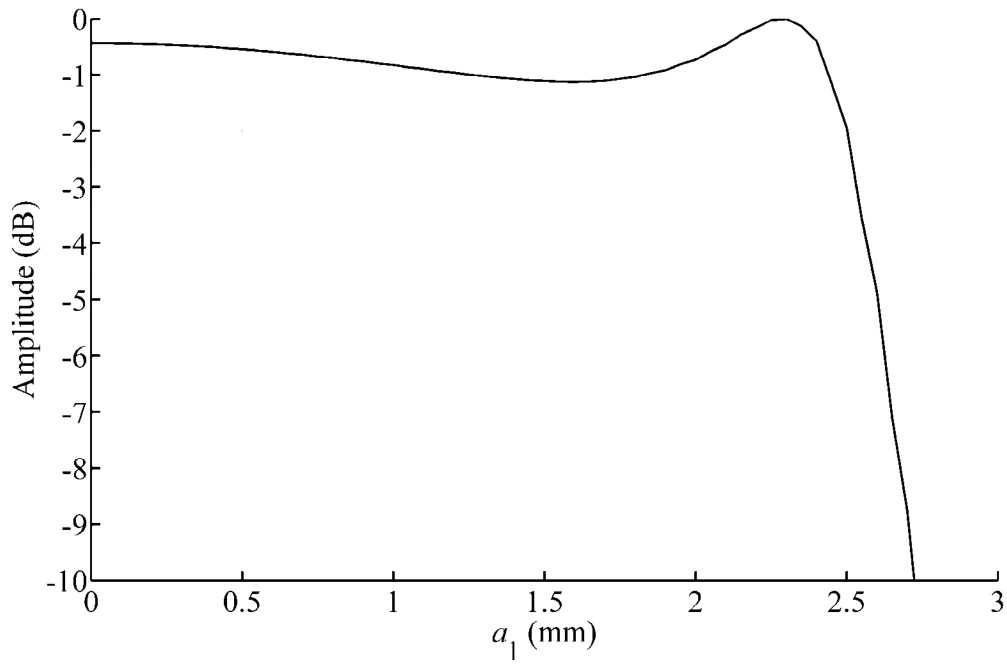

(a)

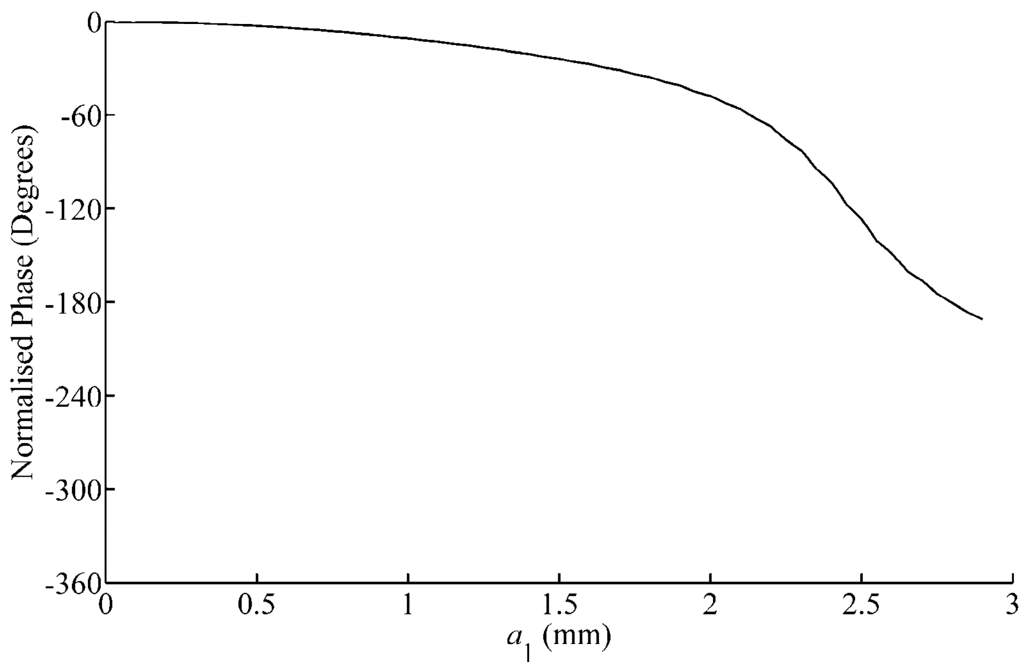

(b)

Figure 3.4-3: Simulated transmission results for double layer with *s* = 3 mm, *h* = 1 mm and ε_r = 2.2 at 30 GHz; (a) amplitude versus strip width, (b) normalised phase versus strip width.

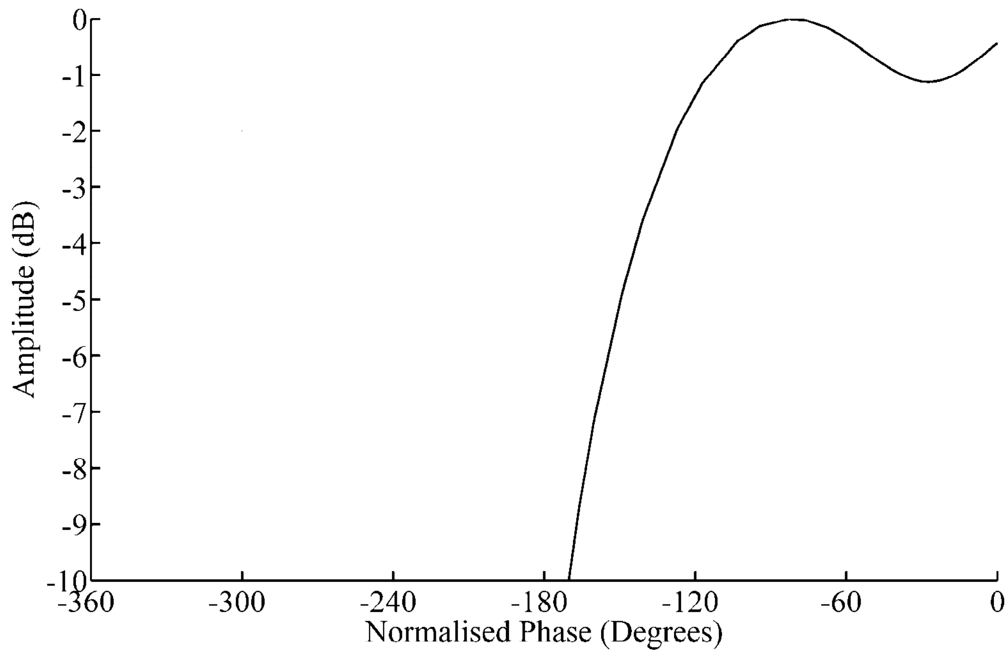

(c)

Figure 3.4-3 (continued): (c) amplitude versus normalised phase.

plots, as shown in Figure 3.4-4(a): at the top, a plot for the physical parameters a_1 and a_2, denoted *Map of physical dimensions*; at the bottom, a plot for the amplitude and normalised phase of the transmission coefficient, similar to the ones presented in Figures 3.4-2(c) and 3.4-3(c), denoted *Map of transmission coefficients*. Each point on the *Map of physical dimensions* corresponds to a point on the *Map of transmission coefficients,* and vice versa. The correspondence is shown by colour arrows; for simplicity, the correspondence is shown for a few points only. Note that the points on the *Map of physical dimensions* reveal that all meaningful physically possible combination of strip width a_1 and a_2 has been simulated for the database.

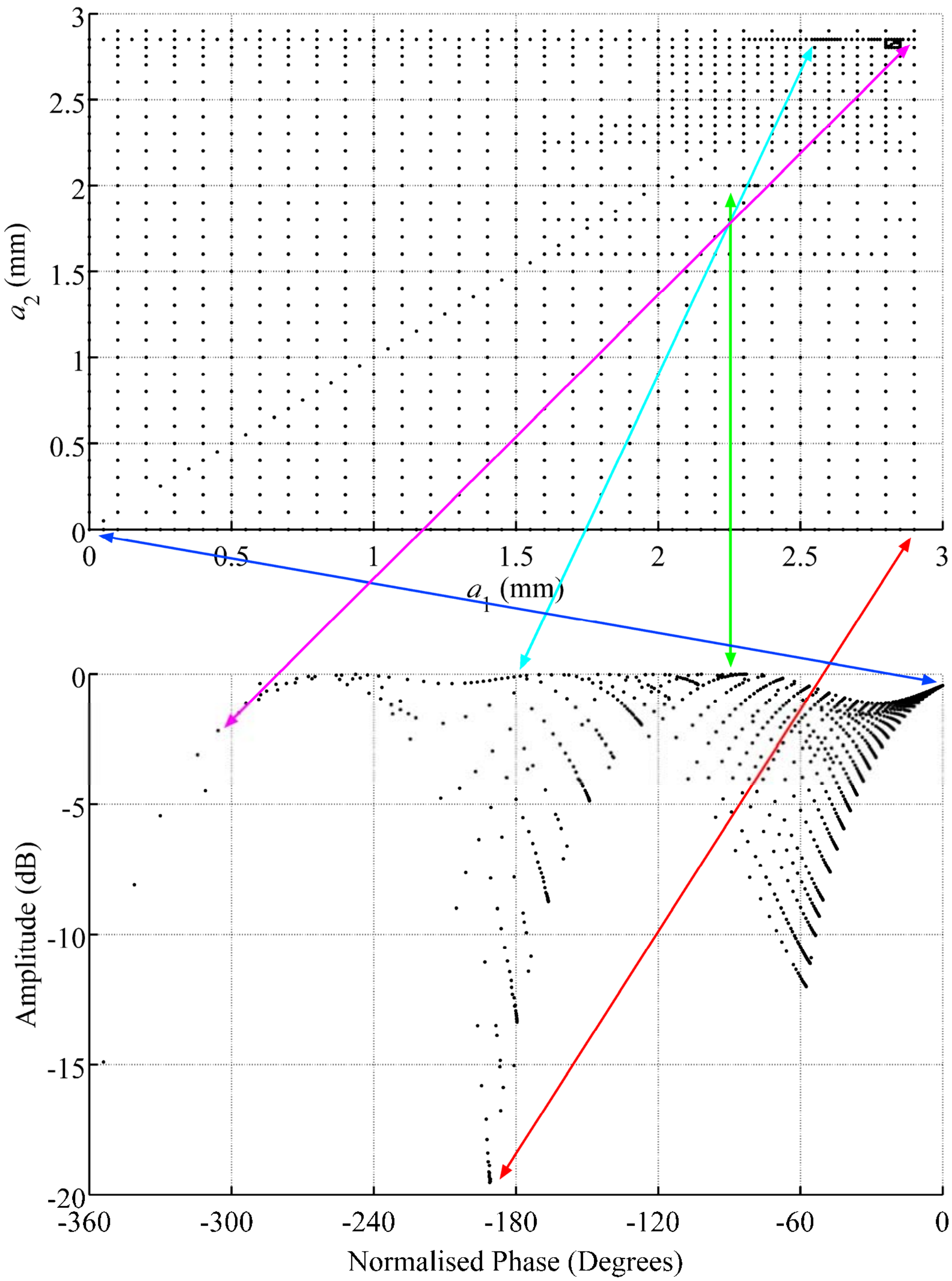

(a)

Figure 3.4-4: Simulated transmission results for three symmetrical independent layers of strips with s = 3 mm, h = 1 mm and ε_r = 2.2 for different values of a_1 and a_2 at 30 GHz; (a) *Map of physical dimensions* and *Map of transmission coefficients*; —— a_1 = 0 mm and a_2 = 0 mm, —— a_1 = 2.85 mm and a_2 = 0 mm, —— a_1 = 2.3 mm and a_2 = 2 mm, —— a_1 = 2.55 mm and a_2 = 2.85 mm, —— a_1 = 2.85 mm and a_2 = 2.85 mm.

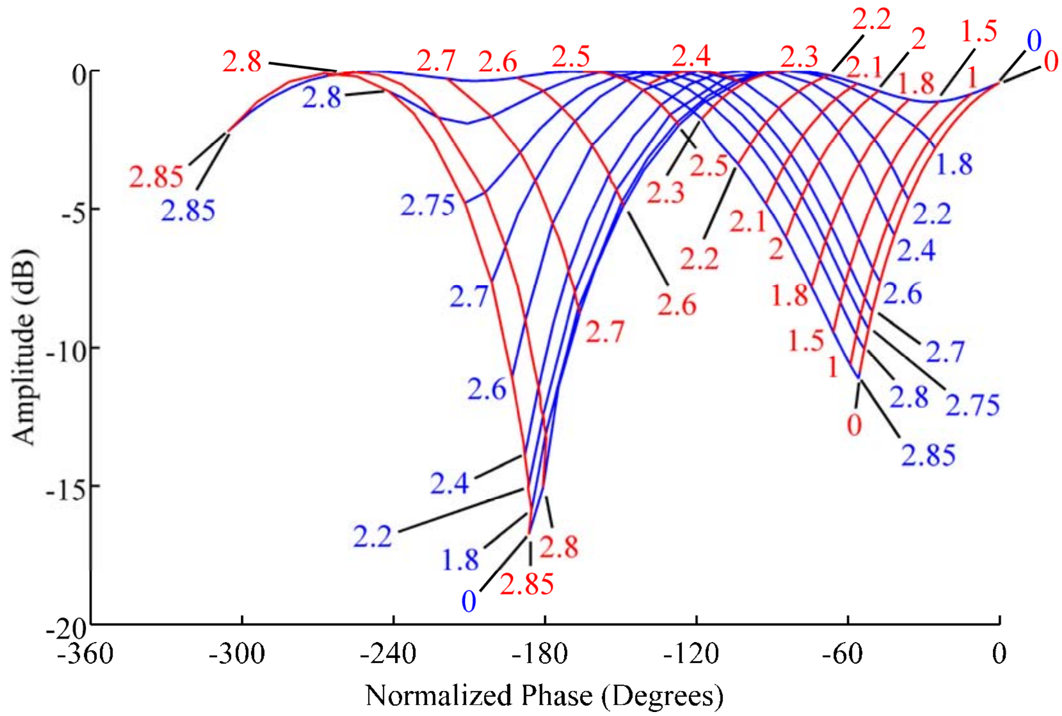

(b)

Figure 3.4-4 (continued): (b) amplitude vs normalised phase; —— fixed a_2 value as a function of a_1, —— fixed a_1 value as a function of a_2. Values of a_1 are shown in red and values of a_2 are shown in blue (units for a_i's are mm).

Another way of representing the results is by using a plot of the amplitude vs normalised phase, as in Figure 3.4-2(c) and 3.4-3(c), with constant physical parameter curves properly labelled. This has been done in Figure 3.4-4(b).

Figure 3.4-5 shows the top "envelope" of the curves in Figure 3.4-4. Analysis of Figures 3.4-4 and 3.4-5 reveals good results when this structure is to be used as a PSS, assuming maximum amplitude transmission is desired (which is the case). Different phase shift range regions are labelled in Figure 3.4-5 and explained in Table 3.4-1, in which a minimum amplitude constraint is given, along with the achievable phase shift range under such constraints. In Table 3.4-1, the maximum and minimum phase shifts correspond to

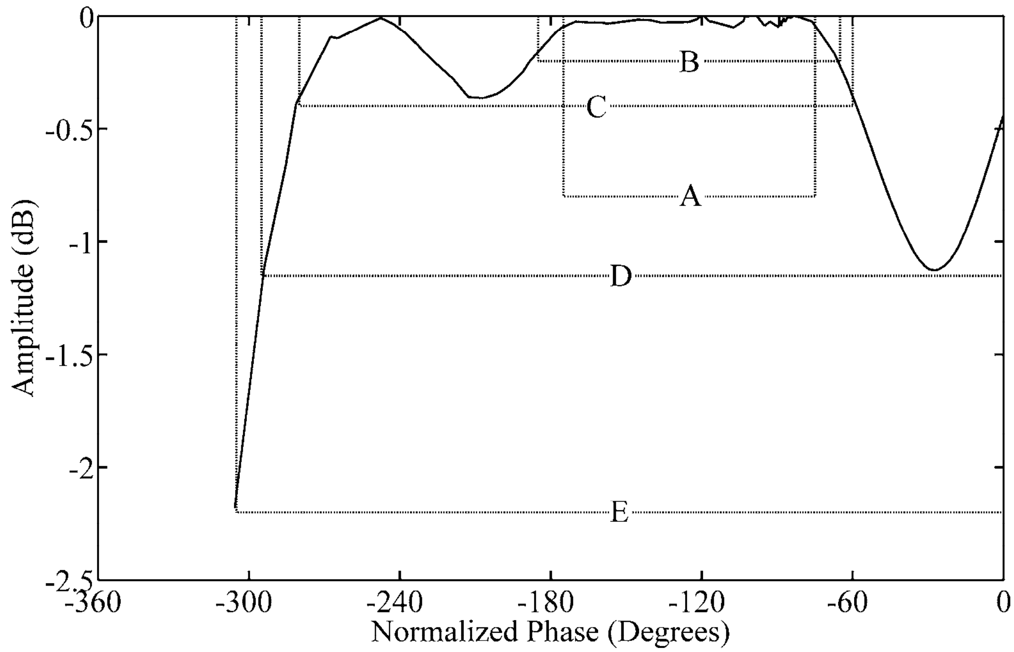

Figure 3.4-5: Best case of amplitude of the transmission coefficient for three symmetrical independent layers of strips for different values of normalized phase for εr = 2.2, h = 1 mm and s = 3 mm obtained from FDTD simulations at 30 GHz; the regions labelled A to E are described in Table 3.4-1.

absolute values. Region A, for example, represents a phase shift range of 100° from −75° to −175°, the amplitude of the transmission coefficient is nearly 0 dB, which corresponds to perfect transmission. A phase shift range from 0° to −295° results in a minimum amplitude of −1.15 dB or 87.6%. The values were considered for a minimum amplitude of −2.2 dB, allowing for a phase shift range of 305°. Consequently, it is to be noted that the entire 360° phase shift range is not achieved for this configuration. However, this configuration is very useful and practical, and it will be used for designing many phase-shifting components to be described in Chapters 4, 5 and 6.

Before proceeding to Section 3.4.4, which examines the 4-layer structure shown in Figure 3.4-1(d), the electric field of the 3-layer structure is studied in some detail. This not only provides increased insight into PSS operation but will facilitate the discussion on its equivalent circuit model in Section 3.6.

The electric field of different cases of symmetrical three independent layers are presented in Figures 3.4-6 to 3.4-9. As mentioned in Section 3.3, the electric field incident on the PSS/PASS is polarised along the *y*-axis, i.e. $E_x = 0$, $E_y \neq 0$, $E_z = 0$. The introduction of conductive strips will result in a component of the electrical field parallel to the *z*-axis (E_z) close to the conductor. Away from the conductor, the electric field is purely polarised along the *y*-axis, whether it is before or after the PSS/PASS layer. Note that the component of the electric field along the *x*-axis, E_x, is initially null and will remain null.

In Figure 3.4-6, the first case is presented, which consists of an air sample. Figure 3.4-6(a) shows no variation within the structure profile, which consists of air only: no dielectric material or metal is present. This results in a uniformly constant amplitude of E_y at every location, as is shown from the surface plot of Figure 3.4-6(b) and the plot of Figure 3.4-6(d). Moreover, the phase of E_y varies linearly, as shown in Figure 3.4-6(e). This case is therefore that of a plane wave propagating in the +*z*-direction. Figure 3.4-6(c) also points out that E_z is zero everywhere.

Table 3.4-1: Regions of phase shift range for three symmetrical independent layers of strips for given minimum amplitude of transmission coefficient. This information is shown graphically in Figure 3.4-5.

Region	Minimum Amplitude (dB)	Minimum Phase Shift (°)	Maximum Phase Shift (°)	Phase Shift Range (°)
A	~ 0	–75	–175	100
B	–0.2	–65	–185	120
C	–0.4	–60	–280	220
D	–1.15	0	–295	295
E	–2.2	0	–305	305

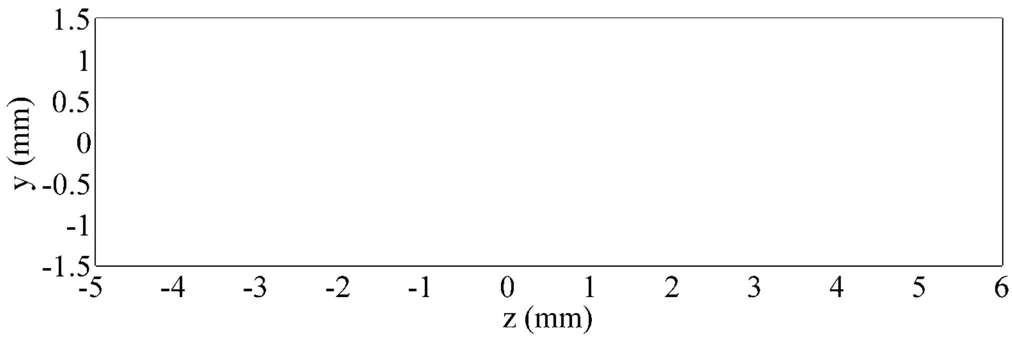

(a)

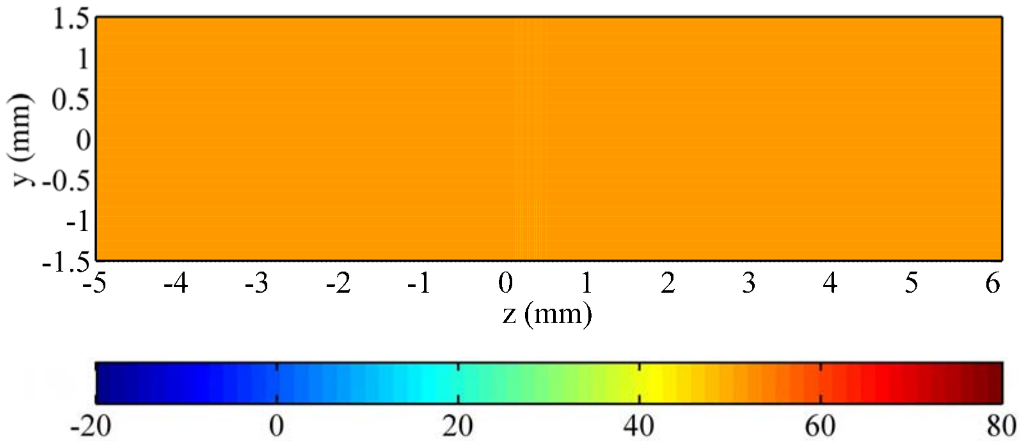

(b)

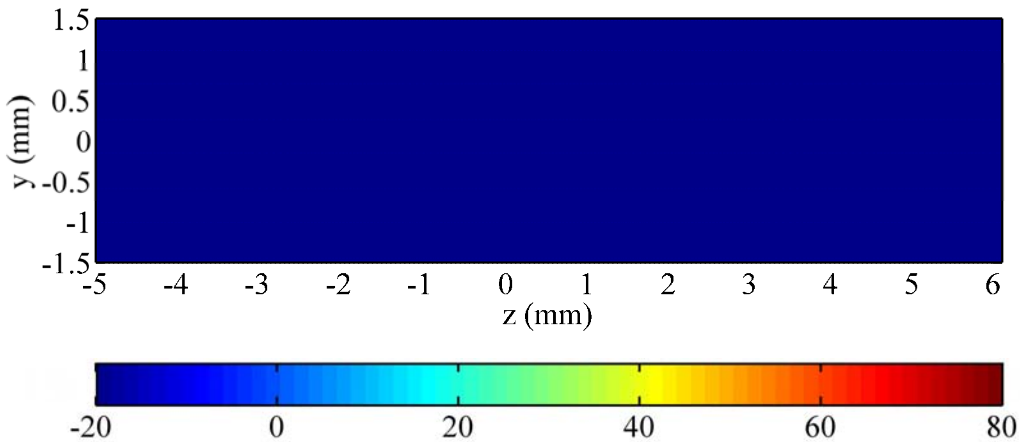

(c)

Figure 3.4-6: Electric field distribution for the case of air obtained from FDTD simulations at 30 GHz; (a) Structure profile (white is air, showing air only), (b) Surface plot of E_y in dB(V/m), (c) Surface plot of E_z in dB(V/m).

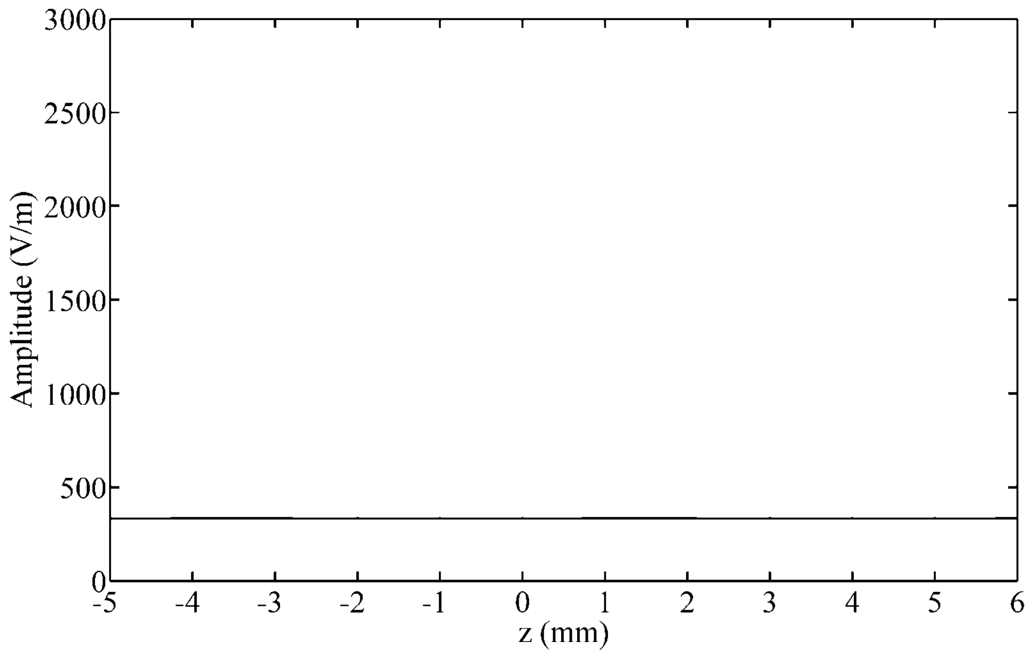

(d)

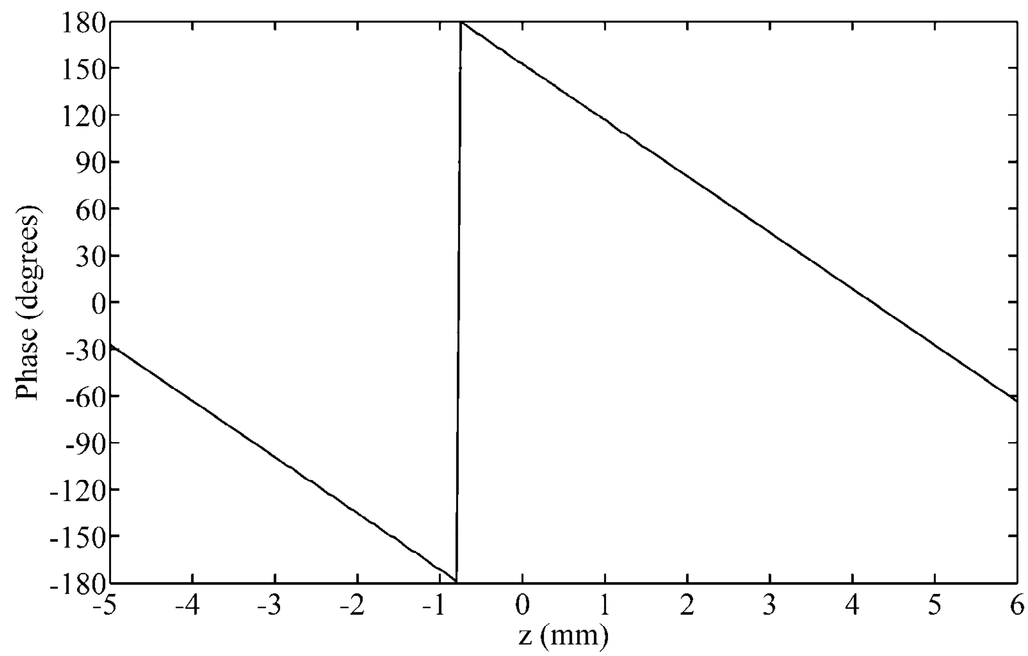

(e)

Figure 3.4-6 (continued): (d) Amplitude of E_y at any value of y, (e) Phase of E_y at any value of y.

The case of a bare dielectric sample is presented in Figure 3.4-7, in which the amplitude of E_y is independent of y but, unlike the case of an air sample presented in Figure 3.4-6, there is a variation along z. This variation is not significant however, as shown in Figure 3.4-7(b) and 3.4-7(d). The amplitude variation of E_y preceding the structure, i.e. for negative z values, is that of a standing plane wave. The amplitude of E_y is unchanged a certain distance past the PSS/PASS structure and beyond, and only the phase varies as shown in Figure 3.4-7(e). Once again, there is no conductor in this case and consequently E_z is zero everywhere, as shown in Figure 3.4-7(c).

Figure 3.4-8 presents the case where a_1 = 0.05 mm and a_2 = 2.85 mm, in which the amplitude of E_y is now dependent of both y and z, as shown in Figures 3.4-8(b) and 3.4-8(d). Interestingly, Figure 3.4-8(e) shows that the phase of E_y at the input and output, away from the PSS/PASS layer, are identical, regardless of the value of y. Because of the presence of conductive material, E_z is no longer equal to zero at the PSS/PASS layer, although it remains null at the input and output, i.e. away from the PSS/PASS layer. This is presented in Figures 3.4-8(c) and 3.4-8(d). In this study, a PEC sheet is placed in the middle of the gap, but it could also be placed in the middle of the strip. Note that E_z is zero at $y = \pm 0.5ns$ (where n is an integer and s is the unit cell height), which respects the boundary conditions regardless of the location of the PEC sheet (middle of the gap or middle of the strip).

Figure 3.4-9 presents the case where a_1 = 2.55 mm and a_2 = 2.85 mm, where once again the amplitude of E_y is dependent of both y and z, as shown in Figures 3.4-9(b) and 3.4-9(d). It is noticed in this case as well that the phase of E_y at the input and output, away

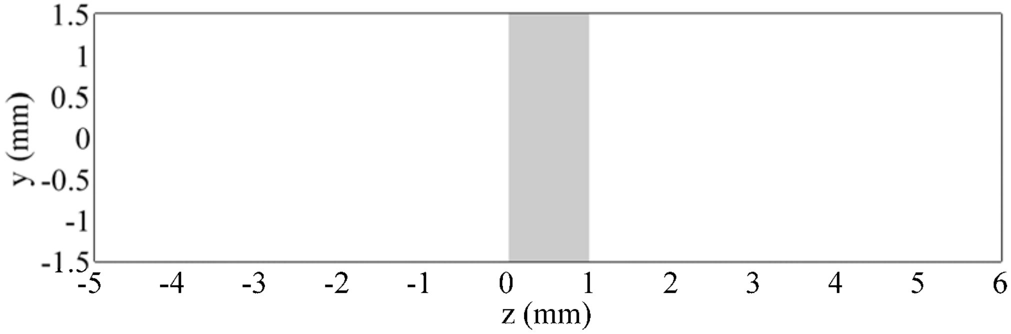

(a)

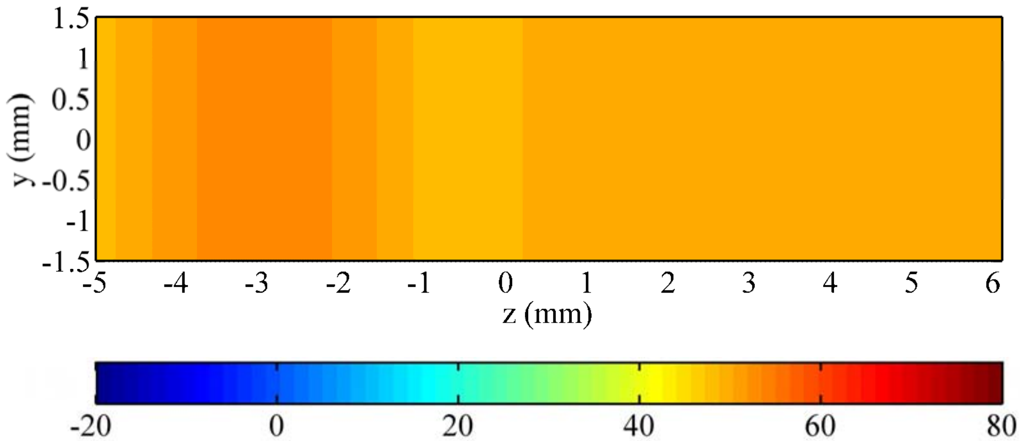

(b)

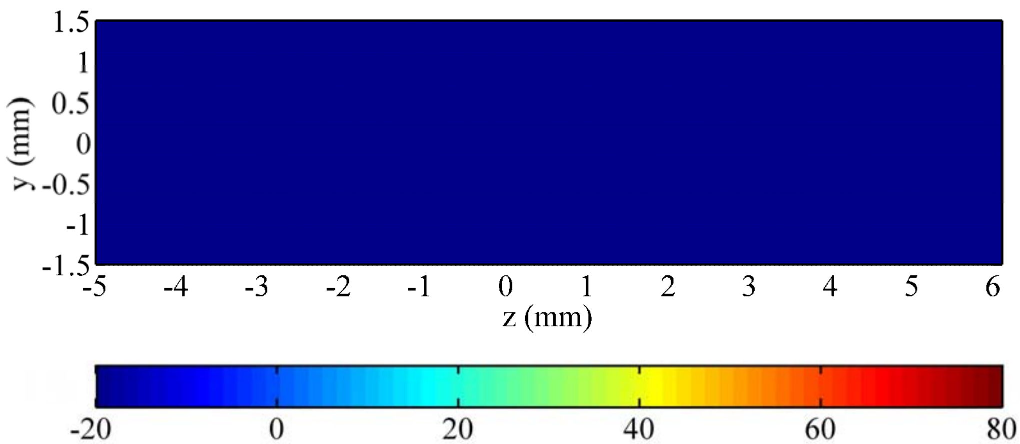

(c)

Figure 3.4-7: Electric field distribution for a bare sample with ε_r = 2.2, h = 1 mm, s = 3 mm (a_1 = 0 mm and a_2 = 0 mm) obtained from FDTD simulations at 30 GHz; (a) Structure profile (white is air, grey is ε_r = 2.2), (b) Surface plot of E_y in dB(V/m), (c) Surface plot of E_z in dB(V/m).

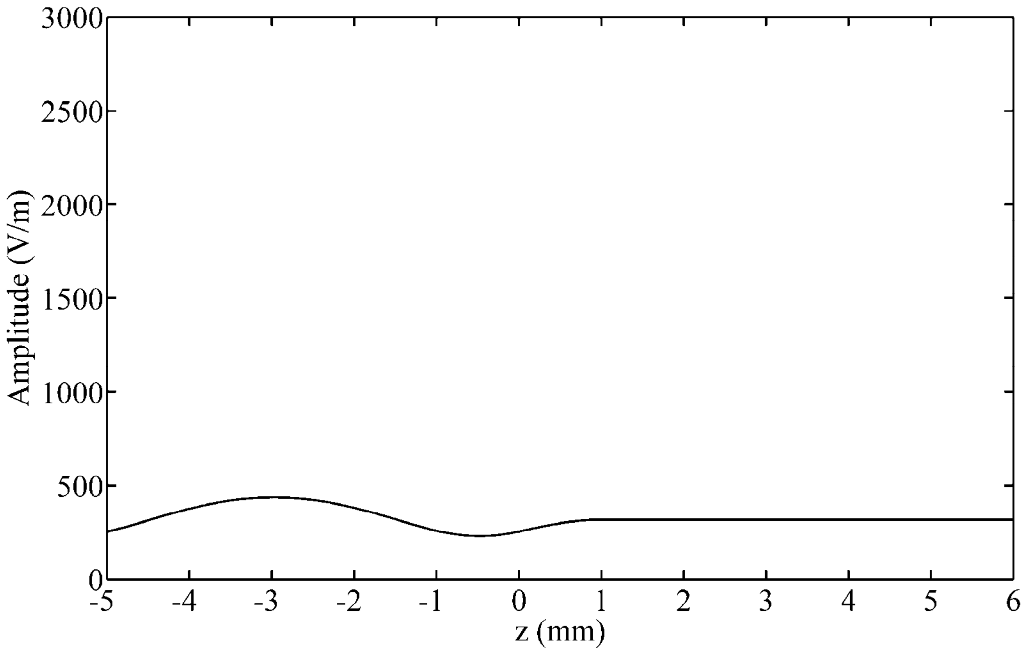

(d)

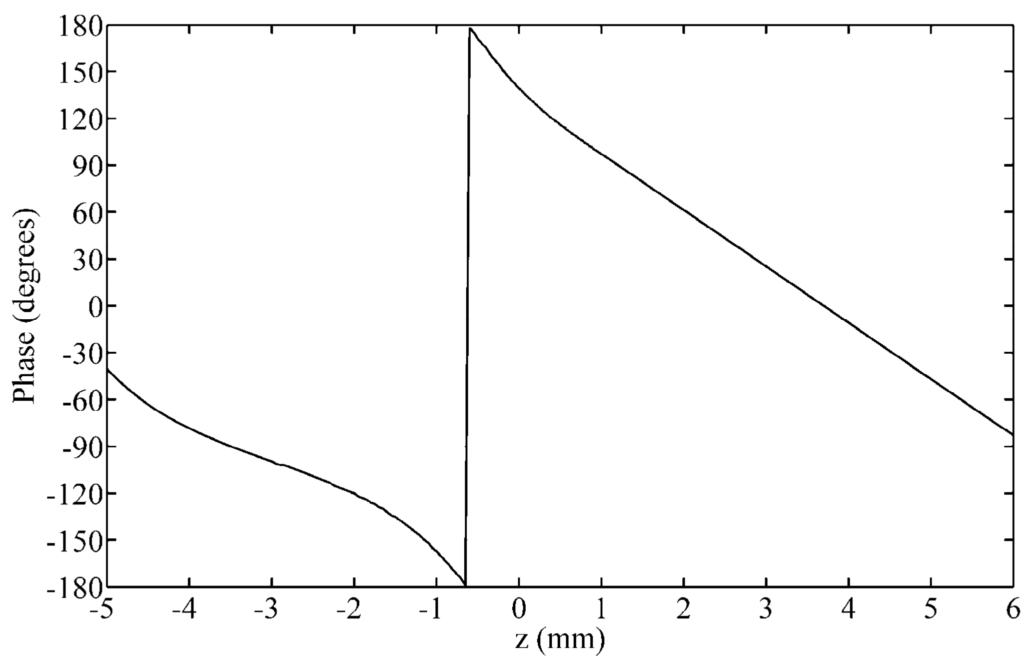

(e)

Figure 3.4-7 (continued): (d) Amplitude of E_y at any value of y, (e) Phase of E_y at any value of y.

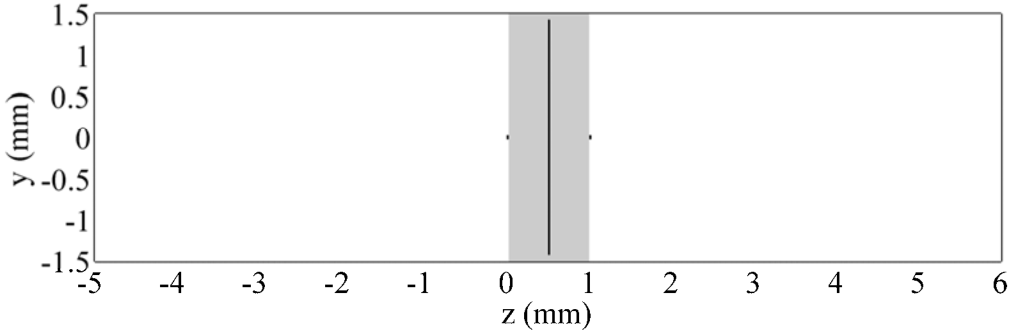

(a)

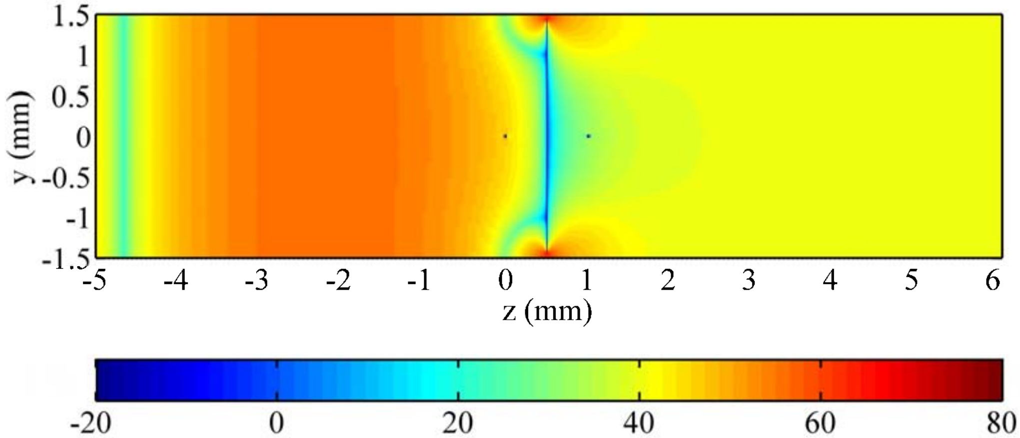

(b)

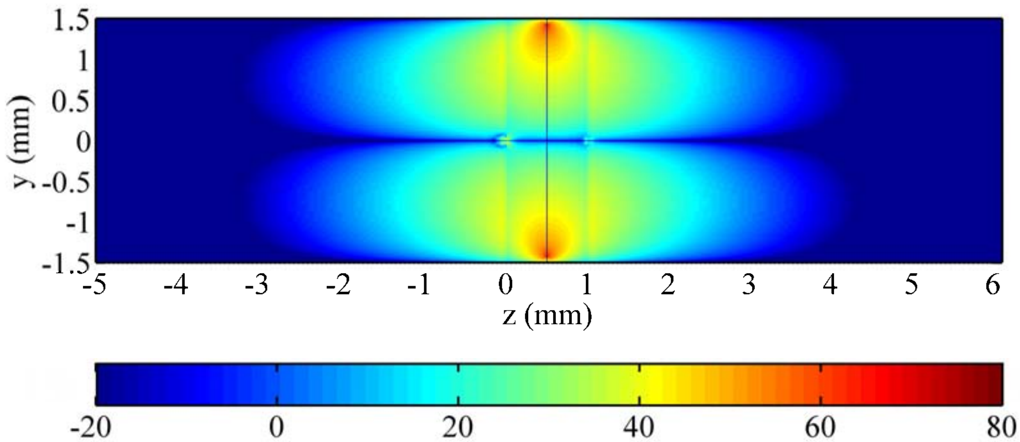

(c)

Figure 3.4-8: Electric field distribution for the case ε_r = 2.2, h = 1 mm, s = 3 mm, a_1 = 0.05 mm and a_2 = 2.85 mm obtained from FDTD simulations at 30 GHz; (a) Structure profile (white is air, grey is ε_r = 2.2, black is metal), (b) Surface plot of E_y in dB(V/m), (c) Surface plot of E_z in dB(V/m).

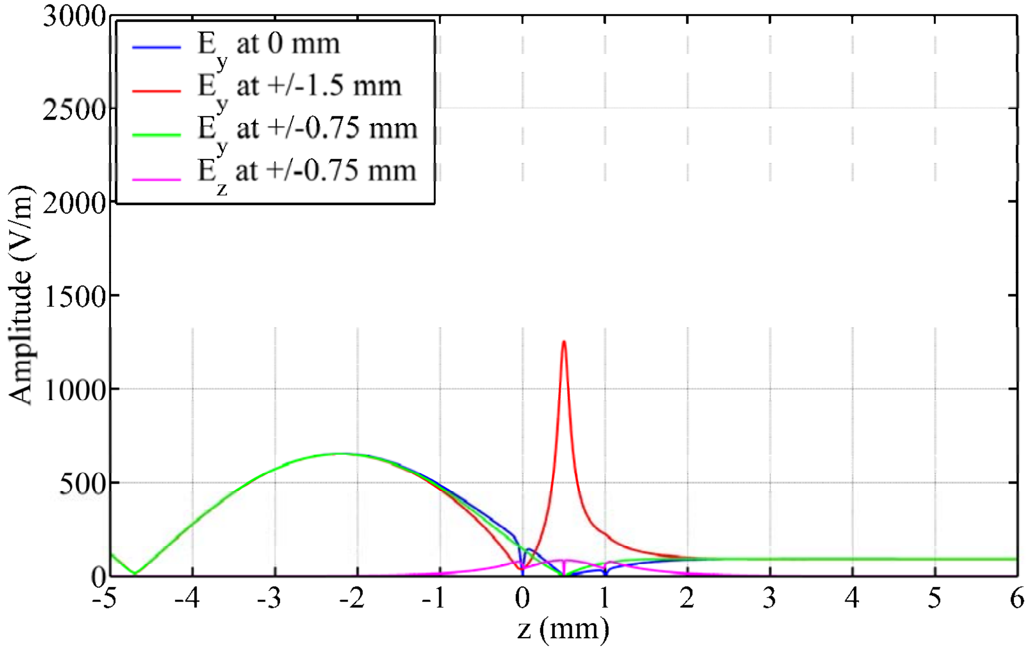

(d)

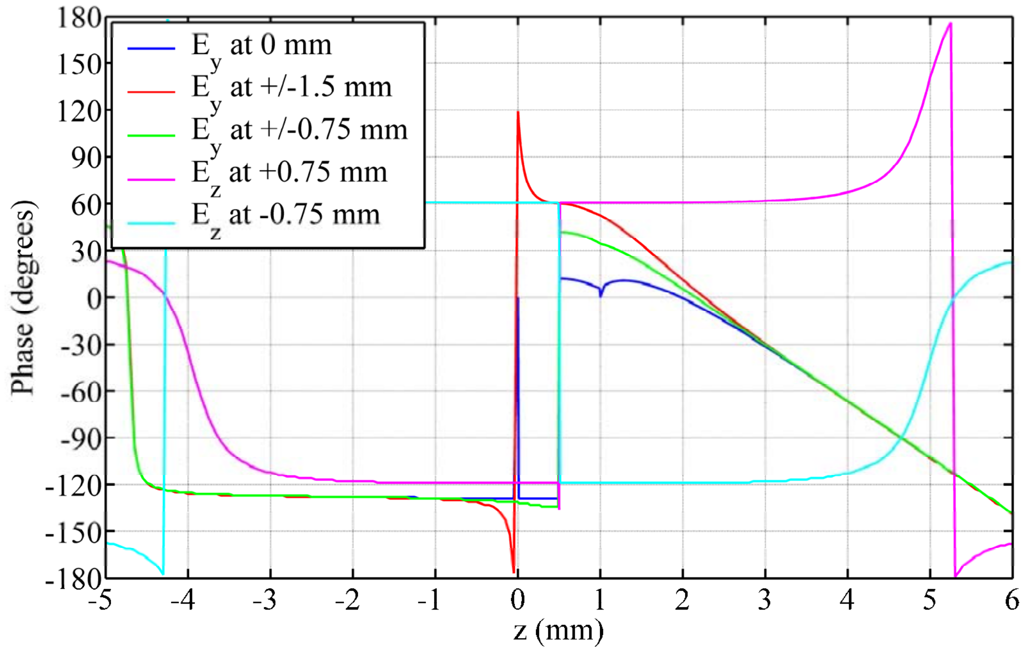

(e)

Figure 3.4-8 (continued): (d) Amplitude at fixed values of *y*, (e) Phase at fixed values of *y*.

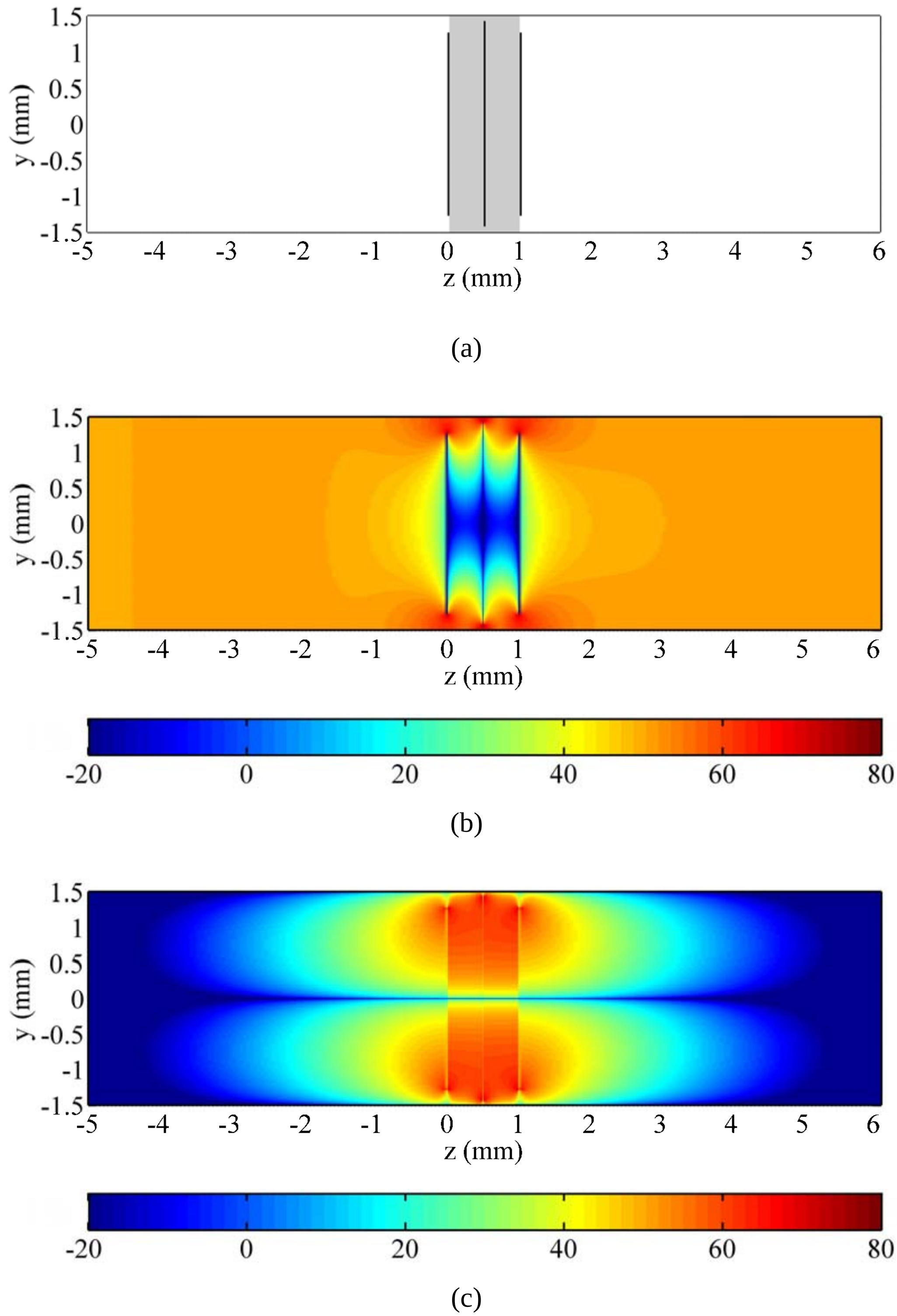

Figure 3.4-9: Electric field distribution for the case ε_r = 2.2, h = 1 mm, s = 3 mm, a_1 = 2.55 mm and a_2 = 2.85 mm obtained from FDTD simulations at 30 GHz; (a) Structure profile (white is air, grey is ε_r = 2.2, black is metal), (b) Surface plot of E_y in dB(V/m), (c) Surface plot of E_z in dB(V/m).

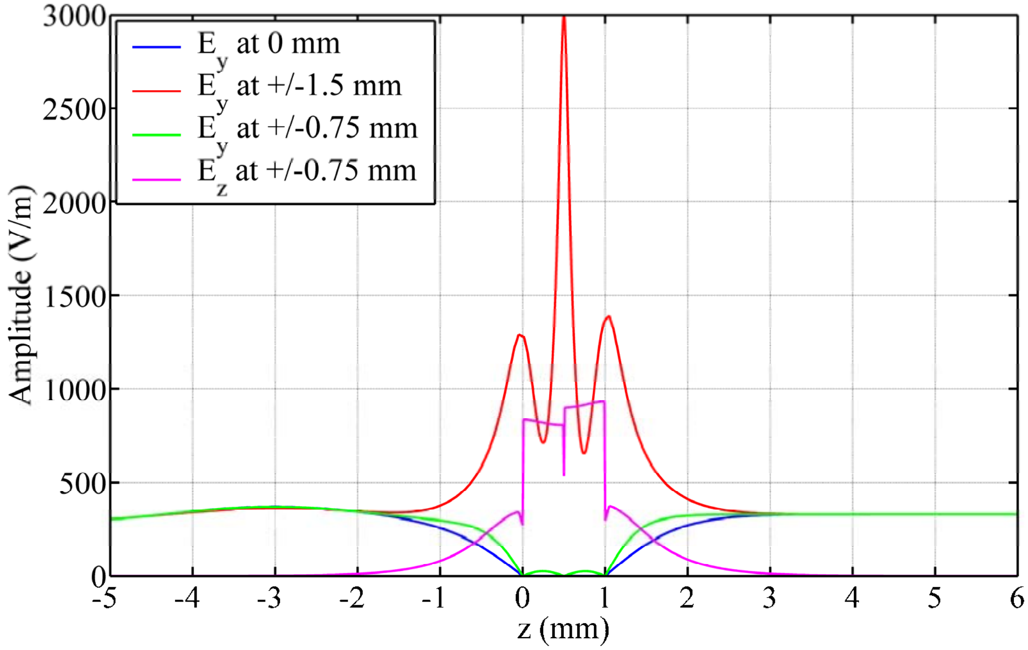

(d)

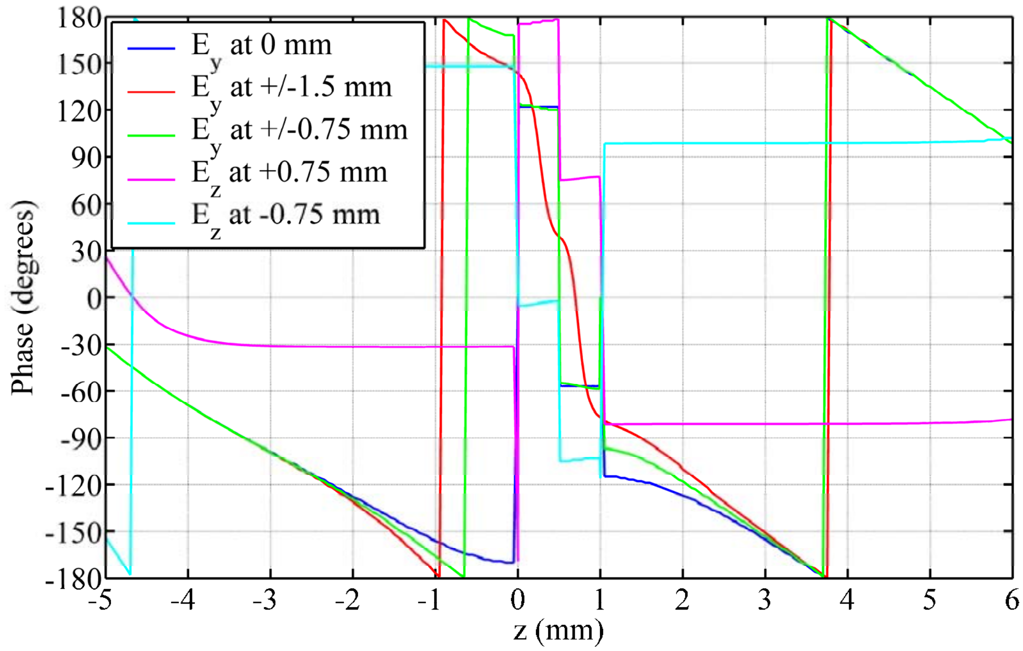

(e)

Figure 3.4-9 (continued): (d) Amplitude at fixed values of *y*, (e) Phase at fixed values of *y*.

from the PSS/PASS layer, are identical, regardless of the value of y. Figure 3.4-9(c) shows that E_z is very strong between the strips, resulting in a series capacitance; this point will be addressed in further detail in Section 3.6. The amplitude of E_y is however very weak between the strips, as shown in Figure 3.4-9(b). Again, E_z is zero at $y = \pm 0.5ns$.

3.4.4 Four fully-independent layers

The number of layers can be further increased in an attempt to improve the range of controllable transmission amplitude and phase combinations. However, using too many layers will significantly add to the fabrication complexity of the structure and may become unattractive due to the extra thickness and weight. Furthermore, the bandwidth will suffer if too many strip layers are used; this will be further investigated in Section 3.7.3. Regardless of these considerations, it was decided to experiment on the four layer structure shown in Figure 3.4-1(d). The dielectric sheets, including the bonding film (when it applies), each have a thickness of 0.5 mm, leading to a final single piece arrangement of thickness h = 1.5 mm. For this particular case, the strip width a_i is independent for each layer. Figure 3.4-10 shows the simulated results of the transmission amplitude and phase. A “cloud” of points is used here as it would be too difficult the show any dependency while using four different physical parameters. Figure 3.4-10 shows that this four layer configuration allows the achievement of a phase shift range of a full 360°, as well as an impressive potential for high amplitude transmission for PSS applications and variable amplitude transmission for different phase values for PASS applications.

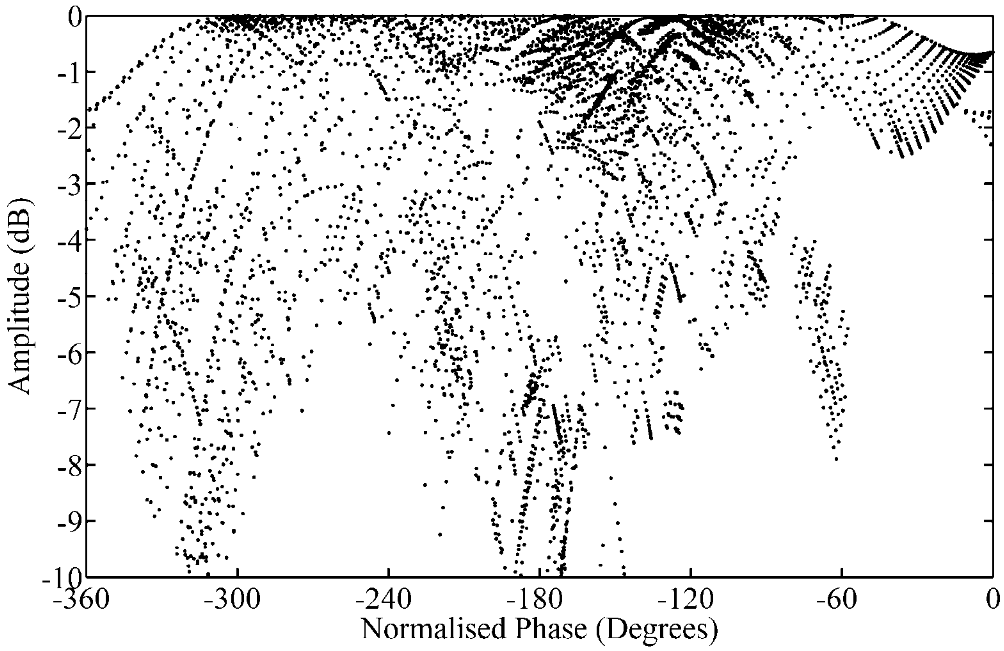

Figure 3.4-10: Simulated transmission results for four fully-independent layers of strips with s = 3 mm, h = 1.5 mm and ε_r = 2.2 at 30 GHz in the amplitude vs normalised phase domain.

For the case of maximised amplitude of the transmission coefficient (always the constraint when the structure is to be used as a PSS only), the phase shift range is clearly better than for the three symmetrical layers. Figure 3.4-11 shows the envelope and Table 3.4-2 summarises the main results. It is important to note that almost perfect transmission is realised for a phase shift range of 250° and that the entire phase shift range of 360° is obtained with worst-case transmission amplitude of –1.7 dB. This is a significant achievement.

The 4-layer structure will be utilised in the design of a PSS lens antenna in Section 6.7. It will also be used for the flat-topped beam antenna design in Chapter 7. In the latter case, it is used as a PASS.

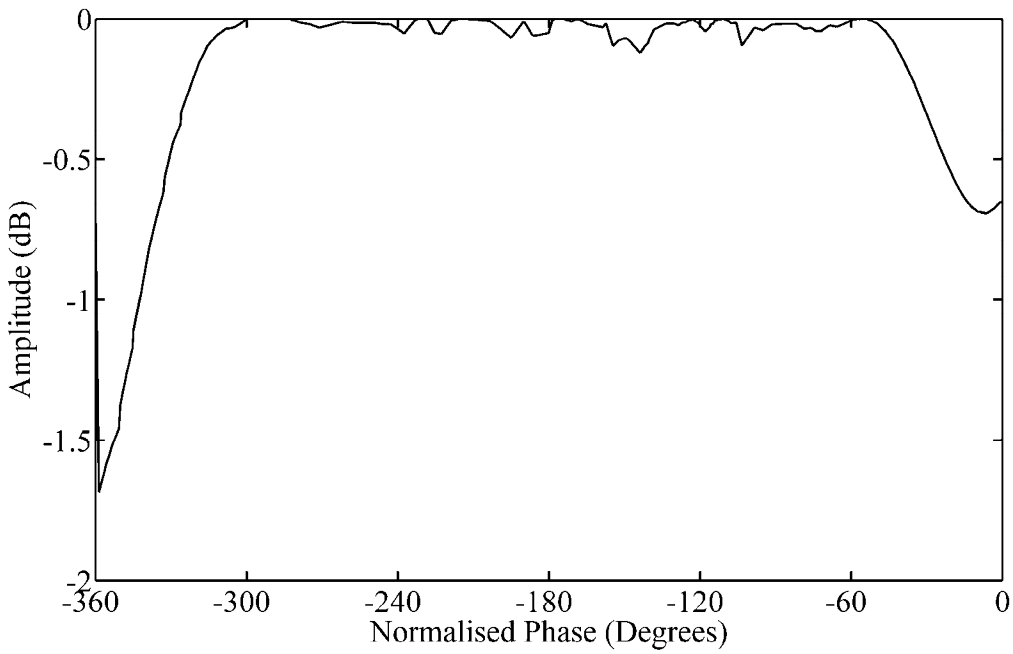

Figure 3.4-11: Best case of amplitude of the transmission coefficient for four independent layers of strips for different values of normalized phase for ε_r = 2.2, *h* = 1.5 mm and *s* = 3 mm obtained from FDTD simulations at 30 GHz.

3.5 Square Unit Cell

This section presents FDTD simulations [EMPI07] for the square unit cells with centred square conductive elements. Although some simulations were previously conducted on single and double layer cases [GAGN08], this section will focus on a symmetrical three independent layer configuration with unit cell size s = 3 mm along both the x- and y-axis, dielectric constant of ε_r = 2.2 and total thickness h = 1 mm, similar to Figure 3.4-1(c). A front view, showing only the front layer, would be similar to Figure 3.3-2(a); a similar illustration is presented in Figure 3.5-1 for the finite-element method (FEM) simulations to be discussed below to complement the FDTD ones. In the simulations, the conductive layers were again assumed infinitesimally thin and perfectly

Table 3.4-2: Regions of phase shift range for four fully-independent layers of strips for given minimum amplitude of transmission coefficient.

Minimum Amplitude (dB)	Minimum Phase Shift (°)	Maximum Phase Shift (°)	Phase Shift Range (°)
~ 0	–50	–300	250
–0.2	–40	–325	285
–0.7	0	–335	335
–1.7	0	–360	360

conducting while the dielectric material was assumed to be lossless. As for the case of strip unit cells, normalised phase assumes that a bare case produces a phase shift of 0°. The frequency of simulation is 30 GHz.

Because high density meshing is required due to the presence of rapidly-varying fields in the unit cell, simulations require many unknowns, which increases the simulation time and computer memory (RAM) requirements. For this reason, only a few different unit cell cases were simulated, unlike the strip-based cases of Section 3.4 for which many cases were simulated, facilitated by a shorter simulation time since fewer unknowns were

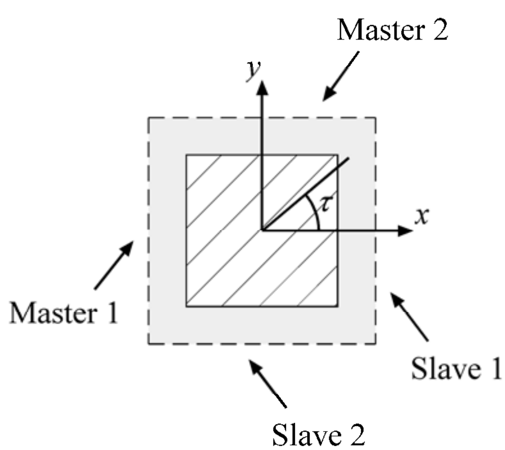

Figure 3.5-1: Front view of the square two-dimensional unit cell with square conductive element, showing boundary conditions as used in the FEM simulations [HFSS07].

needed. Figure 3.5-2 presents the simulated results of the transmission amplitude and phase using a cloud of points, obtained from the FDTD simulations. Some of these cases were also simulated using a commercially available FEM software package [HFSS07], which confirmed the FDTD results. Figure 3.5-2 shows that the phase shift range is about the same as for the 3-layer strip-based unit cell of Section 3.4.3 with similar amplitude levels.

The interest in the square-element based unit cell is that this unit cell can be used for dual-polarisation or circular polarisation applications. The reason is that the squares have 90° rotational symmetry, and thus any two orthogonal polarisations would be supported. The strip-based elements presented in Section 3.4 are not rotationally

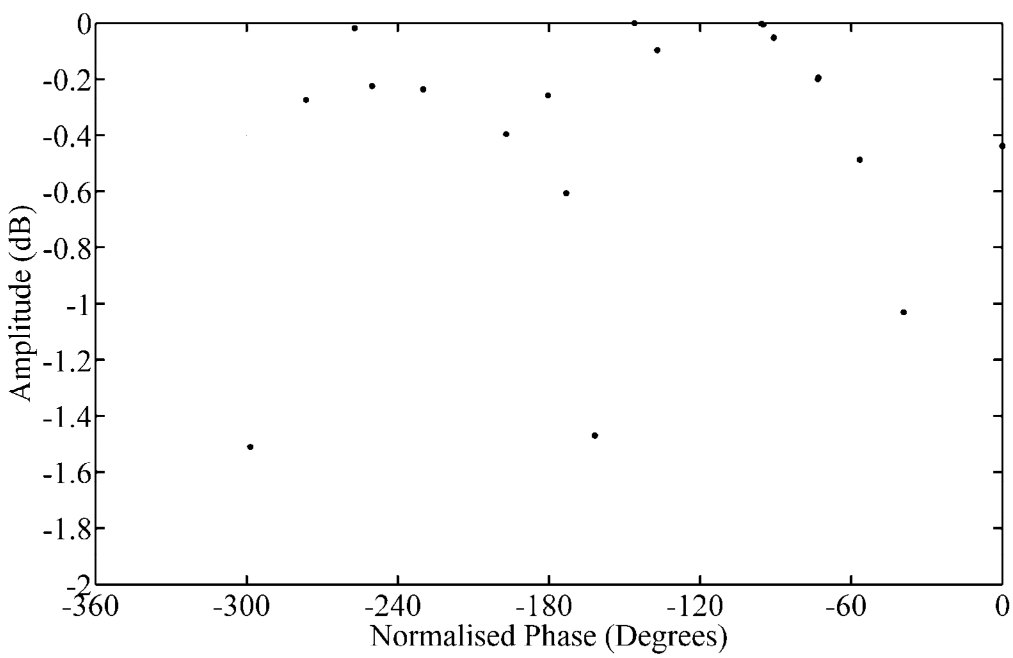

Figure 3.5-2: Simulated transmission results for symmetrical three independent layers of square patches with *s* = 3 mm, *h* = 1 mm and ε_r = 2.2 at 30 GHz in the amplitude vs normalised phase domain.

symmetrical and consequently are polarisation-dependent. Furthermore, for square elements, the transmission coefficient is almost independent of the roll angle τ with respect to the fixed polarisation of the feed, as shown in Figure 3.5-3 for FEM simulations performed on a case with a_1 = 2.4 mm and a_2 = 2.24 mm. The amplitude and angle discrepancy is marginal and can be attributed to the meshing of the structure. The roll angle τ is defined in Figure 3.5-1. Unlike the FDTD simulations performed using [EMPI07], FEM simulations performed with [HFSS07] do not use PEC/PMC boundary conditions. Instead, master and slave boundary conditions are used, which allows for oblique incidence and tilted polarisation, unlike the FDTD model that permits vertical polarisation and normal incidence only.

The fact that the polarisation is independent of the roll angle is now demonstrated theoretically. Considering the incident electric field on a PSS/PASS, denoted E_{inc}, and the electric field transmitted through the PSS/PASS, denoted E_{trans}, the general relationship between the two can be established as

$$E_{trans} = TE_{inc} \tag{3.5-1}$$

where T is the transmission coefficient. This is also the equation for a polarisation-sensitive case.

Assuming the incident field E_{inc} as being a plane wave propagating along the z-direction with no electric field component along the z-axis, E_{inc} has components along the x- and y-axis only. Thus, E_{inc} can be decomposed as

$$E_{inc} = E_x \hat{a}_x + E_y \hat{a}_y \tag{3.5-2}$$

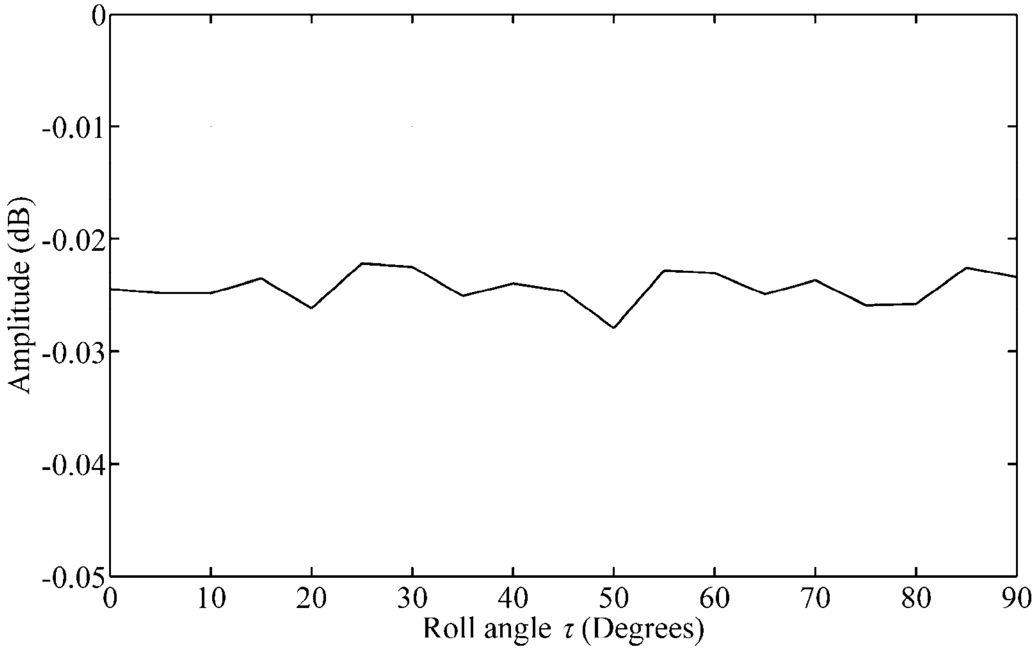

(a)

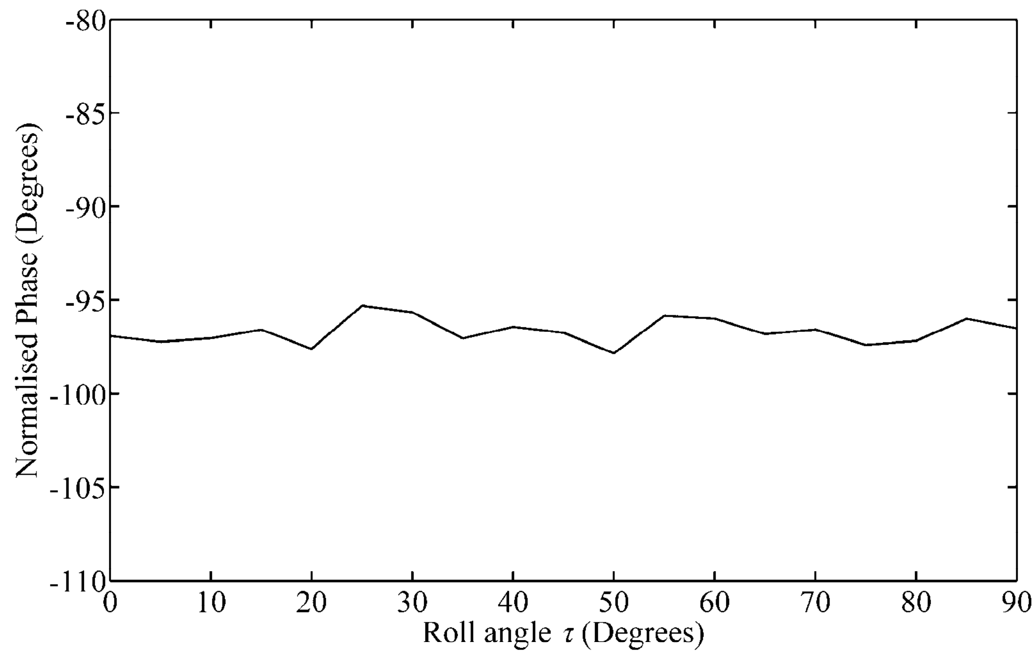

(b)

Figure 3.5-3: Simulated transmission results for symmetrical three independent layers of square patches with a_1 = 2.4 mm, a_2 = 2.24 mm, s = 3 mm, h = 1 mm and ε_r = 2.2 as a function of the roll angle τ at 30 GHz; (a) Amplitude, (b) Phase.

where E_x and E_y depend on the roll angle τ. If the structure is not rotationally symmetrical, then the transmission coefficient would not be the same along the x- and y-axis, such that

$$E_{trans} = T_x E_x \hat{a}_x + T_y E_y \hat{a}_y \tag{3.5-3}$$

where T_x and T_y are the transmission coefficients of the x- and y-components, respectively. Since the structure has 90° rotational symmetry, it can be stated that

$$T = T_x = T_y \tag{3.5-4}$$

Substituting this in (3.5-3) yields

$$E_{trans} = TE_x \hat{a}_x + TE_y \hat{a}_y = T\left\lfloor E_x \hat{a}_x + E_y \hat{a}_y \right\rfloor \tag{3.5-5}$$

The terms in brackets are equal to E_{inc} as defined in (3.5-2), and therefore (3.5-5) becomes

$$E_{trans} = TE_{inc} \tag{3.5-6}$$

which is the same result as (3.5-1). Therefore, according to (3.5-6), whichever values of E_x and E_y are used, or whichever roll angle is used, the transmission coefficient is unchanged, which means that the structure is independent of the polarisation, as was the case in (3.5-1).

3.6 Equivalent Circuit Model

In this section, an equivalent circuit model for the PSS/PASS is derived. Visual inspection of the geometry of the PSS/PASS in Figure 3.4-1 as well as the fields in Figure 3.4-9, intuitively suggests an equivalent circuit model for the unit cell of the PSS. Considering Figure 3.4-1(c) for a 3-layer symmetrical PSS, and knowing that a normal-incidence plane wave is propagating along the z-direction with electric field polarised along the y-axis, the equivalent circuit shown in Figure 3.6-1 is obtained. The shunt

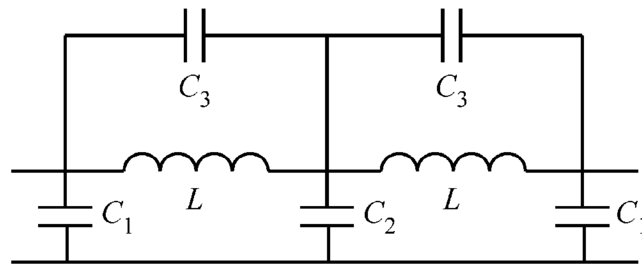

Figure 3.6-1: Equivalent circuit model for the unit cell of a 3-layer PSS.

capacitance results from the charge accumulation at the edge of the strips of two adjacent unit cells, located on the same layer, but separated by a gap along the *y*-axis. The shunt capacitance C_1 depends on the front and back strip widths, a_1, while shunt capacitance C_2 depends on the middle strip widths, a_2. Shunt inductances, in series with these capacitances, should also be present due to current flowing along the *y*-axis on the metallic strips, however their values are negligible for the frequencies of interest and consequently are of importance only at much higher frequencies. For this reason, these shunt inductances were not included in the equivalent circuit model. Keep in mind that the actual model is accurate from very low frequencies (close to DC) to frequencies beyond the desired frequency of operation; however it will not accurately predict the behaviour of the PSS/PASS beyond that point. More details on the accuracy of the equivalent circuit model will be provided in Section 3.7.

The shunt capacitances C_1 and C_2, and series inductance L, also model the transmission-line like characteristics of the dielectric layers. The inductance L is easily approximated theoretically (see e.g. [SIEV08]) as

$$L = \mu d = \mu_r \mu_0 d \tag{3.6-1}$$

where μ is the permeability, μ_r is the relative permeability, μ_0 is the free-space permeability and d is the layer thickness, which corresponds to half the total thickness h for the case of a 3-layer PSS/PASS. Consequently, for dielectric material, μ_r = 1 and therefore L is independent of the material. However, the capacitances are dependent on the relative permittivity of the dielectric material. It is also found that the series inductance L is not affected by the strip width variations, which is consistent with (3.6-1). Since d = 0.5 mm, the series inductance will have a theoretical value of L = 0.628 nH for the case of a 3-layer PSS/PASS shown in Figure 3.6-1.

The series capacitance C_3 represents the capacitance between the strips in the same unit cell but on different layers (that is, with different z-values). Referring to Figure 3.4-9, the electric field, which is polarised along the y-direction before the PSS/PASS (E_y component only), is bent between two consecutive strips within the same unit cell, providing a z-component of the electric field (E_z). Such a behaviour of the electric field is similar to a parallel-plate capacitance in series, labelled C_3 in Figure 3.6-1. The capacitance C_3 depends on both a_1 and a_2. Since the structure is physically symmetrical, as described in Section 3.4-3, the equivalent circuit is also symmetrical. Table 3.6-1 shows the influence of the physical parameters on the components of the equivalent circuit model.

The parameter extraction capability of a commercial software application [ADS06] was used to determine the value of the equivalent circuit components, utilising as input data the reflection and transmission coefficients of full-wave electromagnetic simulations obtained from the FDTD analysis using [EMPI07].

Table 3.6-1: Influence of the physical parameters on the electric components of the equivalent circuit model.

	ε_r	μ_r	h	s	a_1 or g_1	a_2 or g_2
C_1	✓		✓	✓	✓	
C_2	✓		✓	✓		✓
C_3	✓		✓	✓	✓	✓
L		✓	✓	✓		

Numerical values of these components are found to be of the same order of magnitude, and so the equivalent circuit is a meaningful model of the physical reality. It is the combination of the shunt capacitance, series inductance and series capacitance that makes it possible to obtain different transmission amplitude values for the same phase shift, allowing for independently choosing the transmission amplitude and phase. In other words, some contributions of C_1, C_2, C_3 and L will result in different values of both amplitude and phase of transmission coefficient, some of which present very high amplitude of transmission coefficient for a given phase shift. It is important to note that the contribution of the series capacitance C_3 is non-negligible and, without it, it would not be possible to get high amplitude transmission for a broad range of phase shift values. The equivalent circuit is apparently a topology that can exhibit the non-minimum phase properties [BODE45] required to allow somewhat independent control of the amplitude and phase characteristics that is required here.

An equivalent circuit model was successfully obtained for many different physical configurations using [ADS06]. Table 3.6-2 presents a few cases obtained with a three symmetrical layer PSS using the equivalent circuit model of Figure 3.6-1. Note that the inductance L is unchanged for all cases, as expected; its value is close to the approximate value of 0.628 nH obtained with (3.6-1). Also note that the series capacitance C_3 is zero when there are no metallic strips ($a_1 = a_2 = 0$), which is also expected since the electric field then does not have any component along the z-axis anywhere in this case (it remains completely polarised along the y-axis, as shown in Figure 3.4-7). Finally, it is important to mention that the shunt capacitances are not zero in the latter situation; rather their contributions are used to model the transmission line model of the bare dielectric.

The broadband behaviour of the case with an ideal transmission phase of –270° is presented in Figure 3.6-2. The results obtained from full-wave simulations using [EMPI07], as well as the circuit model of Figure 3.6-1 with values from Table 3.6-2 extracted using [ADS06] are compared. The values of the components of the equivalent circuit were optimised from frequencies close to DC up to 45 GHz. The results reveal an excellent agreement between the full-wave simulations and equivalent circuit model from DC to 35 GHz. Because of their low amplitude values (transmission coefficient below –35 dB), the results between 35 GHz and 45 GHz are not displayed since they are meaningless in this case. At this point, it is important to mention that the behaviour of the PSS/PASS appears to be very similar to that of a low-pass filter, for which the order is

Table 3.6-2: Ideal and simulated transmission values at 30 GHz for physical parameters a_1 and a_2 and the component values for the equivalent circuit model (normalised impedance of η_0 = 377 Ω).

Ideal normalised transmission phase (°)	0	–90	–180	–270
Ideal transmission amplitude (dB)	0	0	0	0
Simulated normalised transmission phase (°)	0	–89.3	–175.6	–264.8
Simulated transmission amplitude (dB)	–0.437	0	–0.049	–0.098
a_1 (mm)	0	2.32	2.54	2.83
a_2 (mm)	0	2.00	2.85	2.83
L (nH)	0.596	0.596	0.596	0.596
C_1 (pF)	0.004	0.028	0.032	0.059
C_2 (pF)	0.011	0.021	0.078	0.072
C_3 (pF)	0	0.015	0.023	0.024

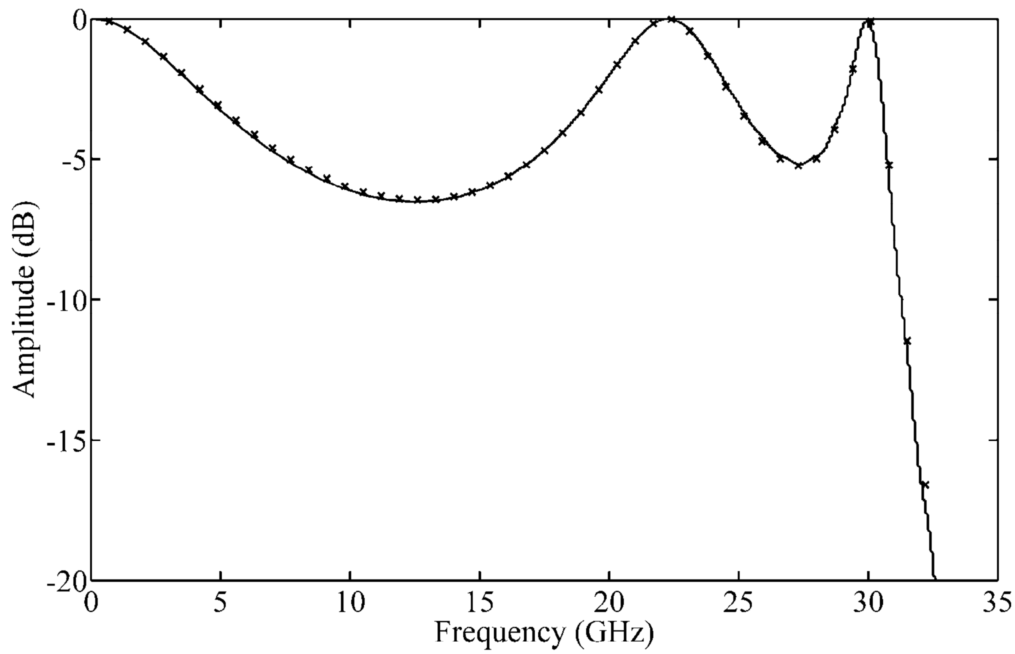

(a)

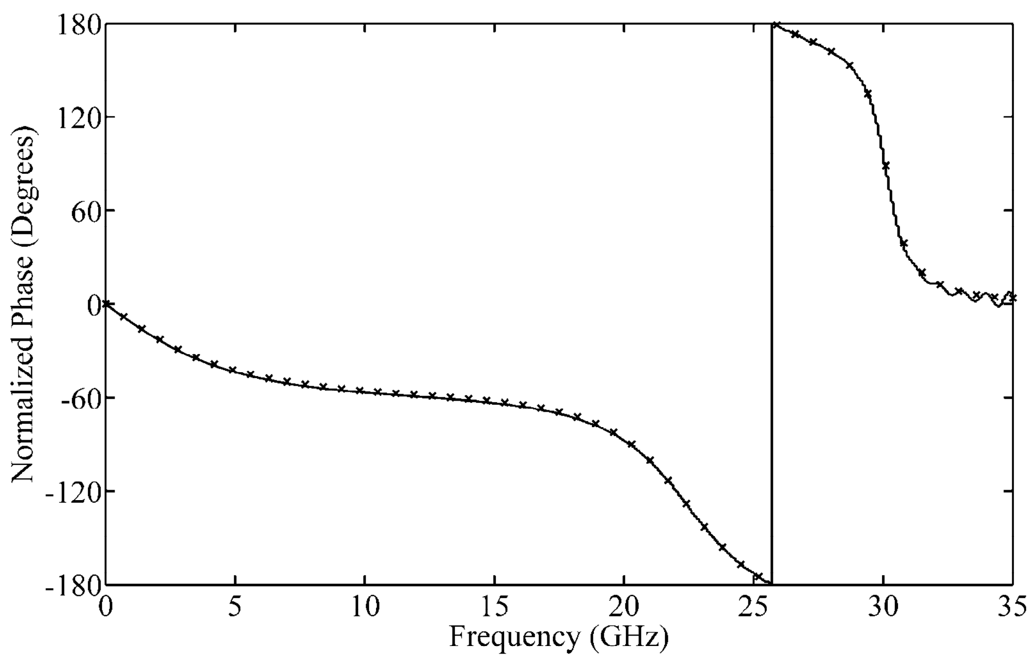

(b)

Figure 3.6-2: Transmission coefficient for an ideal phase shift of –270°; (a) Amplitude, (b) Phase; —— full-wave simulation results, × equivalent circuit model results using the extracted values from Table 3.6-2.

related to the number of layers. In this case, three conductive layers separated by two dielectric layers are used, resulting in an order of 5. The analogy with a low-pass filter should not be a surprise since the equivalent circuit model of Figure 3.6-1 is indeed similar to a low-pass filter, except for the series capacitances C_3. This analogy with a low-pass filter has other implications, which will be addressed in Section 3.7. However, it was found that further extending the simulation bandwidth far beyond the frequency of operation reveals that the structure is not a perfect low-pass filter since the transmission amplitude increases repeatedly as the frequency increases. This is also not a surprise since the circuit model was obtained for a given band only and the shunt inductance was neglected. However, this shunt inductance is of importance far beyond the frequency of operation and constitutes one of the reasons why the transmission amplitude does not remain low throughout the band beyond that covered by the circuit model. Nevertheless, this does not cause any problem regarding the validity of the current model from DC to frequencies beyond the frequency of operation. The model is accurate and meaningful within that frequency range. It is also pointless for the current study to try to extend the validity of the current circuit model; however this option may be considered in the future if one thinks the PSS/PASS can be operated beyond the frequency of validity of the current model. The important thing is to keep in mind that, although the circuit model behaves like a low-pass filter, the PSS/PASS is actually not necessarily behaving that way. The equivalent circuit model was discussed in this section mainly to provide increased insight into the ability of the PSS/PASS structure to allow the near-independent control of its transmission amplitude and phase coefficient.

3.7 Further Considerations of the PSS/PASS Structures

In this section some further discussion on the performance of the PSS/PASS structure is provided.

3.7.1 Number of layers and bandwidth

As mentioned in Section 3.6, the PSS/PASS circuit model is similar to a low-pass filter, albeit not precisely so. However, for the purpose of the present considerations on the number of layers and bandwidth, it will be treated as a low-pass filter. That being said, there is a direct relationship between the number of stages or the order of the low-pass filter circuit model and the number of layers in the PSS/PASS. In Section 3.4, it was shown that when too few layers are used, the PSS/PASS cannot achieve a large enough phase shift range. Consequently, it is tempting to increase the number of layers, which showed to provide a broader phase shift range. From filter theory, increasing the order of a filter results in a smaller transition band between stopband and passband, which corresponds to a more abrupt slope between stopband and passband [RORA97]. This is important to mention since a PSS operates very close to the transition region and a PASS operates close or in the transition region; recalling that the frequency of operation is 30 GHz, see Figure 3.6-2. The PSS and PASS operate at this point because it is the region where the phase changes significantly with the physical parameters. However, increasing the number of layers results in bandwidth limitations since the transition region becomes smaller. Regarding the latter statement, the effect of changing the number of layers from 3 to 4 for the case of a PSS lens antenna is addressed experimentally in Chapter 6, where it shows that the bandwidth reduction is non-negligible. The optimum number of layers for the design of a PSS/PASS is probably around 3 or 4 layers since fewer layers do not result in a large enough phase shift range and more layers will present a significant bandwidth reduction. However, this is not necessarily bad news since it forces the designer to keep the number of layers small, which is beneficial for practical considerations such as thickness, weight and fabrication complexity.

3.7.2 Use of PSS/PASS concept at other frequency bands

By looking at Figure 3.6-2, which represents a typical case of transmission coefficient over frequency, it is seen that, for very low frequencies approaching DC, the transmission amplitude is unity and the transmission phase is null, consequently the structure behaves like a slab of air. At very high frequencies, the transmission amplitude decreases, even though there are some bands where the transmission amplitude is unity or close to it. Note that these bands are not predicted by the equivalent circuit model of Figure 3.6-1. As mentioned is Section 3.7.1, the PSS/PASS structure has a behaviour similar to that of a low-pass filter, except for these passbands at frequencies beyond the validity of the equivalent circuit model in Figure 3.6-1.

As stated in the Section 3.7.1, the PSS/PASS is designed to operate near and at the transition region between the passband and the stopband. Consequently, it is not possible to use the same structure with the same dimensions of unit cell size s and thickness h to operate in the same region at another frequency. Alternatively, the same configuration can be made to work at other frequency bands by performing minor modifications to it, such as scaling. If the same unscaled structure is used at lower frequencies, the operation will be taking place in the passband region where the transmission amplitude is high, therefore it will not be possible to have any PASS applications, but most important the phase will be relatively constant if physical dimensions of the strips or patches (a_i's) are changed, and no interesting phase shift range can be achieved. If the same structure is used at higher frequencies, the operation will most likely take place in the stopband region where the transmission amplitude is low, therefore it will not be possible to have any high-efficiency PSS/PASS application. It is true that some passbands exist at higher frequencies, but the possibility of operating at these passbands has not been investigated. Furthermore, operating the PSS/PASS at these frequencies would lead to large unit cells with respect to the wavelength, which would have bad consequences for the quantisation as well as potential problems regarding the unit cell size, as stated by (3.3-1).

From filter theory [POZA98], for the case of a low-pass filter, all electric components of the filter can be scaled up in values in order to lower the cutoff frequency. This can be accomplished here for the PSS/PASS. From (3.6-1), the only way to increase L is by increasing the thickness h of the PSS/PASS structure. However, increasing L will reduce the value of the series capacitance C_3. In order to increase C_3, either the strip or patch size has to be increased, or the dielectric constant has to be increased, or both. If the size is increased, this requires increasing the unit cell size as well. Furthermore, in order to scale the shunt capacitances C_1 and C_2 as well, there may not be any other option than increasing the unit cell size s.

Figure 3.7-1 presents the transmission coefficient for two cases obtained from full-wave simulations [EMPI07]. The first case is the one presented in Figure 3.6-2 and in the last column of Table 3.6-2, producing a normalised phase shift of –270° at 30 GHz with s = 3 mm, a_1 = 2.83 mm, a_2 = 2.83 mm, h = 1 mm and ε_r = 2.2. The second case is a case

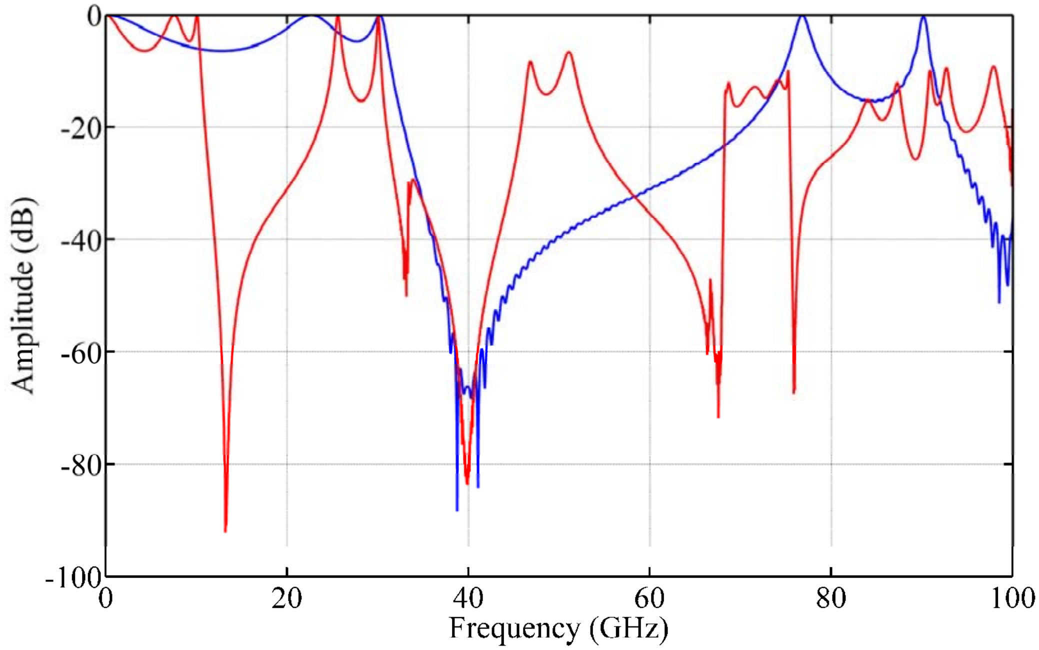

(a)

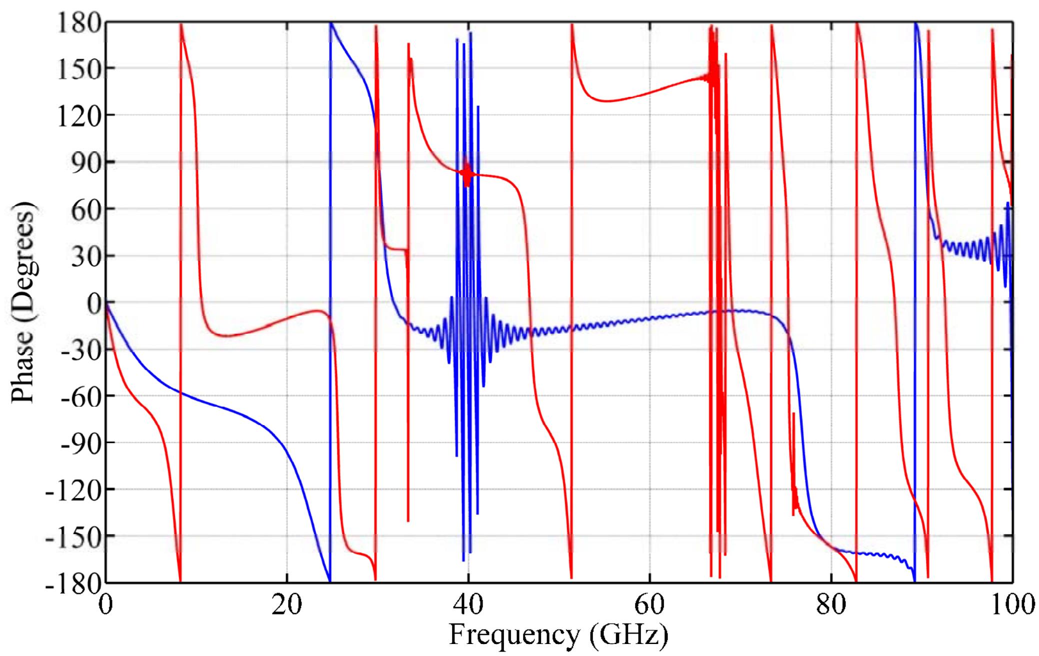

(b)

Figure 3.7-1: Simulated transmission coefficient for an ideal phase shift of –270°; (a) Amplitude in dB, (b) Phase in degrees; —— non-scaled (*s* = 3 mm, *h* = 1 mm), —— scaled three times bigger (*s* = 9 mm, *h* = 3 mm).

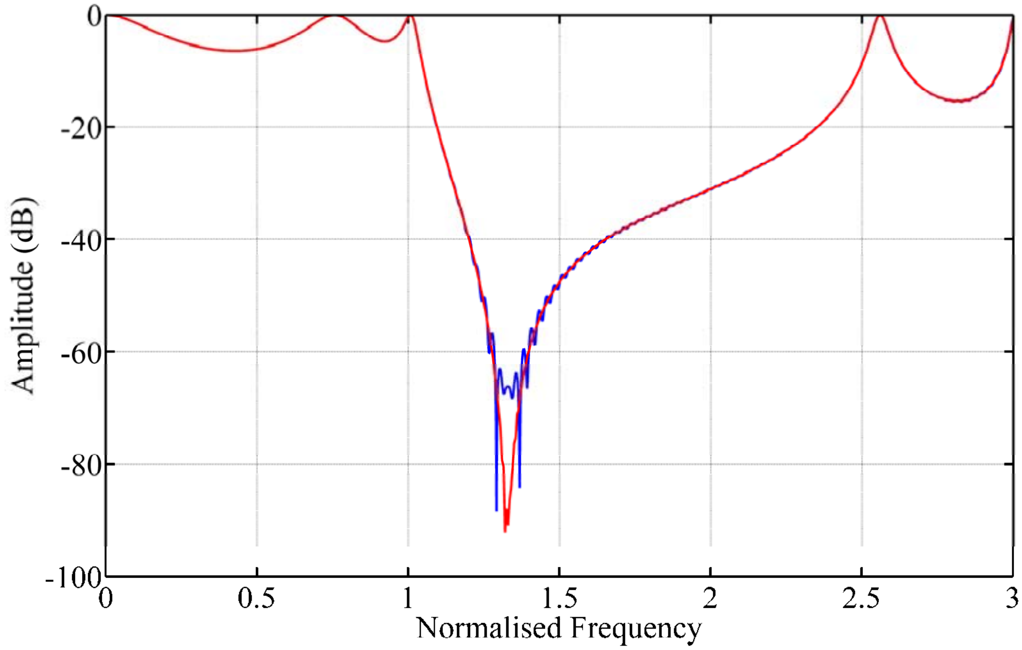

(c)

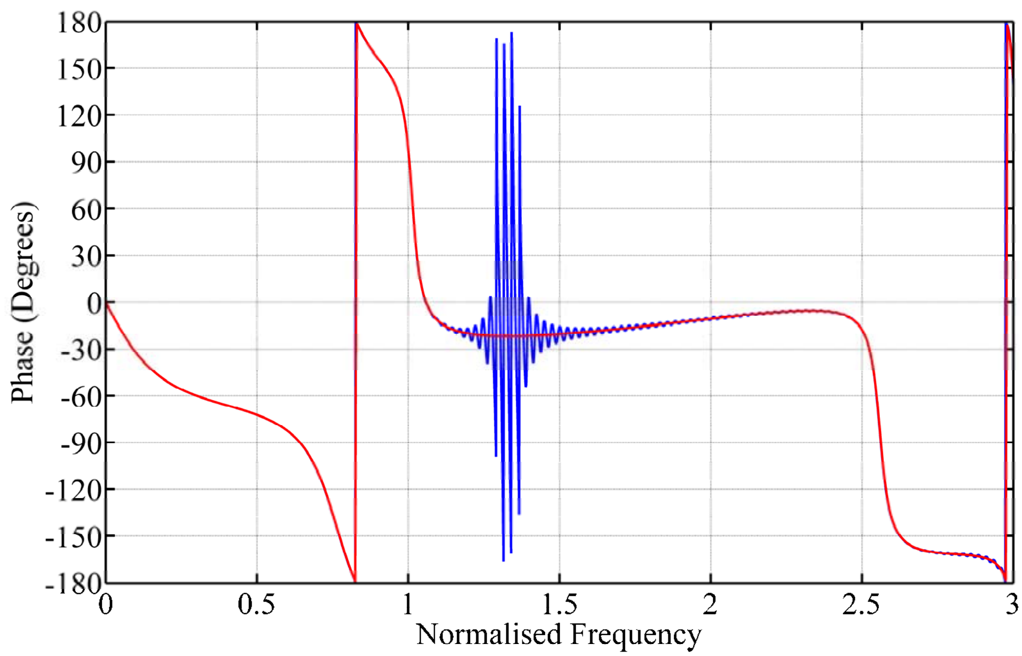

(d)

Figure 3.7-1 (continued): (c) Amplitude in dB with normalised frequency, (d) Phase in degrees with normalised frequency; —— non-scaled (*s* = 3 mm), —— scaled three times bigger (*s* = 9 mm).

scaled up in size by a factor of three, resulting in dimensions of s = 9 mm, a_1 = 8.49 mm, a_2 = 8.49 mm, h = 3 mm, the same relative permittivity ε_r of 2.2, and a normalised phase shift of –270° at 10 GHz. Note the pass bands in Figure 3.7-1(a) at frequencies much higher than the operating frequency. When the frequencies are normalised, the two curves are almost identical, as shown in Figures 3.7-1(c) and 3.7-1(d), except for the very low amplitude region. It is believed that the discrepancy is caused by numerical noise of the full-wave simulation, which is highly present in the unscaled case.

The same exercise can be performed for a PSS/PASS made to operate at higher frequencies. For this to happen, the cutoff frequency must be increased as well. This is accomplished by lowering the values of the electric components. Again the intuitive analysis starts with the series inductance L, which has to be decreased in this case. This is done by reducing the thickness h of the PSS/PASS structure. However, this will increase the value of the series capacitance C_3. In order to decrease C_3, either the strip or patch size has to be decreased, or the dielectric constant has to be decreased, or both. If the size is decreased, this requires decreasing the unit cell size as well. Furthermore, in order to scale the shunt capacitances C_1 and C_2, there may not be any other option than decreasing the unit cell size s. A similar analysis as the one presented in Figure 3.7-1 would show that the scaling can be done for operating at higher frequencies by scaling down the dimensions of the unit cell. Therefore, it is shown that the scaling of the electric components, and the scaling in frequency, is intuitively done by changing the size of the physical parameters.

3.7.3 Electromagnetic wave type and oblique incidence

In the analysis and electromagnetic simulations performed on the PSS/PASS unit cell, it has been assumed up to this point that a normally-incident plane wave with the electric field vertically polarised on the structure, as enforced by the boundary conditions shown in Figure 3.3-2, is used. However, this is only rigorously true if the actual incident electromagnetic fields are normally incident, of the plane-wave type and vertically-polarised.

This assumption is the same as that made in the design of reflectarrays, but it remains an assumption and does not fully represent the actual situation. The reader can be convinced of that statement by considering any such structure, fed by a closely located feed antenna, to figure out that, although the polarisation statement is true, the wave incident on the structure, here the PSS/PASS, is generally neither of the plane-wave type nor normally incident. Figure 3.7-2 presents propagating wavefronts from a finite-sized antenna feed onto a planar lens structure, showing that the incidence wave is not a plane wave and that the angle of incidence of the rays is not normal except for the centre of the lens structure. In fact, the angle of incidence of the rays increases away from the middle of the lens structure. As for the type of wave, before the electromagnetic simulation tools became widely available, all lenses and reflectors were designed using the geometrical optics approximation where any point on the structure was treated locally using ray tracing, i.e. localised plane wave. This is a valid approximation as long as the local regions, i.e. unit cells, are made sufficiently small that the wave appears plane within their area. Furthermore, the PSS/PASS is not made to have a uniform unit cell on its surface, whereas the simulations to set up the database assume uniform unit cells. This is another source of discrepancy.

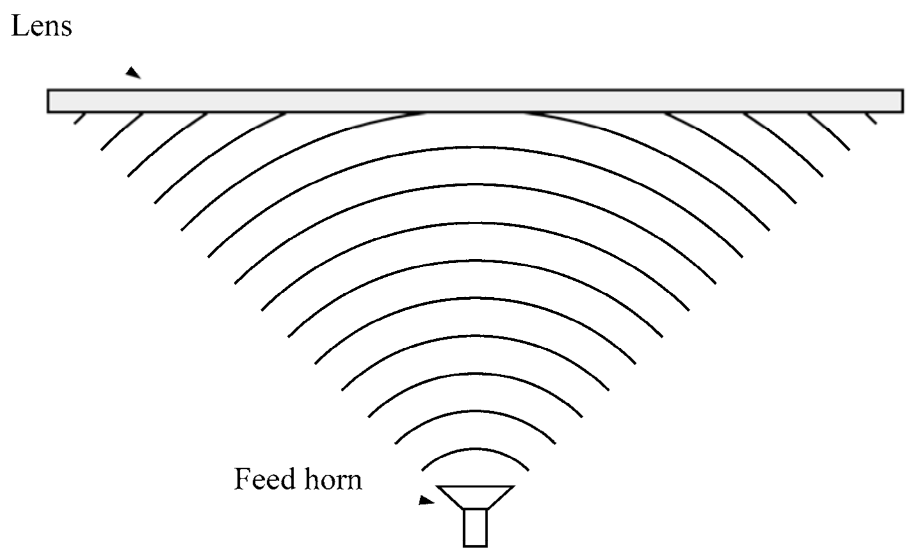

Figure 3.7-2: Propagating wavefronts from a feed antenna onto a planar lens structure.

For small electric size periodic structures, the wave incident on the PSS/PASS can be assumed to be of the plane wave type, i.e. without any amplitude or phasefront curvature within the unit cell. For analysing periodic structures, current full-wave electromagnetic simulation engines generally support plane wave incidence only. Therefore such a type of excitation is commonly assumed, especially since the results obtained usually provide a very good assumption.

A uniform periodic structure – i.e. a periodic structure for which all the cells are identical – is also generally accepted as it provides acceptable results. Furthermore, it is not reasonable to assume each and every cell case to be analysed with neighbouring cells having different physical parameters – as it would be the case in a real life implementation – because it would require an enormous amount of data to be generated.

The angle of incidence is another parameter that could be accounted for in generating a database for PSS/PASS designs. However, the amount of data to be generated would be impractically large, as is the case for the neighbouring cells addressed in the preceding paragraph.

Nevertheless, for small focal length to diameter ratios (F/D), the angle of incidence can be a critical factor that may not be neglected. The FDTD simulation package used for the simulations [EMPI07] supports only normal incidence angles for the analysis of infinite periodic structures; it cannot support oblique incidence angle. However, the FEM simulation package [HFSS07] does support oblique incidence angles when modelling plane wave incidence on an infinite periodic structure.

Figure 3.7-3 presents results of four different types of unit cells with different incidence angles for a symmetrical three-independent layer strip configuration. It is the amplitude of the field propagating directly through the structure that is shown in Figure 3.7-3. The two common polarisation types are presented in Figure 3.7-3: parallel polarisation, as shown in Figure 3.7-4(a), and perpendicular polarisation, as shown in Figure 3.7-4(b) [COLL92]. The different cases presented have phase shift steps of 90°. From Figure 3.7-3, the first thing to be noticed is that the smaller phase shift steps are more stable as the incidence angle increases, especially for the parallel polarisation. For the parallel polarisation cases, the amplitude and phase are fairly stable with incidence angle, at least up to 70°, except for the –270° case. For the perpendicular polarisation, the PSS/PASS is significantly less stable, and the amplitude deteriorates rapidly for all cases except for the –180° case, while a similar degradation is obtained for the phase, except for the 0° case.

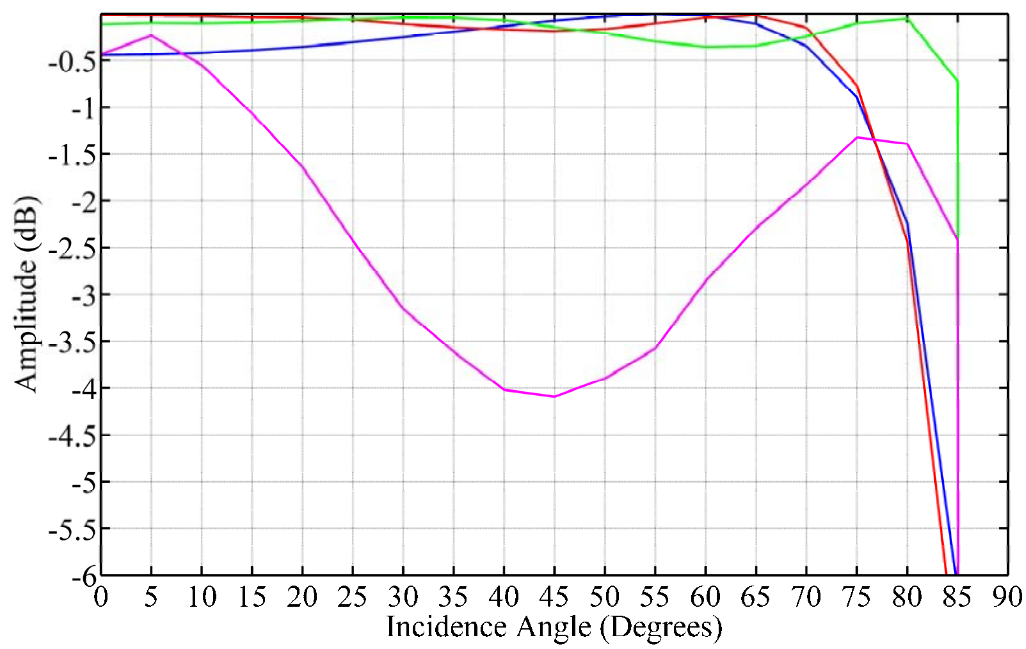

(a)

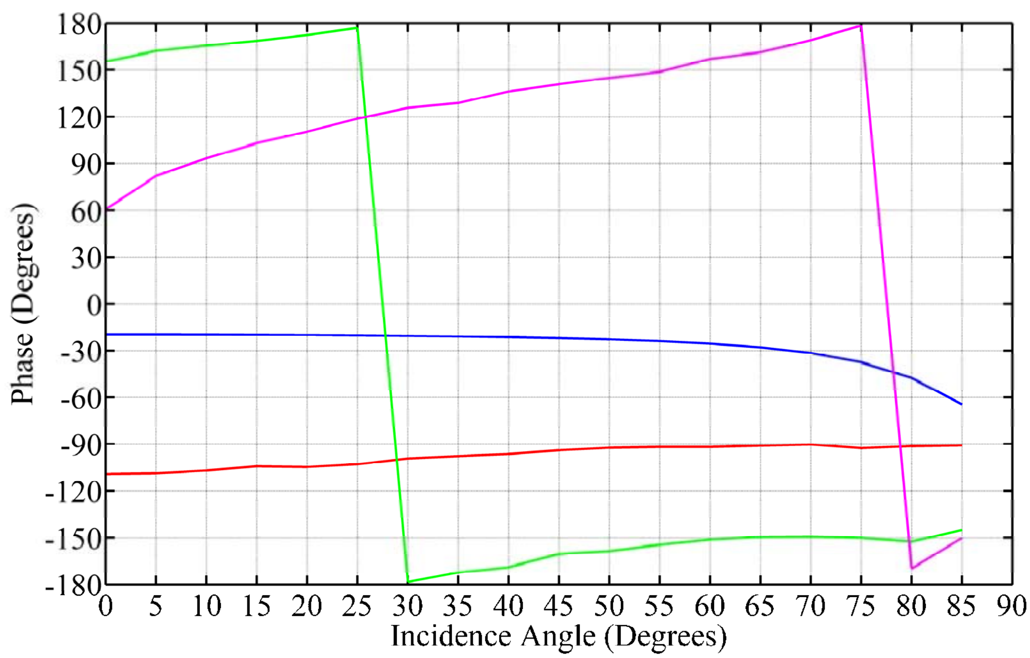

(b)

Figure 3.7-3: Simulated transmission coefficient for different incidence angles for a symmetrical three-independent layer strip configuration; (a) Amplitude in dB for parallel polarisation, (b) Phase in degrees for parallel polarisation; —— a_1 = 0 mm, a_2 = 0 mm (0°); —— a_1 = 2.32 mm, a_2 = 2.00 mm (–90°); —— a_1 = 2.56 mm, a_2 = 2.85 mm (–180°); —— a_1 = 2.85 mm, a_2 = 2.82 mm (–270°).

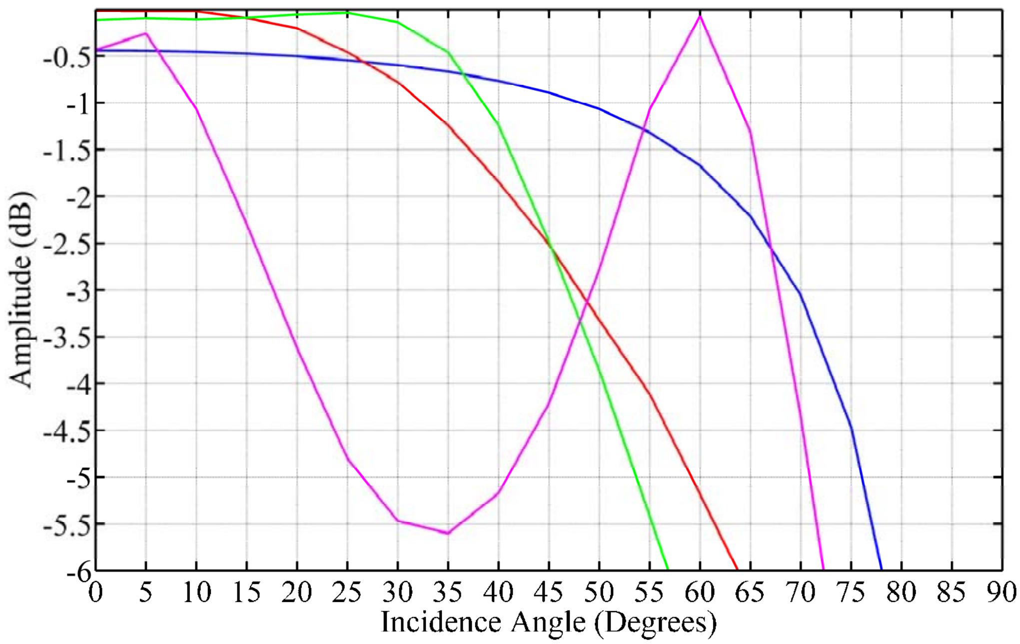

(c)

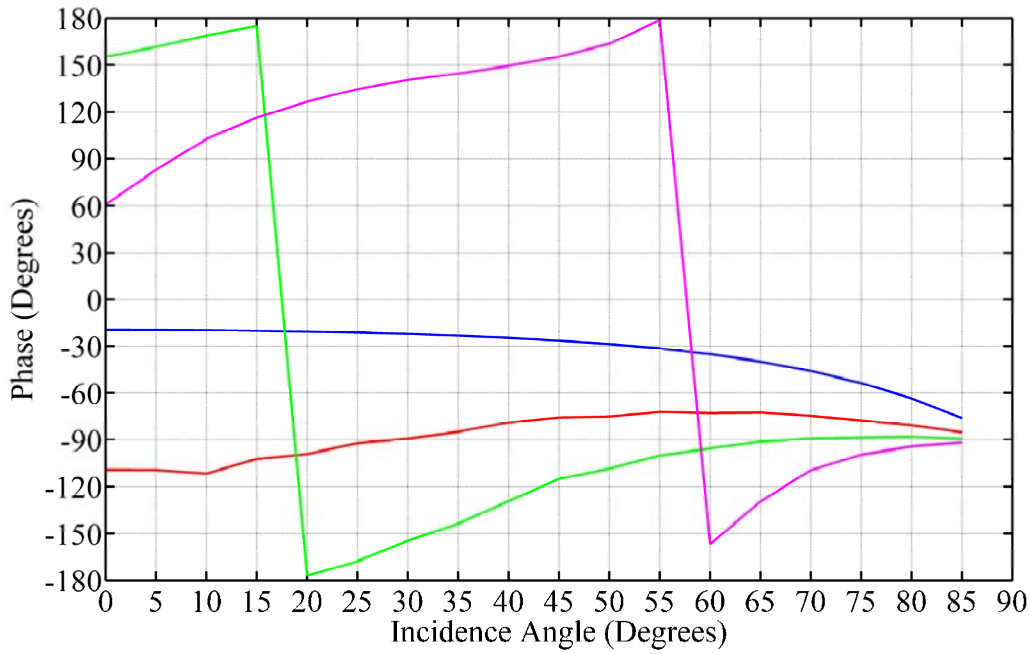

(d)

Figure 3.7-3 (continued): (c) Amplitude in dB for perpendicular polarisation, (d) Phase in degrees for perpendicular polarisation; —— a_1 = 0 mm, a_2 = 0 mm (0°); —— a_1 = 2.32 mm, a_2 = 2.00 mm (–90°); —— a_1 = 2.56 mm, a_2 = 2.85 mm (–180°); —— a_1 = 2.85 mm, a_2 = 2.82 mm (–270°).

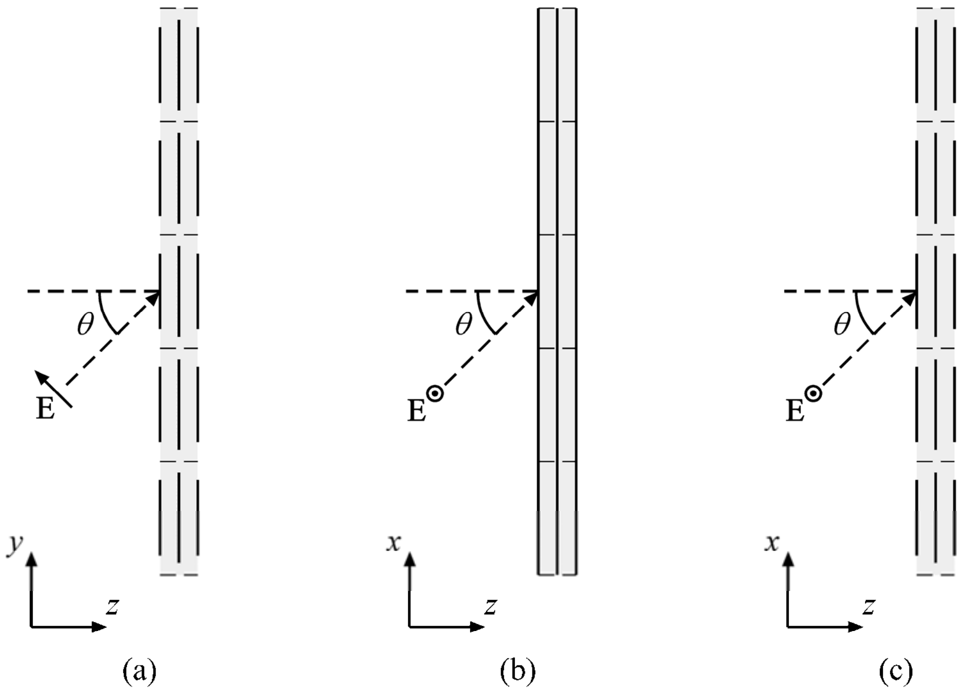

Figure 3.7-4: Representation of oblique incidence for different cases of symmetrical three independent layers; (a) parallel polarisation shown along the side view, (b) perpendicular polarisation shown along the top view for the strip case, (c) perpendicular polarisation shown along the top view for the patch case. The dielectric is shown in grey and the metal is shown in black.

Figure 3.7-5 presents results of four different types of unit cells with different incidence angles for a symmetrical three-independent layer patch configuration. Again the two common polarisation types are shown: parallel polarisation, as shown in Figure 3.7-4(a), and perpendicular polarisation, as shown in Figure 3.7-4(c). The different cases presented have phase shift steps of 90°. From Figure 3.7-5, the first thing to be noticed is that the smaller phase shift steps are less prone to amplitude and phase change as the incidence angle increases, especially for the parallel polarisation. For the parallel polarisation cases, the amplitude and phase do not vary much as the incidence angle

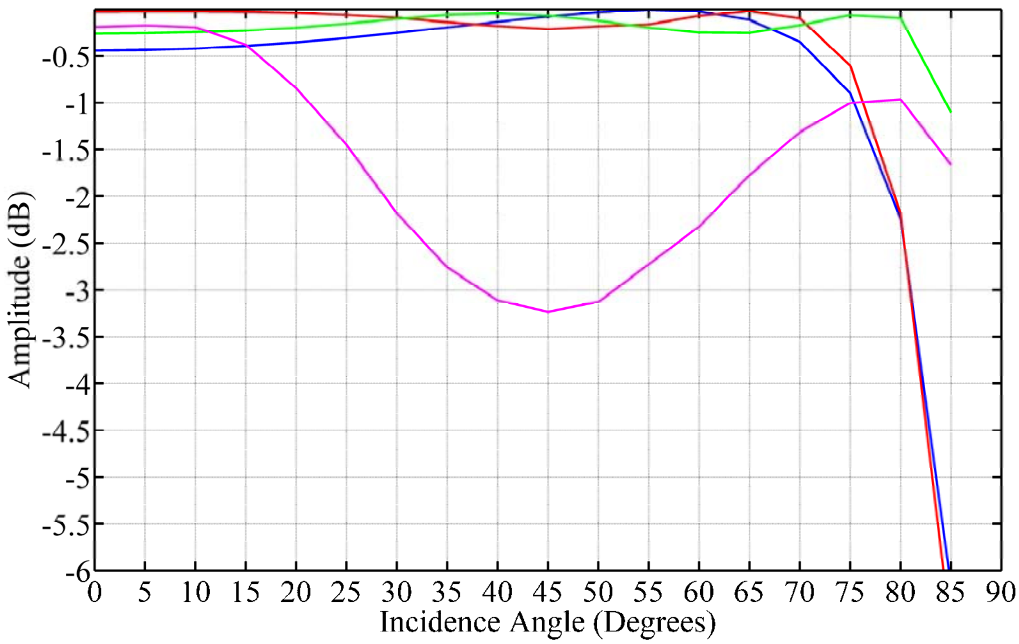

(a)

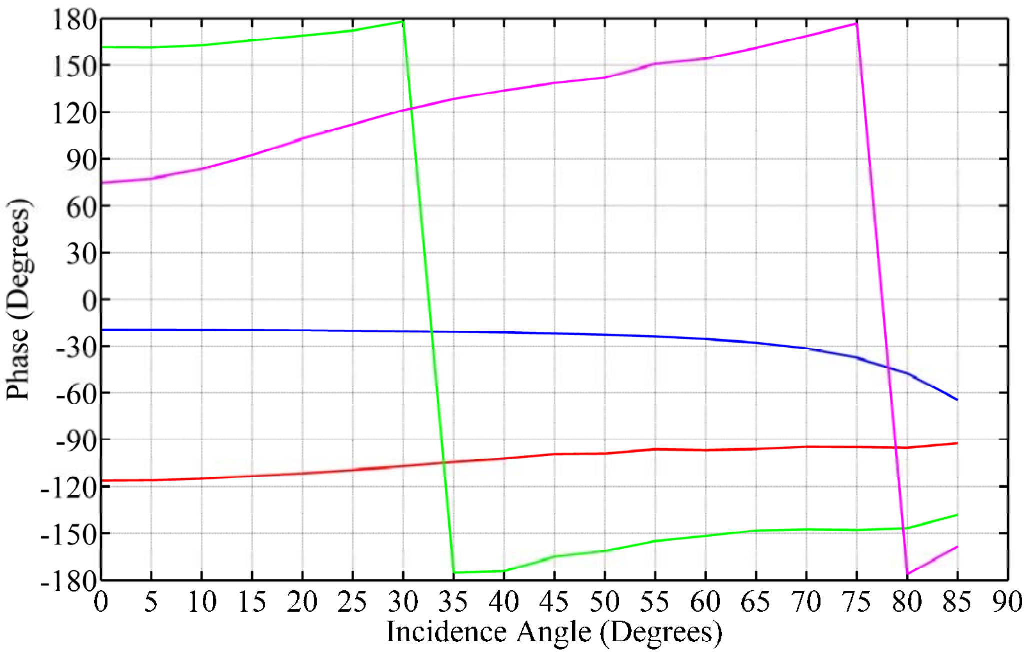

(b)

Figure 3.7-5: Simulated transmission coefficient for different incidence angles for a symmetrical three-independent layer square patch configuration; (a) Amplitude in dB for parallel polarisation, (b) Phase in degrees for parallel polarisation; —— a_1 = 0 mm, a_2 = 0 mm (0°); —— a_1 = 2.4 mm, a_2 = 2.2 mm (–90°); —— a_1 = 2.6 mm, a_2 = 2.84 mm (–180°); —— a_1 = 2.84 mm, a_2 = 2.84 mm (–270°).

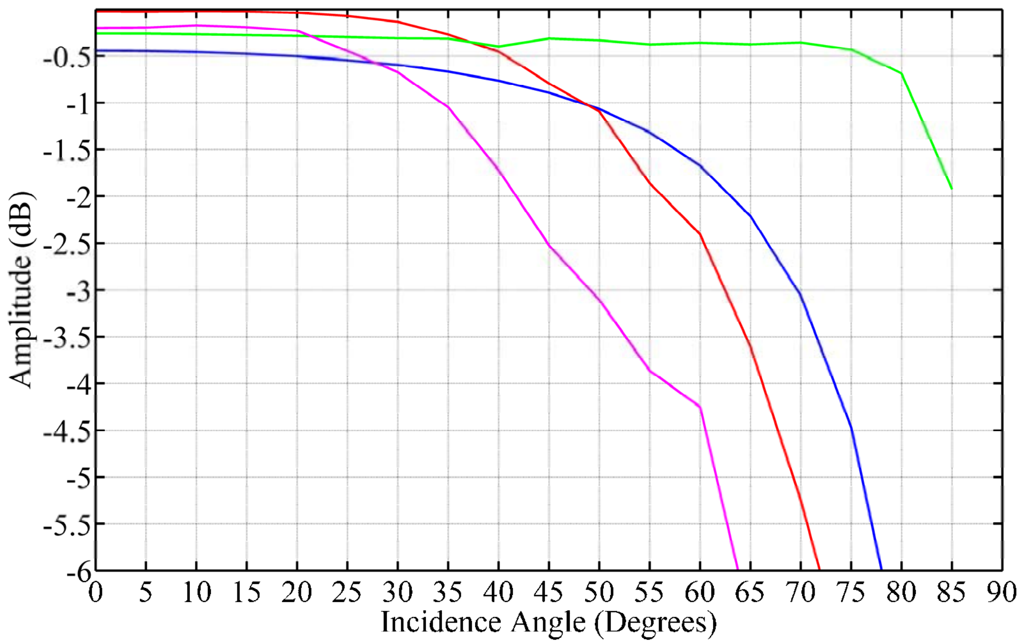

(c)

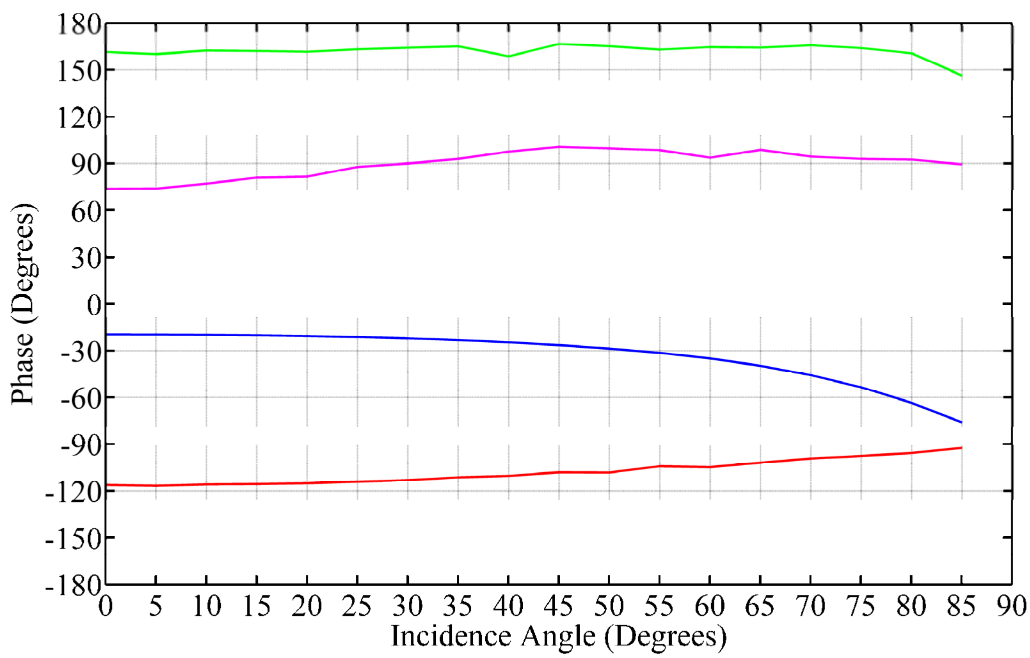

(d)

Figure 3.7-5 (continued): (c) Amplitude in dB for perpendicular polarisation, (d) Phase in degrees for perpendicular polarisation; —— a_1 = 0 mm, a_2 = 0 mm (0°); —— a_1 = 2.4 mm, a_2 = 2.2 mm (–90°); —— a_1 = 2.6 mm, a_2 = 2.84 mm (–180°); —— a_1 = 2.84 mm, a_2 = 2.84 mm (–270°).

changes, at least up to 70°, except for the –270° case. For the perpendicular polarisation, the PSS/PASS has clearly more variation in the amplitude, however in all cases the phase does not vary significantly.

By comparing the strip results from Figure 3.7-3 to the patch results from Figure 3.7-5, it is found that the parallel polarisation cases are very similar. However, the perpendicular polarisation cases are significantly different. In fact, the square patch cases present a much stronger amplitude and phase stability over the incidence angle compared to the strip cases. This is an important advantage that could be of significant importance in the realisation of PSS lensing structures with small focal length distances. In fact, lenses based on the PSS concept with focal length to diameter ratio of 0.5 are reported in Chapter 6. In Section 6.9.1, two 3-layer PSS 90° phase-correcting Fresnel zone plate antennas (PC-FZPAs) – one realised with strips and the other one with square elements – are compared. The comparison – based on experimental results – suggests that the PSS PC-FZPA made of square elements is less sensitive to oblique incidence.

3.7.4 Classification of PSS/PASS

In this section, the relation of the PSS/PASS structures to artificial dielectrics, metamaterials and frequency selective surfaces is briefly discussed. The discussion stresses the uniqueness of the PSS/PASS concept and how it is different to any of these.

3.7.4.1 PSS/PASS vs artificial dielectric

As mentioned in Section 2.2, artificial dielectrics [COHN54] have been used in the past for realising structures such as lenses. Usually the artificial dielectric is obtained by periodically embedding metallic implants [KOCK48], but it is also possible to obtain an artificial dielectric by changing the relative permittivity. This has been reported in [PETO03], in which a slab of high relative permittivity has been perforated to reduce the resulting relative permittivity in some area of the lens.

One may look at the PSS/PASS as an artificial dielectric based on metallic implants. However, in all cases of artificial dielectric, the implants are repeated periodically along the direction of propagation and the thickness is significantly larger than one tenth of a wavelength with a significant number of repetition or layers. The PSS/PASS is too thin to be considered an artificial dielectric and the metallic implants are not repeated along the direction of propagation since they are of different size on each of the metallic layers. Furthermore, an artificial dielectric implies an equivalent relative permittivity, as reported in [COHN54] and [BROW55], whereas the PSS/PASS is simplified in terms of an equivalent circuit model of lumped elements instead of an equivalent relative permittivity (and relative permeability).

3.7.4.2 PSS/PASS vs metamaterial

A metamaterial is an engineered material that exhibits behaviour that can usually not be found in nature. It usually refers to a left-handed material, i.e. a material with negative permittivity and permeability. The concept was first reported in the late 1960's [VESE68], but brought back in the late 1990's [PEND99] and has been the subject of intensive research since the beginning of the 21st century. However, metamaterials are controversial [MUNK09], and there is no clear consensus whether the negative permittivity and permeability behaviour truly occurs [SPIE09], and whether metamaterials proper could really be practical.

The intention here is not to take a position on whether metamaterials exist or not, but rather to make a statement as to whether the PSS/PASS is a metamaterial or not. From the author's point of view, the PSS/PASS is not believed to be a metamaterial. The behaviour of the PSS/PASS can be explained using a simple circuit model. This also happens to be one of the arguments of the filter and networks group debating in [SPIE09]: this group claims that the metamaterial concept is used to explain things that could be explained in other ways. In Section 3.6, it was clearly demonstrated that the behaviour of the PSS/PASS could be explained by a simple circuit model over a reasonable frequency band, therefore it is not necessary to explore the PSS/PASS as a metamaterial.

3.7.4.3 PSS/PASS vs artificial impedance surface

An artificial impedance surface is a surface designed with a specific impedance using a periodic structure approach backed with a ground plane. The concept of an impedance surface has been used quite a lot in surface wave applications; however that of artificial impedance surface was introduced by Sievenpiper and others in the late 1990's [SIEV99]. The artificial impedance surface is usually of high impedance value or designed to reproduce a magnetic conductor, with a reflection phase of 0°, which is different from the 180° reflection phase obtained from a uniform sheet of metal. This has several advantages for some antenna applications, such as a dipole over a ground plane, for which the overall thickness of the antenna can be reduced [SIEV08]. Artificial impedance surfaces can also be used to reduce surface waves, to design antennas based on holographic principles or as a reflectarray.

As for the PSS/PASS, the unit cell size of the artificial impedance surface is subwavelength in size, however the artificial impedance requires a very small unit cell size with respect to a wavelength in order to operate efficiently (typically one tenth of a wavelength [SIEV99]) whereas the unit cell size of the PSS/PASS can work efficiently for any size (as long as it is less than half a free-space wavelength, in order to avoid grating lobes). Although the PSS/PASS and the artificial impedance surface could be similar at first sight, they are actually quite different and must be differentiated. The major difference between the artificial impedance surface and the PSS/PASS is that the artificial impedance surface is a reflective surface, with a conductive layer on the back, whereas the PSS/PASS is a transmissive surface. Furthermore, the reflection of the artificial impedance surface is always unity (if no losses are present). In cases where the impedance surface varies with position, the surface impedance is varied by changing the dimensions of the local elements; however, this surface does not attempt to perform any amplitude transformation since it is a reflective surface. Consequently, the capability of shifting the phase and amplitude independently is one unique aspect of the PASS. The PASS allows for controlling both the amplitude and phase, in transmission, whereas the artificial impedance surface only permits phase control with total amplitude, in reflection.

3.7.4.4 PSS/PASS vs frequency selective surface (FSS)

A frequency selective surface or screen is a resonant structure that allows for transmitting the wave energy over some specific frequencies while blocking it at others [MUNK00], [CWIK08]. In that sense, it consists of a structure that is designed to control the amplitude of an incoming wave, but as a function of frequency. The PASS/PSS is not designed for frequency selectiveness but to apply a spatial amplitude and phase transformation to an incident wavefront. It may act as a filter over frequency, as shown in

Section 3.6, but this is incidental. Furthermore, the PSS/PASS is a non-resonant structure, unlike the FSS.

Another point to mention is that the PSS/PASS is designed specifically for reactive coupling between the different layers. This is not the case for frequency selective surfaces. Generally, when multiple layers are cascaded, each layer is treated independently and the interaction between layers is purposefully reduced [BIRB08].

3.8 Conclusions

In this chapter, the PSS and PASS concepts were thoroughly described. The way the structure was implemented was clearly demonstrated. Simulation data sets – to be used in design of PSS or PASS devices – were provided. The behaviour of the PSS/PASS was fully explained, backed by an equivalent circuit model. Finally, the uniqueness of the concept was validated by comparison with other concepts that could be thought to be the same.

In Chapters 4 to 6, the PSS concept will be applied to the design of phase-correcting devices, including lenses. In Chapter 7, the PASS concept will be applied to the design of a flat-topped beam antenna. All of these implementations show convincing experimental results confirming that the PSS/PASS could be used for designing free-standing structures to be used as viable alternative for many current applications.

CHAPTER 4 PSS Linear Binary Phase Grating

4.1 Introduction

The phase shifting surface (PSS) was initially developed to address the real-estate and high-cost problems of free-standing phase-correcting devices such as lens antennas at microwave, millimetre wave and sub-millimetre wave frequencies. The PSS concept is not limited to antenna applications and can therefore be applied to other applications such as phase holograms. As for lenses, an ideal phase hologram would be thin, flat, light and low-cost.

Phase holograms make use of the phase-shifting surface (PSS) concept rather than the phase and amplitude shifting surface (PASS) concept. In using the PSS approach, the amplitude of the transmitted wave is maximised, so that one can use such a surface for recording phase holograms without any amplitude constraint, as suggested in [BROW69].

This chapter presents the first application of the phase-shifting surface (PSS). It consists of a linear binary phase grating. A grating is a periodic structure that can be considered as a hologram and, consequently, for which the theory of holography can be applied. In Section 4.2, the theory for linear gratings is presented. Section 4.3 presents the generation of linear gratings. Section 4.4 shows the reconstruction of the desired waves. The design of linear gratings is presented in Section 4.5, while the characterisation is done in Section 4.6. The chapter is concluded in Section 4.7.

4.2 Theory of Linear Gratings

A grating is a structure that is used to split an incoming beam into several outgoing beams traveling in different directions. The number of beams and their direction of propagation depend on the grating period. From a holographic viewpoint, a linear grating is generated from the interference between two plane waves. In this section, the recording of a hologram and the reconstruction of the desired wavefront is presented in detail for such a case. In particular, it is shown that reconstructed wavefront U_C is almost always not equal to the desired wavefront U_D, but necessarily contains a term proportional to it. The basic theory of holography, which is provided in Appendix A, is applied to the case of two plane waves interacting with each other. As done in Appendix A, any unimportant constant for the current problem is neglected [GOOD71].

4.2.1 Recording phase

In the simplest application of holography, the desired wavefront is a plane wave. The same carterian space as in Appendix A is assumed here, i.e. the hologram or recording medium is located in the *xy*-plane so that the hologram or recording medium is normal to the *z*-axis. It is assumed here that the direction of propagation of the desired plane wave is in the *xz*-plane, propagating at an output angle Φ with respect to the *z*-axis, normal to the hologram plane, as shown in Figure 4.2-1. Thus the field distribution at the plane of the hologram or recording medium resulting from the desired wavefront is given by U_D, which is defined as follows:

$$U_D(x,y) = \exp\left[-jk(\sin\Phi)x\right] = \exp\left[-j2\pi\left(\frac{\sin\Phi}{\lambda}\right)x\right] = \exp\left[-j2\pi\alpha x\right] \qquad (4.2\text{-}1)$$

Note that, because the wave is propagating in the *xz*-plane, its field distribution U_D has no dependency along the y-axis. Still, the $U_D(x,y)$ syntax is kept in order to keep in mind that the present problem takes place in a three-dimensional environment (with two-dimensional grating), such that a dependency along the *x*- and *y*-axis is possible (the actual case simply being a special case). The same was done in [GOOD71].

At this point, it is important to note that, unlike what is shown in Figure A.2-1, the output angle Φ is in the *xz*-plane because the wave is propagating in this plane. The reader should refer to Figure 4.2-1 showing a top view (*xz*-plane view) with properly defined output angle Φ. In (4.2-1), the other variables are k, the wave number, and α, the spatial frequency.

The spatial frequency is related to the grating period Λ according to

$$\alpha = \frac{1}{\Lambda} \tag{4.2-2}$$

The variables Φ, Λ (and α) and the wavelength λ are related according to Figure 4.2-1 and

$$\sin\Phi = \frac{\lambda}{\Lambda} = \alpha\lambda \tag{4.2-3}$$

In the current case, the reference wavefront is taken as a plane wave propagating along a direction normal to the plane of the hologram, which corresponds to a propagating angle equal to zero and thus leads to

$$U_R(x,y)\big|_{\Phi=0} = \exp\left[-\,jk(\sin 0)x\right] = \exp[0] = 1 \tag{4.2-4}$$

In application, however, illumination with an oblique incidence wave generates normal plane wave and vice versa.

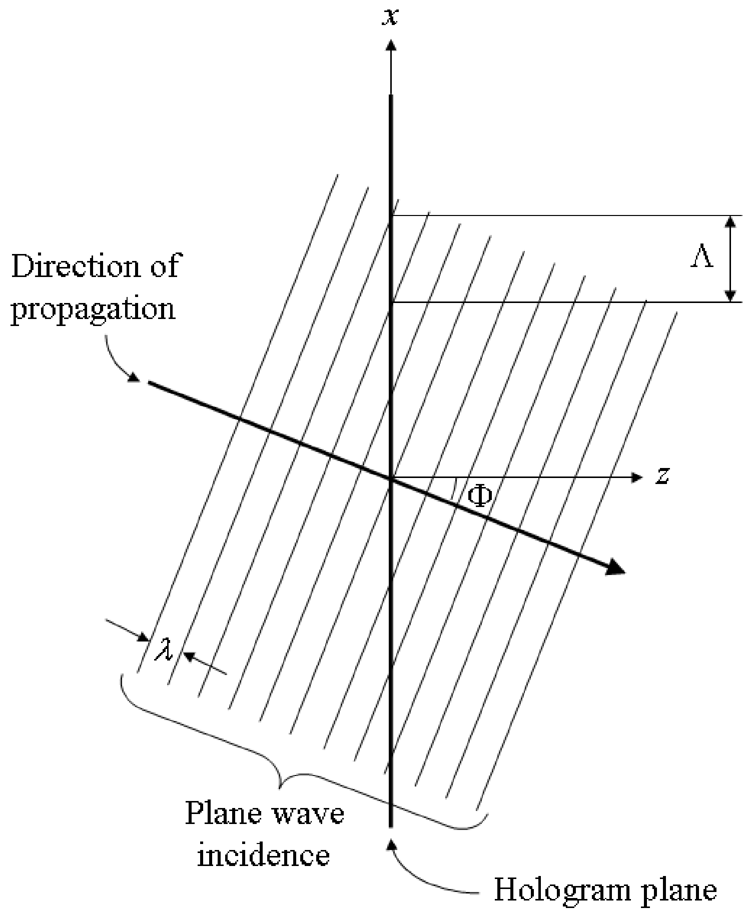

Figure 4.2-1: Plane wave incidence on a hologram plane, showing the relationship between Φ, λ and Λ.

From (4.2-1) and (4.2-4), the variables in (A.2-1) and (A.2-2) defined in Section A.2 are found to be

$$a = 1 \tag{4.2-5a}$$

$$\phi(x, y) = k(\sin\Phi)x = 2\pi\alpha x \tag{4.2-5b}$$

$$A = 1 \tag{4.2-5c}$$

$$\psi(x, y) = 0 \tag{4.2-5d}$$

Inserting (4.2-1) and (4.2-4) in (A.2-6) gives

$$I(x, y) = 2 + 2\cos(-2\pi\alpha x) \tag{4.2-6}$$

Note that (4.2-5a) and (4.2-5c) are chosen as unity for simplicity. Normalisation of (4.2-6) leads to the amplitude transmittance T of the hologram, such that:

$$T(x,y) = \frac{1}{2}\left[1 + \cos\left(-2\pi\alpha x\right)\right] \qquad (4.2\text{-}7)$$

The transmittance T defines the pattern of the hologram.

Holograms generated from (4.2-7) are generally named *analog holograms* since the transmittance is a smoothly varying function of position over the hologram surface. Such holograms can generally be easily generated at optical wavelengths using photographic films. They cannot be realised easily at microwave frequencies because of the absence of practical recording materials. However, the PSS concept introduced in Chapter 3 allows for generating a type of hologram very close to an analog hologram. Nevertheless, at these frequency bands, and even for computer-generated holograms at optical wavelengths, holograms take on what is commonly known as a binary form and, for this reason, are called *binary holograms*. It will be shown in Section 4.3.2 that an analog hologram is not necessarily more efficient (and in some cases may be less efficient) than a binary hologram.

Binary holograms can be either *amplitude holograms* or *phase holograms*. Both cases are generated from a redefined equation given in [HIRV97] as:

$$T_B(x,y) = \begin{cases} 0 \text{ if } 0 \le T(x,y) \le b \\ 1 \text{ if } b \le T(x,y) \le 1 \end{cases} \qquad (4.2\text{-}8)$$

where T_B is the binary transmittance and b is the threshold. In [HIRV97], more complex transmittance T and binary transmittance T_B equations are presented, taking into account a weighting function. If this weighting function is uniform, equations in [HIRV97] become identical to (4.2-8) for $b = 0.5$.

For an amplitude hologram, the null transmittance $T_B(x,y) = 0$ is created by metallic strips and the total transmittance $T_B(x,y) = 1$ through the absence of metallic strips (i.e. transmission through air or the thin substrate layer used to support the hologram [HIRV97]). This can be achieved using conventional photolithographic (wet chemical) etching, which is a mature and low-cost technology.

It is also possible to use (4.2-8) to generate a binary phase hologram. In this case, two different phase regions are used rather than two different amplitude regions. The phase regions are associated to the 0 and 1 values of (4.2-8). The phase shift is usually introduced by changing the thickness of a dielectric material. This process generally implies machining, which is more costly than conventional photolithographic (wet chemical) etching and results in a bulkier structure at microwave, millimetre wave and sub-millimetre wave. For this reason, amplitude holograms are generally preferred in these bands. However, by using the PSS concept, it is possible to generate a phase hologram using conventional photolithographic (wet chemical) etching process resulting in a thin, light and compact multilayer structure with high transmission amplitude.

It is interesting to mention that a mask similar to an amplitude hologram can be used at optical wavelengths to etch off part of a dielectric recording medium and consequently produce a phase hologram [LEE79]. This is currently not a practical fabrication procedure for holograms which operate at the frequencies of interest in this thesis.

4.2.2 Reconstruction phase

The desired wavefront can be reconstructed by illuminating the hologram (defined by T or T_B, or similarly by I since $T \propto I$) with the reference wave U_R, but since U_R is unity in this case (because a normal incidence plane wave is assumed):

$$U_C(x,y) \propto T(x,y) \tag{4.2-9}$$

Inserting (4.2-7) in (4.2-9):

$$U_C(x,y) = \frac{1}{2} + \frac{1}{4}\exp[-j2\pi\alpha x] + \frac{1}{4}\exp[j2\pi\alpha x] \tag{4.2-10}$$

which can be separated in three components, as follows:

$$U_C(x,y) = \frac{1}{2}U_0(x,y) + \frac{1}{4}U_{-1}(x,y) + \frac{1}{4}U_1(x,y) \tag{4.2-11}$$

where:

$$U_0(x,y) = 1 \tag{4.2-12a}$$

$$U_{-1}(x,y) = \exp[-j2\pi\alpha x] \tag{4.2-12b}$$

$$U_1(x,y) = \exp[j2\pi\alpha x] \tag{4.2-12c}$$

The subscript in (4.2-11) and (4.2-12) will become evident in Section 4.3.

From (4.2-12), it is seen that [GOOD71]:

- The term U_0 is related to the reference wave U_R and its corresponding wavefront propagates in the same direction, i.e. normal to the hologram plane.

- The term U_{-1} is related to the desired wave U_D, its corresponding wavefront is a duplicate of the desired wavefront used to generate the hologram, as seen in (4.2-1), and it propagates at an angle Φ.

- The term U_1 is similar to the term U_{-1} and its corresponding wavefront propagates at an angle $-\Phi$.

Mathematically, a perfect reconstruction of the wavefront would be obtained if only the desired term U_{-1} could be obtained in (4.2-11). Practically, a perfect reconstruction is possible if the propagating angles of the different wavefronts are highly different from each other. If the output angle Φ is zero, all the terms will propagate along this direction and the term U_{-1} cannot be recovered. Similarly, if the angle Φ is small, U_0, U_{-1} and U_1 cannot be separated. On the other hand, if the output angle Φ is different (and far enough) from zero, all the wavefronts propagate in different directions. The wavefront associated with the component U_{-1} is then the only component propagating in the desired direction Φ, and can be easily recovered.

The existence of the term U_1 is very interesting and could have been easily predicted. To demonstrate this, consider the case of a binary amplitude hologram. Since the hologram grating generated by the interference of two plane waves is composed of periodic dark (metallic) and clear strips, and because the reference plane wave is normal to the hologram, it is clear that, for a grating made to obtain propagation at an angle Φ, there will also be a beam of equal weighting propagating at an angle -Φ since the grating cannot determine which angle (Φ or -Φ) it was designed for. In other words, (4.2-10) would have been the same if the hologram were generated for a propagation angle -Φ.

4.2.3 Phase grating vs amplitude grating

An amplitude hologram is characterised by a constant phase and variable amplitude. As stated in Section 4.2.2, in its binary version, which was found [BROW69] to be more efficient than its continuous or grey counterpart, the transmission is either unity or null; the unity transmission assumes clear material and the null transmission is created by blocking the incoming wave using obstacles. This can be achieved using conventional photolithographic (wet chemical) etching process, where the unity transmission corresponds to the regions where there is no metal and the null transmission corresponds to the region where the metal is present. Since the photolithographic (wet chemical) etching process is a mature and low-cost technology, amplitude holograms are very attractive, especially at microwave, millimetre wave and sub-millimetre wave frequencies. However, even though binary amplitude holograms are more efficient than continuous amplitude holograms, binary amplitude holograms realised in this way suffer from poor diffraction efficiency (i.e. the amount of power in the desired diffracted beam divided by the total power) of no more than 10% [BROW69]. Nevertheless, microwave holograms are traditionally of the amplitude type ([IIZU75], [KOCK68], [LÉVI01]).

A phase hologram is characterised by a constant unity amplitude and a variable phase [BROW69]. The phase is usually introduced by changing the thickness of a dielectric material. This process generally implies machining, which is more costly than conventional etching and results in a bulkier structure at microwave, millimetre wave and sub-millimetre wave. Other techniques were developed to record the phase while trying to reduce the thickness and fabrication cost ([BROW66], [TRIC70]), but they also suffer from major drawbacks, including complexity and size. For these reasons, amplitude holograms are generally preferred in these bands.

4.3 Generation of Linear Grating

In this section, a linear hologram grating is generated using different techniques to obtain an output beam propagating at $\Phi = 45°$. As stated previously, a normal-incidence plane wave is considered for the reference beam. Figure 4.3-1 presents the setup used by the linear grating. From (4.2-3), the resulting spatial frequency is $\alpha = 1/\left(\sqrt{2}\lambda\right)$. Inserting this value of α into the transmittance equation (4.2-7) will lead to the grating shown in Figure 4.3-2. The binary hologram would be generated from (4.2-8), as shown in Figure 4.3-3 for a threshold b = 0.5. According to (4.2-2), this leads to a period of $\Lambda = \sqrt{2}\lambda \cong 1.4\lambda$. Consequently, since the threshold is b = 0.5, the dark and clear strips both have width of 0.7λ.

4.3.1 Phase grating

A parallel between the previous results in Section 4.2.2 and [LEE79] can be made for the case of a phase grating. In [LEE79], the diffraction efficiency of multiple beam gratings is discussed for the case of binary phase gratings. The phase profile of the grating is presented as a Fourier series [LEE79]:

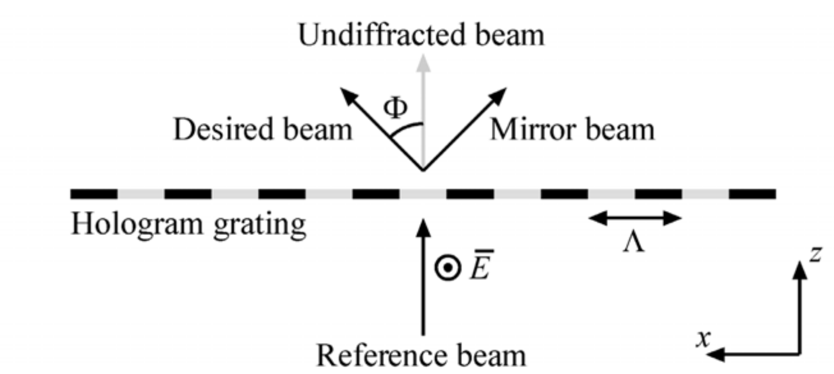

Figure 4.3-1: Linear grating with normally-incident reference beam and desired beam propagating at angle Φ; binary version shown, with grey used for clear regions are black used for dark regions in the amplitude grating; grey used for –180° and black used for 0° for the phase gratings. Details of the PSS phase grating reported in Table 4.5-1.

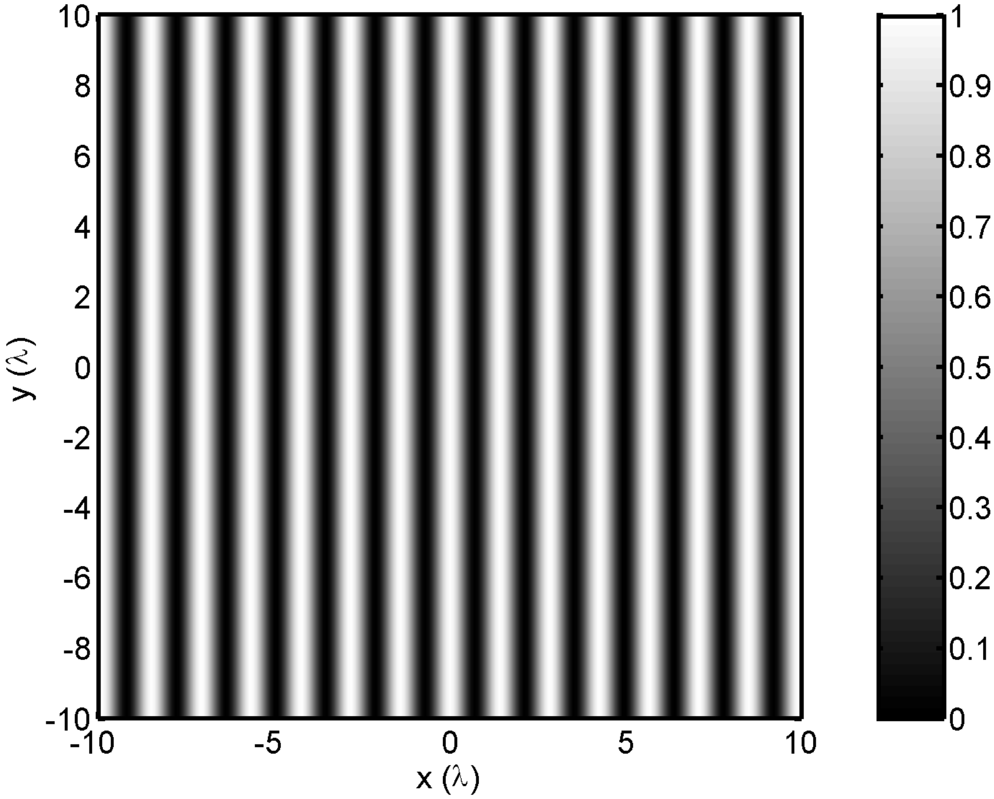

Figure 4.3-2: The linear grating generated by the interference between two plane waves, with an output angle Φ = 45°.

$$f(x) = \sum_{m=-\infty}^{\infty} \frac{\sin(\pi m q)}{\pi m} \exp[j 2\pi m x / \Lambda] \qquad (4.3\text{-}1)$$

where m corresponds to the diffracted beam order and $q\Lambda$ is the width of the grating regions introducing a phase of $-\theta$. The medium intrinsic phase is $+\theta$, thus the total phase shift is 2θ. In [LEE79], it is also mentioned that, for M phase shift transitions within the period of a phase grating, there will be $M + 1$ diffracted orders. For cases where $M \geq 3$, the gratings are modulated. Otherwise, there are only two transitions ($M = 2$), resulting in three diffracted orders. Note that, for simplicity, the summation in (4.3-1) can be reduced for the range of m values based on M.

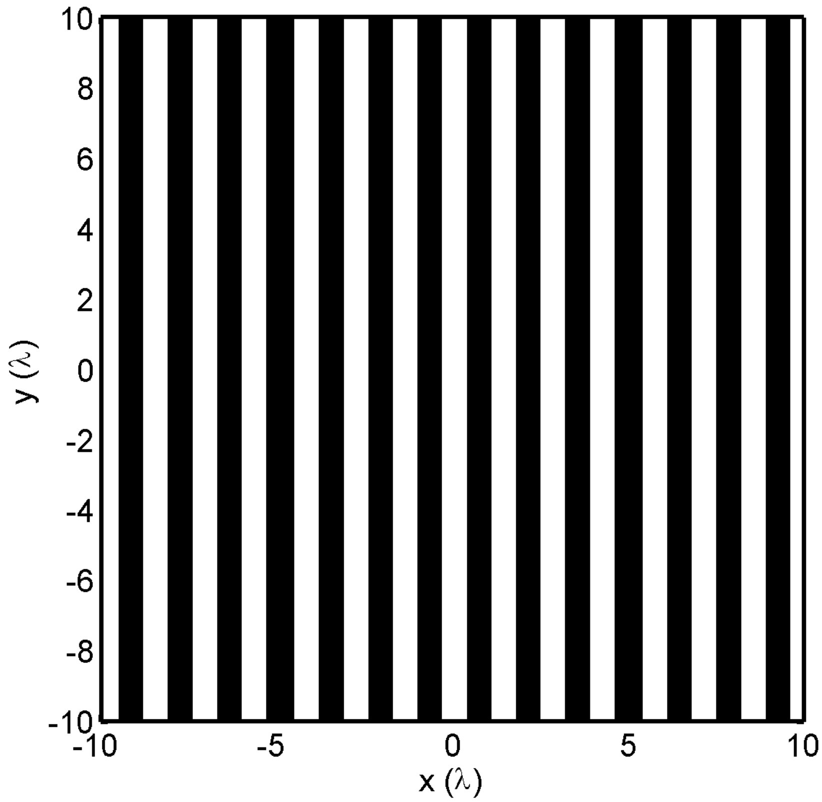

Figure 4.3-3: The binary version of the grating in Figure 4.5-2, using *b* = 0.5.

The three orders present in the phase grating proposed in this section are m = -1, 0, 1, where m = 0 is the undiffracted beam, and m = ±1 are the first-order diffracted beams. The subscripts in (4.2-11) and (4.2-12) were chosen to correspond to m, so that the U_m's are shown there. The result in (4.2-12) is in agreement with [LEE79]. If an amplitude analog transmittance function is used, the power in each beam will be as expressed by (4.2-10), subject to the assumptions in (4.2-5a) and (4.2-5c). This will be shown in Section 4.4.

In [LEE79], equations for calculating the amplitude of the beams are also presented for binary phase gratings. For the case of the undiffracted and first-order beams, the amplitudes are:

$$a_0 = (2q-1)\sin\theta + j\cos\theta \tag{4.3-2a}$$

$$a_1 = a_{-1} = 2\frac{\sin(\pi q)}{\pi}\sin\theta \tag{4.3-2b}$$

where $\pm\theta$ corresponds to the phases to be introduced, as mentioned previously. The value of q is related to that of b; for two transitions in a grating period, q = 0.5 if b = 0.5 in (4.2-8). From (4.3-2), the amplitude in the undiffracted beam can be made null if q = 0.5 and θ = 90°; this would also maximise the amplitude in the first-order beams since it will make a_1 and a_{-1} equal to $2/\pi$ or 0.6366.

If multiple beams are desired, it is possible to adjust both q and θ in an attempt to equate the amplitudes in the beams [LEE79].

4.3.2 Amplitude grating

Binary holograms, if properly constructed, can achieve better diffraction efficiencies than analog holograms. From (4.2-11), analog holograms have an undesired undiffracted beam of amplitude greater than the desired diffracted beam, which is not the case, say, for binary phase holograms with q = 0.5 and θ = 90° since the undiffracted beam component becomes null.

The comparative study between an analog hologram and different threshold levels for binary amplitude holograms has recently been addressed by [PETO08] for the case of an elementary hologram where similar conclusions were drawn. Moreover, [PETO08] showed that using a digitizing rule based on the argument of $U_R(x,y)+U_D(x,y)$ presented in (A.2-3) of Appendix A would lead to better results than using any threshold b presented in (4.2-8). According to [PETO08], the best cases for a threshold are obtained for b = 0.5. The proposed digitizing rule in [PETO08] leads to a Fresnel zone plate configuration.

Based on the material presented earlier in Section 4.3, the following gratings are generated:

- Analog grating with a transmittance as shown in Figure 4.3-2.

- Binary phase grating having q = 0.5 and θ = 90°, which would correspond to the grating in Figure 4.3-3 having the white (clear) regions with a phase shift of, say, 0° and the dark regions with a phase shift of 180°.

- Binary amplitude grating having q = 0.5 and θ = 90°, which would correspond to the grating in Figure 4.3-3 having the clear regions with a perfect transmittance and the dark regions with no transmittance (i.e. metallised).

4.4 Desired Wave Reconstruction

The desired wave reconstruction is first studied using a mathematical analysis implemented in MATLAB [MATL03]. The number of periods used is 50. For the three gratings described in Section 4.3, the amplitude of the field U_C is obtained in the far field. To do so, the technique described in [BAGG93] is used. The results are presented in Figure 4.4-1. These results are normalised to the case of a plane wave occupying the same number of periods, i.e. the same size. Table 4.4-1 presents the beam amplitude results for the three gratings analysed.

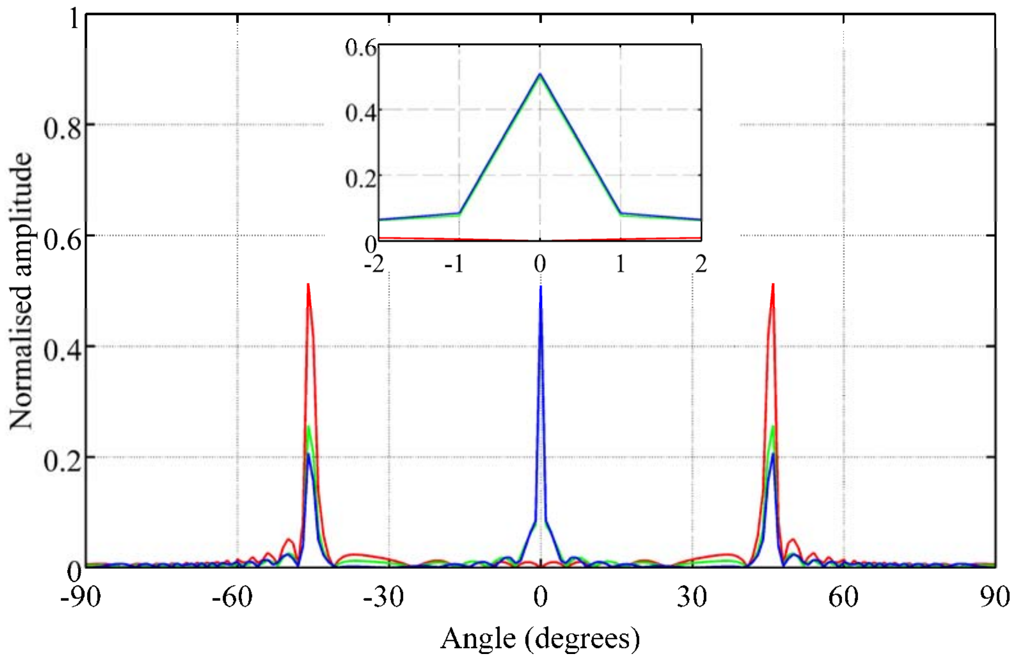

Figure 4.4-1: The field amplitude in the far-field of the hologram generated by the interference between two plane waves with 50 periods and Φ = 45°; —— Analog grating; —— Phase grating; —— Amplitude grating.

The analog hologram, which results from directly applying (4.2-7), offers the worst performance of the three cases studied. This could be explained by the fact that such a hologram has significant contributions from components that will not add constructively in the far-field. Note that the beam amplitudes are almost as predicted by (4.2-11), i.e. ¼, ½, ¼ for a_{-1}, a_0, a_1, respectively. Despite the fact that it blocks half of the incoming field, the amplitude hologram produces a similar undiffracted beam level as the analog hologram but slightly improved first-order diffracted beams levels. Finally, the phase hologram performs much better than the two other holograms, with amplitude levels about two times higher compared to the two other cases for the first-order diffracted beams and no power in the undiffracted beam. This result is no surprise and could have been determined from the equations in [LEE79], but is confirmed here.

Table 4.4-1: Amplitude of the beams.

	a_{-1}	a_0	a_1
Analog grating	0.21	0.51	0.21
Binary phase grating	0.51	0	0.51
Binary amplitude grating	0.26	0.5	0.26

4.5 Design of Linear Gratings

Three binary gratings are fabricated and measured at 30 GHz: an amplitude grating, a dielectric phase grating and a PSS phase grating. Since Section 4.4 revealed that analog gratings are less efficient than binary gratings, it was decided not to design an analog grating. The fabricated gratings are shown in Figures 4.5-1 to 4.5-3. The amplitude grating was easily etched on low-cost FR4 where opaque regions were used for the null transmission and clear regions were used for the total transmission. The FR4 substrate is only used to support the metal strips, and full-wave electromagnetic simulations using [EMPI07] revealed that the FR4 had only a marginal effect on the results. The dielectric phase grating was machined from a block of Plexiglas. It is composed of different thicknesses for the different regions such that a 180° phase difference is obtained between the two regions. The PSS phase grating was designed based on the PSS concept introduced in Chapter 2. The 3-layer symmetrical configuration of Section 3.4.3 was used. As for the dielectric phase grating, the PSS phase grating consists of phase shift regions out-of-phase by 180°. The PSS grating realises the 180° phase shift by using two high-transmission cases from Figure 3.4-4. Along the width (x-axis), the grating geometry is constant within each 180° phase shift region. In each 0° phase shift region, the conductors are simply

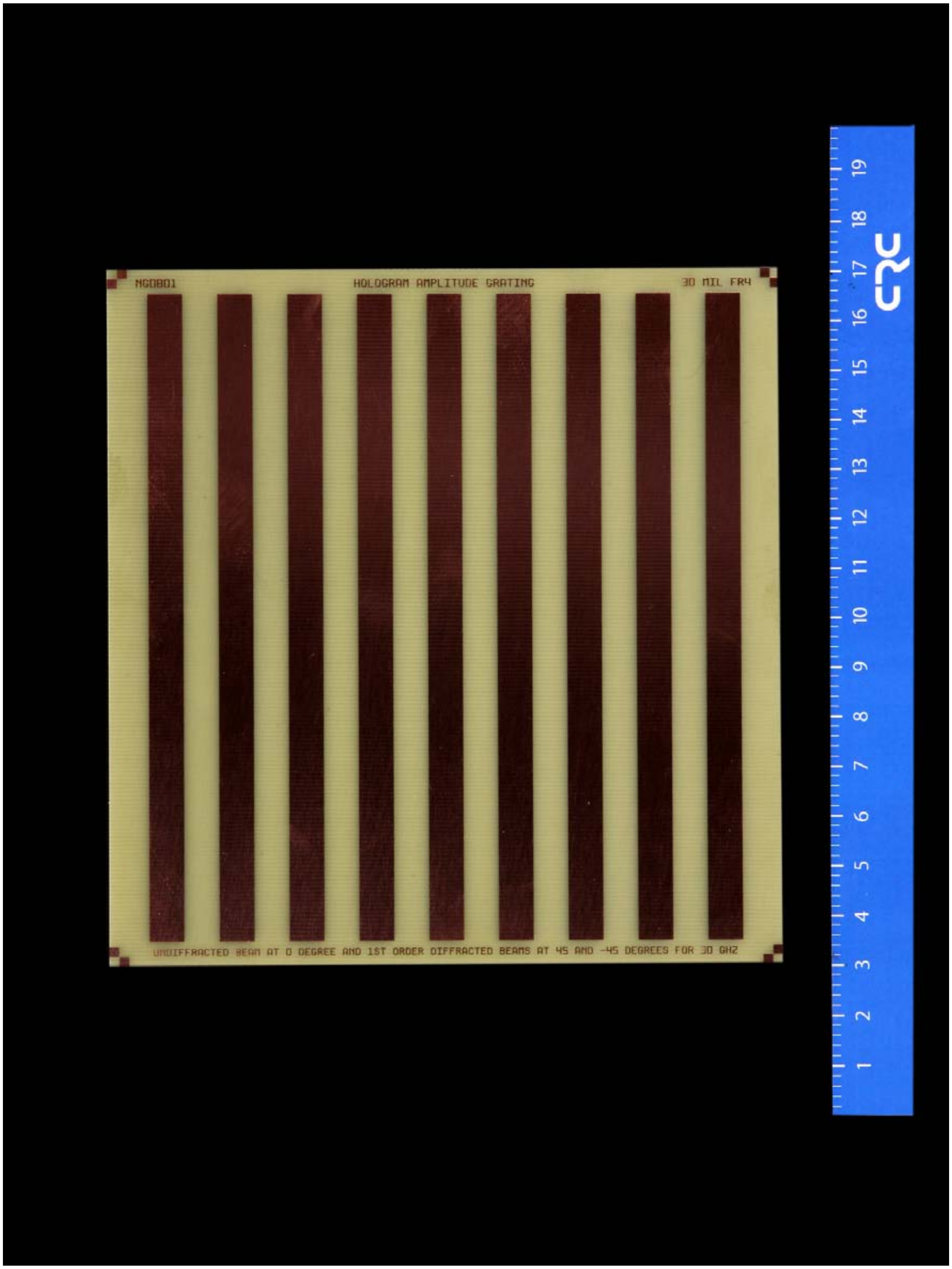

Figure 4.5-1: Photographs of the linear amplitude grating fabricated on 28 mil FR4 with 9 periods.

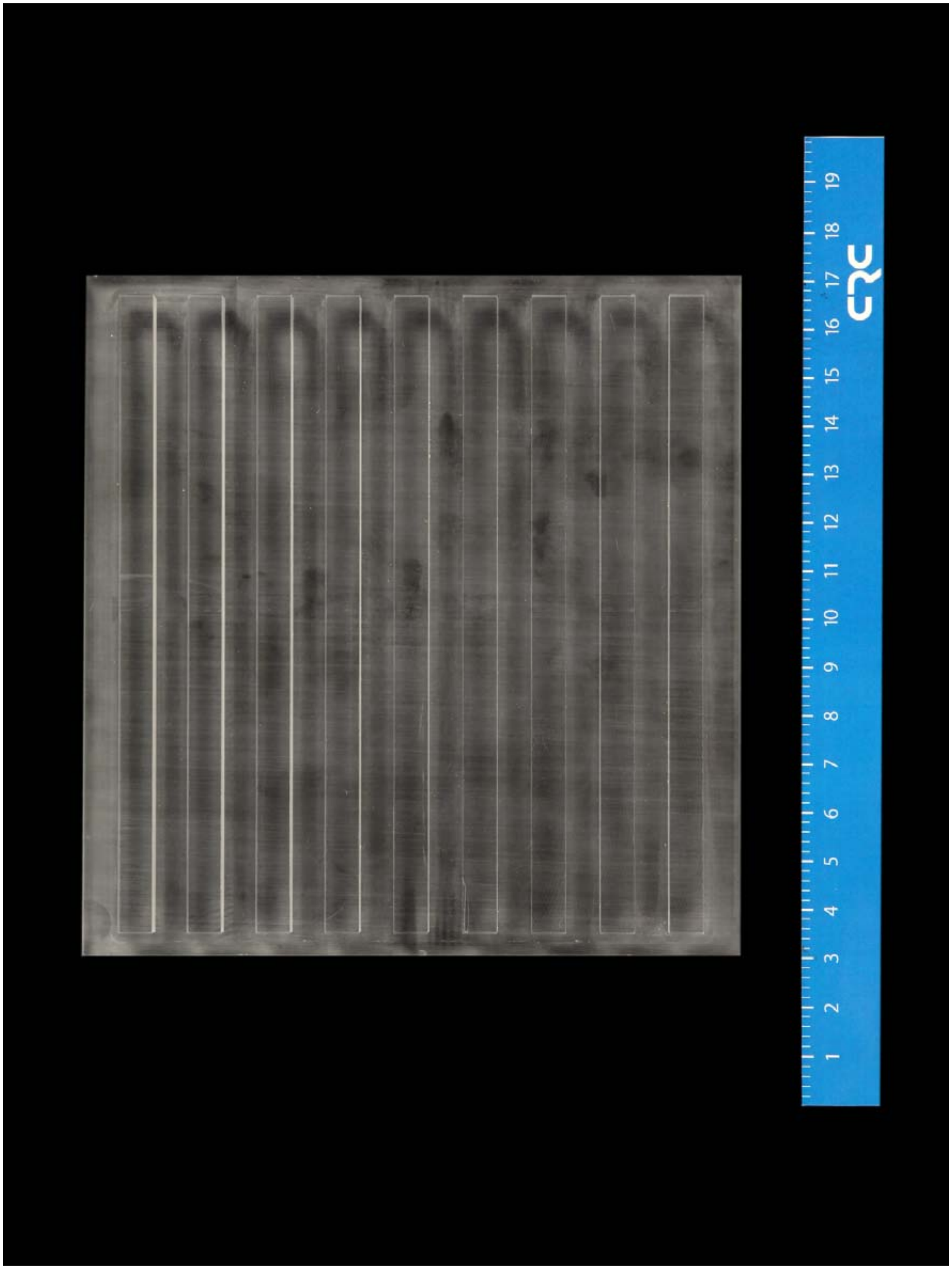

Figure 4.5-2: Photographs of the linear dielectric phase grating machined in Plexiglas with 9 periods.

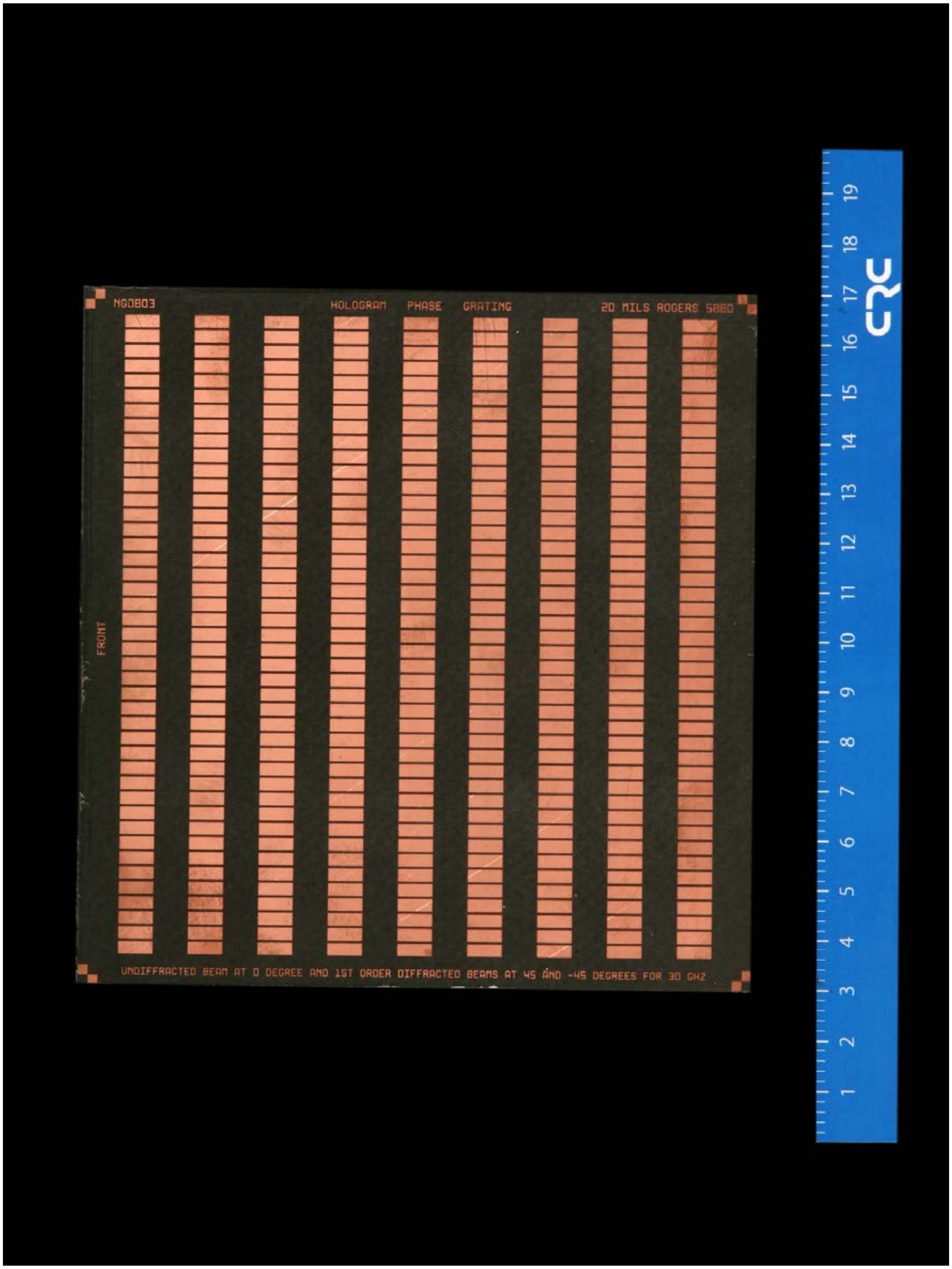

Figure 4.5-3: Photographs of the linear PSS phase grating fabricated on Rogers 5888 with 9 periods.

omitted (a_1 = 0 mm and a_2 = 0 mm); in each 180° region, a_1 = 2.55 mm and a_2 = 2.85 mm. Table 4.5-1 provides more details on the design values of the PSS phase grating.

Due to material thickness availability and the need for a bonding film, the total thickness was not exactly 1 mm and the middle metal layer was not perfectly located in the centre, as described in Chapter 3. Furthermore, the conductive layers are not made of perfect conductor and are not infinitesimally thin, and the dielectric material has losses associated to it, although these losses are low. The final phase grating composition is as follows:

- 0.017 mm copper layer (front layer).
- 0.508 mm low loss dielectric material with ε_r = 2.2.
- 0.017 mm copper layer (middle layer).
- 0.1016 mm low loss bonding film with ε_r = 2.7.
- 0.381 mm low loss dielectric material with ε_r = 2.2.
- 0.017 mm copper layer (back layer).

This gives a total thickness of about 1.04 mm, which is close to the 1 mm used in the simulations.

Table 4.5-1: Design values of the PSS phase grating at 30 GHz.

Region	Ideal Transmitted Phase (°)	Ideal Transmitted Amplitude (dB)	Simulated Transmitted Phase (°)	Simulated Transmitted Amplitude (dB)	a_1 (mm)	a_2 (mm)
	0	0	0	–0.437	0	0
	–180	0	–178.2	–0.073	2.55	2.85

4.6 Characterisation of Linear Gratings

The gratings are measured in a free-space quasi-optical measurement system described in [GAGN03]. The free-space quasi-optical measurement system is initially calibrated using the procedure summarised in [GAGN03],[GAGN05] and detailed in [GAGN02]. Photographs of the setup are presented in Figure 4.6-1, showing the amplitude linear grating under test. The system was calibrated with the two phase-corrected feed-horns facing each other, as shown in Figure 4.6-1(a) (albeit with the grating removed). The phase-corrected feed-horns collimate the beam to a size significantly smaller than the grating and ensure that quasi-plane waves are present at the input and output of the grating. The small-size beam allows one to neglect the diffraction at the edge of the grating. After the system is calibrated, the output phase-corrected feed horn, used as a sensor, was moved along the azimuth plane (*xz*-plane) at different receiving angles in order to collect data while the input phase-corrected feed horn was used for illuminating the grating with a normal incidence, acting as a plane wave reference beam. This is shown in Figure 4.6-1(b).

The transmission coefficient measurement results for the three linear gratings are shown in Figure 4.6-2. The 0 dB level corresponds to total transmission obtained without any device inserted and the two phase-corrected feed-horns of the quasi-optical measurement system facing each other (0° normal incidence), as obtained from calibration. For clarity, only the beams resulting from the $n = -1$ and $n = 0$ spatial harmonics are shown in Fig. 4.6-2; the negative angles, and consequently the $n = +1$ spatial harmonic, have been omitted. Measurements were performed at every degree for positive angles up to 60°, which is the limit set by the measurement system and cable length.

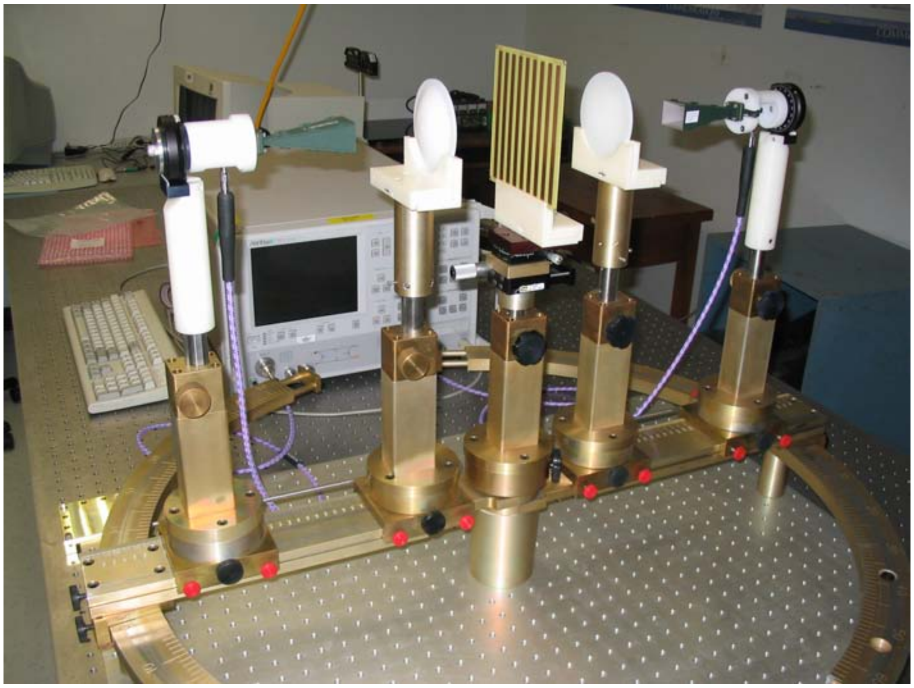

(a)

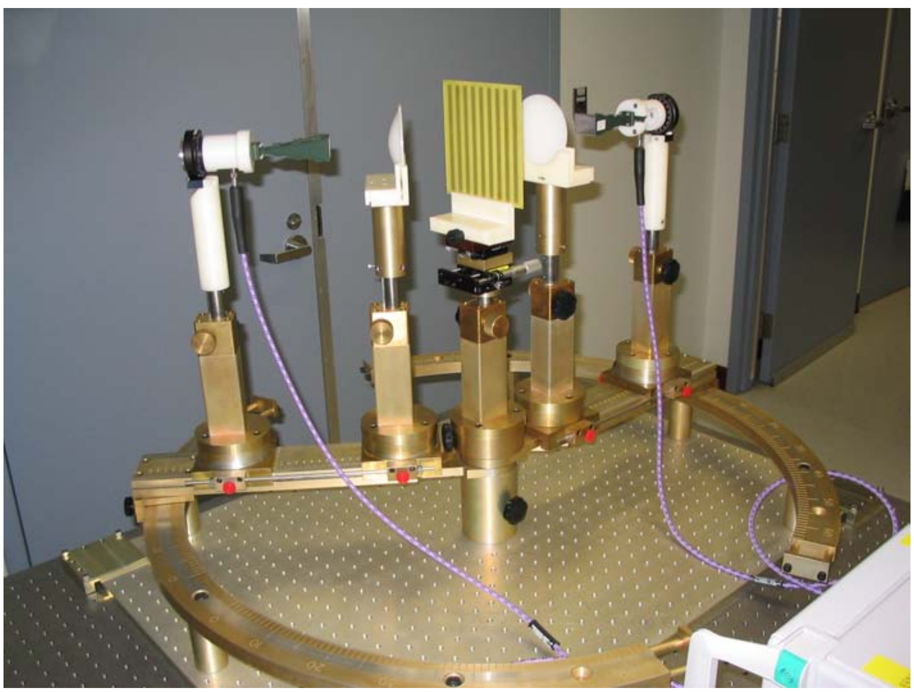

(b)

Figure 4.6-1: Photographs of the free-space quasi-optical measurement system used to characterised the linear gratings; (a) normal incidence state, also used for calibrating the system, (b) arbitrary incidence state.

From Figure 4.6-2, it is seen that the amplitude grating had much poorer performance compared to the phase gratings: the transmitted power in the $n = -1$ spatial harmonic is lower by 3.7 dB compared to the undesired $n = 0$ spatial harmonic (which is the undiffracted beam). Also from Figure 4.6-2, it can be seen that the thin PSS phase grating has a better performance than the dielectric phase grating. This is attributed to the fact that the PSS phase grating has a higher transmission through its surface and lower reflection since the phase-shifting cases selected for the design were specifically chosen to reduce the mismatch at the air-PSS interface. The dielectric phase grating was not optimised to minimise reflection in this case; however even if this would have been done there is no guarantee that the mismatch would have been reduced as much as for the case

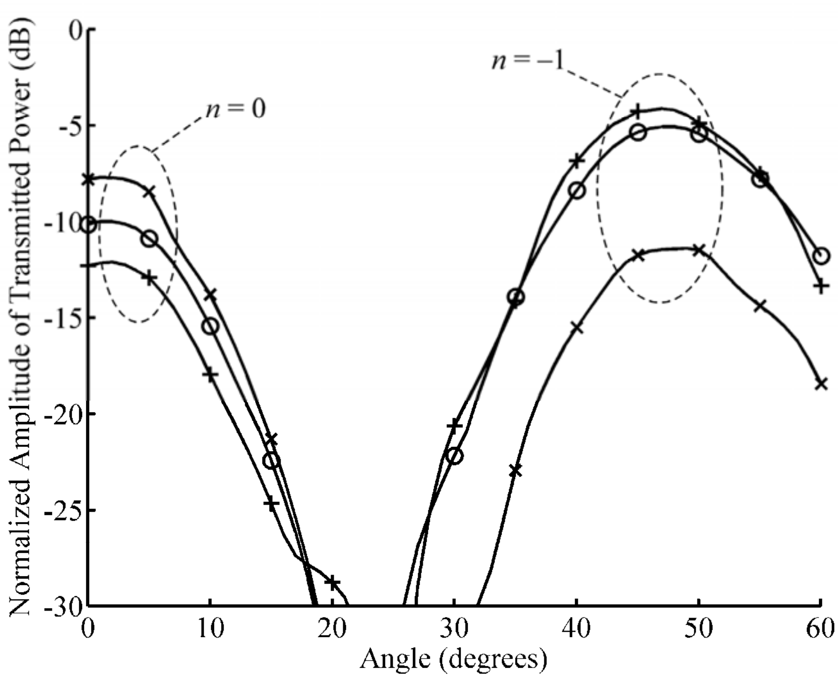

Figure 4.6-2: Normalized amplitude of transmitted power as a function of angle for three phase gratings obtained from measurements in a free-space quasi-optical measurement system at 30 GHz; + Thin PSS phase grating, O Dielectric phase grating, × Amplitude grating.

of the PSS phase grating since uniform dielectric does not allow independent control of the amplitude and phase as does the PSS.

Table 4.6-2 shows the maximum level of transmission coefficient measured in each of the beams. Table 4.6-3 shows the fraction of power for each beam based on the results from Fig. 4.6-2 and Table 4.6-2. The diffracted beam column shows the fraction of power in the beams resulting from both the $n = -1$ and $n = +1$ spatial harmonics. The results are quite impressive for the thin PSS phase grating, showing that 78% of the incident beam is actually being transmitted in the two desired diffracted beams corresponding to the $n = -1$ and $n = +1$ spatial harmonics. This value, corresponding to the diffraction ratio for the desired beams, is within 4% of the idealised theoretical value, that is within 2% if we consider each individual beam separately.

4.7 Conclusions

This chapter presented the first proof of concept of the PSS. The concept consisted in a simple binary phase grating, and proved to be conclusive. The experimental results showed that the PSS phase grating has a higher diffraction efficiency than a traditional phase grating at Ka band, with results close to the theoretical values. The results obtained

Table 4.6-2: Transmission coefficient for each beam at 30 GHz.

Gratings	Diffracted Beams ($n = \pm 1$)	Undiffracted Beam ($n = 0$)
Thin PSS Phase Grating	-4.1 dB	-12.1 dB
Dielectric Phase Grating	-5.1 dB	-10.0 dB
Amplitude Grating	-11.4 dB	-7.7 dB

Table 4.6-3: Fraction of power in each beam at 30 GHz.

Phase Grating	Diffracted Beams ($n = \pm 1$)	Undiffracted Beam ($n = 0$)	Reflected and/or Higher-Order Beams
Thin PSS Phase Grating	78%	6%	16%
Dielectric Phase Grating	62%	10%	28%
Amplitude Grating	14%	17%	69%
Idealized Theoretical Analysis [LEE79]	82%	0%	18%

in this chapter clearly show that the binary phase grating designed using the PSS is indeed a phase shifting surface in the sense that it behaves as a phase grating rather than as an amplitude grating.

CHAPTER 5 PSS Cylindrical Lens Antenna

5.1 Introduction

This chapter presents the second application of the phase shifting surface (PSS), namely to implement a 90° phase correcting cylindrical Fresnel zone plate antenna. Cylindrical lens antennas are briefly addressed in Section 5.2. A traditional 90° phase correcting cylindrical Fresnel zone plate antenna is described in Section 5.3, followed by the PSS version of the type of same lens in Sections 5.4 and 5.5. Section 5.6 concludes the chapter.

5.2 Cylindrical Lens Antennas

Unlike the traditional full lenses, traditional cylindrical lenses are a type of lens that is used to collimate the beam in one plane only, rather than performing a full three-dimensional collimating of the beam. As a result, the cross-sectional shape of the lens is cylindrical. Consequently, any type of lens, like the one stated in Appendix B, can be of the cylindrical type. This is done by keeping the geometry unchanged along one axis and modifying the lens along the other, according to the prescribed equation (see Appendix B).

5.3 Cylindrical Phase-Correcting Fresnel Zone Plate Antenna

A cylindrical dielectric 90° phase-correcting Fresnel zone plate antenna (PC-FZPA) has been previously designed using (B.3-4) and (B.3-6) and built from a material with relative permittivity of ε_r = 3 using a machining technique [KADR05]. The operating frequency is 30 GHz. The lens has a focal length F of 76.2 mm and a size D of 152.4 mm for an F/D ratio of 0.5. Since the structure has a phase correction of 90°, P = 4. From (B.3-4), this results in a step thickness s of 3.42 mm. Using (B.3-5), the thickness of the dielectric PC-FZPA is 10.26 mm. A backing section of thickness equal to 4.74 mm is used, resulting in a total lens thickness of 15 mm. Figure 5.3-1 shows the physical dimensions of the dielectric PC-FZPA, where the zones were calculated from (B.3-6). Figure 5.3-2 shows a photograph of the dielectric PC-FZPA. Measurement results for this lens antenna will be reported in Section 5.6.

5.4 Generation and Design of PSS Cylindrical 90 Degree PC-FZPA

A cylindrical 90° PC-FZPA based on the symmetrical three independent layer strip PSS of Section 3.4.3 is designed in this section. The zones are made identical to the ones from the traditional dielectric grooved PC-FZPA, i.e. obtained from (B.3-6) and shown on the left side of Figure 5.3-1 (the right side shows the profile, which is not relevant here). Figure 5.4-1 presents the cylindrical PSS PC-FZPA setup. The details of each phase-shift zone are provided in Table 5.4-1. The frequency of operation is 30 GHz. Figure 5.4-2 provides photographs of the cylindrical PSS PC-FZPA. Note that the electric field is vertically polarised in Figure 5.4-2. The lens collimated the beam in the H-plane only. As mentioned in Chapter 3, the PSS structure based on strips, like the one used here, is polarisation dependent. Consequently, this lens is only designed to operate in one polarisation and, unlike traditional dielectric lenses, it will not work properly if rotated by 90° in an attempt to collimate the beam in the E-plane. A different design would be required for such a case.

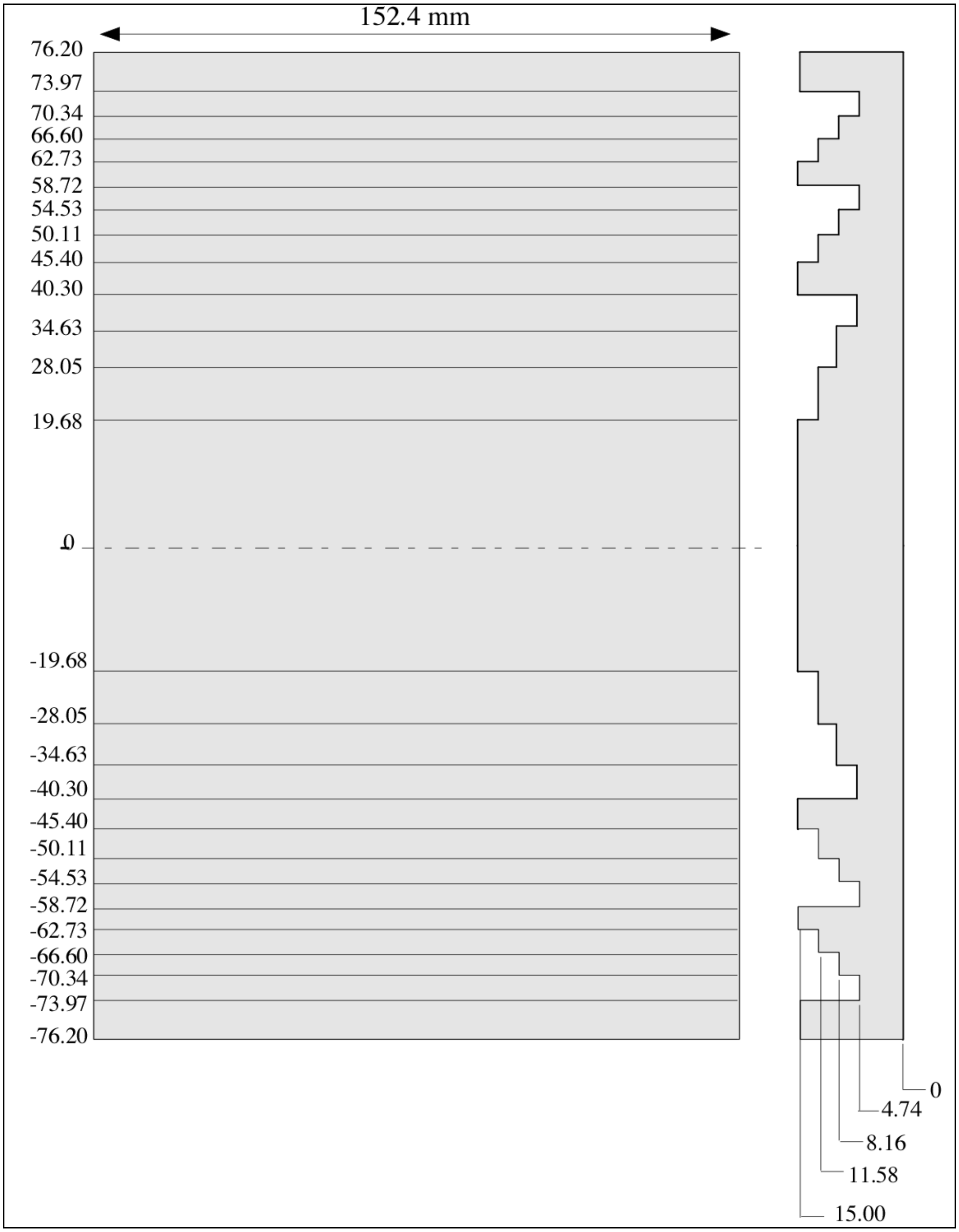

Figure 5.3-1: Front and side view of a cylindrical dielectric 90° phase-correcting Fresnel zone plate antenna. Reprinted with permission from [KADR05]. © 2005 IEEE.

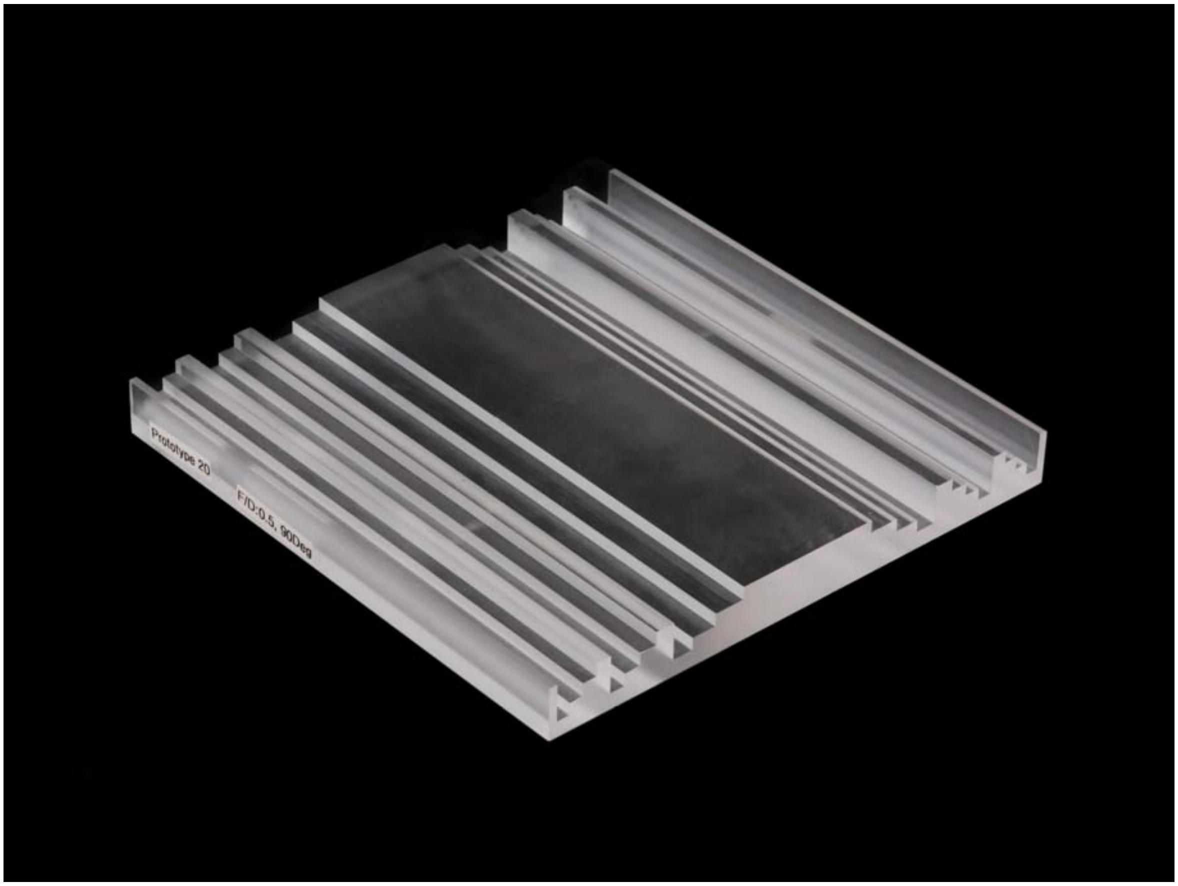

Figure 5.3-2: Photograph of the cylindrical dielectric 90° phase-correcting Fresnel zone plate antenna (PC-FZPA) reported in [KADR05].

In Figure 5.4-2, it is seen that the unit cell of height *s* is repeated vertically (i.e. along the *E*-plane) in each zone. In Figure 5.4-2(b), the unit cell height *s* is identified for better understanding and the zones are shown by white vertical dashed lines. The phase shift introduced in each zone is shown at the bottom of the figure by the color code used in Table 5.4-1. Furthermore, since the cell height is less than half a free-space wavelength, the structure respects the rule given in (3.3-1) on periodic structure theory. Therefore, there will not be any undesired beam diffraction occurring within a single zone. Along the *H*-plane (horizontally), the unit cell is constant in each zone, but varies from one zone to another. It is along this axis that the phase correction is achieved.

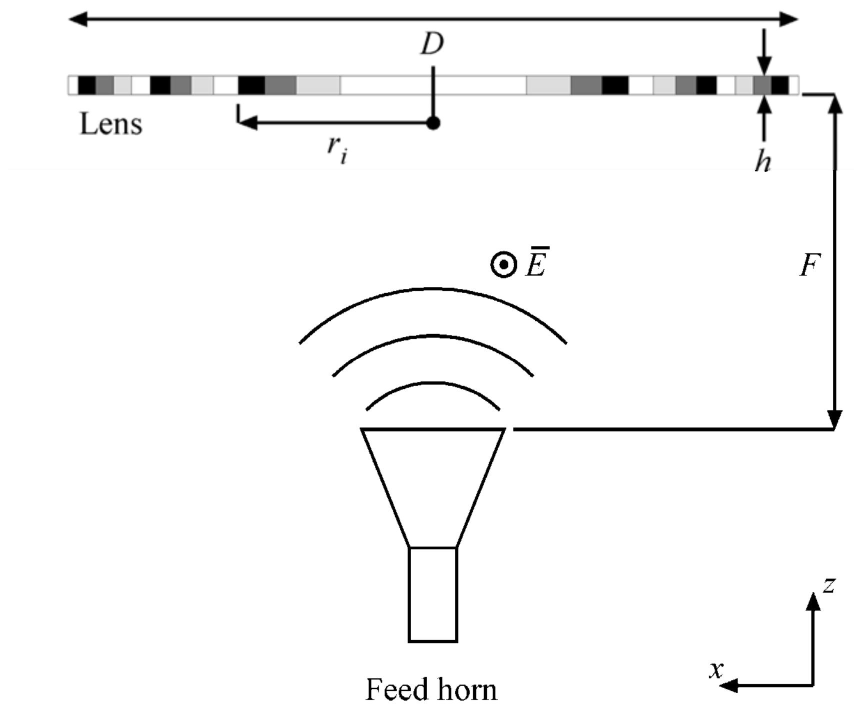

Figure 5.4-1: Cylindrical lens antenna design; the details of different zones are provided in Table 5.4-1 for the cylindrical PSS PC-FZPA case.

Table 5.4-1: Design values for the cylindrical PSS PC-FZPA.

Zone	Ideal Transmitted Phase (°)	Ideal Transmitted Amplitude (dB)	Simulated Transmitted Phase (°)	Simulated Transmitted Amplitude (dB)	a_1 (mm)	a_2 (mm)
	0	0	0	–0.437	0	0
	–90	0	–89.3	0	2.32	2.00
	–180	0	–175.6	–0.049	2.54	2.85
	–270	0	–264.8	–0.098	2.83	2.83

5.5 Measurement of Cylindrical 90 Degree PC-FZPAs

The far-field radiation patterns of the cylindrical dielectric PC-FZPA and the cylindrical PSS PC-FZPA were measured in a far-field anechoic chamber. The two

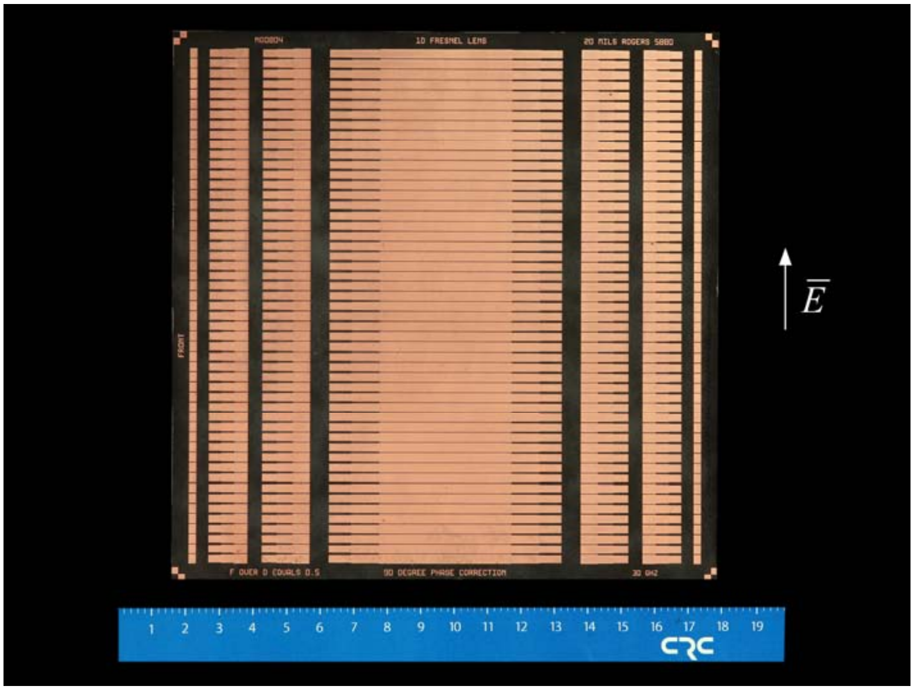

(a)

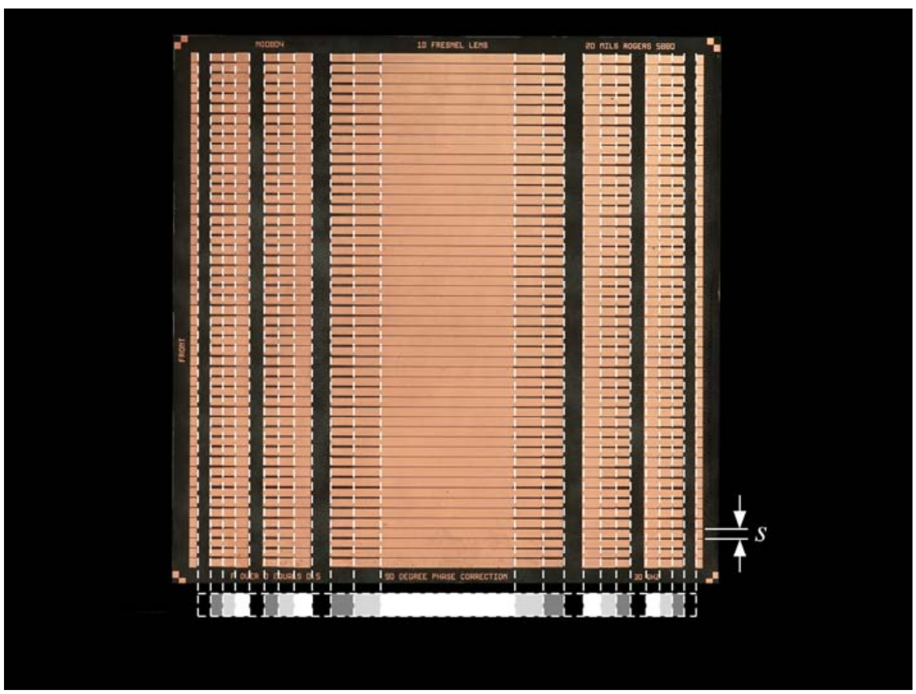

(b)

Figure 5.4-2: Photographs of the cylindrical PSS PC-FZPA; (a) showing ruler and electric field orientation, (b) showing unit cell height and zones (see details in Table 5.4-1).

PC-FZPAs have precisely the same size of 152.4 mm by 152.4 mm. This allows a comparison between the two structures. A feed horn with 14.4 dBi of gain is used to feed the two cylindrical PC-FZPAs, resulting in an edge taper of 14 dB. The feed horn is initially placed at a location close to the focal point, then adjusted to lead to the maximum boresight realised gain. This procedure is repeated for both PC-FZPAs.

Although the cylindrical PSS PC-FZPA was designed for operation at 30 GHz, the best results are obtained at slightly lower frequencies, mainly in the frequency range from 29 GHz to 29.5 GHz. Figure 5.5-1 presents the measured *H*-plane co-polarisation far-field radiation patterns at the frequency of 29.5 GHz. Recall that the *H*-plane is the plane in which the beam is collimated by the lens. Figure 5.5-1 clearly shows that both the dielectric PC-FZPA and PSS PC-FZPA produce beam collimation since the gain of these

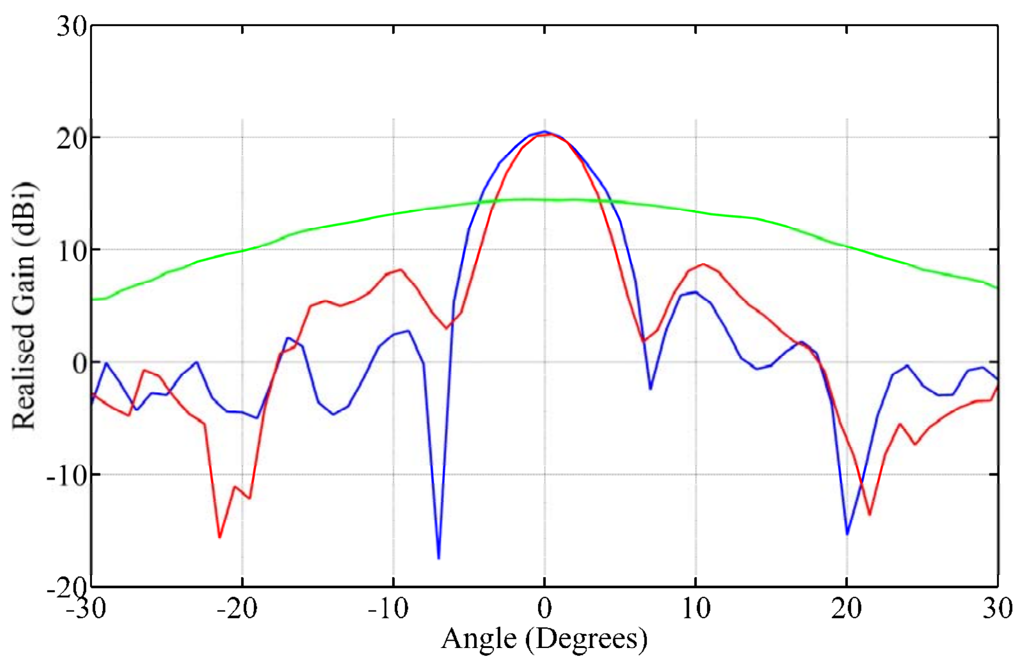

Figure 5.5-1: Measured H-plane co-polarisation far-field radiation patterns of the cylindrical PC-FZPAs and feed horn at 29.5 GHz; —— PSS PC-FZPA, —— Dielectric PC-FZPA, —— Feed horn.

two antennas is about 6 dB higher than the feed horn alone (also shown in Figure 5.5-1). Furthermore, the boresight realised gain is almost identical. The only difference is that the main beam is slightly wider, and the sidelobe levels lower, for the PSS PC-FZPA. Figure 5.5-1 also reveals a minor pattern asymmetry. This may be caused by a slight off-axis displacement of the feed horn with respect to the lens in the plane perpendicular to the direction of propagation (the *z*-axis). The cross-polarisation levels are below the –20 dBi level for all cases over the angular range shown, consequently they do not appear in Figure 5.5-1.

Figure 5.5-2 presents the measured boresight realised gain as a function of frequency. Recall that the realised gain takes into account the impedance mismatch at the input of the antenna. From 28.6 GHz to 29.7 GHz, the gain performance of the PSS

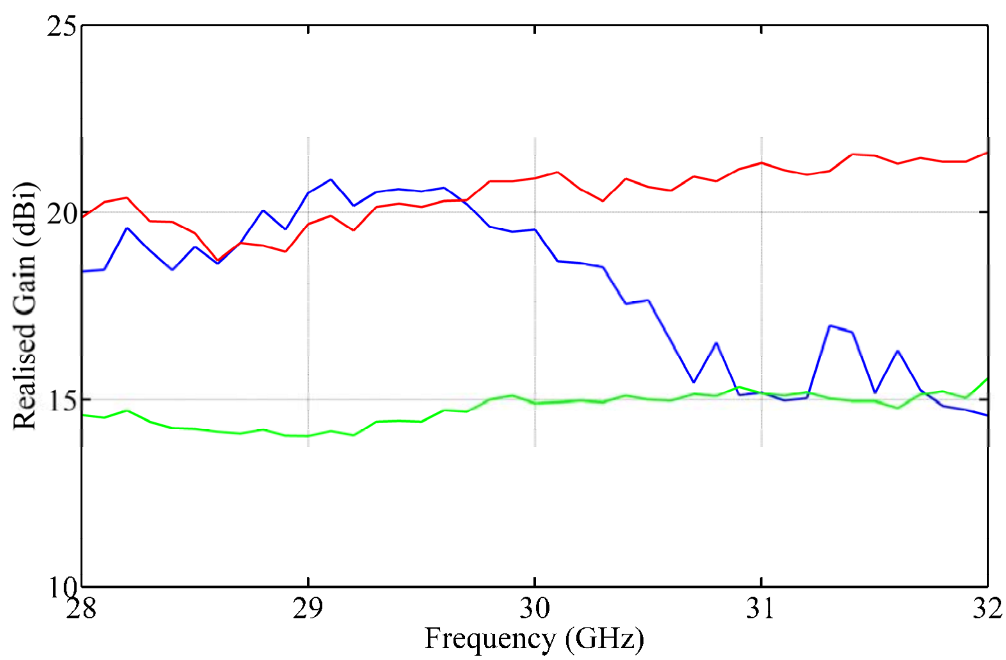

Figure 5.5-2: Measured boresight gain of the cylindrical PC-FZPAs and feed horn; —— PSS PC-FZPA, —— Dielectric PC-FZPA, —— Feed horn.

PC-FZPA is higher than that of the dielectric PC-FZPA. However, from about 30 GHz, the PSS PC-FZPA suffers from severe boresight gain degradation caused by the bandwidth limitation of the PSS (as discussed in Section 3.7.1). As expected, the dielectric PC-FZPA has a wider gain bandwidth. Nevertheless, the gain bandwidth of the PSS PC-FZPA is at least 5%, which is still more than acceptable for many different types of application.

5.6 Conclusions

The cylindrical PSS PC-FZPA offers equal or better performance compared to the cylindrical dielectric PC-FZPA over a 1.1 GHz bandwidth at Ka band, which is beyond the requirements for many different applications in this frequency band. Moreover, there is a significant cost, weight and thickness reduction in the case of the PSS PC-FZPA compared to other phase-correcting lenses, such as a dielectric PC-FZPA. Therefore, it is believed that there is a niche for the use of a thin PSS realization of a lens antenna.

Finally, the work presented in this chapter has been previously reported in a transactions paper ([GAGN10b]).

CHAPTER 6 PSS Lens Antennas

6.1 Introduction

This chapter presents the third application of the phase shifting surface (PSS), which consists of different types of lens antennas, mostly phase-correcting Fresnel zone plate antennas and Fresnel lenses based on the PSS concept. Some generalities are presented in Section 6.2. In Section 6.3, prototypes of some of the traditional lens antennas introduced in Section 2.3 are presented. Section 6.4 describes some theory to be used for designing flat lenses. Section 6.5 describes how the theory developed in Section 6.4 and the PSS concept described in Chapter 3 are applied to the design of full lenses. This approach leads to thin flat profile lenses and allows for maximising the transmission amplitude for gain enhancement. In Sections 6.6, 6.7 and 6.8, different implementations of PSS phase-correcting Fresnel zone plate antennas (PC-FZPA) are reported. The discussion is presented in Section 6.9 and the Chapter is concluded in Section 6.10.

6.2 Generalities

All of the lenses presented in this chapter have a focal length F of 76.2 mm and a diameter D of 152.4 mm, which result in an F/D ratio of 0.5. The design frequency is 30 GHz. The pyramidal horn shown in Figure 6.2-1 is used as the antenna feed in all cases. The radiation patterns of the pyramidal feed horn are presented in Figure 6.2-2, showing a gain of approximately 11 dBi. When trying to measure the cross-polar pattern, the resultant shape as shown in Figure 6.2-2 was not what one expects from a horn antenna, and is thus

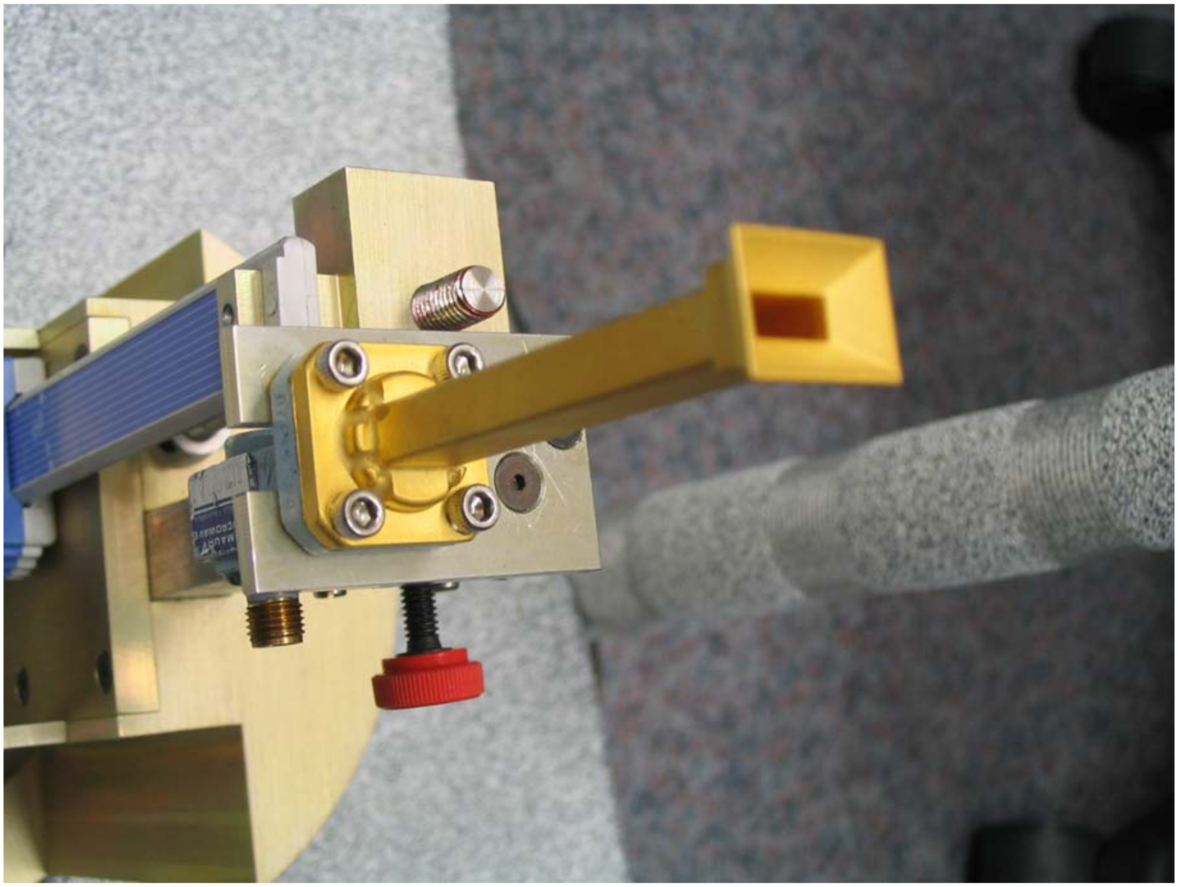

Figure 6.2-1: Photograph of pyramidal horn used as the feed antenna for the lenses presented in this chapter.

considered to be noise. The actual cross-polar levels are below this. For an $F/D = 0.5$, this feed horn has a resulting edge taper close to 10 dB, which is close to the optimum trade off between taper efficiency and spillover efficiency for maximizing the illumination efficiency [GOLD97]. The reflection coefficient of the feed horn is presented in Figure 6.2-3. A good match is shown through the frequency band; in particular, the reflection coefficient is below –15 dB at 30 GHz.

All antennas are measured in an anechoic chamber following the same procedure and under the same conditions. The distance between the transmitting and receiving

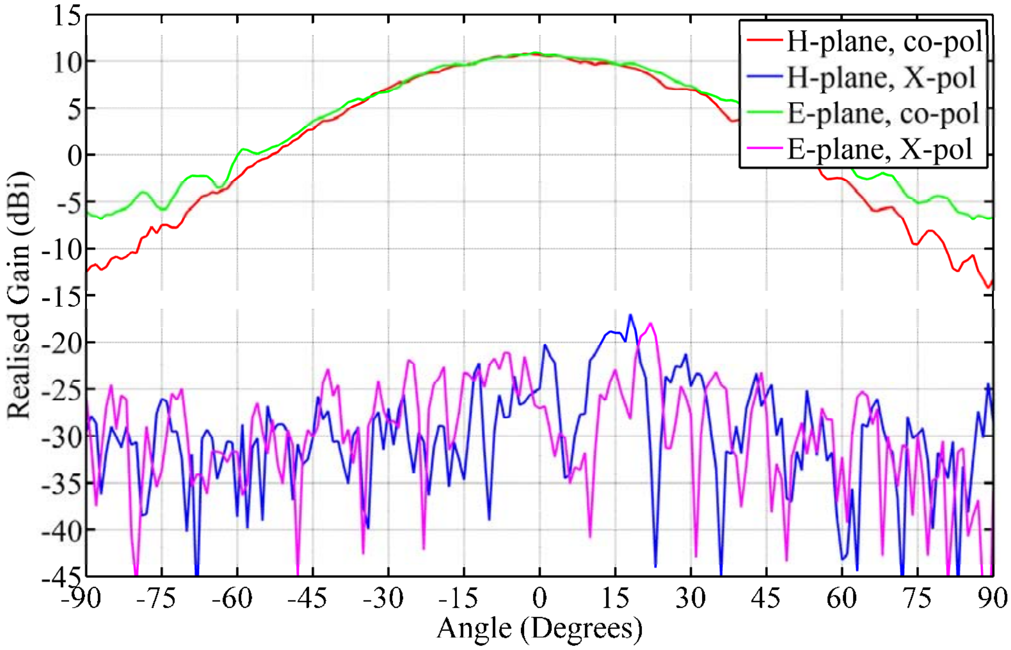

Figure 6.2-2: Measured far-field radiation patterns of the pyramidal feed horn at 30 GHz.

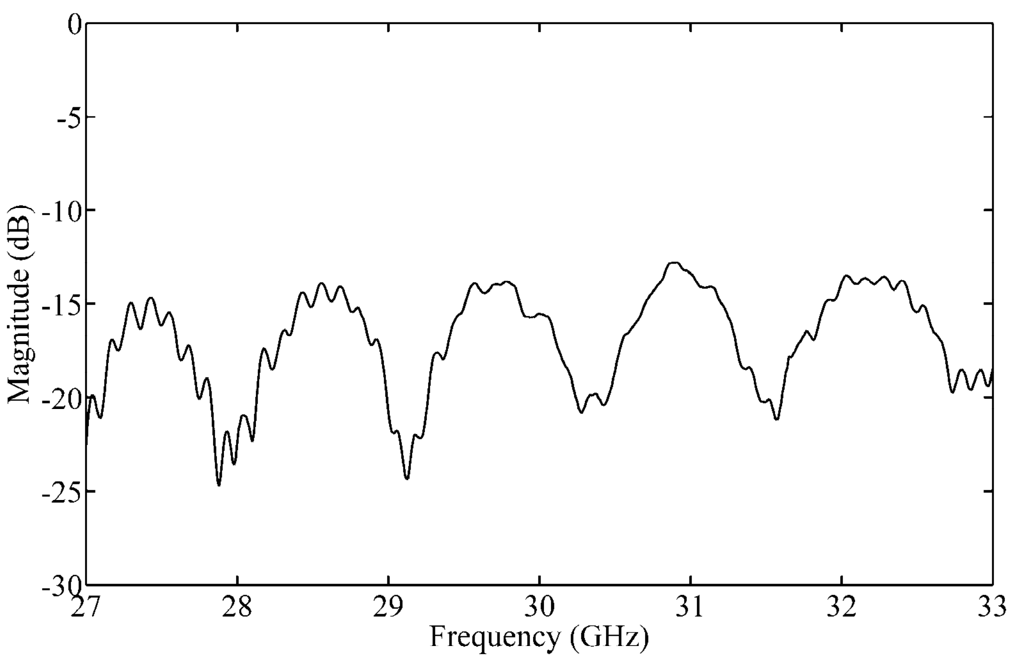

Figure 6.2-3: Measured reflection coefficient of the pyramidal feed horn.

antennas is 5 metres. The gain transfer method is used as the calibration procedure, using Hughes 45821H-2020 standard gain horn as receiving antenna for calibration and transmitting antenna. During calibration, the aperture of the standard gain horn on the receiving side is located at the centre of the azimuth rotation axis. After calibration the receiving standard gain horn is removed and replaced by the antenna under test, namely one of the lens antennas. The transmitting antenna remains the same. The position of the lens antenna under test is then adjusted so that its aperture is as close as possible to the centre of the azimuth rotation axis.

For each of the lenses, the pyramidal horn was positioned close to the focal point (see Figure 6.4-1) and its location then carefully adjusted to produce a maximum gain at 30 GHz for each case. The pyramidal feed horn of Figure 6.2-1 was mounted on the main part of the measurement jig. Four Plexiglas posts were attached to the main jig to support a flat piece of foam, on which the lensing device under test was fixed with adhesive tape. Foam was used for its low relative permittivity close to unity, therefore mimicking a free-space environment. Figure 6.2-4 shows a lens antenna under test (here a Fresnel zone plate antenna or FZPA) in the far-field anechoic chamber. Note that the measured gain reported in this thesis is the realised gain, which takes into account the effect of the return loss.

Some near-field measurements were also conducted on two PSS-based lens antennas. The near fields were scanned at a distance of 10 cm from the physical aperture of the lens. The reported results in Sections 6.6 and 6.8 are back-projected local fields at the output surface of the physical aperture. The measurement scanning was performed on a span of 58.4 cm × 58.4 cm. Not all antennas were measured in the near-field measurement system due to time constraints and resource availability.

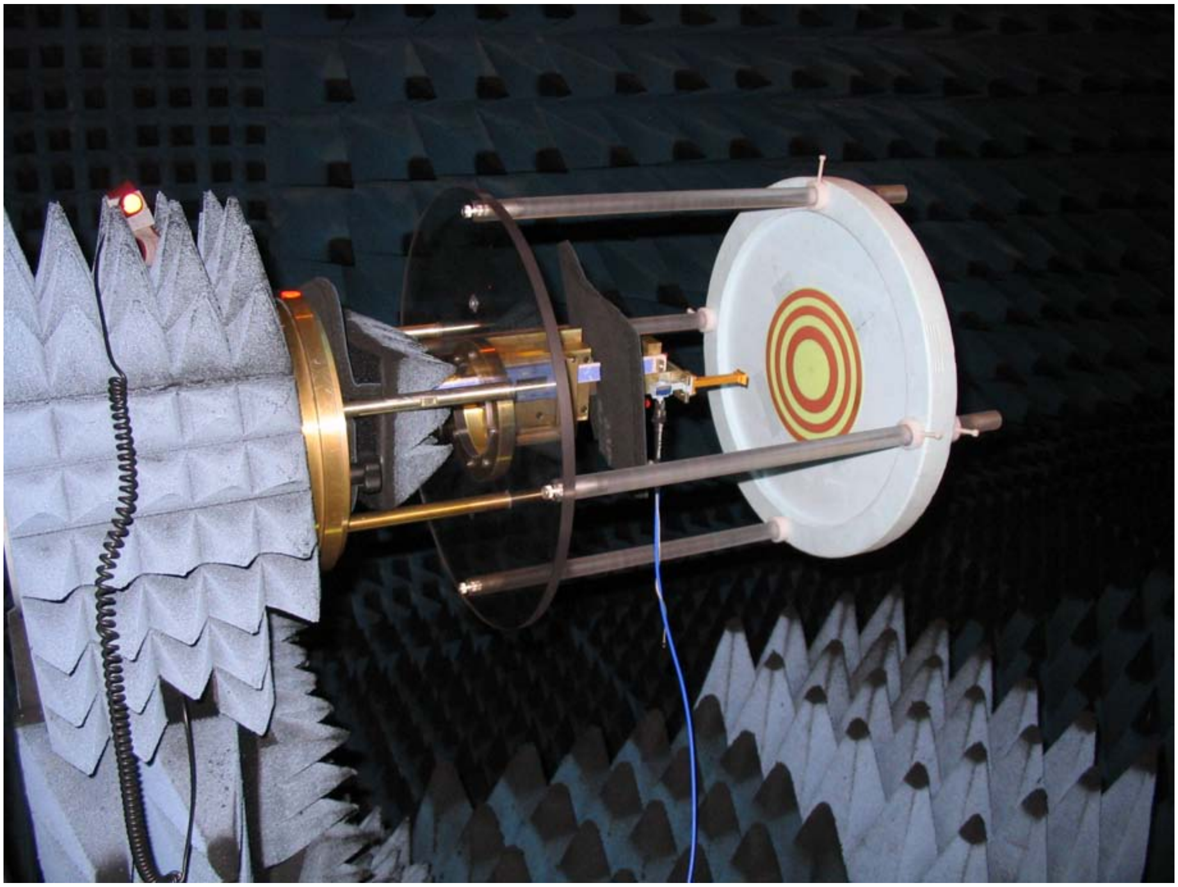

Figure 6.2-4: Photograph of a lens antenna under test in the far-field anechoic chamber (here an FZPA is shown).

6.3 Conventional Lens Antennas

In this section, three conventional lens antenna technologies are selected in order to perform a comparative study of their experimental performance and physical characteristics of each other as well as with thin flat PSS antennas introduced subsequently. The three types of antenna are a dielectric plano-hyperbolic lens antenna (DPHLA), a dielectric phase correcting Fresnel zone plate antenna (PC-FZPA) and a Fresnel zone plate antenna (FZPA). These antennas were initially introduced in Section 2.3. Theoretical information relative to these three types of antennas is presented in Appendix B.

The three following subsections present brief design guidelines for these three lens antennas. The fourth subsection presents far-field measurement results for these conventional antennas.

6.3.1 Dielectric plano-hyperbolic lens antenna (DPHLA)

The DPHLA shown in Figure 6.3-1 is designed using the well-known expression for single-surface lenses given by (B.2-5) and found in the literature [GOLD97]. The material used is Plexiglas, which has a relative permittivity ε_r of 2.56. The profile of the lens is given in Figure B.2-2. A backing section of thickness t_0 = 3.5 mm is added on the flat size in order to maximise the gain at 30 GHz [GAGN09], which leads to a total thickness of 41.876 mm. The thickness of the backing section is optimised using a

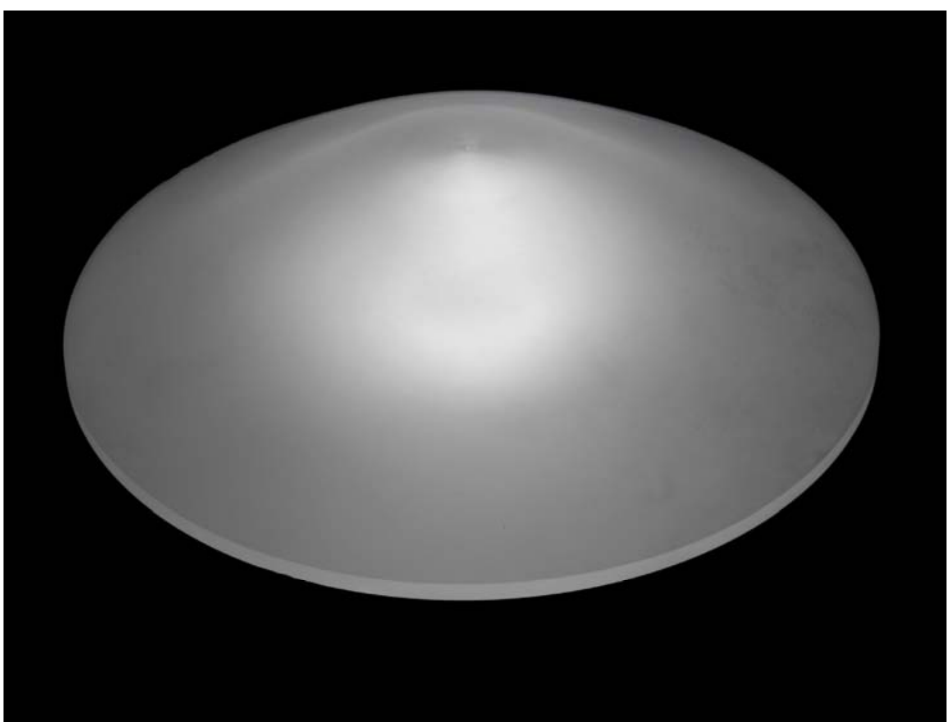

Figure 6.3-1: Dielectric plano-hyperbolic lens antenna (DPHLA).

commercial finite-difference time-domain electromagnetic simulation software package [EMPI07]. Note that, in the optimisation process, no loss is assumed in the dielectric lens and the antenna used to feed the lens is an open waveguide. In the current study, the feed antenna is a small horn of the same waveguide type as the open waveguide, consequently the thickness of the backing section may not be fully optimised in this case.

6.3.2 Dielectric phase-correcting Fresnel zone plate antenna (PC-FZPA)

The dielectric PC-FZPA shown in Figure 6.3-2 was previously reported in [PETO06]. In [PETO06], different dielectric PC-FZPA designs are reported for different relative permittivities. The thickness of the backing section was optimised the same way as for the DPHLA. Only the best case from [PETO06] is presented here for comparison

Figure 6.3-2: Dielectric phase-correcting Fresnel zone plate antenna (PC-FZPA).

purposes. This case corresponds to a 90° phase correction, relative permittivity ε_r of 5.8 and backing thickness t_0 = 2.66 mm. The step height is calculated using (B.3-4) and leads to s = 1.78 mm. Consequently, the total thickness is 8 mm. The rings' radii are calculated using (B.3-6). The cross-section and front views are presented in Figure 6.3-3.

6.3.3 Fresnel zone plate antenna (FZPA)

The FZPA shown in Figure 6.3-4 is designed according to Section B.4 of Appendix B. The opaque zones are made of metal while the transparent zones are those where the metal is etched off using a conventional photolithographic (wet chemical) etching process. A very thin layer (t = 0.127 mm) of FR4 material with relative permittivity $\varepsilon_r \approx 4.2$ is used to support the metal pattern. Full-wave electromagnetic simulations performed with [EMPI07] confirmed that the FR4 layer has a marginal effect on the electromagnetic performance of the FZPA. Figure 6.3-5 presents cross-section and front views of the FZPA. Table 6.3-1 presents the radii values of the FZPA, calculated from (B.3-6) with P = 2.

6.3.4 Far-field measurement results

The far-field radiation patterns for these three conventional lensing devices are presented in this section. Figure 6.3-6 presents the H-plane co-polarisation results while Figure 6.3-7 presents the E-plane co-polarisation results. The boresight gain over frequency is presented in Figure 6.3-8. Comments on the measured performance will be given when comparing it to that of the lens antennas realised using PSS structures in Section 6.9.

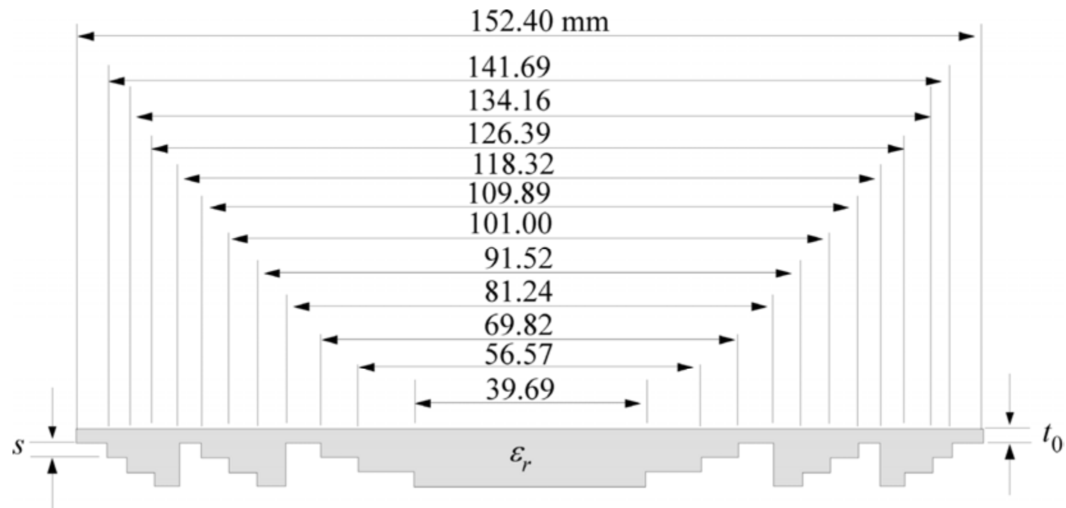

(a)

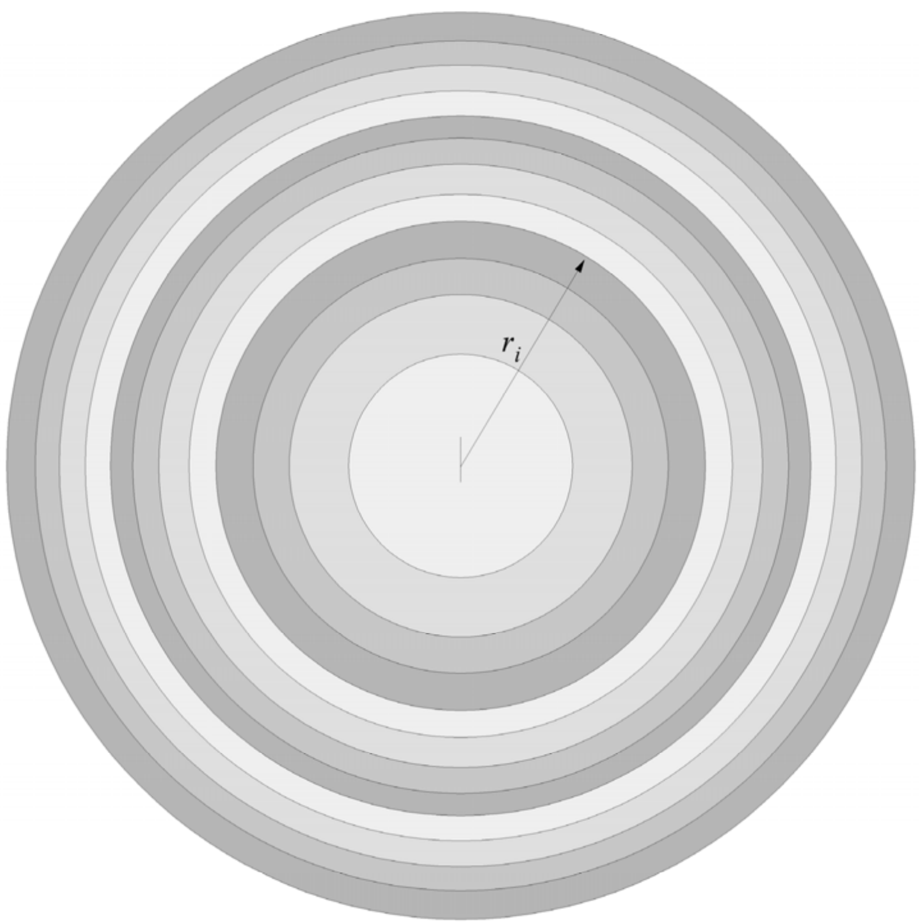

(b)

Figure 6.3-3: Sketch of the PC-FZPA with *F*/*D* = 0.5; (a) Cross-section view, (b) Front view. Reprinted with permission from [PETO06].

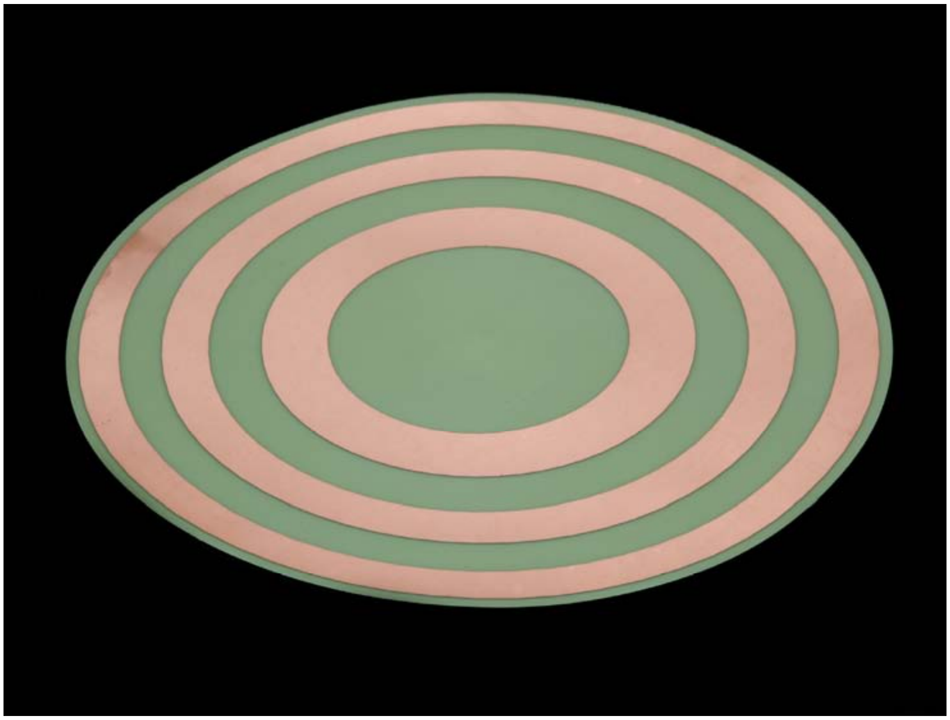

Figure 6.3-4: Fresnel zone plate antenna (FZPA).

6.4 Phase Shifting Surface Flat Lens Theory

An expression for the required phase correction ϕ imparted by the phase-shifting surface (PSS), at each point over its aperture, in order to achieve a lens antenna behaviour is next described. In order to maximise the far-field gain, the PSS must apply a different phase correction at each point so that the phase is uniform everywhere over its output surface. Using Figure 6.4-1, a principle similar to the one presented in Section B.2 can be applied here. Using a ray-tracing type approach, one finds that the required condition, similar to (B.2-2), can be expressed as

$$\frac{2\pi}{\lambda_0}F - \phi_0 = \frac{2\pi}{\lambda_0}R - \phi \tag{6.4-1}$$

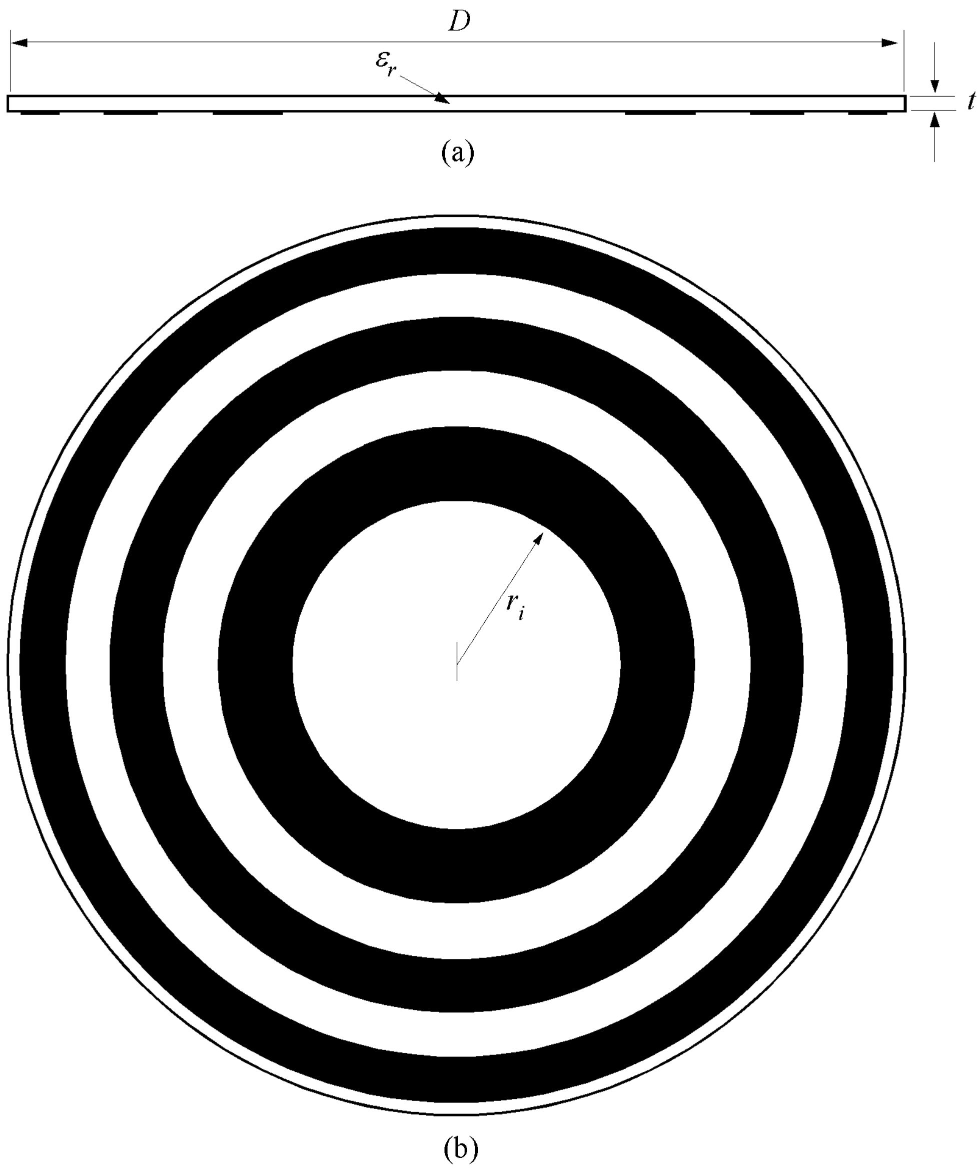

Figure 6.3-5: Sketch of the FZPA with *F*/*D* = 0.5; (a) Cross-section view, (b) Front view; see Table 5.2-1 for radii values.

Table 6.3-1: Radius values for the FZPA.

i	r_i (mm)
1	28.05
2	40.30
3	50.11
4	58.72
5	66.60
6	73.97

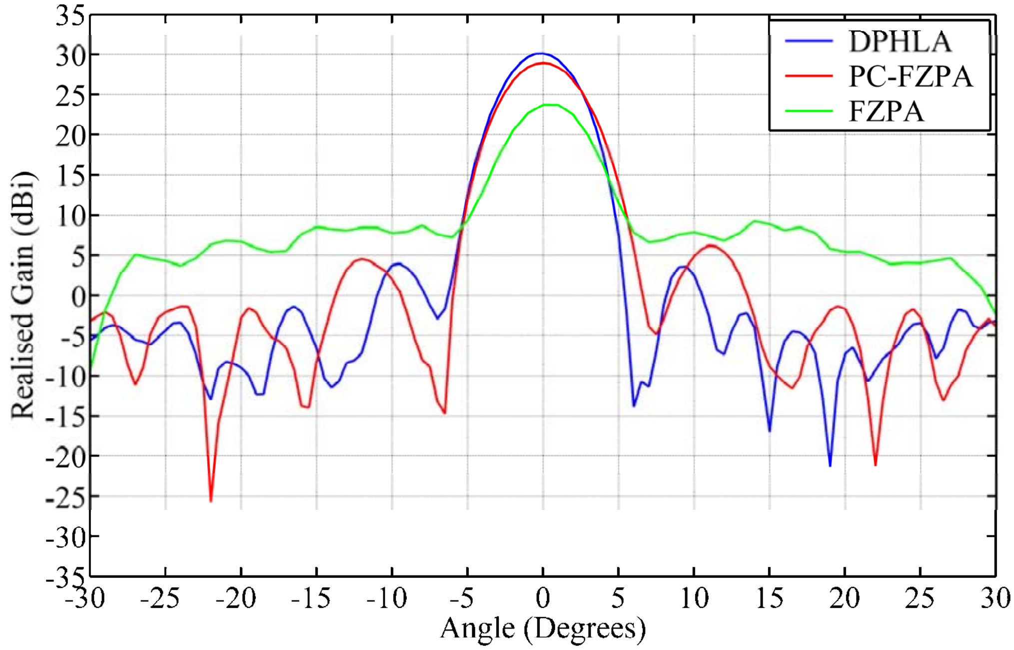

Figure 6.3-6: Measured *H*-plane co-polarisation far-field radiation patterns of the conventional lensing antennas at 30 GHz.

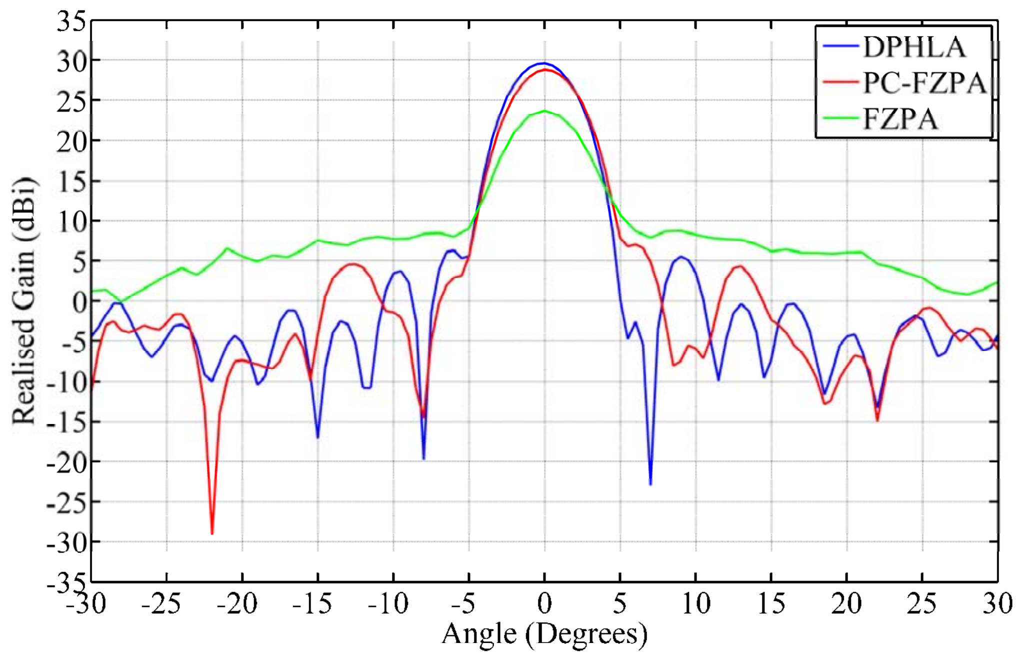

Figure 6.3-7: Measured *E*-plane co-polarisation far-field radiation patterns of the conventional lensing antennas at 30 GHz.

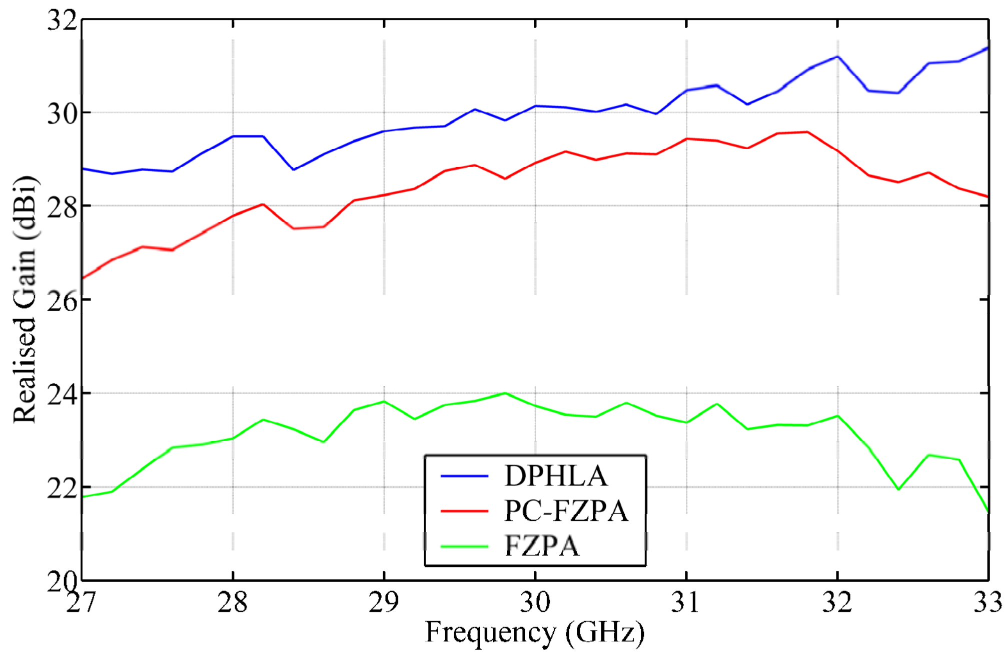

Figure 6.3-8: Measured boresight gain of the conventional lensing antennas.

from which the required phase correction ϕ at each point over the lens aperture can be determined. In (6.4-1), λ_0 is the free-space wavelength, F is the focal length, and R is the distance from the focal point to a point on the lens. The term ϕ_0 is the required phase correction in the middle of the lens, for normal incidence angle, and is assumed to be zero. The fact that R and ϕ in (6.4-1) are functions of the radiation angle θ, is best shown explicitly:

$$\frac{2\pi}{\lambda_0}F = \frac{2\pi}{\lambda_0}R(\theta) - \phi(\theta) \qquad (6.4\text{-}2)$$

Because the PSS lenses are flat, R is not the unknown, as it is the case in Section B.2 for a shaped lens. Instead, the unknown here is the required phase correction ϕ. The term R can simply be found from trigonometry to be

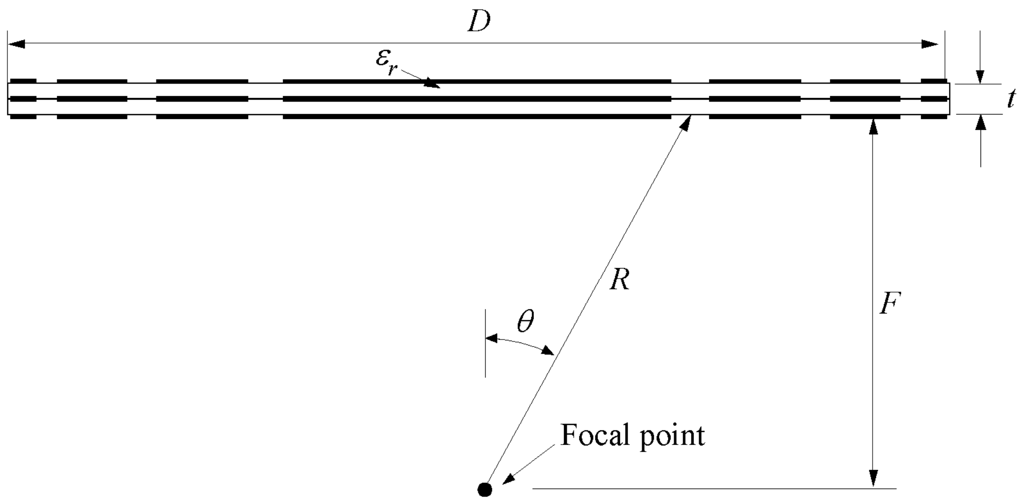

Figure 6.4-1: Side view of a PSS lens antenna, this specific case showing a 3-layer PSS.

$$R(\theta) = \frac{F}{\cos\theta} \tag{6.4-3}$$

Inserting (6.4-3) in (6.4-2) gives

$$\frac{2\pi}{\lambda_0} F = \frac{2\pi}{\lambda_0} \frac{F}{\cos\theta} - \phi(\theta) \tag{6.4-4}$$

Simplification of (6.4-4) yields

$$\phi(\theta) = \frac{2\pi}{\lambda_0} \frac{F}{\cos\theta} - \frac{2\pi}{\lambda_0} F \tag{6.4-5}$$

that reduces to

$$\phi(\theta) = \frac{2\pi F}{\lambda_0} \left(\frac{1}{\cos\theta} - 1 \right) \tag{6.4-6}$$

and hence

$$\phi(\theta) = \frac{2\pi F}{\lambda_0} \left(\frac{1 - \cos\theta}{\cos\theta} \right) \tag{6.4-7}$$

6.5 Phase Shifting Surface Flat Lens Implementation

Equation (6.4-7) is used to design the thin flat phase-shifting surface phase-correcting Fresnel zone plate antennas (PSS PC-FZPAs). In order to realise the phase distribution over the aperture, the lens aperture is divided into $N_x \times N_y$ rectangular cells of dimensions $\Delta x \times \Delta y$, as shown in Figure 6.5-1. This process leads to quantisation of the aperture distribution and, unless $\Delta x \rightarrow 0$ and $\Delta y \rightarrow 0$ (which is usually not the case), this process also leads to quantisation error. Each cell is assigned an index m and a position (x_m, y_m) corresponding to its centre, as shown in Figure 6.5-1. The position (x_m, y_m) also

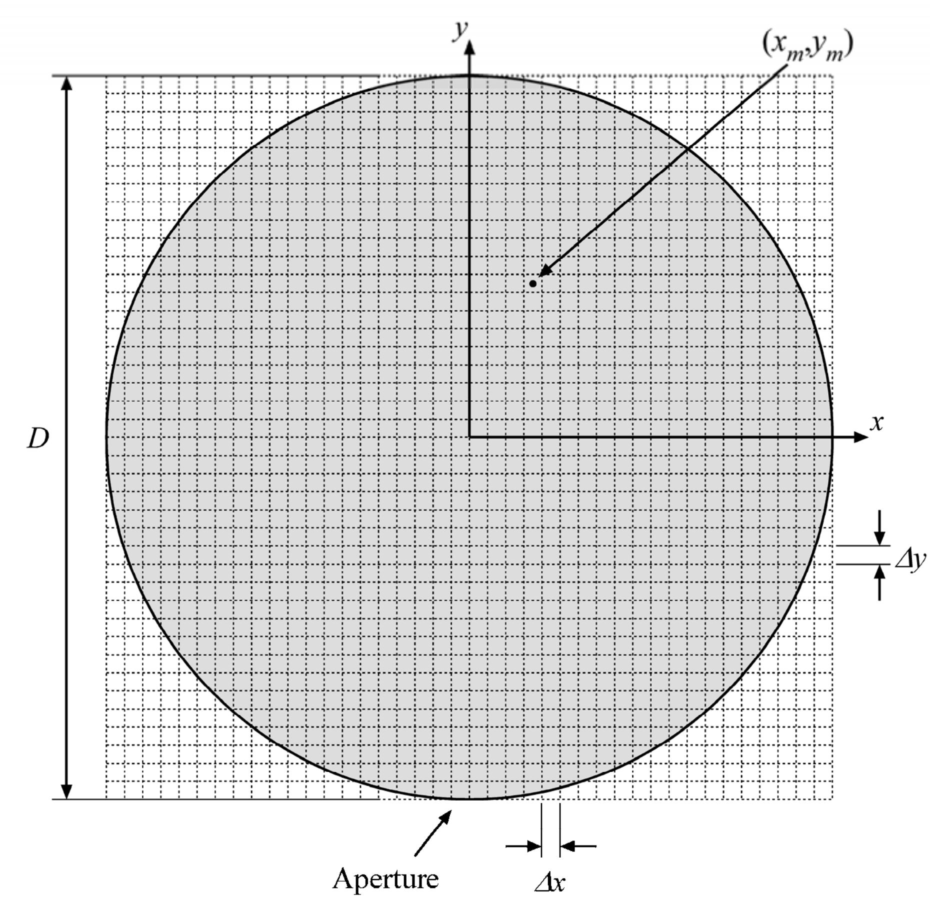

Figure 6.5-1: Quantisation of the circular lens aperture in rectangular cells.

corresponds to the location at which the required phase is sampled. An algorithm is used to minimise the difference between the implemented phase correction (available from a database such as that in Figures 3.4-4, 3.4-5, 3.4-10, 3.4-11 and 3.5-2) and the ideal continuously varying phase correction at every position (x_m, y_m) on the lens aperture surface for the different implementations of PSS PC-FZPA presented in Sections 6.6, 6.7 and 6.8. The algorithm is simply based on minimising the phase error by selecting the phase correction from the available data set, which is specific for each PSS configuration. The data sets are graphically represented in Sections 3.4 and 3.5, but in the implementation a look-up table is used. The whole process is automated and implemented in MATLAB [MATL03]. The output consists of the physical dimensions referred to as a_i's in Chapter 3 for each element of index m. The physical parameters are then imported into a CAD tool for generating files to be used for fabricating the masks used in the photolithographic (wet chemical) etching process.

6.6 Polarisation-Sensitive 3-Layer PSS PC-FZPAs

The PSS transmission data for the polarisation-sensitive symmetrical three independent layer case presented in Section 3.4.3 is used to design the PSS PC-FZPAs in this section. Since the gain is maximised for the highest values of transmission coefficient, only the combinations of local dimensions (a_1, a_2) which give the highest transmission amplitude for a required transmission phase are selected as potential candidates for the realisation of PSS PC-FZPAs. These results are extracted from the cases presented in Figure 3.4-5. A modified version of Figure 3.4-5 is presented in Figure 6.6-1, where only the selected cases needed for the three different PSS PC-FZPA realisations to be described shortly are shown.

Three polarisation-sensitive 3-layer PSS PC-FZPAs are designed with 90°, 45° and quasi-continuous phase correction schemes. The expression *quasi-continuous* is used to denote the fact that the PSS allows for continuous phase compensation in the −305° to 0° phase range only, as explained in Section 3.4.3. From the data provided in Figure 6.6-1, three different sets of phase shifts, corresponding to the three desired phase-correction schemes, are generated.

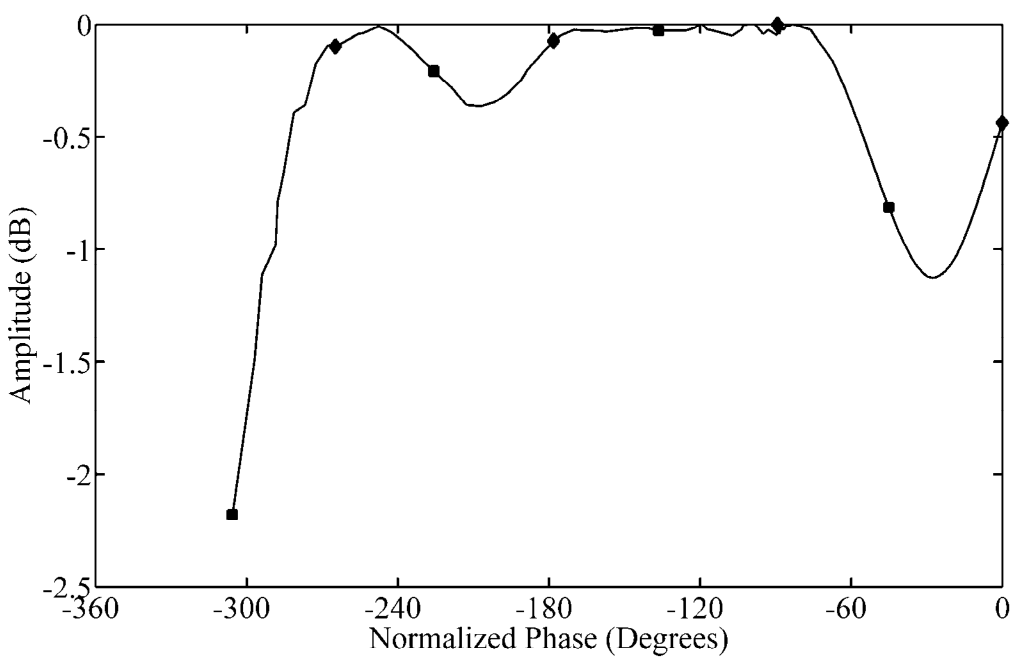

Figure 6.6-1: Highest transmission coefficient amplitude for three symmetrical independent layers of strips for different values of normalised transmission coefficient phase for ε_r = 2.2, *h* = 1 mm and *s* = 3 mm obtained from FDTD simulations at 30 GHz. The data is used to realise PSS PC-FZPA with 90 degree phase correction (♦), 45 degree phase correction (♦, ■) and quasi-continuous phase correction (——).

The implementation is done according to the guidelines provided in Section 6.5. This unit cell has a fixed height of s = 3 mm and consequently Δy, the subdivision dimension along y, is equal to s, namely Δy = 3 mm. Along x the unit cell is made continuous, as explained in Section 3.3. Consequently the dimension Δx can be chosen as desired. In this case, the value is chosen to be 0.1 mm as a compromise for improving the quantisation error and limiting the computer resources required for generating the layout.

Unlike the traditional grooved dielectric PC-FZPAs presented in Section B.3, the thickness of the PSS PC-FZPA is independent of the phase correction implemented. In fact, the thickness is constant and equal to the thickness of the PSS itself. Recall that (6.4-7) is used in the implementation of PSS PC-FZPAs, which has no thickness implications. Therefore, there is no physical disadvantage in increasing the number of steps (what would correspond to increasing P in a dielectric PC-FZPA); increasing the number of steps simply translates into increasing the number of cases in the database or set of available steps, which results in smoother phase shift variation. Indeed, the fact that three different PSS PC-FZPA realisations are investigated next, namely the 90°, 45° and quasi-continuous cases, allows for examining the effect of the number of steps in a similar manner as would be the case for looking at the effect of P in a dielectric PC-FZPA (in which case 90° would correspond to P = 4, 45° would correspond to P = 8 and quasi-continuous would correspond to $P \rightarrow \infty$ or an implementation close to that of a Fresnel lens, keeping in mind that only correcting phases from –305° to 0° can be implemented).

The 90° phase correction PSS PC-FZPA uses the phase values shown by diamonds (♦) in Figure 6.6-1; the 45° phase correction PSS PC-FZPA uses the phase values shown by diamonds (♦) and squares (■) in Figure 6.6-1; the quasi-continuous phase correction

PSS PC-FZPA uses the continuous line of data in Figure 6.6-1, i.e. all the available cases in the extracted database of highest amplitude.

Photographs of the three PSS PC-FZPA realisations are shown in Figure 6.6-2. As the number of steps increases, i.e. as the phase correcting step decreases, the resulting metallisation pattern varies in a smoother way (as opposed to a somewhat staircase variation), which suggests a smoother, more continuous, phase-shifting behaviour.

Figures 6.6-3 and 6.6-4 respectively present the *H*-plane and *E*-plane co-polarisation radiation patterns obtained from measurements at 30 GHz for the three polarisation-sensitive 3-layer PSS PC-FZPAs. Figure 6.6-5 presents the measured boresight gain over frequency for the same three lenses.

Figure 6.6-6 presents the back-projected measured near-fields at the output surface of the aperture at the frequency of 30 GHz for the polarisation-sensitive 3-layer quasi-continuous PSS PC-FZPA. The near-fields were measured using a planar near-field scanner as described in Section 6.2.

The reflection coefficient of the polarisation-sensitive 3-layer quasi-continuous PSS PC-FZPA is presented in Figure 6.6-7. It shows that a return loss of 10 dB or higher is obtained over the frequency band; in particular, the return loss is 19.5 dB at 30 GHz and reaches levels higher than 20 dB from 30.05 GHz to 30.3 GHz.

Experimental results are discussed in Section 6.9. The comparison is done for results presented within this section, and also for results of the conventional lenses presented in Section 6.3 and for results of other PSS PC-FZPA realisations presented in Sections 6.7 and 6.8 that follow.

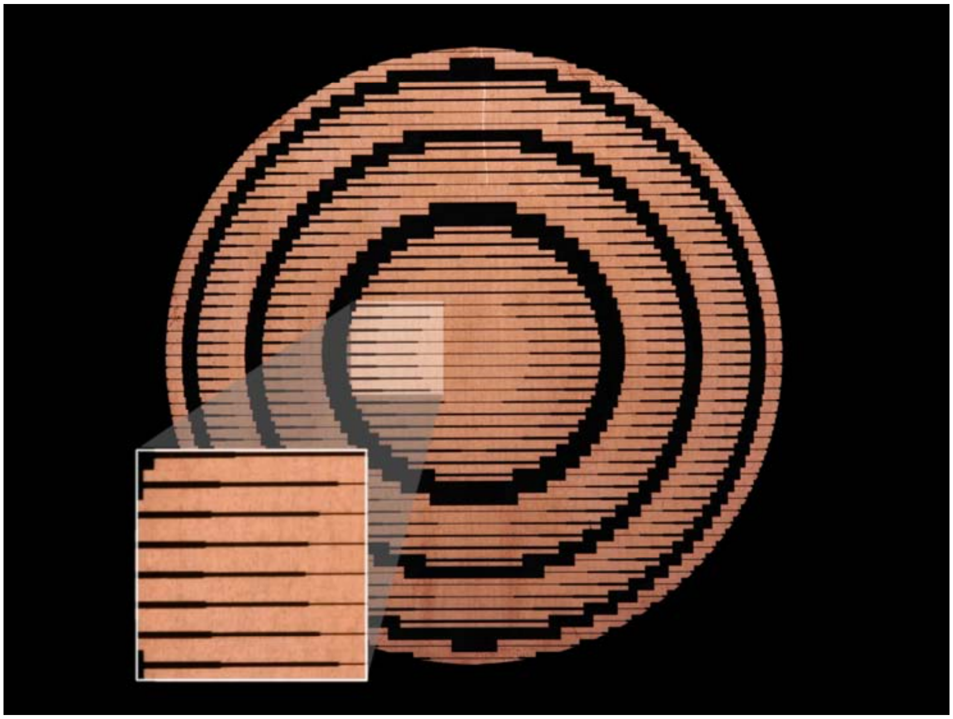

(a)

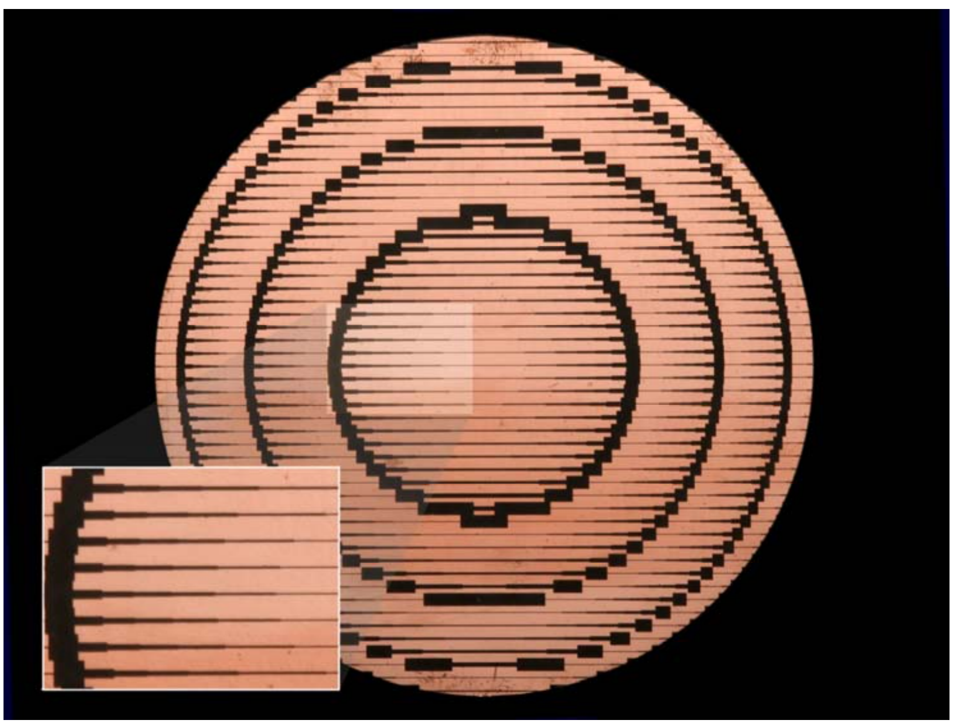

(b)

Figure 6.6-2: Photographs of the polarisation-sensitive 3-layer PSS PC-FZPAs; (a) 90 degree phase correction, (b) 45 degree phase correction.

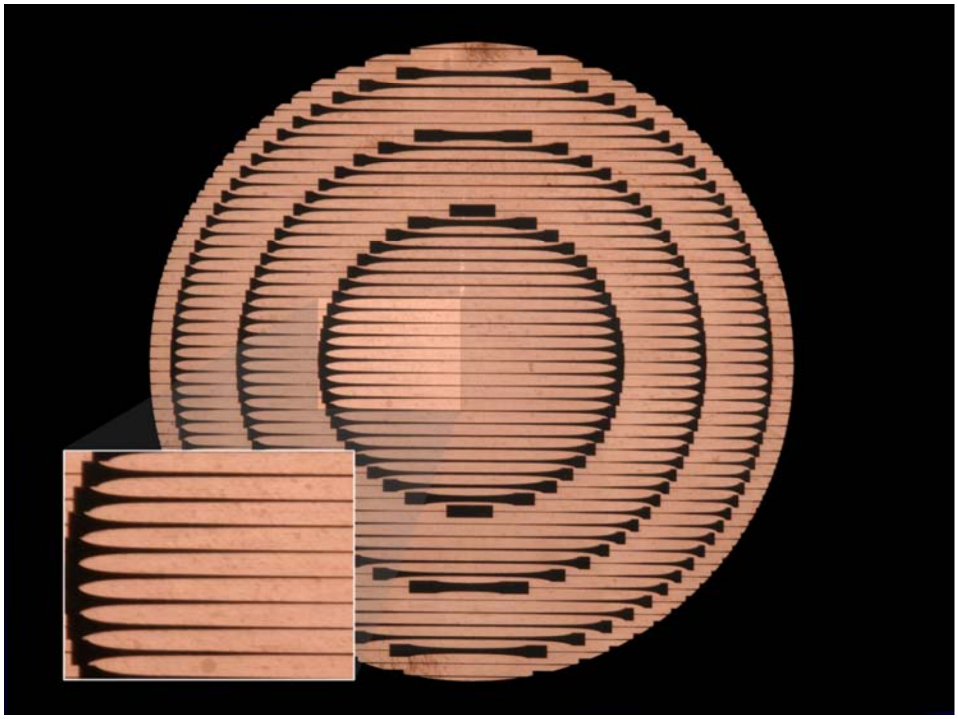

(c)

Figure 6.6-2 (continued): (c) quasi-continuous phase correction.

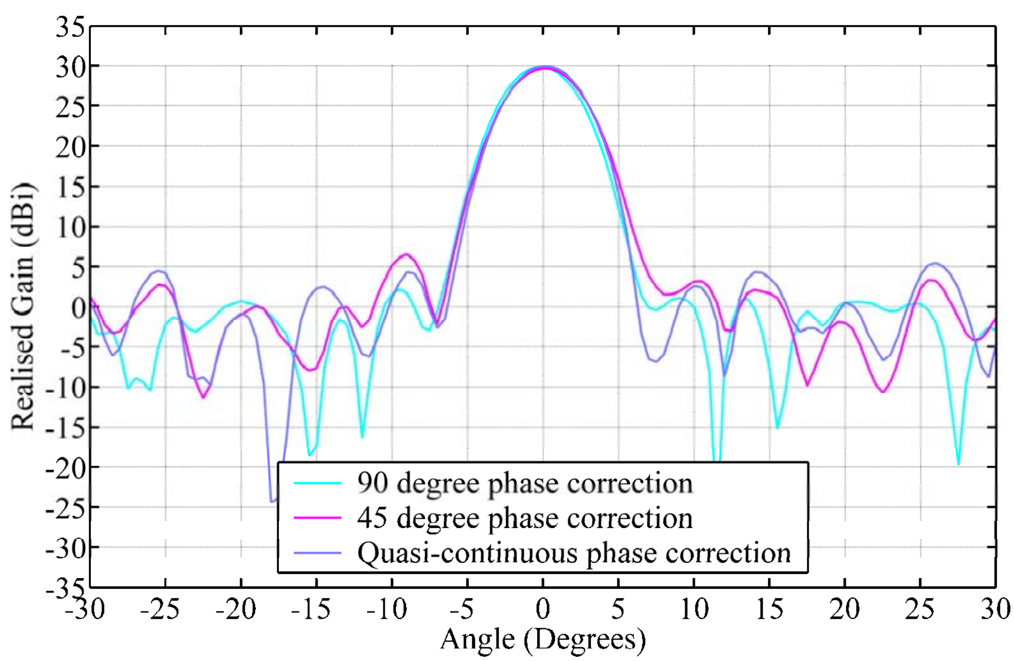

Figure 6.6-3: Measured *H*-plane co-polarisation far-field radiation patterns of the polarisation-sensitive 3-layer PSS PC-FZPAs at 30 GHz.

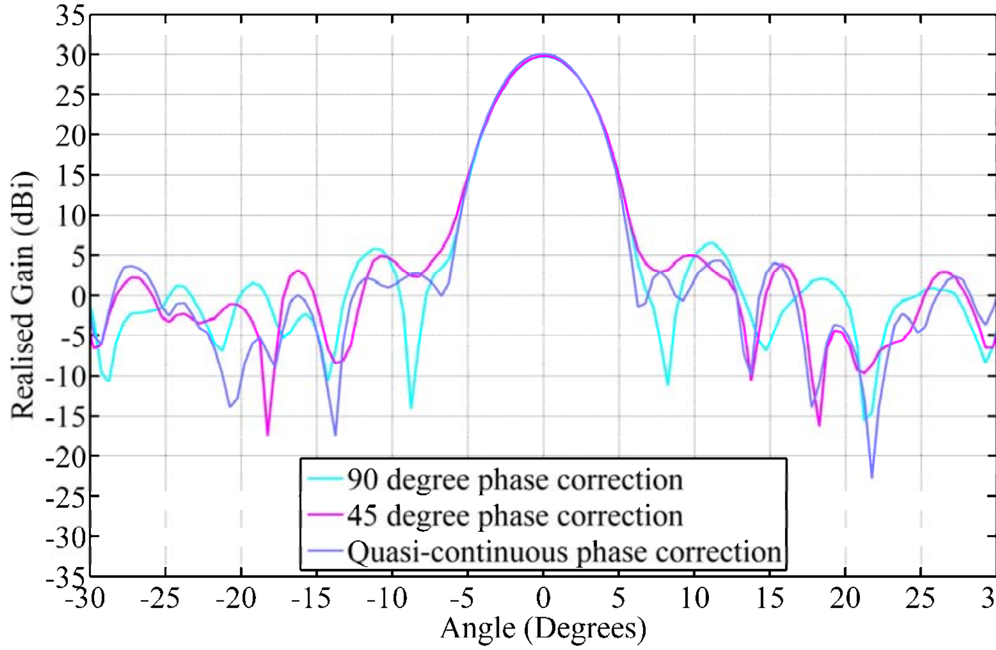

Figure 6.6-4: Measured *E*-plane co-polarisation far-field radiation patterns of the polarisation-sensitive 3-layer PSS PC-FZPAs at 30 GHz.

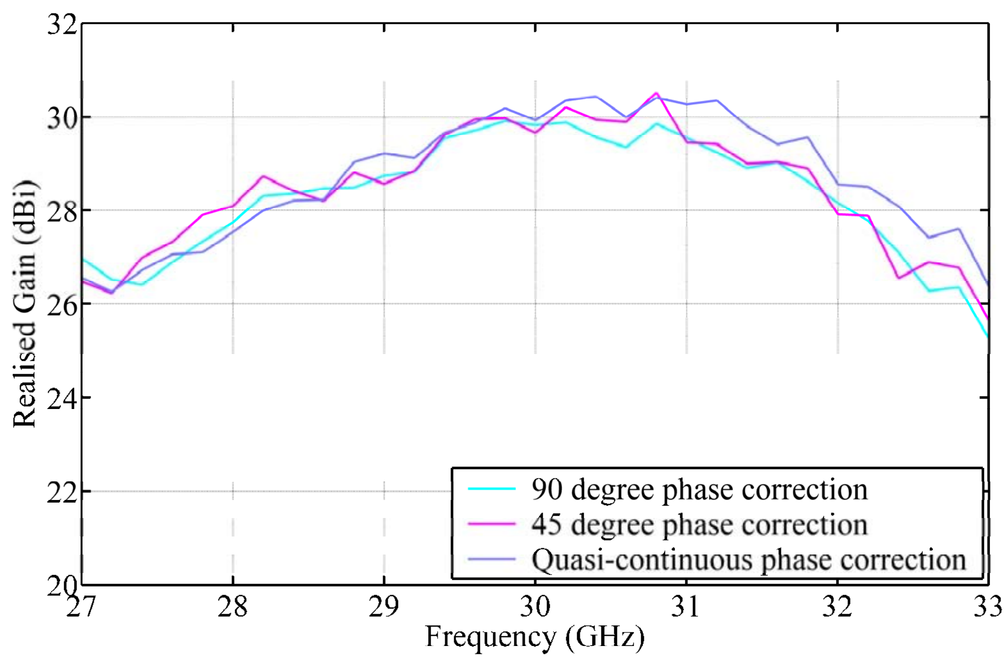

Figure 6.6-5: Measured boresight gain of the polarisation-sensitive 3-layer PSS PC-FZPAs.

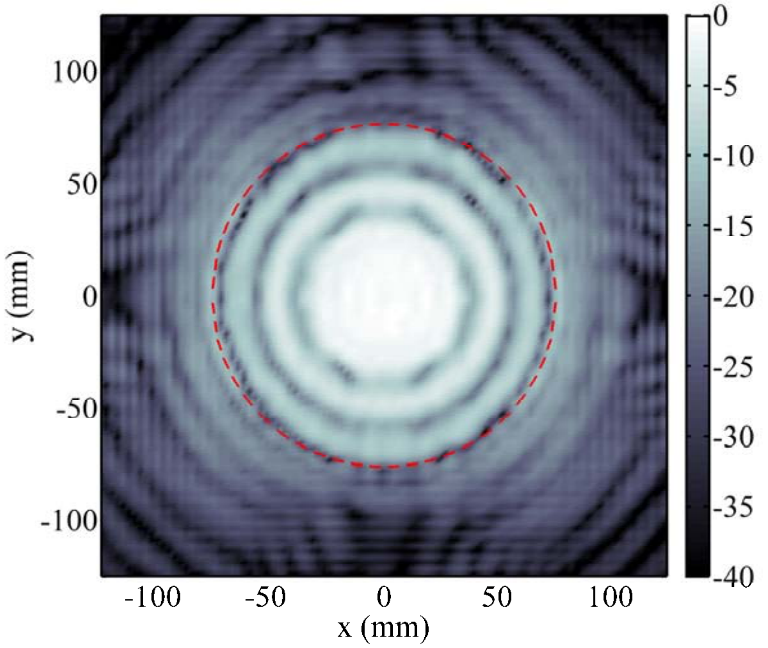

(a)

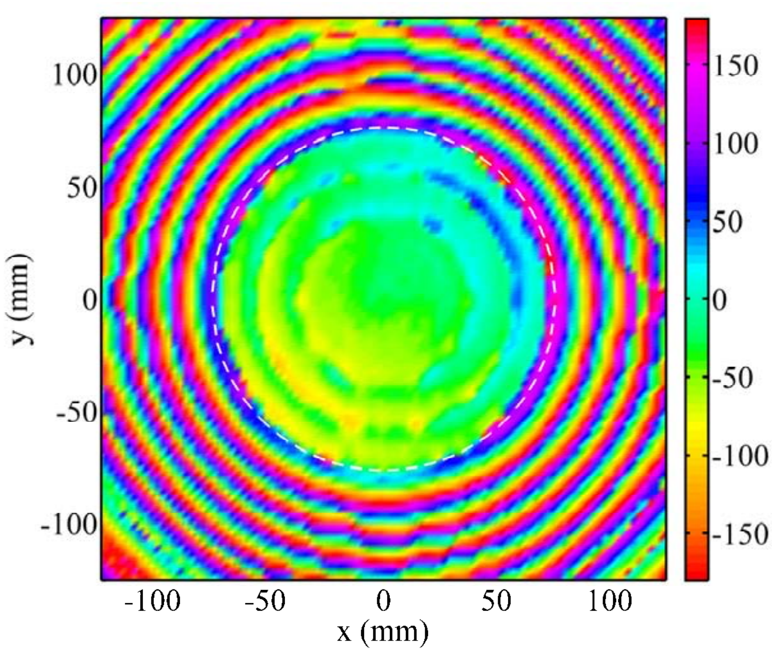

(b)

Figure 6.6-6: Measured near-fields at the surface of the aperture for the polarisation-sensitive 3-layer quasi-continuous PSS PC-FZPA at 30 GHz; (a) Amplitude (in dB), (b) Phase (in degrees). The physical boundary of the antenna is shown as an overlaid dashed line.

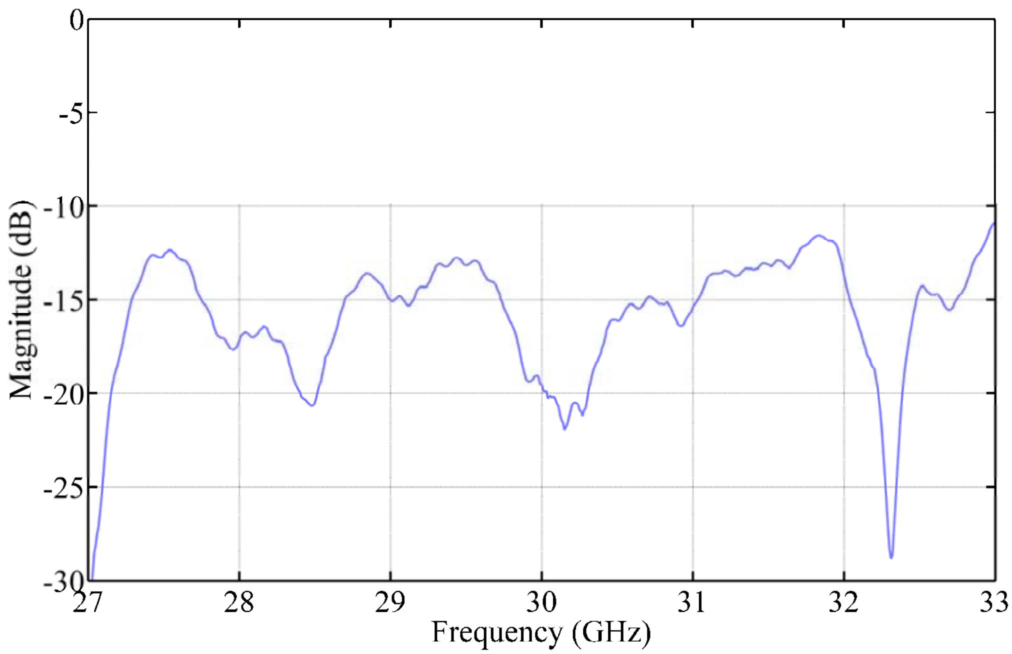

Figure 6.6-7: Measured reflection coefficient of the polarisation-sensitive 3-layer quasi-continuous PSS PC-FZPA.

6.7 Polarisation-Sensitive 4-Layer PSS Fresnel Lens Antenna

The PSS transmission data for the polarisation-sensitive fully-independent 4-layer case presented in Section 3.4.4 is used to design the continuous PSS PC-FZPA in this section. As for the three cases in Section 6.6, only the combinations of local dimensions (a_i's) which give the highest transmission amplitude for a required transmission phase are selected. These results correspond to the cases presented in Figure 3.4-11. A single polarisation-sensitive 4-layer PSS PC-FZPA is designed to implement a continuous phase correction scheme. Note that the expression *continuous* is used here since the polarisation-sensitive PSS with four fully-independent layers allows for continuous phase compensation in the whole range from −360° to 0°, as detailed in Section 3.4.4. Because the phase correction is continuous, this is similar to the Fresnel lens case presented in

Appendix B (with $P \rightarrow \infty$) and explains the title of this section. Figure 6.7-1 shows a photograph of the polarisation-sensitive 4-layer PSS Fresnel lens antenna.

Figure 6.7-2 presents the *H*-plane co-polarisation radiation patterns at 30 GHz for the polarisation-sensitive 4-layer PSS Fresnel lens antenna; the *E*-plane co-polarisation radiation patterns are presented in Figure 6.7-3. Figure 6.7-4 shows the boresight gain over frequency. A discussion of these results is delayed until Section 6.9 for reasons given at the end of Section 6.6.

6.8 Polarisation-Insensitive 3-Layer PSS 90 Degree PC-FZPA

The PSS transmission data for the polarisation-insensitive 3-layer PSS presented in Section 3.5 is used to design the 90 degree PC-FZPA in this section. Only four combinations of local dimensions (a_1, a_2) which lead to high transmission amplitude are selected. These selected cases, presented in Table 6.8-1, lead to a 90° phase correction. Since the simulations of square element cases are lengthy compared to the strip cases, only a single example is designed as a proof of concept. In fact, the cases used are not fully optimised due to simulation time constraints. They are nevertheless acceptable in both amplitude and phase. Figure 6.8-1 shows a photograph of the polarisation-insensitive 3-layer PSS 90° PC-FZPA.

The effect of altering the roll angle τ of the lens (shown in Figure 3.5-1) with respect to the fixed feed or fixed electric field polarisation is also investigated. Figure 6.8-2 presents the radiation patterns at 30 GHz for the polarisation-insensitive 3-layer PSS 90° PC-FZPA for multiple roll angles as indicated in the insets. Figure 6.8-3 shows the

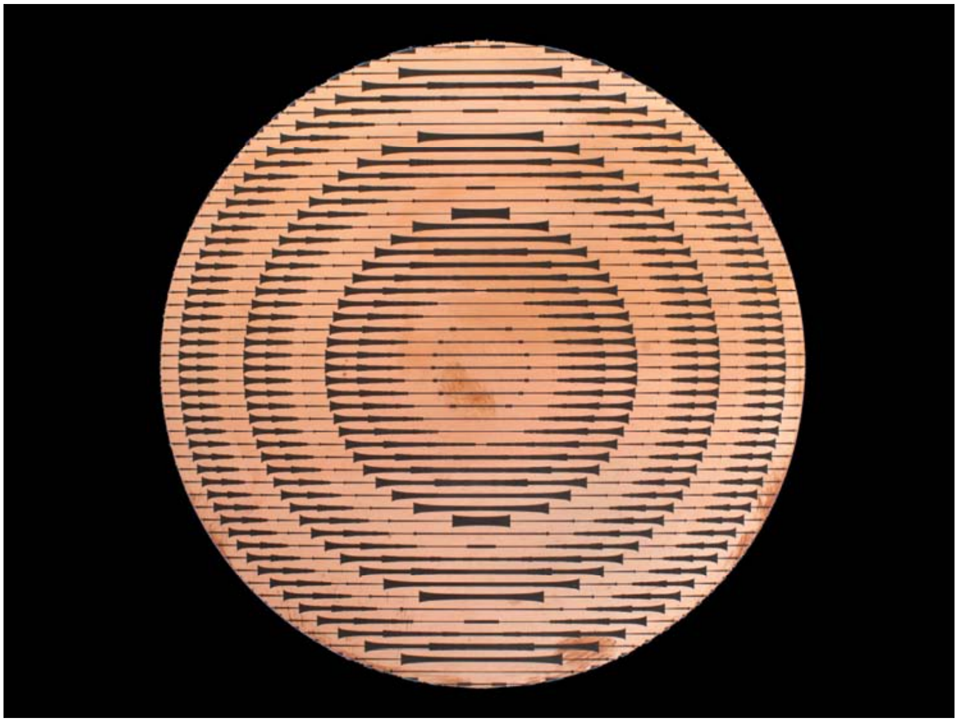

(a)

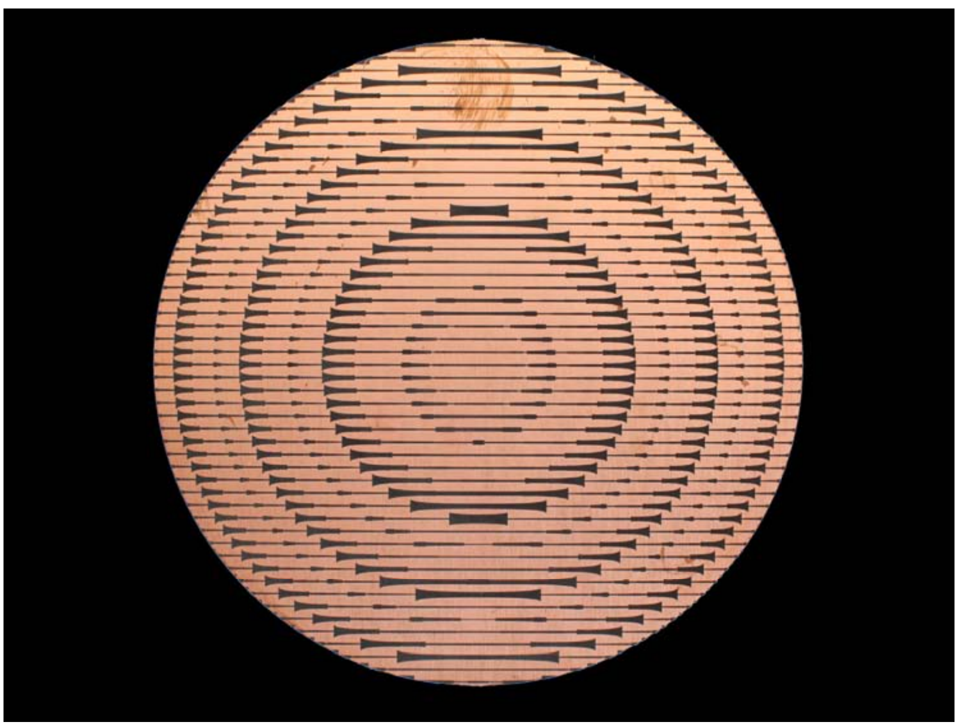

(b)

Figure 6.7-1: Photograph of the polarisation-sensitive 4-layer layer PSS Fresnel lens antenna; (a) Front view, (b) Back view.

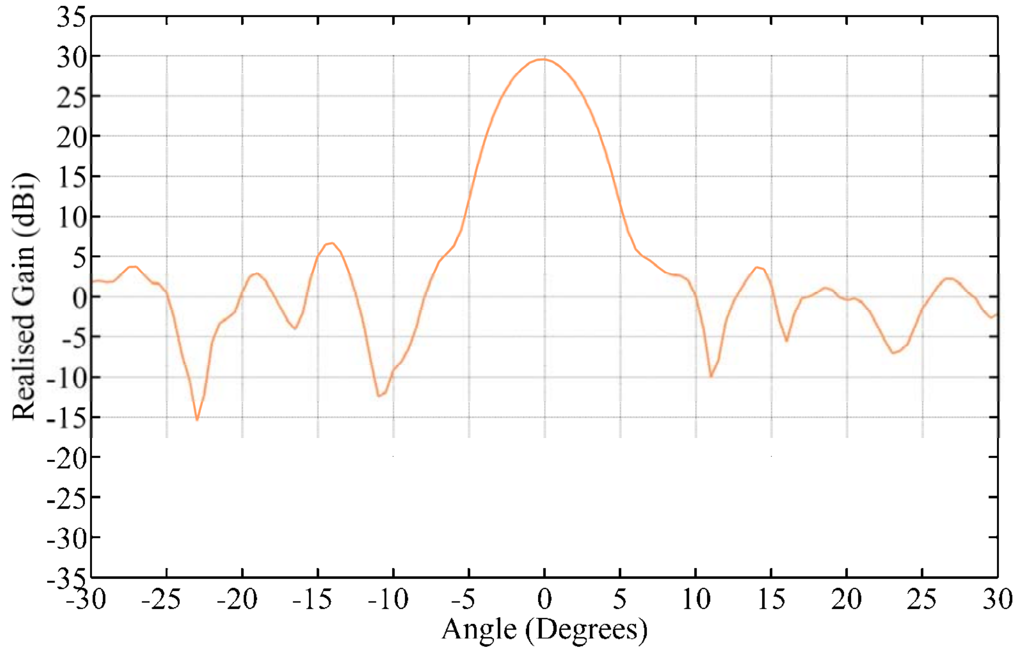

Figure 6.7-2: Measured *H*-plane co-polarisation far-field radiation pattern of the polarisation-sensitive 4-layer PSS Fresnel lens antenna at 30 GHz.

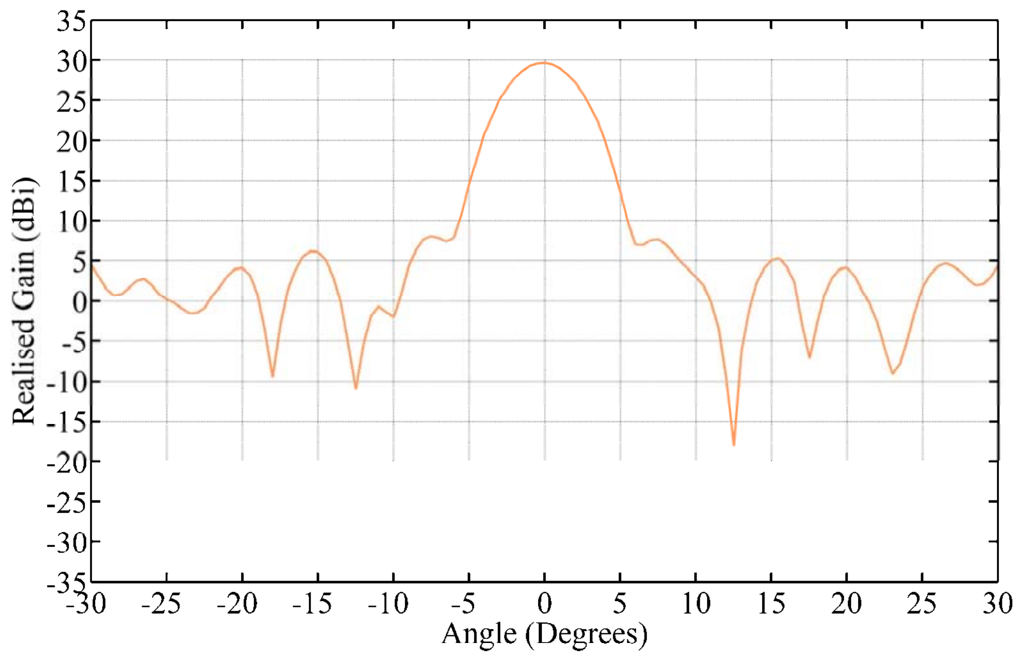

Figure 6.7-3: Measured *E*-plane co-polarisation far-field radiation pattern of the polarisation-sensitive 4-layer PSS Fresnel lens antenna at 30 GHz.

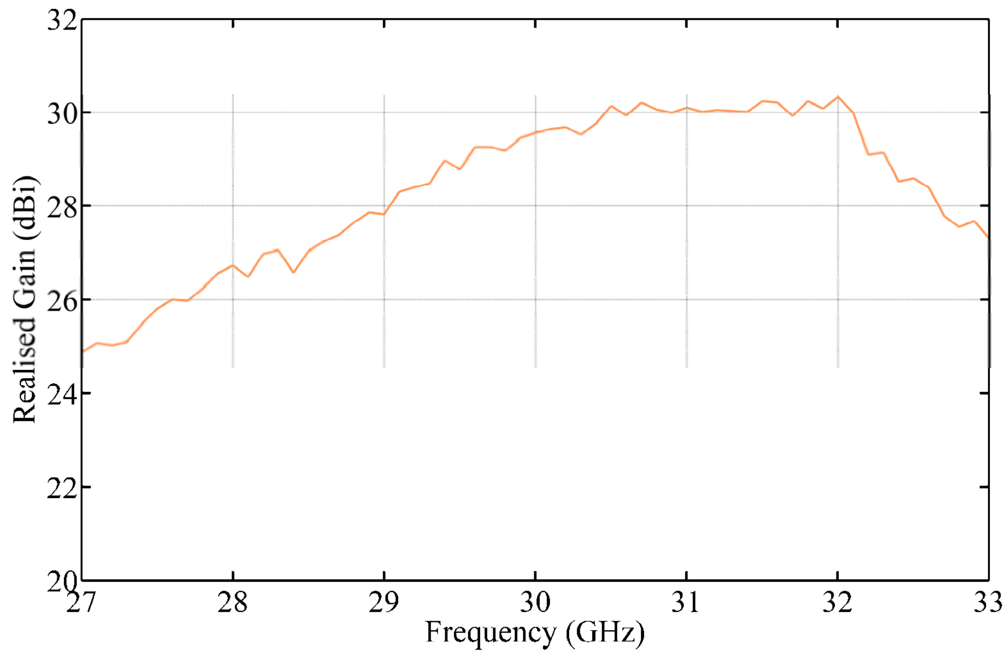

Figure 6.7-4: Measured boresight gain of the polarisation-sensitive 4-layer PSS Fresnel lens antenna.

Table 6.8-1: Design values for the polarisation-insensitive 3-layer PSS 90 degree PC-FZPA.

Ideal Transmitted Phase (°)	Ideal Transmitted Amplitude (dB)	Simulated Transmitted Phase (°)	Simulated Transmitted Amplitude (dB)	a_1 (mm)	a_2 (mm)
0	0	0	–0.437	0	0
–90	0	-95.0	–0.006	2.40	2.20
–180	0	-180.4	–0.258	2.60	2.84
–270	0	-276.4	–0.274	2.84	2.84

boresight gain over frequency for different roll angles. It is seen that the roll angle has only a marginal effect on the boresight gain and gain bandwidth of the polarisation-insensitive 3-layer PSS 90° PC-FZPA.

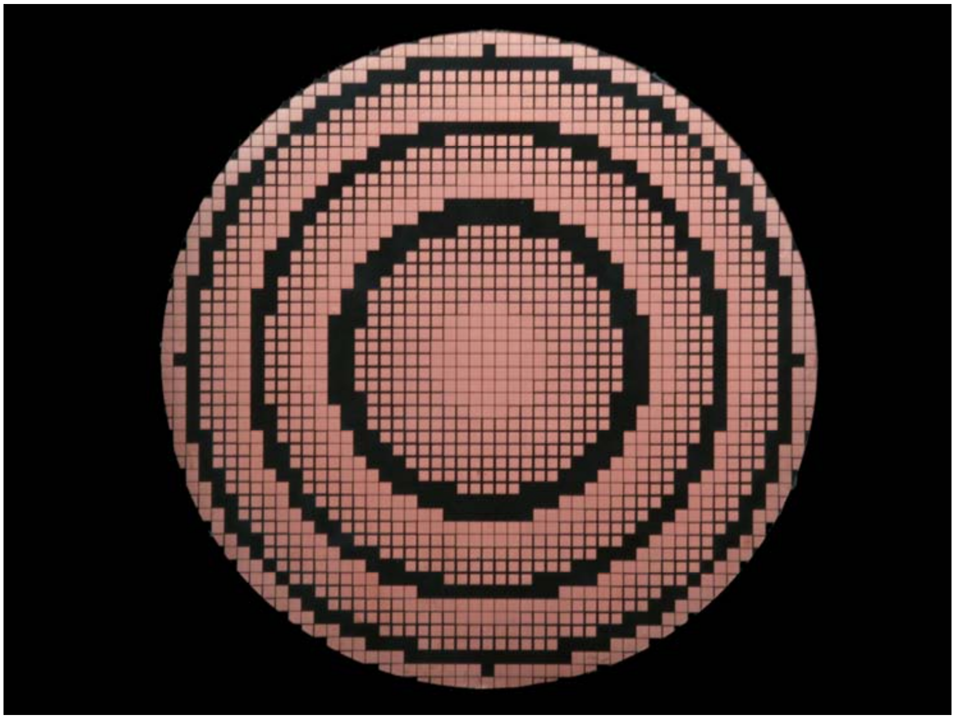

Figure 6.8-1: Photograph of the polarisation-insensitive 3-layer layer PSS 90 degree PC-FZPA.

Figure 6.8-4 shows the measured realised boresight gain and maximum cross-polarisation level against the lens roll at the frequency of 30 GHz. Small sketches representing the tilted polarisation-insensitive 3-layer 90° PSS PC-FZPA are added on top of the plot to help visualise the roll angle. From Figure 6.8-4, it is seen that there is a marginal gain degradation of about 0.25 dB when the lens is tilted from 0° to 45°. The cross-polarisation was also measured and it was found that its maximum level increased by 13.5 dB as the lens is tilted from 0° to 45°, reaching a maximum value of 5.5 dBi. The maximum cross-polarisation ratio is still within an acceptable range for the worst-case value of 5.5 dBi at 45°, with a value of –24 dB.

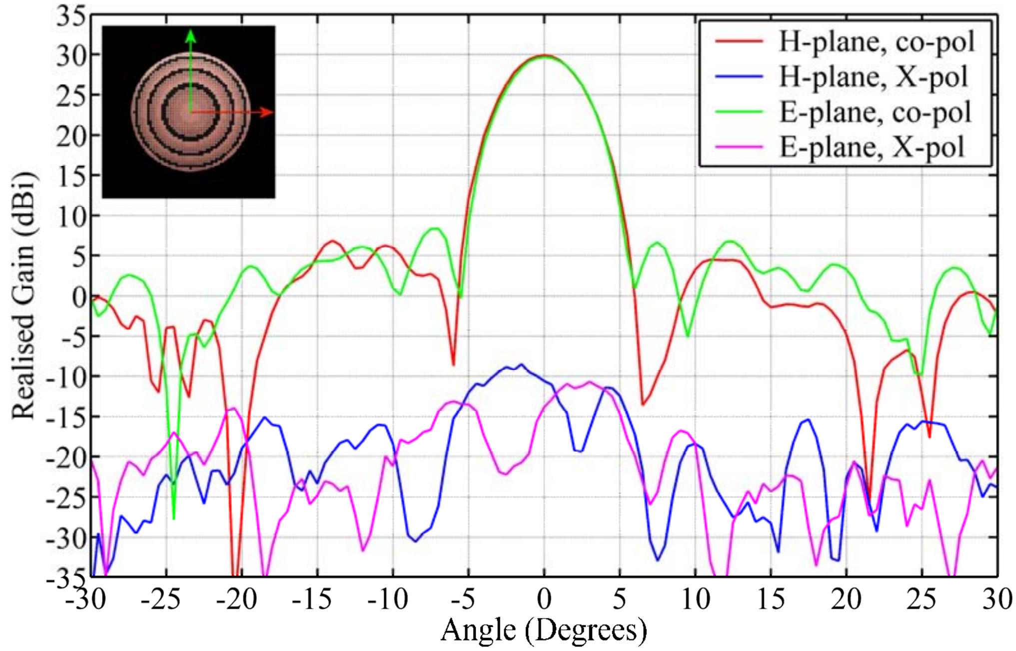

(a)

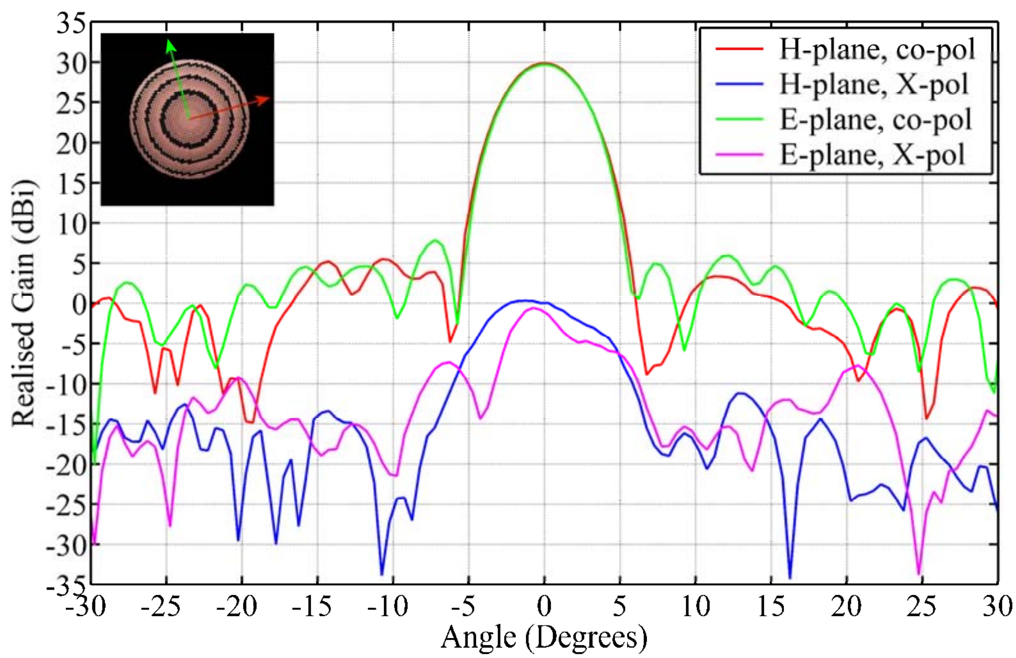

(b)

Figure 6.8-2: Measured far-field radiation patterns of the polarisation-insensitive 3-layer 90° PSS PC-FZPA at 30 GHz; (a) 0° roll angle, (b) 15° roll angle.

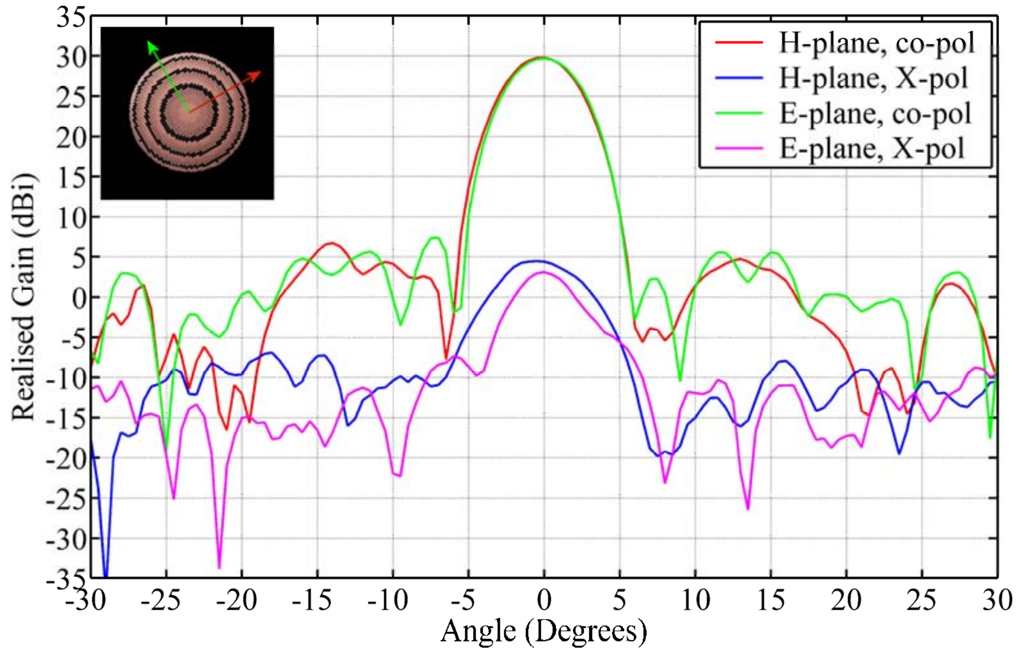

(c)

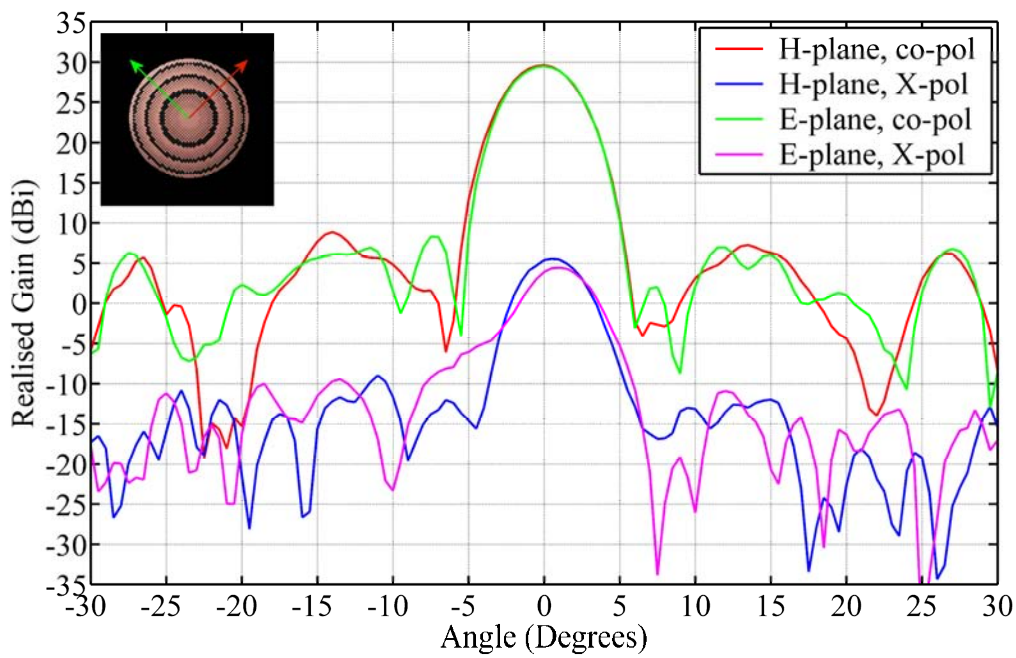

(d)

Figure 6.8-2 (continued): (c) 30° roll angle, (d) 45° roll angle.

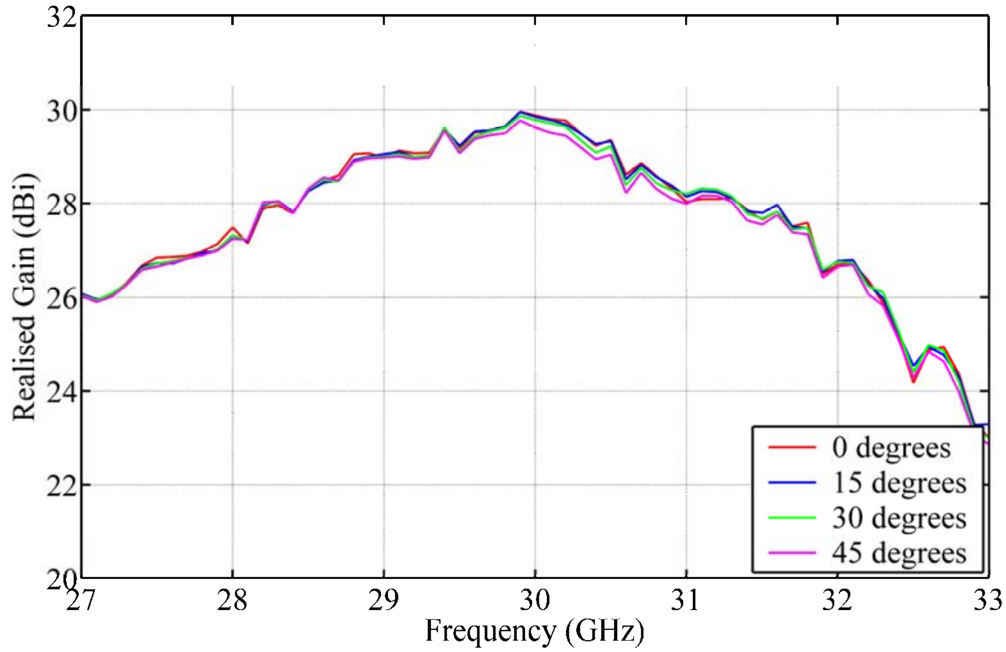

Figure 6.8-3: Measured boresight gain of the polarisation-insensitive 3-layer 90° PSS PC-FZPA for different roll angles.

Figure 6.8-5 presents the back-projected measured near-field pattern at the output surface of the aperture at the frequency of 30 GHz for the polarisation-insensitive 3-layer 90° PSS PC- FZPA. Details on the near-field measurements are provided in Section 6.2. A roll angle of 0° is used in the measurements. Figure 6.8-6 shows a photograph of the polarisation-insensitive 3-layer 90° PSS PC-FZPA under test in the near-field measurement facility.

The reflection coefficient of the polarisation-insensitive 3-layer 90° PSS PC-FZPA is presented in Figure 6.8-7. It shows that a return loss of 10 dB or higher is obtained over the entire frequency band, except for a small bandwidth near 32 GHz. At 30 GHz, the return loss is 16.6 dB.

Further discussion on the results provided in this section to follow in Section 6.9.

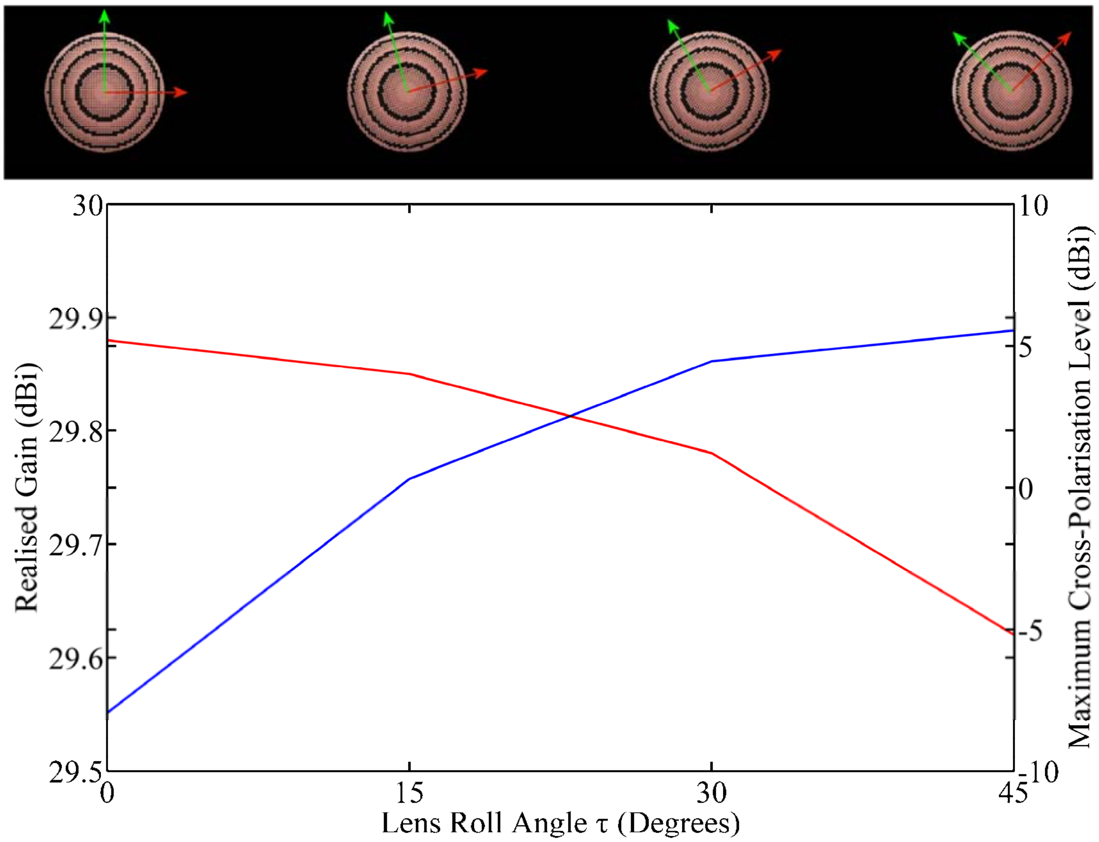

Figure 6.8-4: Measured realised boresight gain and maximum cross-polarisation level against lens roll angle of the polarisation-insensitive 3-layer 90° PSS PC-FZPA at 30 GHz; —— Realised gain, —— Maximum cross-polarisation level.

6.9 Discussion of the Measured Performance of the Five Different PSS PC-FZPA Realisations

In this section, the results presented in Sections 6.3, 6.6, 6.7 and 6.8 are compared and discussed. Table 6.9-1 provides a concise summary of the most important results for all conventional and PSS lenses presented in this chapter.

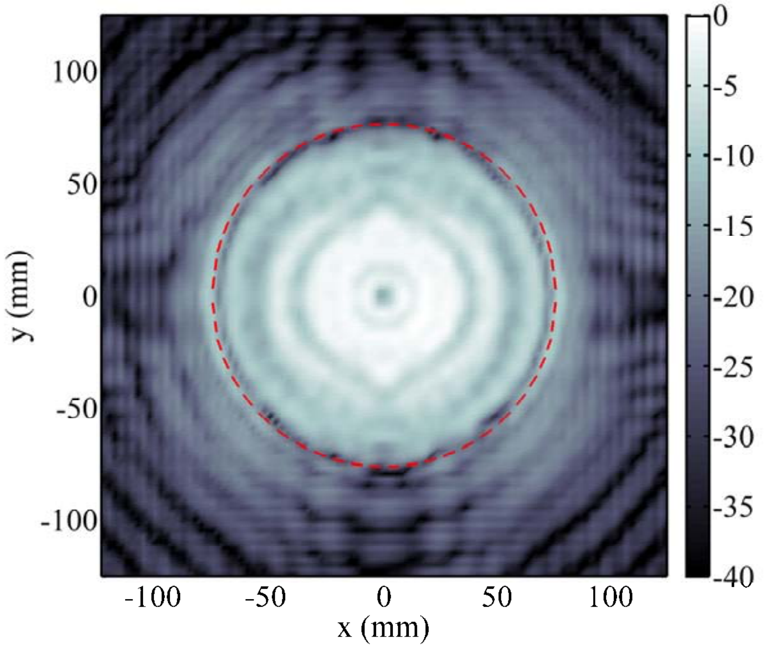

(a)

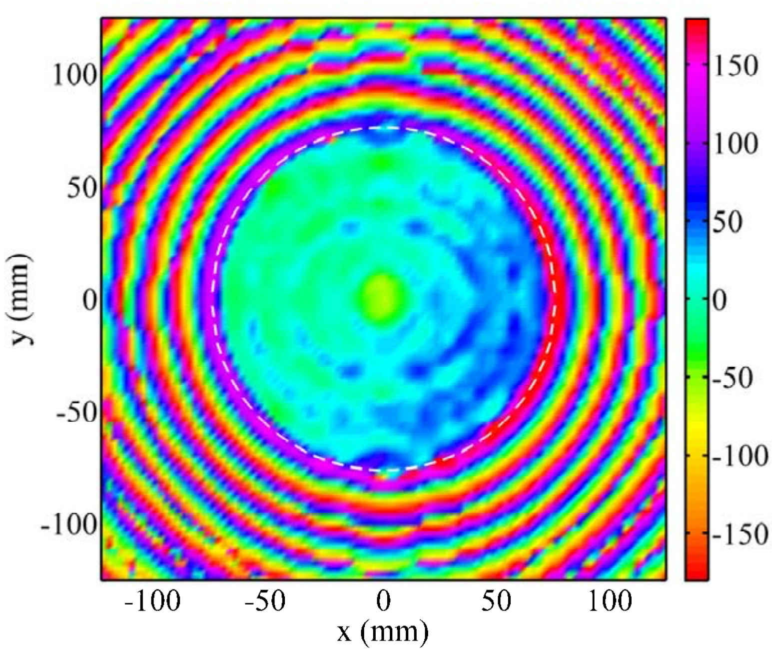

(b)

Figure 6.8-5: Measured near-fields at the surface of the aperture for the polarisation-insensitive 3-layer 90° PSS PC-FZPA at 30 GHz; (a) Amplitude (in dB), (b) Phase (in degrees). The physical boundary of the antenna is shown as an overlaid dashed line in each case.

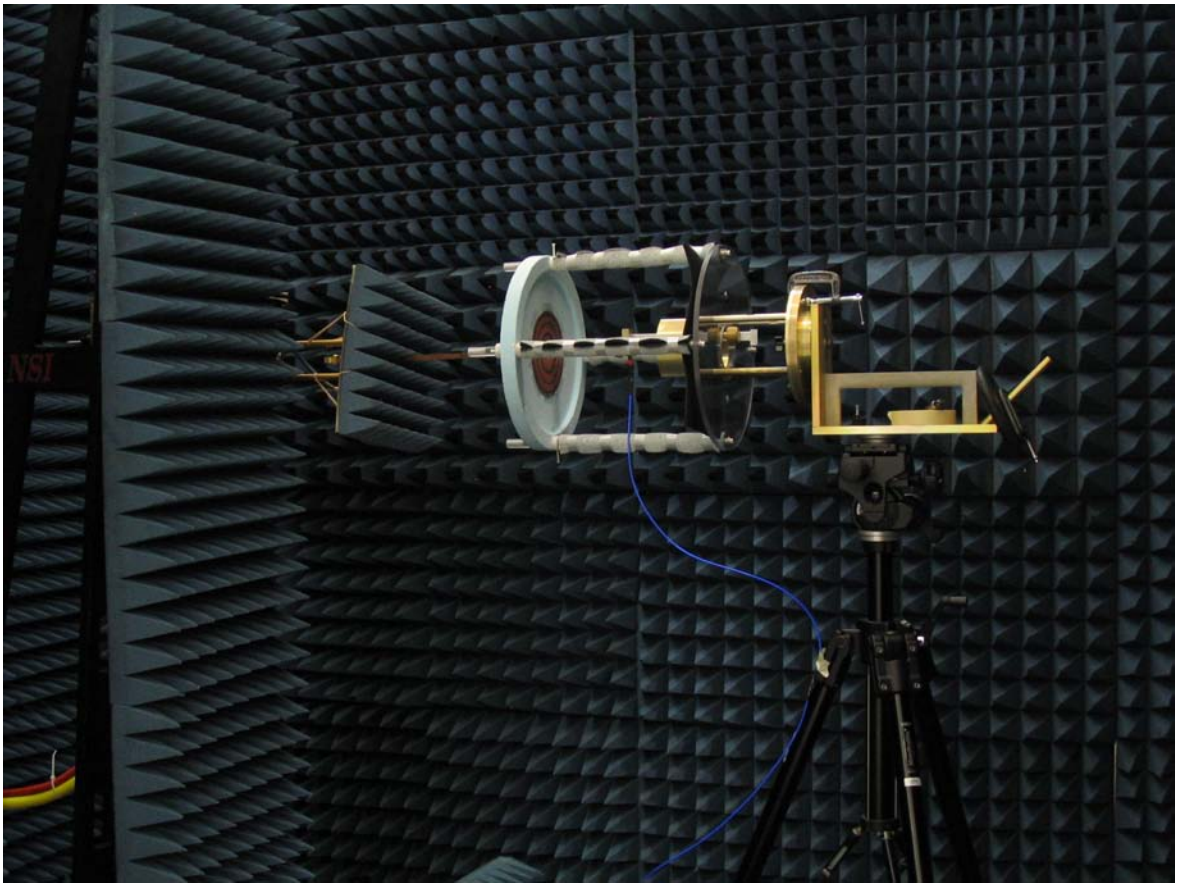

Figure 6.8-6: Photograph of polarisation-insensitive 3-layer 90° PSS PC-FZPA under test in the near-field measurement facility.

6.9.1 Polarisation-sensitive vs polarisation insensitive PSS PC-FZPAs

To begin with, the polarisation-sensitive (strip elements) and polarisation-insensitive (square patch elements) 3-layer PSS 90° PC-FZPAs are compared. For the polarisation-insensitive case, the results with roll angle $\tau = 0°$ are used here. Although the gain values and cross-polarisation levels are similar, the 1 dB gain bandwidth drops from 7.4% for the polarisation-sensitive case down to 5.9% for the polarisation-insensitive case. This can be explained by the field concentration, which is higher for the polarisation-

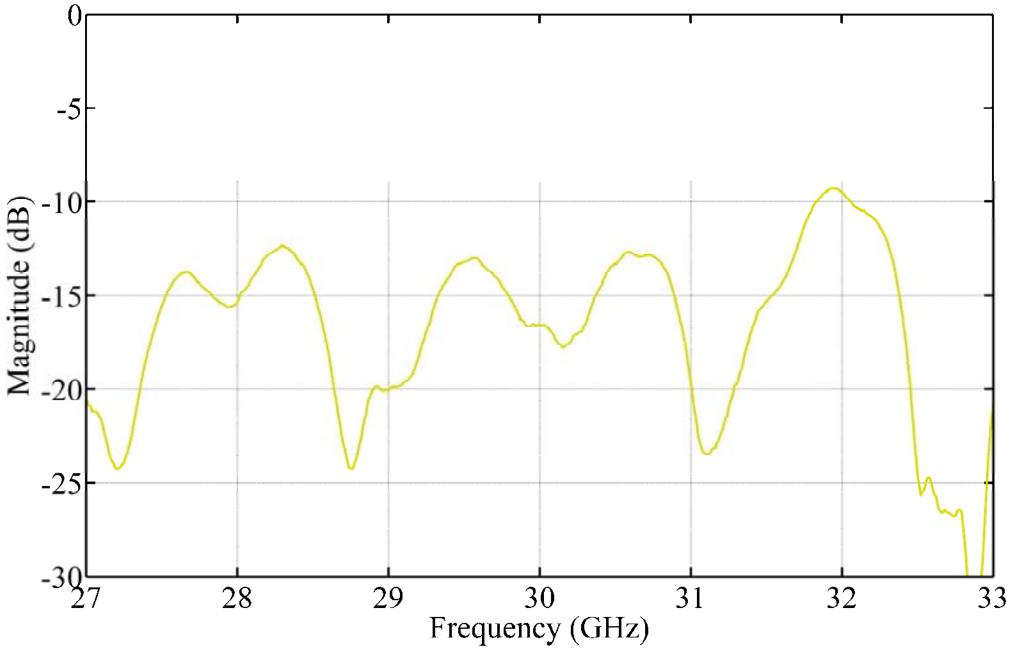

Figure 6.8-7: Measured reflection coefficient of the polarisation-insensitive 3-layer 90° PSS PC-FZPA.

insensitive (square elements) PSS 90° PC-FZPAs, and tends to reduce the bandwidth [SIEV08]. Therefore, there seems to be a tradeoff between enhanced polarisation flexibility and bandwidth. The fact that the gain values are similar is unexpected since the polarisation-insensitive cases are not as optimised as polarisation-sensitive cases. It could be that the marginal suboptimal dataset (see Table 6.8-1) is compensated by the reduced sensitivity of the polarisation-insensitive cases to oblique incidence angles compared to the polarisation-sensitive cases, as discussed in Section 3.7.3.

6.9.2 3-layer polarisation-sensitive PSS PC-FZPAs comparison

Considering the polarisation-sensitive (strip elements) PSS PC-FZPAs, a comparison is performed between the three polarisation-sensitive 3-layer PSS PC-FZPAs

Table 6.9-1: Summary results for lens antennas

Description	**Dielectric plano-hyperbolic lens antenna**	**Dielectric phase-correcting Fresnel zone plane antenna**	**Fresnel zone plate antenna**	**Phase-shifting surface phase-correcting Fresnel zone plane antenna**				
Acronym	DPHLA	PC-FZPA	FZPA	PSS PC-FZPA				
Diameter – D (mm)	152.4							
F / D ratio	0.5							
Fabrication technique	Machining		Single layer etching	Multilayer etching				
Dielectric material	Plexiglas	Lavarock	FR4	Rogers RT/duroid® 5880				
Relative permittivity – ε_r	2.56	5.8	4.2 (Substrate)	2.2 (Substrate)				
Number of layers	N/A		1	3				4
Total thickness (mm)	41.876	8.0	0.127	1.05	1.06	1.05	1.07	1.57
Weight (g)	435.3	250.9	5.5	44.9	45.2	45.5	45.6	67.7
Unit cell type	N/A			Square	Strip			
Phase correction	Continuous	90°	None; amplitude correction only	90°		45°	Quasi-continuous	Continuous
Maximum gain (dBi)	-*	29.6 @ 31.8 GHz	24.0 @ 29.8 GHz	30.0 @ 29.9 GHz†	29.9 @ 29.8 GHz	30.5 @ 30.8 GHz	30.4 @ 30.4 GHz	30.3 @ 32 GHz
Gain @ 30 GHz (dBi)	30.1	28.9	23.7	29.9†	29.8	29.7	29.9	29.3
Maximum cross-polarisation level @ maximum gain (dBi)	-	8.8	–8.4	–5.3†	–7.2	–6.1	–12.7	–1.5
Maximum cross-polarisation level @ 30 GHz (dBi)	0.27	6.6	–13.9	–8.0†	–8.9	–7.2	–12.9	–1.8
1 dB Gain bandwidth (GHz)	-*	3.1	3.6	1.8	2.2	1.6	2.5	2.3
1 dB Gain bandwidth (%)	-*	9.7	12.1	5.9	7.4	5.2	8.2	7.2
Photograph	6.3-1	6.3-2	6.3-4	6.8-1	6.6-2(a)	6.6-2(b)	6.6-2(c)	6.7-1
Section	6.3	6.3	6.3	6.8	6.6	6.6	6.6	6.7
Trace color								
Figures references (for trace color)	6.3-6 6.3-7 6.3-8	6.3-6 6.3-7 6.3-8	6.3-6 6.3-7 6.3-8	6.8-7 6.9-3	6.6-3 6.6-4 6.6-5	6.6-3 6.6-4 6.6-5	6.6-3 6.6-7 6.6-4 6.9-1 6.6-5 6.9-2	6.7-2 6.7-4 6.7-3 6.9-1

*Theoretically, the hyperbolic lens has no bandwidth limitation. The gain increases with frequency, as is clear from Figure 6.3-7, since the electrical size increases.

†Results for the square element phase-correcting phase-shifting surface lens antenna are those for the case of a 0° roll angle ($\tau = 0°$).

presented in Section 6.6. The first noticeable aspect is that, when the phase correction is improved or the phase correction step is decreased (which would result in increasing P for a dielectric PC-FZPA), there is a slight trend towards increasing the gain, reaching a maximum of 29.9 dBi at 30 GHz for the PSS quasi-continuous PC-FZPA. It is worth mentioning that this value is only slightly less than that of the DPHLA of 30.1 dBi. The PSS 45° PC-FZPA and the PSS quasi-continuous PC-FZPA have maximum gain values of respectively 30.5 dBi and 30.4 dBi, whereas the maximum gain of the PSS 90° PC-FZPA is 29.9 dBi, so roughly 0.5 dB less. This therefore confirms the gain improvement that can be obtained by reducing the size of the phase-correcting step.

Furthermore, for some frequencies between 29 GHz and 31 GHz, the gain of the PSS 45° PC-FZPA and the PSS quasi-continuous PC-FZPA is higher than the gain of the DPHLA, in which cases the aperture efficiency is higher than 45%. The cross-polarisation levels are also significantly lower for the PSS PC-FZPAs than the DPHLA, with an improvement of 7.5 dB or higher at 30 GHz.

The 1 dB gain bandwidth also increases with a reduction of the phase-correction step size, reaching a value of 8.2% for the PSS quasi-continuous PC-FZPA compared to 7.4% for the PSS 90° PC-FZPA. The PSS 45° PC-FZPA shows a significant gain bandwidth reduction compared to the other two cases, which is attributed to the fact that its maximum gain at 30.5 GHz is significantly higher than all the other points for this particular configuration. Nevertheless, Figure 6.6-5 clearly shows a bandwidth enhancement as the phase correction step is decreased. The maximum 1-dB gain bandwidth for PSS PC-FZPAs is thus obtained for the PSS quasi-continuous PC-FZPA, for which an 8.2% value is reported. This is beyond the requirements for many applications at Ka band, as well as other bands.

Finally, it is worth mentioning that reducing the phase correcting step in PSS PC-FZPAs does not lead to any major drawbacks, as is the case for PC-FZPAs where such a reduction leads to an increased thickness, weight and volume, as well as an increased manufacturing complexity. For the PSS PC-FZPAs, changing the phase correcting step simply results in a modified etching pattern without affecting the fabrication process. The design is not more complicated, even though the required database necessitates more simulated cases.

6.9.3 3-layer vs 4-layer polarisation-sensitive PSS PC-FZPAs

Since it has been established that the smallest phase correcting step leads to the best results, it is next worth comparing two similar PSS PC-FZPAs that have a different number of layers. The polarisation-sensitive 3-layer PSS quasi-continuous PC-FZPA is therefore compared to the polarisation-sensitive 4-layer PSS continuous PC-FZPA. Recall from Section 3.4.3 that a 3-layer PSS continuous PC-FZPA is not possible because of the phase shift range of the symmetrical three independent layer PSS; this is one of the reason why a 4-layer PSS first discussed in Section 3.4.4 is considered.

Figure 6.9-1 presents the measured boresight gain over frequency for the polarisation-sensitive 3-layer PSS quasi-continuous PC-FZPA and the polarisation-sensitive 4-layer PSS continuous PC-FZPA. These results are directly taken from Figures 6.6-5 and 6.7-4 but superimposed here for better comparison.

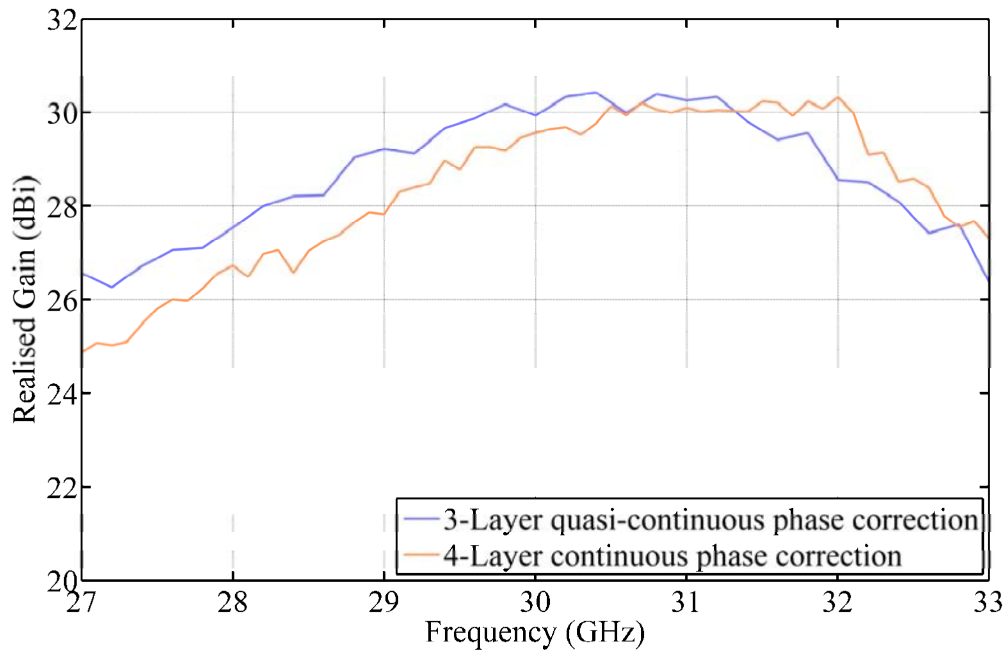

Figure 6.9-1: Measured boresight gain of the polarisation-sensitive 3-layer PSS quasi-continuous PC-FZPA and the polarisation-sensitive 4-layer PSS continuous PC-FZPA.

Surprisingly, although the phase correction covers a wider range in the polarisation-sensitive 4-layer PSS continuous PC-FZPA case, this translates into a marginal maximum gain drop, as shown in Figure 6.9-1. The gain drop could be attributed to a number of factors:

- The additional layer causes increased losses (dissipation and ohmic) even though it is known that the dielectric material has a fairly low loss tangent and that copper, which has a high conductivity, is used as the conductor.
- Although this has not been studied, the 4-layer PSS implementation could be more sensitive to the angle of incidence.
- By comparing Figure 6.7-1 with Figure 6.6-2(c), the 4-layer PSS continuous PC-FZPA metallisation pattern is not as smooth as that of the 3-layer PSS quasi-

continuous PC-FZPA. In fact, the metallisation pattern is characterised by a larger number of abrupt transitions between low metal concentration and high metal concentration. It is believed that the electromagnetic model, which assumes an infinite periodic structure, cannot realistically be applied in these regions, leading to erroneous results. More will be said in Section 6.9.4 on this topic, with near-field measurement results presented as support.

More noticeable is the 1 dB gain bandwidth reduction, which drops from 8.2% for the 3-layer PSS quasi-continuous PC-FZPA case down to 7.2% for the 4-layer PSS continuous PC-FZPA case. This bandwidth reduction could easily be attributed to the increasing number of layers resulting in a reduced transition band, as remarked in Section 3.7.1. It can therefore be assumed that the number of layers should be kept as small as possible since the 3-layer PSS quasi-continuous PC-FZPA, despite a slightly poorer phase-correction implementation, provides increased electromagnetic performance compared to a 4-layer PSS continuous PC-FZPA.

6.9.4 Near-field measurement analysis

In order to further investigate the behaviour of the PSS PC-FZPAs, near-field measurements were conducted on two of them, namely the polarisation-sensitive 3-layer PSS quasi-continuous PC-FZPA and the polarisation-insensitive 3-layer PSS 90° PC-FZPA. The results were presented in Figures 6.6-5 and 6.8-5. From these figures, it is noticed that the phase is fairly constant over the aperture, which is desired in order to maximise the gain. However, over the aperture region the amplitude does not monotonically roll off as it would be expected; more specifically, the amplitude is characterised by ripples. The location of these ripples is of interest and, for that reason, the near-field intensity was overlaid with the phase correction profiles along the two principal axes in Figures 6.9-2 and 6.9-3. The horizontal axes in these figures cover the region of the physical aperture only. For both cases, the maxima in the ripples correspond to the normal field roll off caused by the lens feed antenna. It is seen that when the phase correction is near 0° (bare sample) or of large value (generally close to –270°), the minima in the ripples occur. This is attributed to a combination of two factors:

- The cases producing large phase shift, namely close to –270°, are more sensitive to the angle of incidence, as shown in Figure 3.7-3 and 3.7-5, particularly for the amplitude.
- The transition when the phase shift changes from 0° to large values (generally close to –270°) is physically realised by an abrupt transition between a bare (unclad) region and a region with high metal concentration, where it is believed that the electromagnetic model, which assumes an infinite periodic structure, cannot realistically be applied.

The presence of these ripples is expected to contribute in degrading the performance of the PSS PC-FZPAs, but experimental measurements confirm that the performance of these PSS PC-FZPAs is nevertheless good. Potential improvements could be realised by taking into account the angle of incidence rather than using normal plane wave incidence results over the entire aperture of the PSS PC-FZPAs, but this would require the generation of an enormous amount of data. Another possible improvement

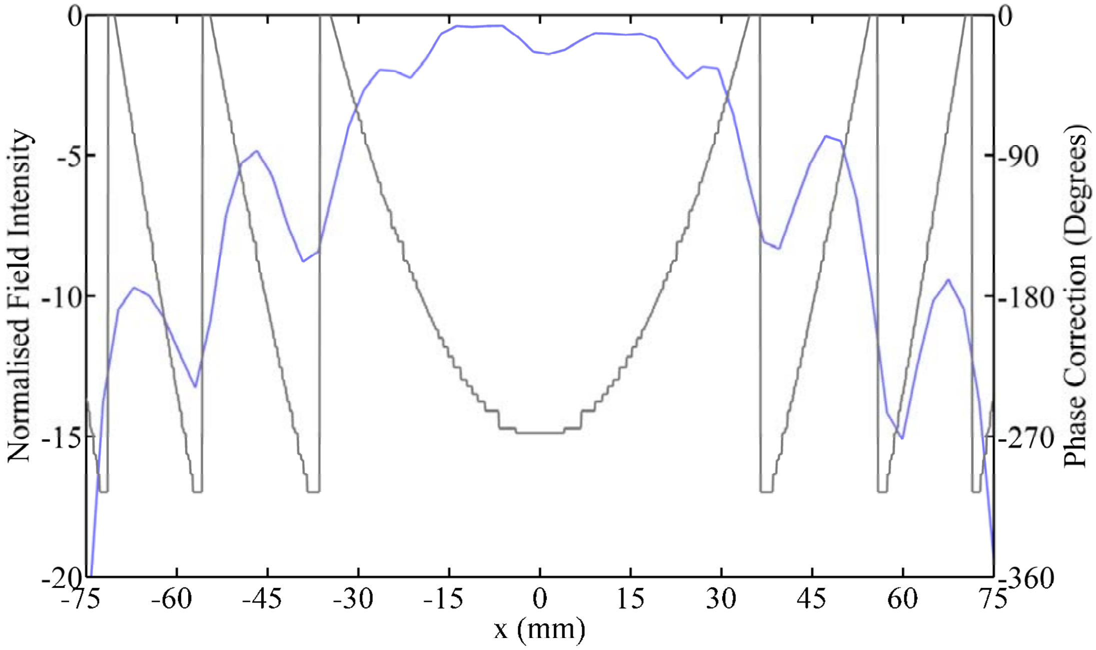

(a)

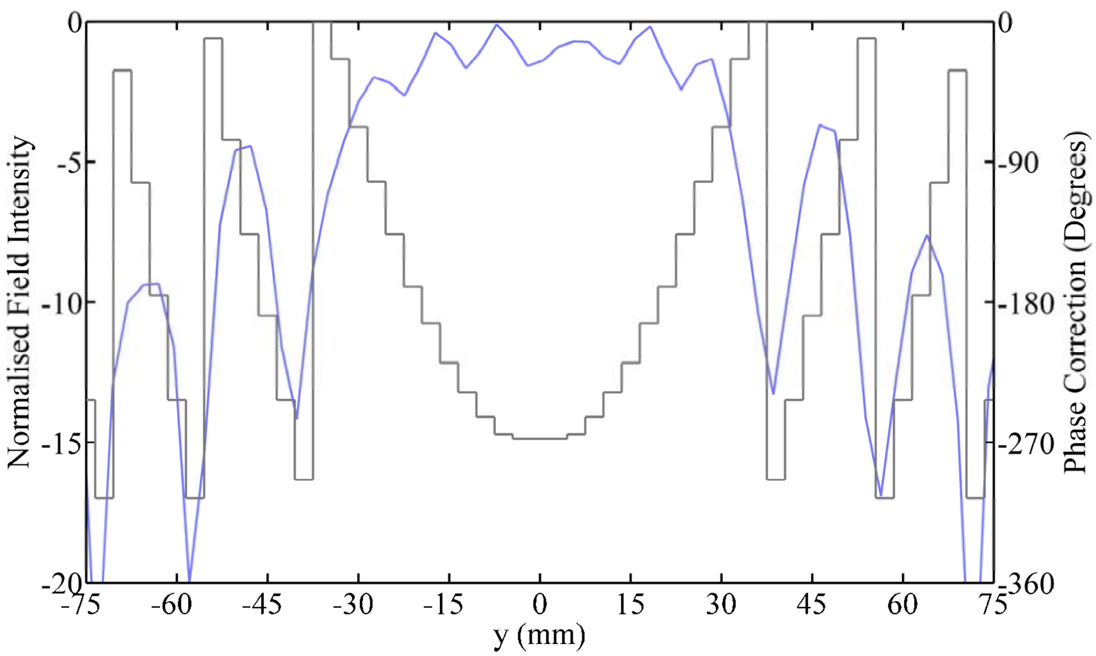

(b)

Figure 6.9-2: Measured near-field intensity at the surface of the aperture and phase correction for the polarisation- sensitive 3-layer quasi-continuous PSS PC-FZPA at 30 GHz; (a) y = 0 mm, (b) x = 0 mm; — Field intensity, — Phase correction.

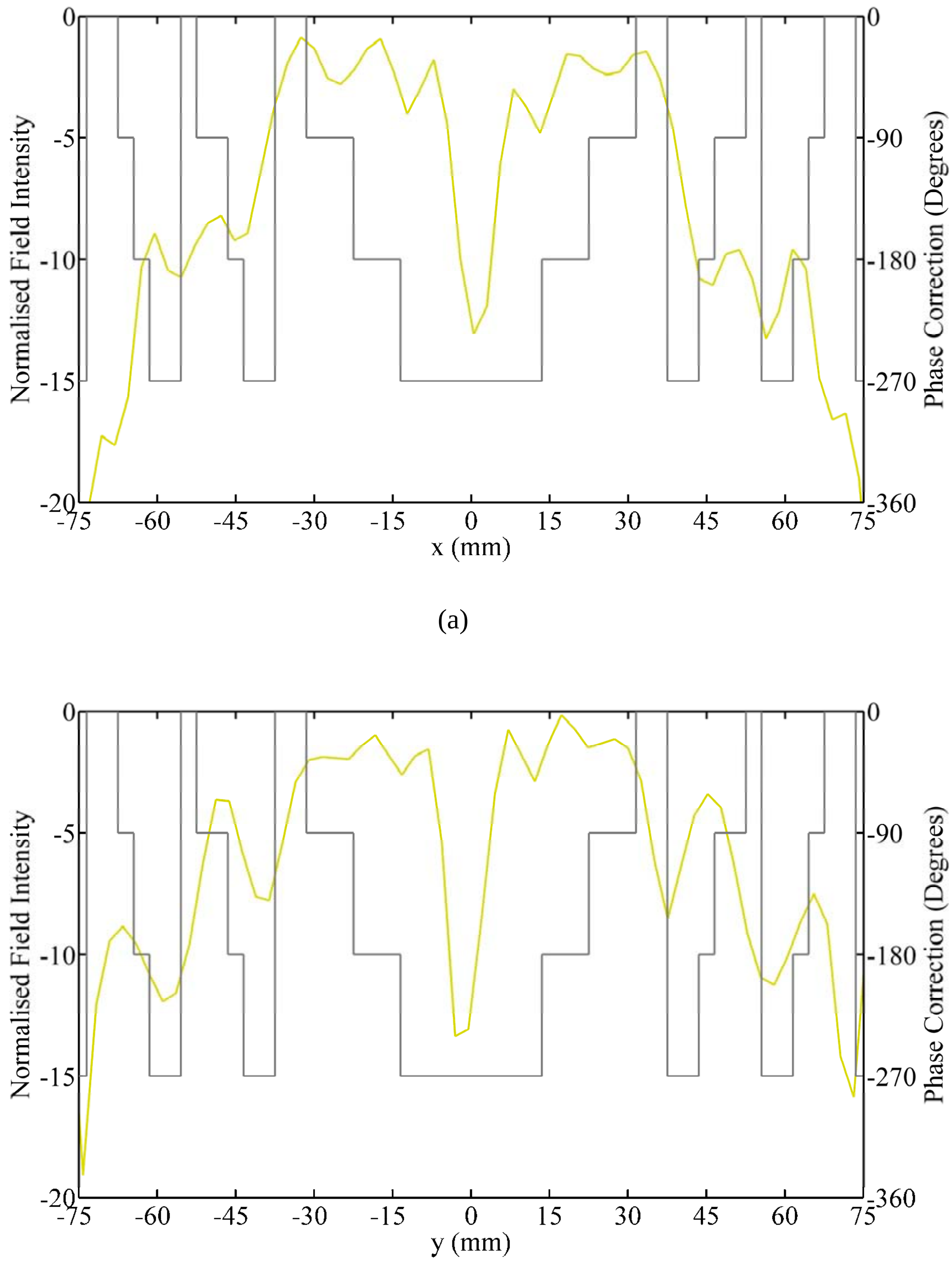

(a)

(b)

Figure 6.9-3: Measured near-field intensity at the surface of the aperture and phase correction for the polarisation-insensitive 3-layer 90° PSS PC-FZPA at 30 GHz; (a) *y* = 0 mm, (b) *x* = 0 mm; — Field intensity, — Phase correction.

could be realised if PSS PC-FZPAs with larger phase shift range – typically greater than 360° – could be achieved. However, it is not certain how this could be achieved at this stage.

6.9.5 PSS PC-FZPA vs conventional lens antennas

In this section, the 3-layer PSS quasi-continuous PC-FZPA is compared to the conventional lens antenna technologies presented in Section 6.3. The measured results given there confirm that the DPHLA offers the best performance (except for cross-polarisation, in which case the PSS PC-FZPAs are superior) with virtually no bandwidth limitation and the highest gain at 30 GHz, even though this gain is only marginally better than that of the PSS PC-FZPAs, including the 3-layer PSS quasi-continuous PC-FZPA. However the DPHLA is expensive and time-consuming to fabricate by machining and it suffers from large thickness and heavy weight. In fact, the 3-layer PSS quasi-continuous PC-FZPA is about ten times lighter, 40 times thinner and has significantly better cross-polarisation performance compared to the DPHLA.

The dielectric PC-FZPA – for which it is important to mention once more that it is not a PSS-based structure – offers acceptable thickness reduction and is almost half the weight of the DPHLA; however its gain is reduced by roughly 1 dB at 30 GHz and the cross-polarisation is significantly increased. Furthermore, sharp grooves, which are required in the different zones, are more difficult to machine than a smooth hyperbolic surface. When comparing the dielectric PC-FZPA to the 3-layer PSS quasi-continuous PC-FZPA, the only advantage of the dielectric PC-FZPA is its 1 dB gain bandwidth, which is 9.7% instead of 8.2%, all other criteria being significantly worse, including a gain reduction of almost 1 dB, a weight of about five times heavier and a thickness superior by about eight times.

The FZPA – which is also not a PSS-based structure – is the thinnest and the lightest of all the reported technologies. In fact, it is about eight times thinner than the 3-layer PSS quasi-continuous PC-FZPA and eight times lighter. On the other hand, despite its good cross-polarisation performance and larger bandwidth, it suffers from a significant gain degradation: its gain is about 6 dB less than the gain of the 3-layer PSS quasi-continuous PC-FZPA proposed in this thesis.

The far-field performance of the PSS PC-FZPAs is even more impressive when considering the practical aspects of its design. Even though the DPHLA offers virtually unlimited gain bandwidth, it is expensive and time-consuming to fabricate, especially when machined. Additionally, it suffers from large thickness and heavy weight. On the other hand, any PSS PC-FZPAs design can easily be mass-produced at low cost using a conventional photolithographic (wet chemical) etching process. Furthermore, its physical parameters make it a very attractive alternative. Despite its smaller bandwidth, having a maximum value of 8.2% for the 3-layer PSS quasi-continuous PC-FZPA, PSS PC-FZPAs are viable alternatives and serious potential candidates for many applications.

6.10 Conclusions

The far-field performance of five different PC-FZPAs based on the PSS concept developed in this thesis was reported in this chapter. These PSS PC-FZPAs were compared to conventional lens antenna technologies. It is found that PSS PC-FZPAs offer impressive far-field performance compared to other lens antenna technologies. This performance is even more impressive when considering the practical aspects of their design. In fact, PSS PC-FZPAs have thicknesses in the range of 0.1-0.15λ in addition to being flat, light and easily fabricated using a low-cost conventional photolithographic (wet chemical) etching process. In particular, the 3-layer PSS quasi-continuous PC-FZPA offers equal or better performance compared to the DPHLA over a 1.5 GHz bandwidth at Ka band. Clearly, PSS PC-FZPAs are a viable alternative for many applications, such as terrestrial wireless point-to-point communications and low-cost ground terminal antennas for satellite communications.

Finally, the work presented in this chapter has been previously reported in antennas and propagation conferences ([GAGN09], [GAGN10c], [GAGN10d]) as well as in a peer-reviewed periodical ([GAGN10a]).

CHAPTER 7 PASS Flat-Topped Beam Antenna

7.1 Introduction

Chapters 4, 5 and 6 showed that the concept of the phase shifting surface (PSS) can be applied successfully to free-standing phase correcting devices like lenses. As mentioned in Chapter 3, this concept implies that only the phase is corrected, and maximum transmission amplitude is usually desired to maximise the aperture efficiency of the device. However, some applications like beam shaping require that both a phase-shifting and amplitude-shifting mechanism be implemented at the surface of the device. This chapter presents an application of the phase and amplitude shifting surface (PASS) to design a lens antenna with a flat-topped beam.

7.2 Local Electric Field Determination from PASS Data

The first step in the process of generating a desired antenna beam pattern is to determine the required local electric field distribution on the output surface for a given far-field radiation pattern. In this particular example, the far-field radiation pattern is that of a flat-topped beam antenna, in which the main beam is made maximally flat from –20° to +20° and the side lobes are minimized. The antenna is made to operate at 30 GHz. There exist different synthesis methods for obtaining the far-field radiation patterns from the local electric field distribution and vice versa. The method used here is the one reported in [ELLI88] to provide a flat-topped beam pattern as described above, which is based on a scalar pattern prediction model. A continuous circular aperture distribution of diameter equal to 152.4 mm is used in this case. The desired rotationally symmetric amplitude and phase distributions are shown as the blue curves in Figure 7.2-1. The strip unit cell with four fully-independent layers, presented in Section 3.4.4, is used to implement the flat-topped beam antenna.

In order to realise the phase and amplitude distribution, the aperture of the PASS is divided into $N_x \times N_y$ rectangular cells of dimensions $\Delta x \times \Delta y$, as shown in Figure 6.5-1. However, the contribution of the feed horn to the amplitude and phase of the electric field at the output of the PASS also has to be taken into account, which can be done as follows:

$$E_{out}(x,y) = T_{PASS}(x,y) \cdot E_{in}(x,y) \tag{7.2-1}$$

where E_{in} is the incoming electric field at the input surface of the PASS, T_{PASS} is the complex transmission coefficient through the PASS and E_{out} is the outgoing electric field at the output surface of the PASS. E_{in} thus depends on the feed antenna, and E_{out} is the desired field at the output of the PASS for a prescribed far-field radiation pattern. The PASS must then implement a transformation between E_{in} and E_{out}. All variables in (7.2-1) have an x and y dependency since they are non-uniform and consequently different at every location on the surface of the PASS located in the xy-plane. In fact, the structure is discretised the same way as the PSS lensing devices in Section 6.5, and so (7.2-1) can be rewritten as

$$E_{out}^{m}(x_m, y_m) = T_{PASS}^{m}(x_m, y_m) \cdot E_{in}^{m}(x_m, y_m) \tag{7.2-2}$$

To find the contribution of the PASS at every discretised location (x_m, y_m), (7.2-2) must be reorganised as follows:

$$T_{PASS}^{m}(x_m, y_m) = \frac{E_{out}^{m}(x_m, y_m)}{E_{in}^{m}(x_m, y_m)} \tag{7.2-3}$$

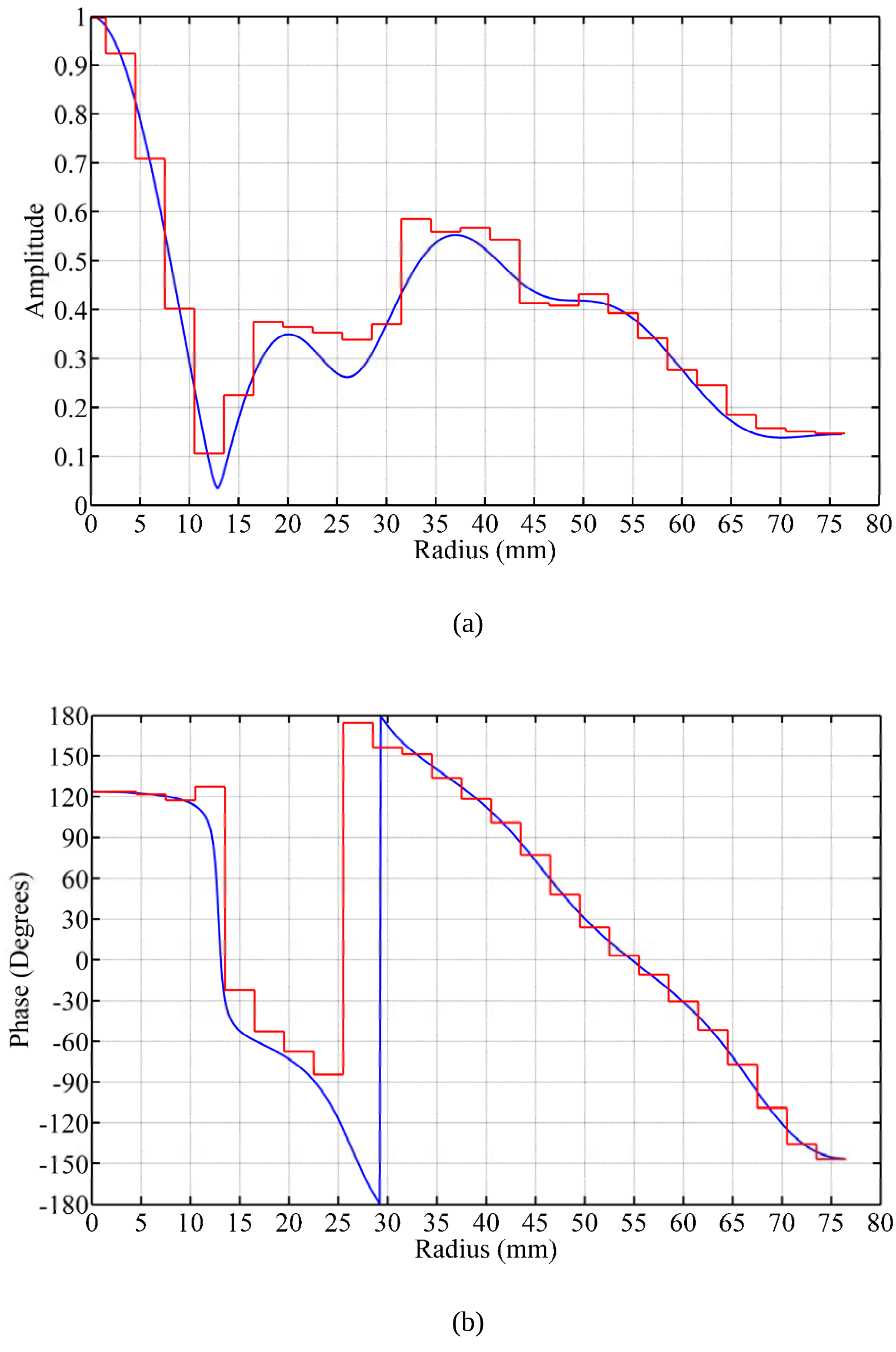

Figure 7.2-1: Electric field distribution at the PASS for a 40° beamwidth flat-topped beam antenna at 30 GHz; (a) amplitude, (b) phase; —— Ideal (using [ELLI88]), —— Calculated (from the dataset results of Figure 3.4-10, with step size of 3mm).

which consists of dividing the amplitudes of the electric fields and subtracting the phases. In other words, the incoming electric field from the horn must be divided (in the complex domain) from the desired outgoing electric field in order to obtain the contribution from the PASS. At the plane where the PASS is to be located, the local electric field from the horn is known from full-wave electromagnetic simulations conducted with [HFSS07].

The synthesised complex transmission coefficient $T_{PASS}{}^{m}(x_m, y_m)$ is sampled at the centre of the given cell, located at (x_m, y_m). In other words, the PASS structure is used to provide the amplitude and phase values for each cell with index m. It is assumed that the amplitude and phase values are constant over the entire area of the cell, given by $\Delta x \times \Delta y$, as shown in Figure 6.5-1. The resulting PASS is thus a quantised version of the original continuous case. Moreover, the different cases to be implemented at the PASS are selected from the dataset of results for the strip unit cell with four fully-independent layers, which is shown in Figure 3.4-10. Figure 7.2-2 shows the database of results as in Figure 3.4-10, in which a curve of T_{PASS} varying with the radius was overlaid. In this case, however, the radius information is lost, but the benefit is that it allows for visualising if there are enough points in the database to allow for a reasonable realisation of the ideal case by the implemented complex transmission coefficients. Since the desired phase is a relative value, the desired phase includes a variable reference phase value that allows for moving the curve (from left to right) in Figure 7.2-2. The curve of desired values can then be adjusted to match the simulated cases as much as possible; this was done in Figure 7.2-2. It is to be noted that it is more crucial to match the values with higher amplitude.

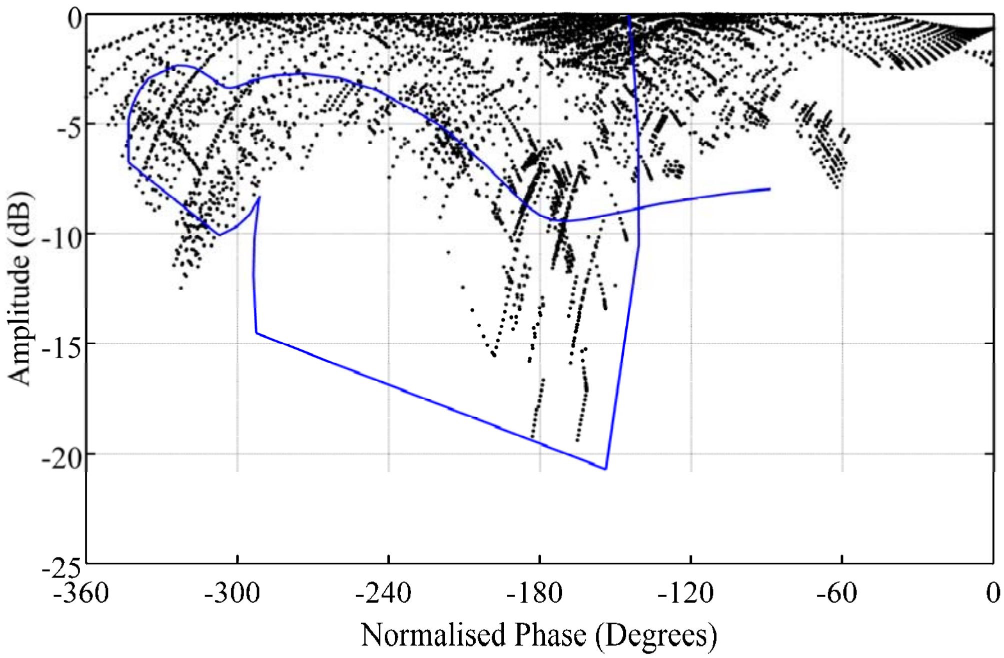

(a)

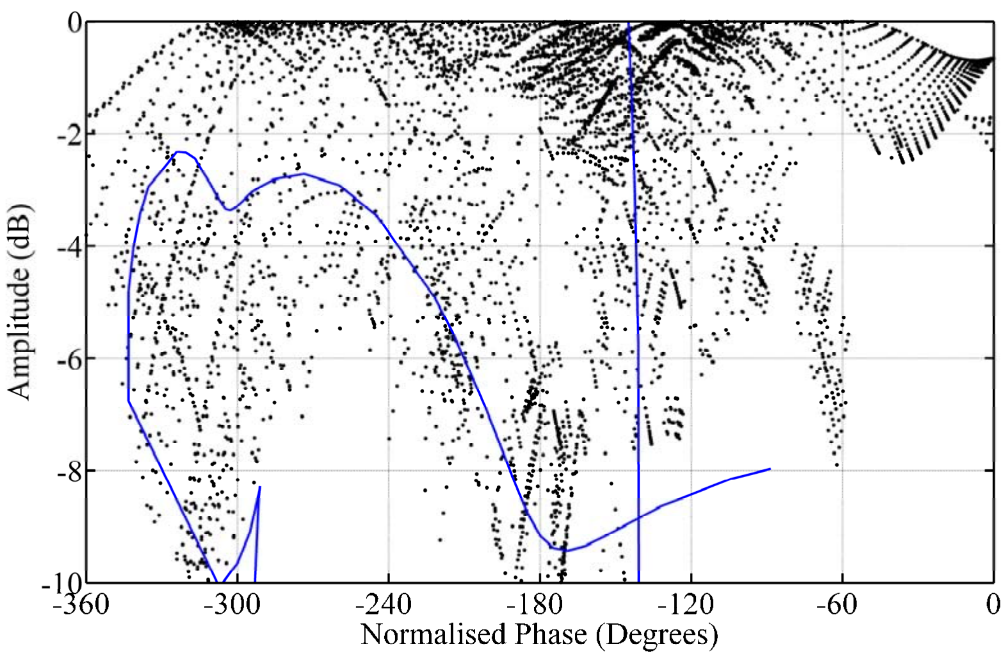

(b)

Figure 7.2-2: Transmission results for the four fully-independent layers dataset at 30 GHz (see Figure 3.4-10); (a) Amplitude span of 25 dB, (b) Amplitude span of 10 dB; • Simulated cases, —— Desired values for ideal implementation.

Figure 7.2-2(a) presents an amplitude span of 25 dB in order to allow for displaying the complete curve of T_{PASS}; Figure 7.2-2(b) repeats the plot with the same amplitude span as in Figure 3.4-10, for which the curve of T_{PASS} is not fully displayed due to an amplitude span limited to 10 dB. The curve begins at the point of 0 dB amplitude, for which the radius is zero. The curve exhibits a quick variation at the low amplitude values, which correspond to a radius ranging from about 10 mm to 15 mm for which the phase changes rapidly: Figure 7.2-1 gives an insight of this rapid phase variation.

In Figure 7.2-2, not all cases of desired values coincide perfectly with a simulated case of transmission coefficient. To minimise the error, the following error function is defined:

$$\zeta \equiv \sum_m \zeta_m \left| T_{PASS}^{desired}\left(x_m, y_m\right) \right| \tag{7.2-4}$$

where

$$\zeta_m \equiv \left[\mathrm{Re}\left(T_{PASS}^{simulated}\left(x_m, y_m\right)\right) - \mathrm{Re}\left(T_{PASS}^{desired}\left(x_m, y_m\right)\right)\right]^2$$
$$+ \left[\mathrm{Im}\left(T_{PASS}^{simulated}\left(x_m, y_m\right)\right) - \mathrm{Im}\left(T_{PASS}^{desired}\left(x_m, y_m\right)\right)\right]^2 \tag{7.2-5}$$

The function ζ is minimised by adjusting the reference phase of the desired curve.

The red curves in Figure 7.2-1 show the calculated electric field distribution (with a step size of 3 mm) obtained from the best match of the simulation data and best reference amplitude and phase, i.e. by minimising the errors using (7.2-4) and (7.2-5). Since the unit cell height s = 3 mm or Δy = 3 mm, the red curves in Figure 7.2-1 are fairly realistic along the discretised direction (y-axis or vertical); however the discretisation along the x-axis is made as small as possible to mimic a continuously varying unit cell. In this case, Δx is chosen to be 0.2 mm. The curves for this value are presented in Figure 7.2-3. It is seen, in both Figures 7.2-1 and 7.2-3, that the calculated curves do not perfectly match the ideal curves. This is of course going to affect the actual radiation pattern, as discussed next.

7.3 Far-Field Patterns from Local Electric Field Distribution

By knowing the electric field distribution at the output surface of the aperture of the PASS structure, denoted E_{out} in Section 7.2, the expected scalar field pattern $F(\theta,\phi)$ of the flat-topped beam antenna can be calculated. In the computation of $F(\theta,\phi)$, the contribution of each unit cell composing the output surface of the aperture is considered using elementary array theory [STUT98], resulting in a quantised distribution that is mathematically expressed as

$$F(\theta,\phi) = F_e(\theta,\phi) \sum_m \alpha_m \, e^{j\psi_m} \, e^{jk_o x_m \sin\theta\cos\phi} \, e^{jk_o y_m \sin\theta\sin\phi} \tag{7.3-1}$$

where α_m is the amplitude and ψ_m is the phase, which correspond to E_{out}. Equation (7.3-1) is a scalar equation that does not account for polarisation. In calculating the field pattern with (7.3-1), one can consider the aperture of the PASS as a planar array composed of elements corresponding to rectangular cells with uniform phase and amplitude over each cell. The radiation pattern of such a single element is given by

$$F_e(\theta,\phi) = \frac{\sin\left(\dfrac{k_0\Delta_x}{2}\sin\theta\cos\phi\right)}{\dfrac{k_0\Delta_x}{2}\sin\theta\cos\phi} \frac{\sin\left(\dfrac{k_0\Delta_y}{2}\sin\theta\sin\phi\right)}{\dfrac{k_0\Delta_y}{2}\sin\theta\sin\phi} \tag{7.3-2}$$

The directivity is given by the following equation [STUT98]:

$$D(\theta,\phi) = \frac{4\pi\left|F(\theta,\phi)\right|^2}{\iint\left|F(\theta,\phi)\right|^2 d\Omega} = \frac{4\pi\left|F(\theta,\phi)\right|^2}{\int_0^{2\pi}\int_0^{\pi}\left|F(\theta,\phi)\right|^2 \sin\theta d\theta d\phi} \tag{7.3-3}$$

The directivity defined in (7.3-3) uses the scalar field pattern.

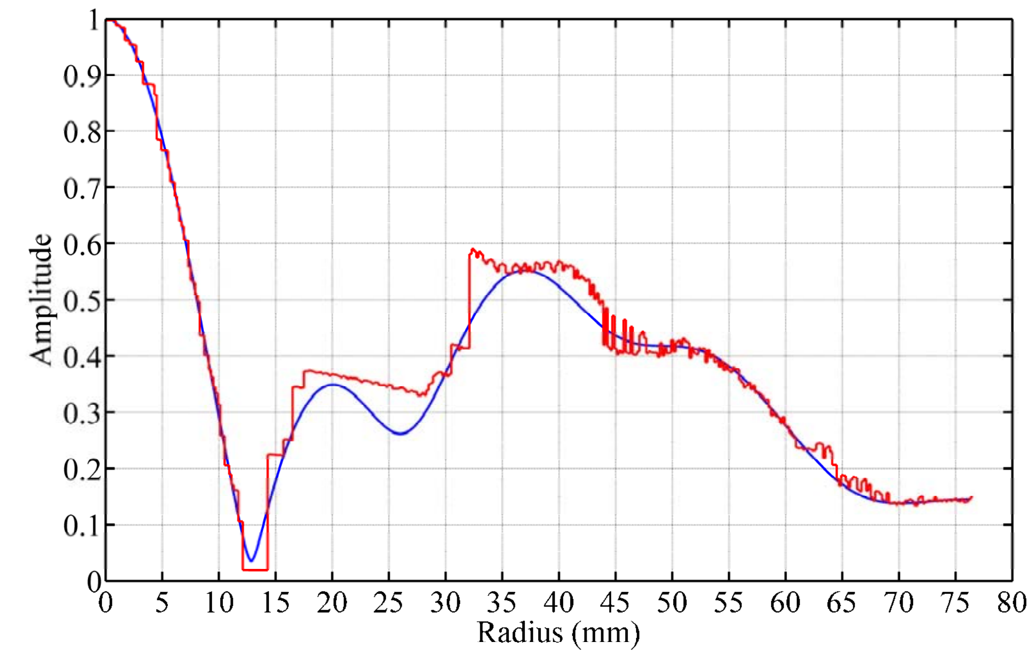

(a)

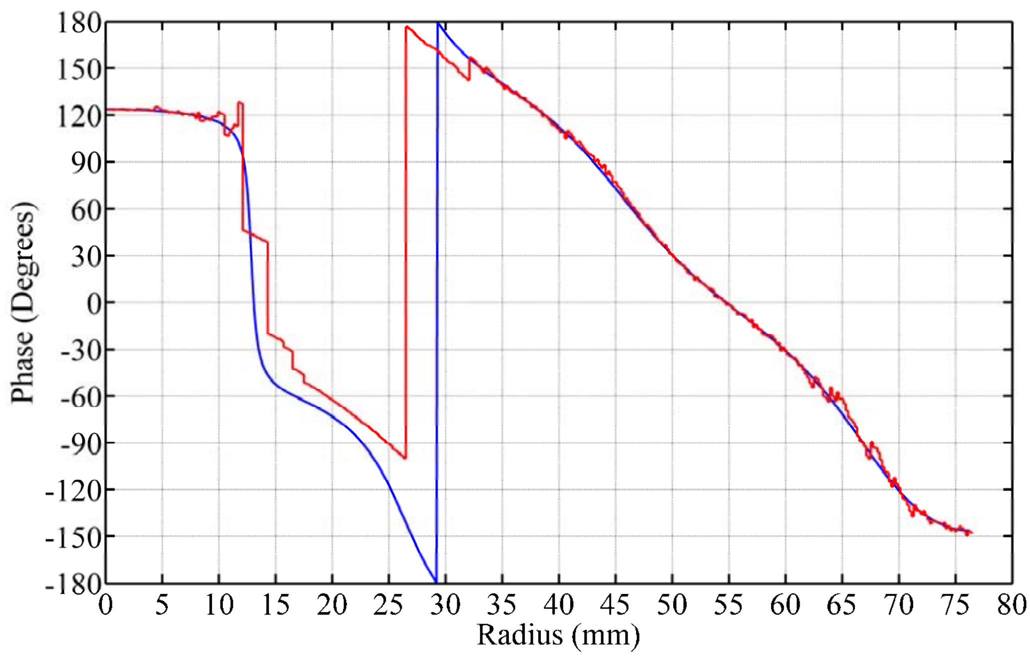

(b)

Figure 7.2-3: Electric field distribution at the PASS for a 40° beamwidth flat-topped beam antenna at 30 GHz; (a) amplitude, (b) phase; —— Ideal (using [ELLI88]), —— Calculated (from the dataset results of Figure 3.4-10, with step size of 0.2 mm).

Figure 7.3-1 shows the ideal and calculated radiation patterns, which were determined using (7.3-1) to (7.3-3). The calculated radiation patterns show higher ripples in the main beam and higher side lobes than the ideal case. This results from the difference in the ideal and calculated transmission coefficients at the aperture of the PASS, as shown in Figures 7.2-1 and 7.2-3. Nevertheless, the ripples remain fairly small and the sidelobes are fairly low for the calculated cases.

7.4 Design and Measurement of the Phase and Amplitude Shifting Surface for Flat-Topped Beam Radiation Pattern

The dataset in Section 3.4.4, more particularly the cases shown in Figure 3.4-10, were used to generate the PASS shown in Figure 7.4-1. Equations (7.2-4) and (7.2-5) were used to select the appropriate cases from the dataset in Figure 7.2-2 to produce the aperture distribution in Figure 7.2-1 and Figure 7.2-3, and the radiation patterns of Figure 7.3-1.

The antenna used to feed the PASS aperture is a feed horn with 14.4 dBi of gain, the same as the one used for the cylindrical PC-FZPAs described in Section 5.5. The separation between the feed horn and PASS is 132 mm.

The far-field radiation patterns of the flat-topped beam antenna were directly measured in an anechoic chamber. The results are presented in Figure 7.4-2. The near-fields were measured at a distance of 12 cm using a planar near-field scanner. Figure 7.4-3 shows the surface plots of the local fields back-projected to the aperture surface of the flat-topped beam antenna. Figures 7.4-4 and 7.4-5 present cuts along the *x*- and *y*-axis, respectively. The ideal and calculated results are presented in Figures 7.4-4 and 7.4-5 for

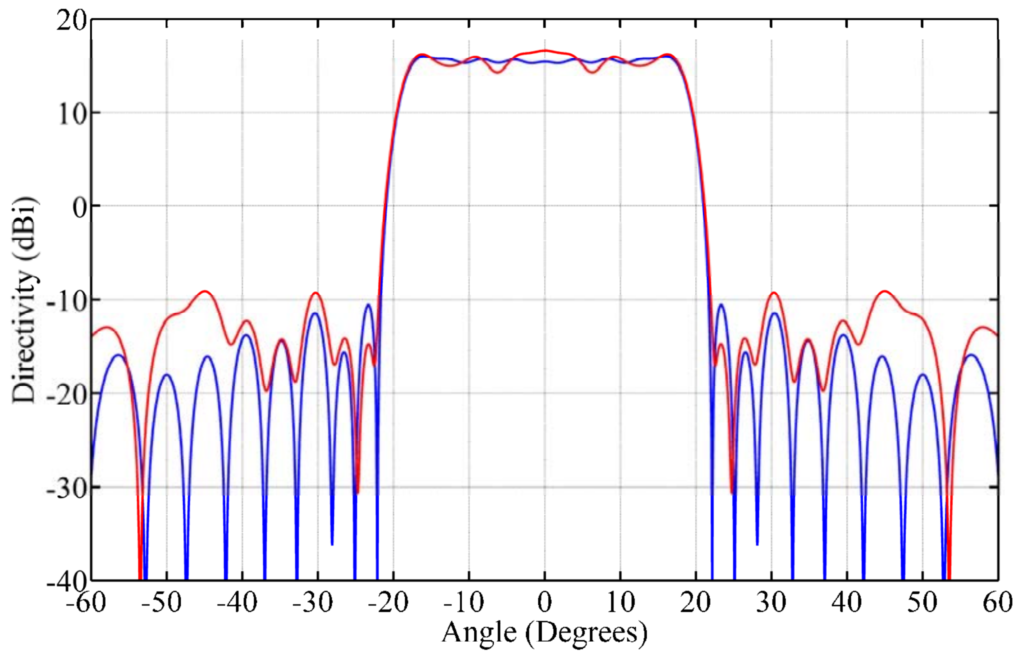

(a)

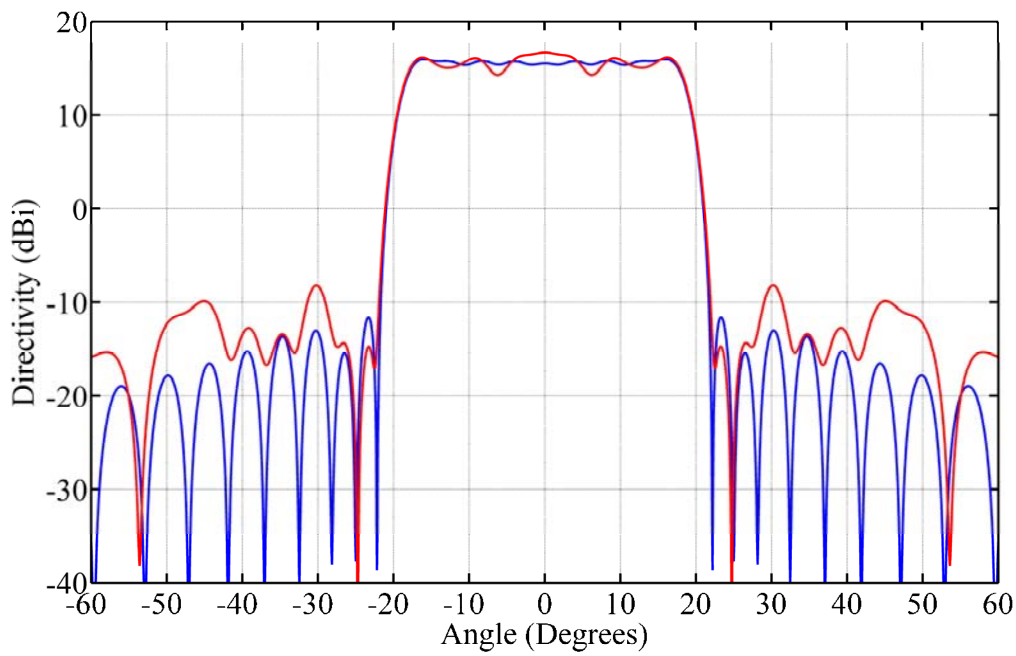

(b)

Figure 7.3-1: Far-field radiation patterns of the PASS flat-topped beam at 30 GHz; (a) *H*-plane, (b) *E*-plane; —— Ideal, —— Calculated.

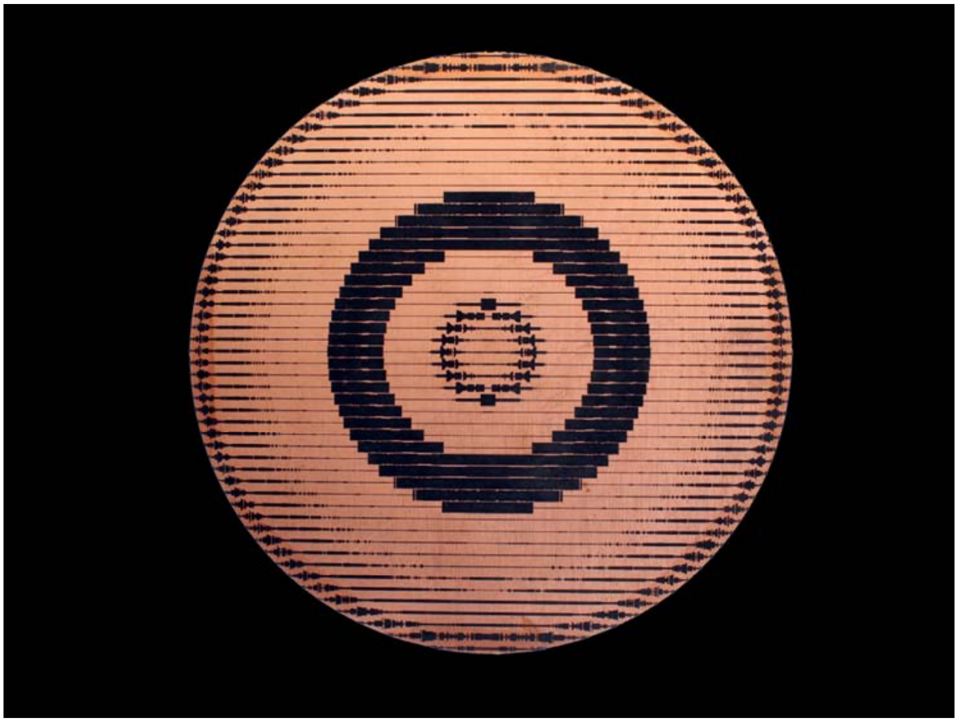

(a)

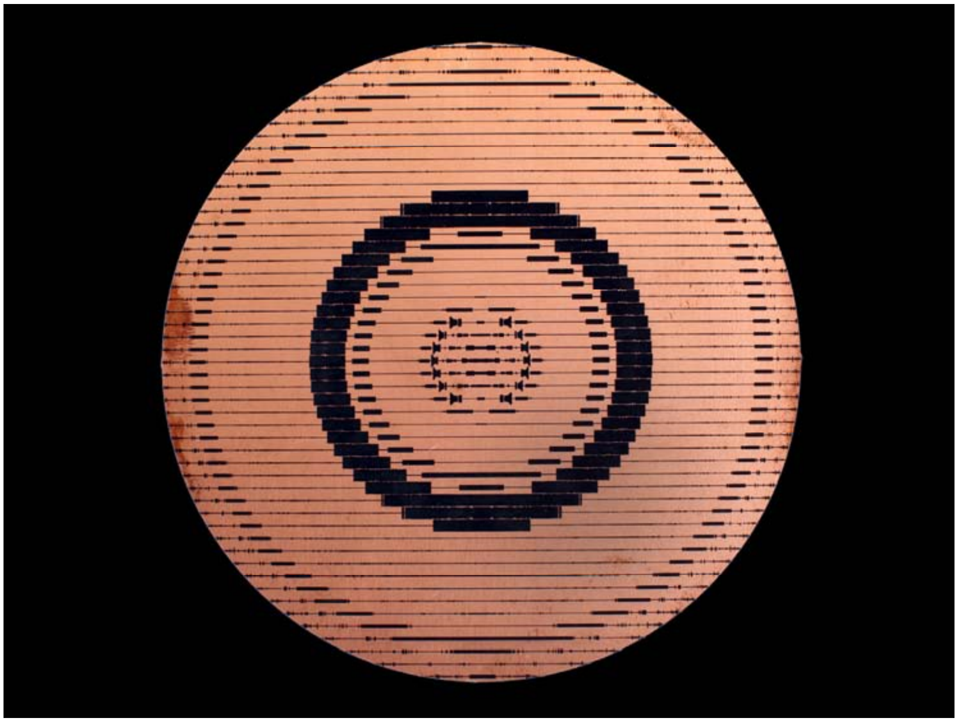

(b)

Figure 7.4-1: Photograph of the polarisation-sensitive four-layer PASS flat-topped beam antenna; (a) Front view, (b) Back view.

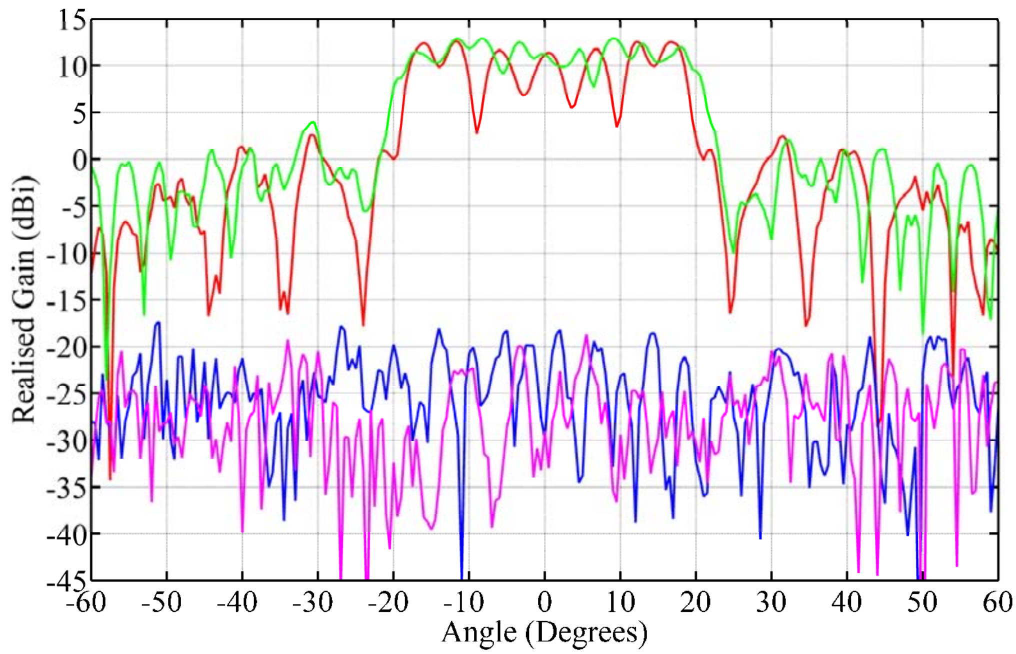

Figure 7.4-2: Measured far-field radiation patterns of the PASS flat-topped beam at 30 GHz; —— *H*-plane, co-pol; —— *H*-plane, X-pol; —— *E*-plane, co-pol; —— *E*-plane, X-pol.

the discussion that follows in Section 7.5. Additional details on the far-field and near-field measurements are provided in Section 6.2.

7.5 Discussion

In this section, the results presented in Section 7.4 are compared and discussed. From Figure 7.4-2, the cross-polarisation levels are seen to be at the –20 dBi level and the gain in the main beam is fluctuating around 10 dBi, which corresponds to at least 30 dB cross polar discrimination. This is a good result for the cross-polarisation, which is expected since similarly good results were obtained with the PSS PC-FZPAs presented in Chapter 6.

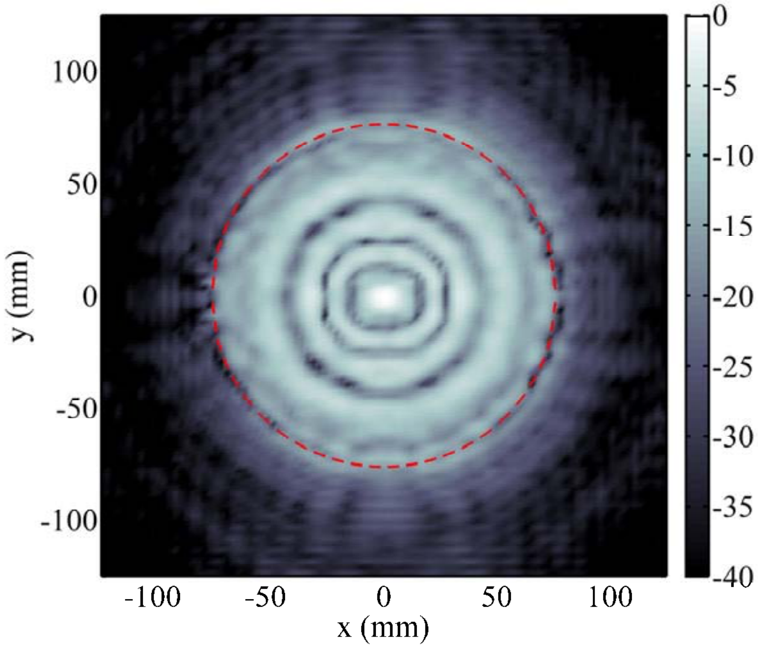

(a)

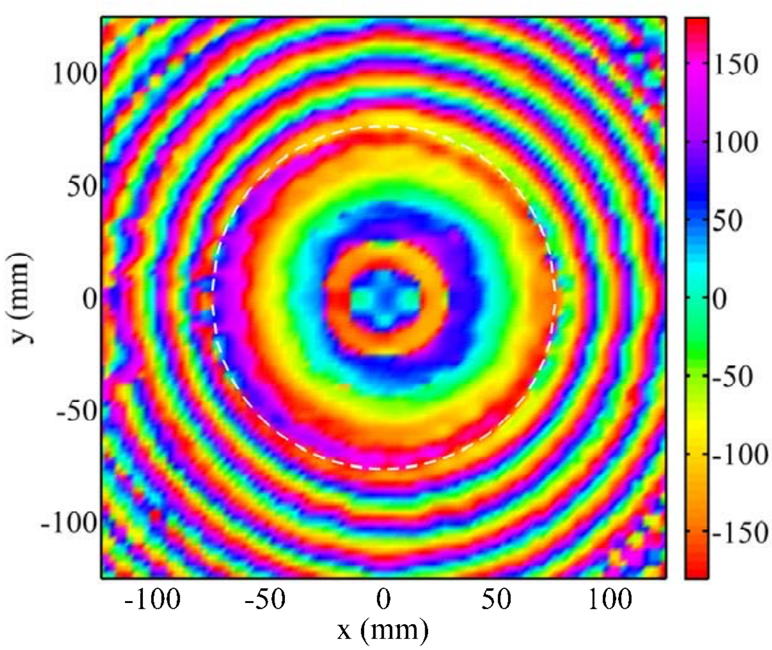

(b)

Figure 7.4-3: Measured near-fields at the surface of the aperture for the PASS flat-topped beam antenna at 30 GHz; (a) Amplitude (in dB), (b) Phase (in degrees). The physical boundary of the antenna is shown as an overlaid dashed line in each case.

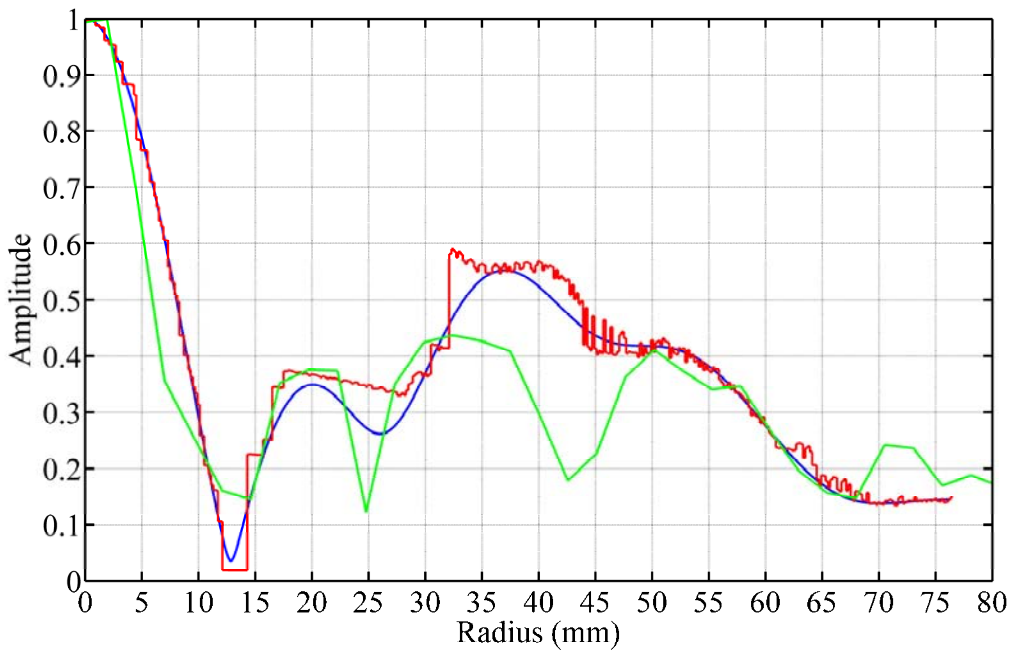

(a)

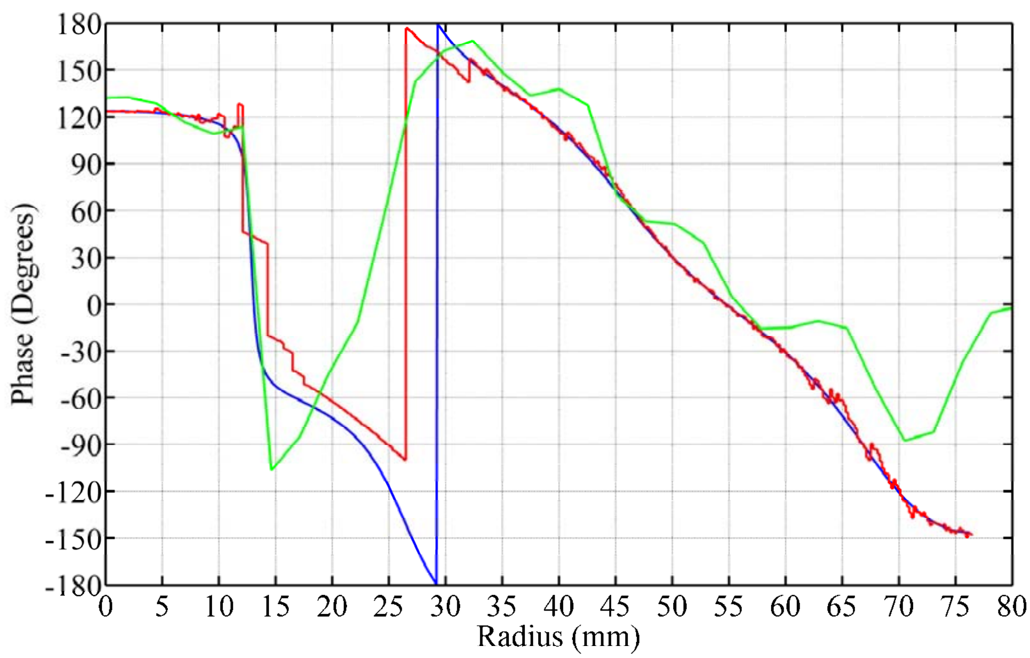

(b)

Figure 7.4-4: Electric field distribution at the PASS along the *x*-axis for a 40° beamwidth flat-topped beam antenna at 30 GHz; (a) Amplitude, (b) Phase; —— Ideal (using [ELLI88]), —— Calculated (from the dataset results of Figure 3.4-10, with step size of 0.2 mm), —— Near-field measurement.

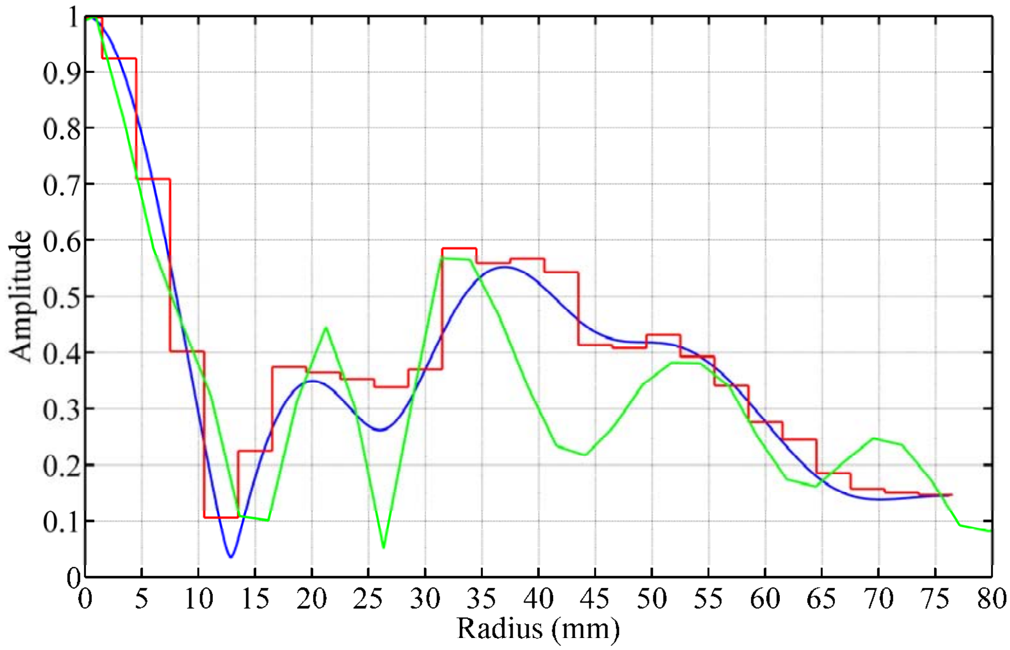

(a)

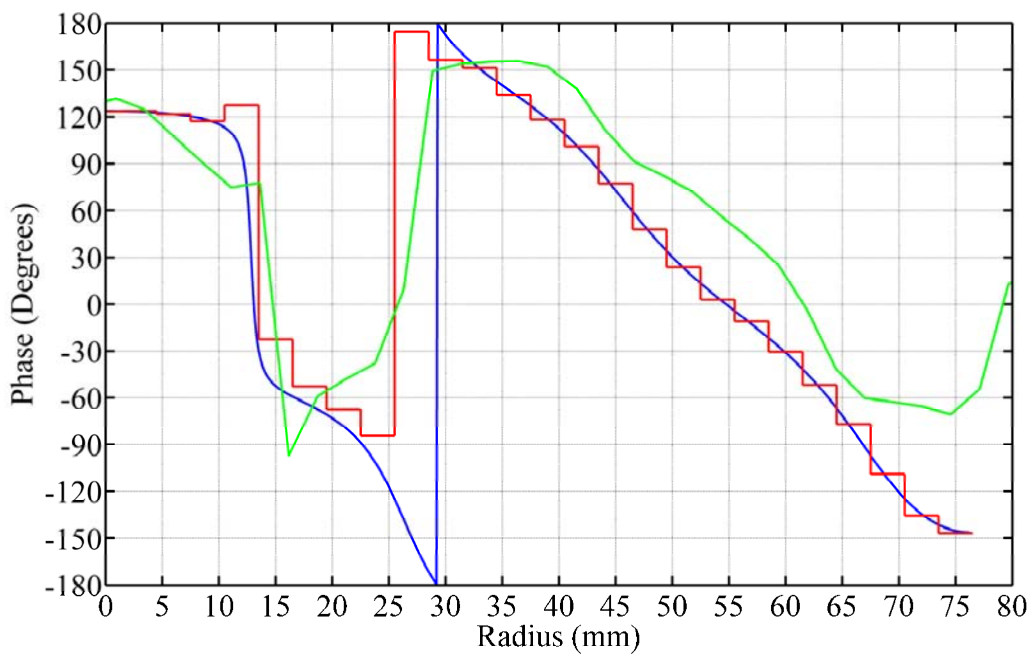

(b)

Figure 7.4-5: Electric field distribution at the PASS along the *y*-axis for a 40° beamwidth flat-topped beam antenna at 30 GHz; (a) Amplitude, (b) Phase; —— Ideal (using [ELLI88]), —— Calculated (from the dataset results of Figure 3.4-10, with step size of 3 mm), —— Near-field measurement.

Figures 7.4-4 and 7.4-5 presented the electric field distribution at the aperture for the ideal, calculated and measured cases. Recall that the ideal distribution was generated from the method reported in [ELLI88] and that the calculated distribution was obtained from the best match of the simulation data and best reference amplitude and phase. The measured data were obtained from near-field measurements. It is first noticed that the phase agreement is good. The measured results for radii located between 15 mm and 30 mm have values in the expected range although the slopes appear opposite. The measured amplitude behaviour generally follows the ideal trend; however, the values of amplitude are not always as expected. The discrepancies between the expected and measured amplitude values are attributed to the sensitivity of the PASS to the angle of incidence, which was previously addressed in Section 3.7.3.

Figure 7.5-1 shows plots of the co-polarisation far-field radiation patterns for the ideal, calculated and measured cases. The measured results are those directly obtained from the far-field measurements previously presented in Figure 7.4-2. First, it is to be noted that the ideal and calculated cases present values of directivity while the measured case presents the realised gain. Consequently, it is noticed that the gain of the measured case is lower than the directivities of the ideal and calculated cases, which is expected. Second, the ripples in the main beam are higher for the measured case compared to the ideal or calculated cases, especially for the *H*-plane cut. From Figure 7.4-4, the amplitude of the electric field aperture distribution along the *x*-axis, i.e. in the *H*-plane cut, does not show as good an agreement as the one along the *y*-axis, i.e. in the *E*-plane cut, presented in Figure 7.4-5. This amplitude error of the fields at the PASS aperture translates into a

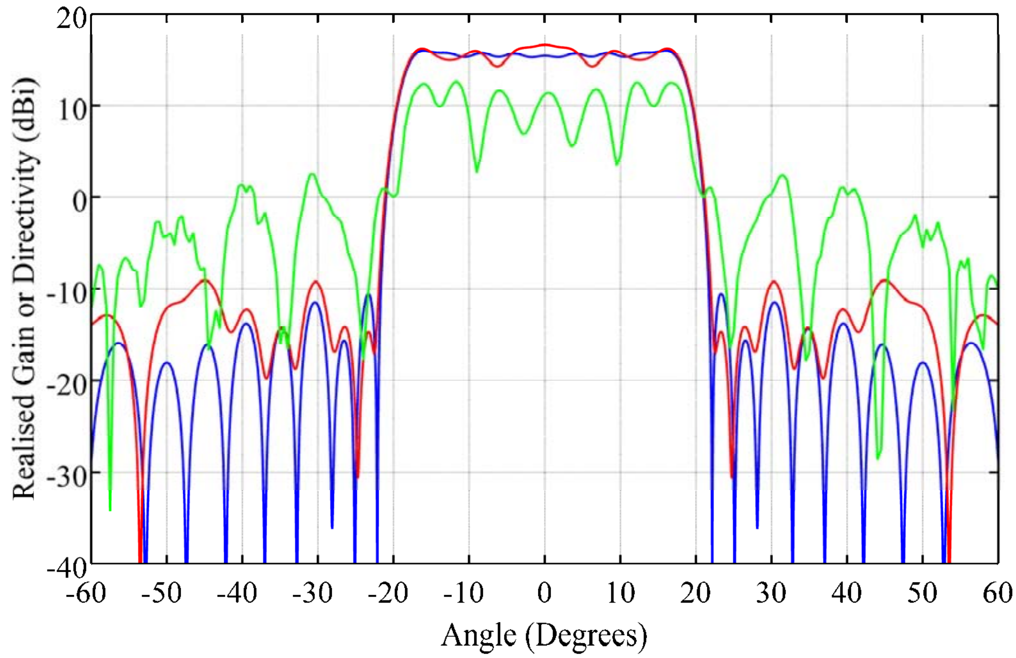

(a)

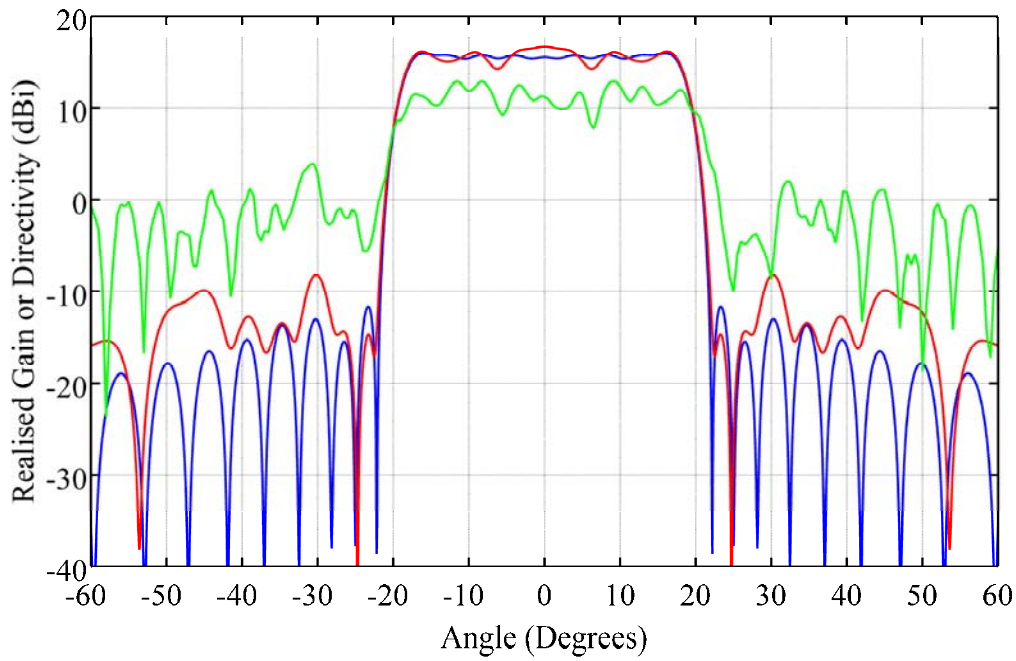

(b)

Figure 7.5-1: Co-polarisation far-field radiation patterns of the PASS flat-topped beam at 30 GHz; (a) *H*-plane, (b) *E*-plane; —— Ideal (directivity), —— Calculated (directivity), —— Measured (realised gain).

discrepancy in the far-field patterns, with the ripples in the *H*-plane cut being worse than in the *E*-plane cut. The higher disagreement in the *H*-plane pattern is attributed to the fact that the perpendicular polarisation, which is located along the *H*-plane cut, suffers more from the oblique incidence angle than the parallel polarisation, as previously discussed in Section 3.7.3.

The high sidelobe levels of the far-field measurement results compared to the ideal and calculated ones are also worth investigation. In fact, the sidelobes are as much as 10 dB higher in the measured case. The aperture field distribution of the PASS was examined in an attempt to explain the far-field discrepancies. In order to do so, the data obtained from near-field measurements in Figures 7.4-4 and 7.4-5 is used to generate the far-field radiation patterns for the ideal and measured cases. The pattern generation technique is described in [ELLI88] and assumes that the field distribution at the aperture is rotationally symmetrical. This technique is selected for its simplicity and short computation time. It will of course lead to an approximation of the radiation patterns; however it will give important insight into the behaviour of the sidelobes for such an aperture field distribution.

Figure 7.5-2 presents the far-field results computed from the aperture field distribution using [ELLI88]. The far-field obtained from the measured aperture field distribution with this technique present high sidelobe levels. In fact, the sidelobe levels are close to the ones obtained in the far-field measurements. The main beam also exhibits high ripples, as was also the case for the measurement results obtained from far-field measurements. On the other hand, the main beam generated from the aperture field

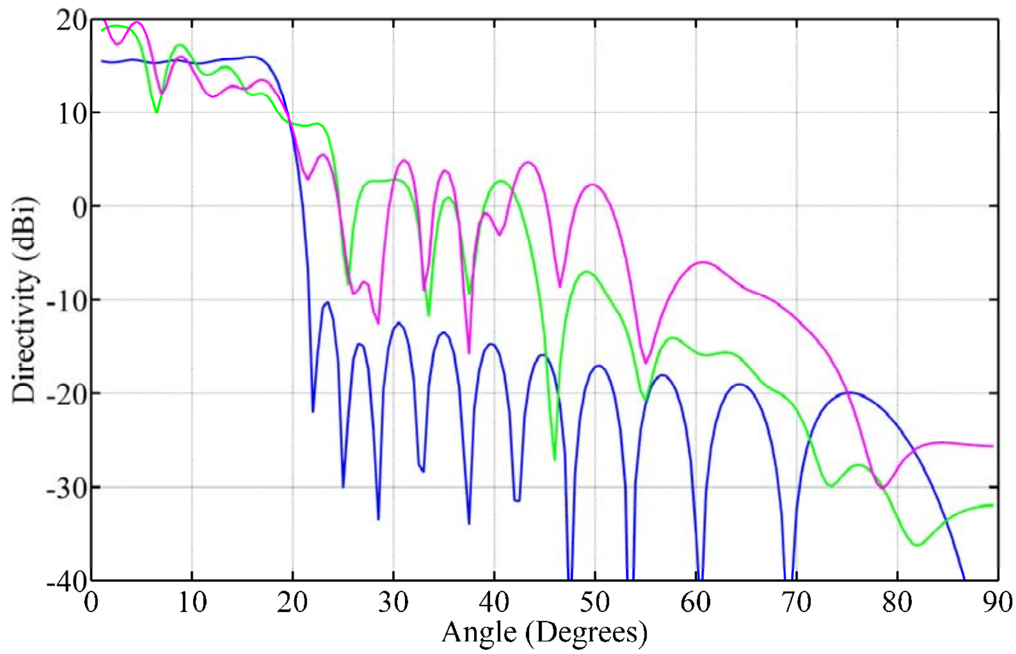

Figure 7.5-2: Far-field radiation patterns of the PASS flat-topped beam at 30 GHz assuming a rotationally symmetric field distribution at the aperture of the PASS; —— Ideal, —— From measurement results in Figure 7.4-4, —— From measurement results in Figure 7.4-5.

distribution does not exhibit a flat-top shape as seen on the results obtained from the far-field measurements; recall that the main beam obtained from the far-field measurements had a shape close to the desired flat-top, with abrupt roll-off near ±20°, as presented in Figure 7.4-2. Using the technique in [ELLI88] to generate the far-field radiation patterns from the aperture field distribution reveals a change in the main beam width and a main beam shape that does not exhibit a flat-top shape.

The discrepancy in the far-field main beam results between the processed measured aperture field results and the far-field measurement results could be explained by the sensitivity of the near-field measurement. It was reported previously that far-field patterns cannot be efficiently computed from near-field results for antennas with gain below 15 dBi [GRAY02]. In the current case the gain is clearly below 15 dBi, as shown in Figure 7.4-2.

Another contributing factor to the main beam discrepancy is a slight tilt of the PASS during the measurement since it was difficult to ensure that the plane of the PASS was perfectly parallel to the plane of the near-field scan. In fact, from Figure 7.4-3(b), inspection of the phase shows a slight discrepancy that is attributed to a tilt of the PASS. The phase discrepancy is more evident near the edges of the PASS aperture. Nevertheless, achieving beam-shaping using a PASS has been clearly demonstrated.

7.6 Conclusions

The far-field performance of a PASS capable of producing a flat-topped beam has been reported in this chapter. The PASS has a clear advantage of allowing the realisation of virtually any type of radiation pattern by controlling the amplitude and phase distribution over the aperture. The drawback is that the aperture efficiency is reduced when the amplitude is not maximised; however this is true for any shaped beam antenna.

CHAPTER 8 Conclusions and Future Work

8.1 Summary

This thesis has described the development of a phase shifting surface (PSS) at Ka band to be used for free-standing transmissive devices. This novel concept was methodically presented and analysed. The feasibility of free-standing structures based on the PSS concept was clearly demonstrated through numerous prototypes, including a linear phase grating, a cylindrical lensing device and different types of full lensing devices for high-gain antenna applications.

An extension of this concept, the phase and amplitude shifting surface (PASS), was also presented. A prototype of a flat-topped beam antenna developed using this approach was demonstrated.

Free-standing devices based on the PSS/PASS concept have clear advantages as compared to those of the present state of the art:

- They rely on conventional photolithographic (wet chemical) etching, which is a mature and low-cost fabrication process.
- Their geometry is thin and flat, leading to low weight, low volume and low usage of material, which leads to additional cost reduction.
- Their antenna gain is comparable or superior over a decent bandwidth, making them a viable alternative for many applications.
- Their cross-polarisation levels are significantly improved.

8.2 Thesis Contributions

The primary contributions of this thesis are as follows:

- The invention and development of a low-cost, thin and lightweight structure called a *phase shifting surface* (PSS) that can be used to achieve different transmission phase shifts while maintaining a high amplitude of transmission through a combination of closely spaced conductive shapes etched on multilayer low-permittivity dielectric sheets.
- The design of multiple free-standing phase-correcting devices using the PSS, including a linear grating, a cylindrical lensing device, and different types of full lensing devices with different phase corrections and polarisation capabilities.
- An exhaustive comparison of the physical parameters and far-field performance of lens antennas designed using the PSS concept and conventional lens antennas (including a shaped dielectric lens, a dielectric phase-correcting Fresnel zone plate, and a Fresnel zone plate).
- The design of a proof-of-concept flat-topped beam antenna in order to demonstrate the feasibility of the PASS concept.

8.3 Most Recent Research Work on Thin Lens Structures

The desire for achieving thin lens structures is very timely. Within the last year, several conference papers have been published on this topic. The objective of this section is to present the most relevant concurrent work on the subject. The work presented in this section has not been presented in the background of Chapter 2 because it has been published at the time when the research work on this thesis was nearly completed.

Nevertheless, because of the similar nature of the work, it is worth mentioning in this thesis.

8.3.1 Microwave lens using non-resonant sub-wavelength miniaturized multiple-order FSS elements

A recently published work making use of similar cell elements as those reported in this thesis has been reported in [ALJO10a]. A representation of the structure, with equivalent circuit model, is presented in Figure 8.3-1. The major difference of this work

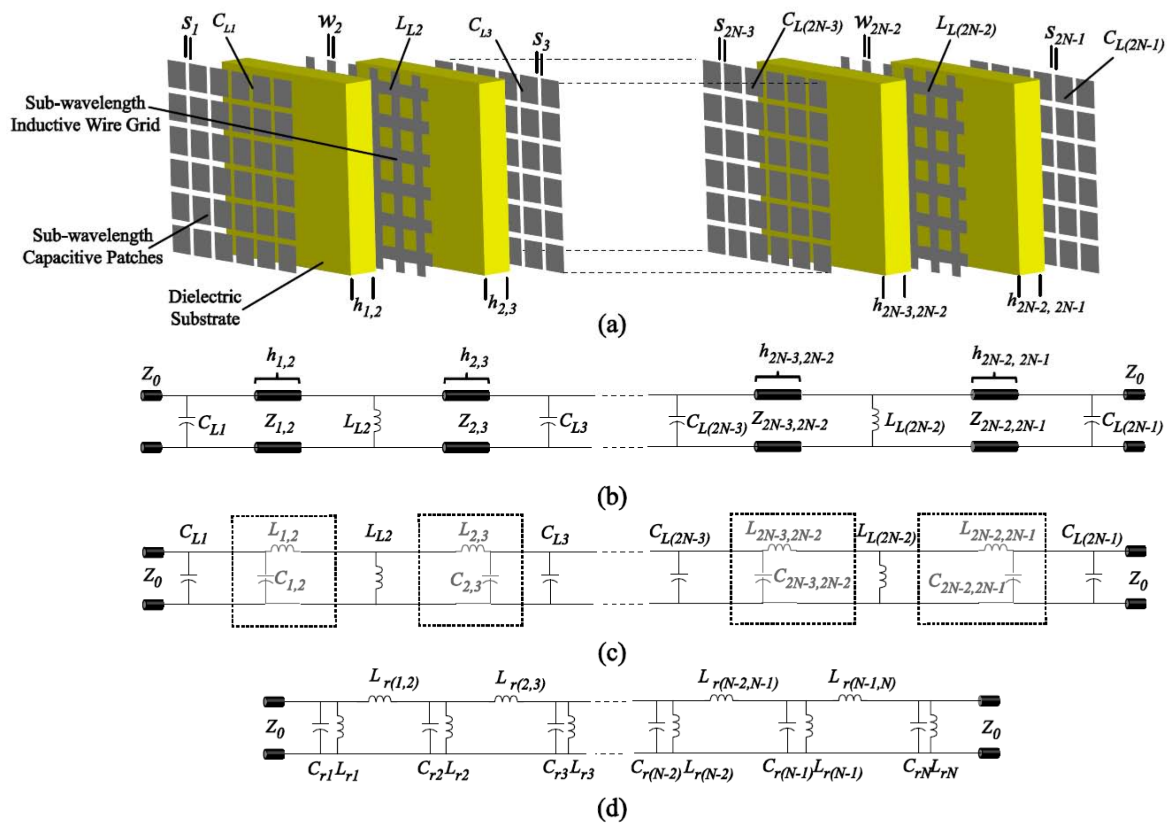

Figure 8.3-1: Multiple order FSS structure used for microwave lens; (a) Three-dimensional exploded view (the dielectric is shown in yellow and the metal is shown in grey), (b) Transmission line equivalent circuit model, (c) FSS lumped element equivalent circuit model, (d) Multiple order circuit model. Reprinted with permission from [ALJO10b]. © 2010 IEEE.

compared to the one reported in this thesis is the use of not only capacitive patch elements similar to those presented in Section 3.5, but also inductive grids, making it a bandpass structure while the reported structures in this thesis have a low-pass nature (see Section 3.6). The configuration is used for lens applications, but can also be used for FSS applications [ALJO10b]. Many layers are cascaded in the reported work, leading to improved bandwidth operation, but also additional complexity resulting in the use of many dielectric sheets, conductive layers and bonding films. Typical reported technologies make use of a minimum of five conductive layers, which is more than any reported configuration presented in this thesis. Simulations were conducted at X-band and, despite the use of more layers, the electrical thickness is in the same range as the work reported in this thesis.

8.3.2 Microwave planar lens using Jerusalem Cross FSS elements

Another recently published work reports the design of a so-called *planar lens using artificial dielectrics* [ZHAN10]. The structure is in fact a typical transmitarray making use of Jerusalem Cross FSS elements to obtain the required phase shift. Multiple layers are cascaded, spaced by air gaps to avoid undesired mutual coupling between layers. One of the benefits of using Jerusalem Crosses is their stable response to incidence angle.

8.3.3 Microwave polariser-lens based on multiple resonances

In [SHIB10], a flat thin polariser lens that converts linear polarisation to circular polarisation (or the other way around) is reported. The structure is presented in Figure 8.3-2. To introduce additional phase shift, additional resonance slots are added on the ground plane. The cross-slot dimensions are controlled to realise the desired phase shift

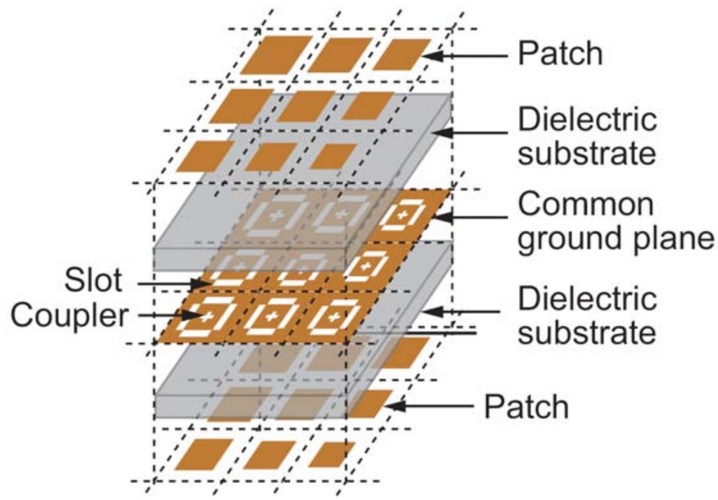

Figure 8.3-2: Schematic representation of the polariser-lens based on multiple resonances. The dielectric is shown in grey and the metal is shown in orange. Reprinted with permission from [SHIB10]. © 2010 IEEE.

as well as 90° phase shift between the two orthogonal polarisations. This microwave polariser-lens uses three conductive layers (two patch layers and a ground plane) spaced by dielectric layers. The element spacing is half a wavelength and the thickness is slightly less than a tenth of a wavelength.

8.3.4 High-efficiency microwave array lens for circular polarisation

In [PHIL10a], an array lens with high efficiency is proposed. The structure converts linear polarisation into circular polarisation (or the other way around) by using multiples stacked patches and cross slots with different dimensions and orientations. The emphasis is put on the high aperture efficiency of the structure, with a 48% claim. Figure 8.3-3 presents the element used in the design of the structure, where it is noticed that five conductive layers and four dielectric layers are used, leading to additional complexity compared to the work reported in this thesis.

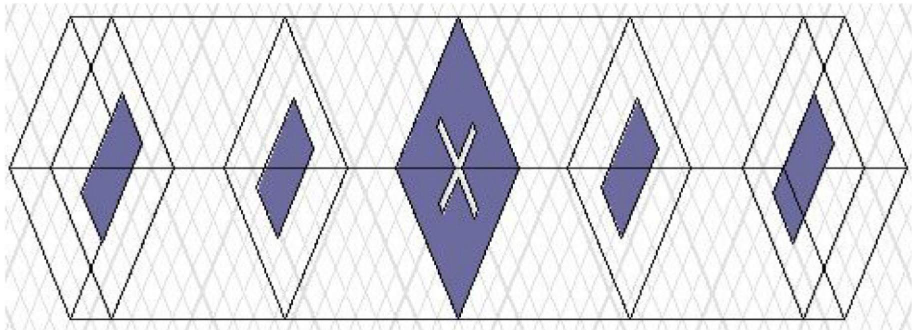

Figure 8.3-3: Schematic representation of the element design used for the microwave array lens for circular polarisation. Reprinted with permission from [PHIL10a]. The metal is shown in purple and the spacing between layers has been increased.

In [PHIL10a] and [PHIL10b], the versatility of the technology is demonstrated through additional configurations, such as beam squinting and beam splitting. The beam splitting is performed by a so-called circular polarisation splitting prism, which converts an incoming linearly polarised wave from a feed antenna into two orthogonal circular polarisation components (right-hand and left-hand) propagating at different angles.

8.4 Future Work

The amount of work on the PSS and PASS concepts presented in this thesis is considerable and constitutes a good basis for new research in this field. Areas for future work are described in what follows.

8.4.1 Simulation time improvement

The simulations of different PSS and PASS cases were performed using IMST Empire XCcel™ [EMPI07] and Ansoft HFSS™ [HFSS07]. These software packages are commercially available and are not customised for simulations of the PSS/PASS problem. For example, the simulations involving polarisation-dependent unit cells composed of strips are two-dimensional problems, but the above three-dimensional packages were used in the simulations, which results in significantly longer simulation times.

The database results presented in Chapter 3 was established for dielectric materials with specific thicknesses and dielectric constants. If these parameters happen to change, the dataset will not be valid and will need to be entirely regenerated. At this point, with IMST Empire XCcel™ [EMPI07], it takes several weeks, or even months, to generate a complete dataset, especially for the PASS cases, which require a larger dataset.

In the case of the polarisation-dependent elements, the best solution would be the development of a customised code using a two-dimensional approach specifically optimised for such a case, i.e. plane wave illumination of a slab of dielectric material with metallic implants. For polarisation-independent unit cells, a two-dimensional code would not be suitable, but a customised code could still greatly decrease the simulation times.

8.4.2 Oblique incidence

Many of the results presented in this thesis showed that the PSS and PASS structures are sensitive to incidence angle. Even though the results presented are good, there seems to be potential for further improvement if the angle of incidence is taken into account. In particular, it could reduce the sensitivity of the PASS flat-topped beam implementation presented in Chapter 7. Moreover, taking into account the angle of incidence could allow for achieving improved lens performance for smaller values of focal lengths, which may be problematic if not addressed. The drawback is that an even larger amount of data would need to be generated. Since it currently takes several weeks or even many months to generate a dataset for only one angle of incidence (normal incidence), the time to generate a dataset could easily be measured in years, which is not practical. One solution would be to speed up the simulation times as suggested in Section 8.4.1, with the customised simulation code being able to deal with oblique incidence of course.

8.4.3 Presence of a radome

In many real-life applications, antennas need to be protected by a soft or hard cover sheet, or enclosed in a radome. These have the effect of altering the antenna performance, which is more evident as the frequency gets higher. Usually, the antenna performance is degraded rather than improved unless the effect of a cover sheet or radome is taken into account. Consequently, in such cases the protective sheets would need to be included in the simulation model of the PSS/PASS structures, requiring a whole new data set. Nevertheless, preliminary work on employing a radome located directly at the aperture of a PSS lensing device revealed that the presence of a radome may not affect the performance when compared to a non-radome case (such as those presented in Chapter 6). This could be a significant advantage of the PSS/PASS designs since many other types of printed antennas are much more sensitive to the presence of a radome.

8.4.4 Improved PSS/PASS antenna versatility by using rectangular elements

This thesis mostly addressed two types of PSS/PASS unit cell elements: the strip (polarisation-sensitive) and the square (polarisation-insensitive). In Figure 3.3-2, a rectangular conductive shape within a square unit cell was also introduced. Although not yet studied, this geometry has a high potential for realising free-standing antenna structures capable of achieving different behaviour depending on the polarisation. One example is a single PSS lens antenna that could be designed to have a given focal length in one plane and another focal length in the orthogonal plane. Another example is to use a 45°

polarisation to obtain an outgoing circular polarisation from an incoming linear polarisation (or the other way around).

One of the drawbacks of these elements is that they require as long simulation times as the square elements, in addition to requiring simulations of both polarisations, which translates into twice the simulation time. Furthermore, with twice as many variables (height and width of rectangles, rather than simply the size for the squares) and potential correlation between the height and width, the database may be difficult to generate and take even longer time.

8.4.5 Improved bandwidth using combined patch-grid layers

In Section 8.3.1, a geometry similar to the patch element of Section 3.5 was introduced, with the addition of inductive wire grid layers. The inductive wire grids improve the bandwidth; however the resulting configuration requires additional conductive and dielectric layers.

With the structure reported in Section 8.3.1 in mind, the idea came of combining the conductive patch layer with the inductive wire grid layer. The resulting unit cell looks as shown in Figure 8.4-1. Additional work must be performed on such a configuration in order to attest if it can improve the bandwidth without compromising other parameters.

8.5 Conclusions

The excellent performance obtained from the PSS-based devices, and their sheer practicality, make them potential candidates for replacing existing conventional lensing

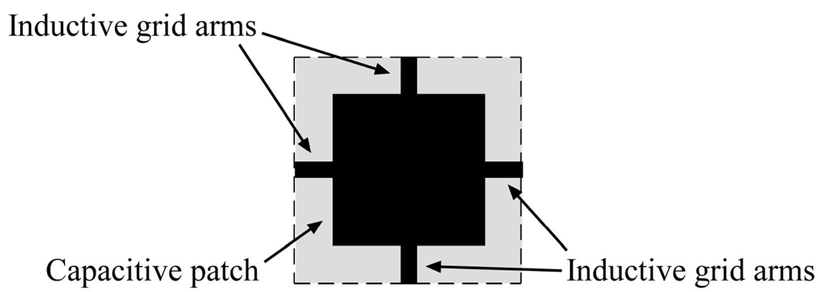

Figure 8.4-1: Front view of the unit cell showing a patch-grid configuration. The dielectric is shown in grey and the metal is shown in black.

devices. Furthermore, such a low-cost, light-weight, easy-to-manufacture, high-performance alternative could expand the deployment of such type of lensing devices.

APPENDIX A Holography Theory

A.1 Introduction

A.1.1 Definition of Hologram

A hologram is a medium that contains information for the reconstruction of one beam from another beam. In optics, a hologram is created from the interference between a reference beam and the beam resulting from an object (by either reflection or transmission) [GOOD96]. It is generally recorded using an interferometric technique on special photographic films [GOOD96]. The image of the object is reconstructed by illuminating the hologram using the reference beam in the absence of the object [GOOD71], [KOCK68].

A.1.2 Microwave Holograms

At microwave frequencies, as well as millimetre wave and sub-millimetre wave frequencies, holograms are usually considered to be transmission holograms. In design, the microwave hologram is used to generate a desired electromagnetic beam from a given input or reference beam [KOCK68]. In most applications, the desired beam is a plane wave and the reference beam consists of a spherical wavefront from a given antenna; this is referred to as an elementary hologram [WATE66b]. However, microwave holography is not limited to this case only; other applications exist, for example beam splitting [LEE79].

At microwave frequencies, the recording of the hologram cannot be practically performed using the same technique as in optics since there are no efficient sensitive recording devices similar to photographic films at these frequencies. It is true that some recording media exist, but the amount of power required for recording a hologram impractically large. Consequently, the holograms in these frequency bands are generated from analytical or computer techniques [GOOD96] and are generally called computer-generated holograms. At the time most of the research on holograms was performed, i.e. in the 1960's and early 1970's, computers were not as distributed and used as today, and the terminology *computer-generated holograms* was used to differentiate them from the traditional holograms produced on photographic films. Nowadays the terminology may appear obsolete since most designs use computer assistance. Nevertheless, the terminology has been kept over the years; for example, Goodman was still using it in his 1996 textbook [GOOD96]. Therefore the same terminology will also be used in this thesis.

The following sections provide background information on holography that is relevant to the theory of amplitude and phase gratings used in Chapter 3. The interested reader may refer to [GOOD71] for further theoretical background.

A.2 Recording Phase

The recording process of a hologram is shown in Figure A.2-1. It consists in recording, in a medium, the interference created by two wavefronts or beams, one resulting from a desired wavefront and the other resulting from a reference wave, e.g. a plane wave, a spherical wave or the radiation pattern of a given antenna (horn, patch, etc.). In Figure A.2-1, the desired wavefront is represented by the object. Mathematically, assuming the hologram or recording medium is positioned in the *xy*-plane, and neglecting

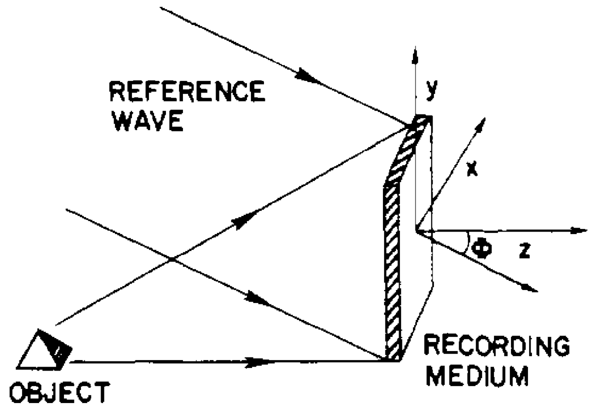

Figure A.2-1: The recording process of a hologram. Reprinted with permission from [GOOD71]. © 1971 IEEE.

unimportant constants as proposed in [GOOD71] (such as time dependency), the field distributions at the surface of the hologram or recording medium for each wavefront are written as

$$U_D(x,y) = a(x,y)\exp\left[-j\phi(x,y)\right] \tag{A.2-1}$$

$$U_R(x,y) = A(x,y)\exp\left[-j\psi(x,y)\right] \tag{A.2-2}$$

Quantity U_D represents the field distribution of the desired wavefront in the plane of the hologram or recording medium, a its magnitude and ϕ its phase. Quantity U_R represents the field distribution of the reference wavefront in the plane of the hologram or recording medium, A its magnitude and ψ its phase. The hologram is generated from the interference I of the two wavefronts in the plane of the hologram or recording medium. The mathematical definition of the interference pattern between the wavefronts U_D and U_R is

$$I(x,y) = \left|U_R(x,y) + U_D(x,y)\right|^2 \tag{A.2-3}$$

which can be expanded to give the following result:

$$I(x,y) = \left|U_R(x,y)\right|^2 + \left|U_D(x,y)\right|^2 + U_R^*(x,y)U_D(x,y) + U_R(x,y)U_D^*(x,y) \tag{A.2-4}$$

The complex conjugates appear because the magnitude or absolute value is squared. Inserting (A.2-1) and (A.2-2) in (A.2-4), the following equation is obtained:

$$\begin{aligned} I(x,y) &= |A(x,y)|^2 + |a(x,y)|^2 + A(x,y)a(x,y)\exp[j\psi(x,y) - j\phi(x,y)] \\ &+ A(x,y)a(x,y)\exp[j\phi(x,y) - j\psi(x,y)] \end{aligned} \tag{A.2-5}$$

which simplifies to

$$I(x,y) = |A(x,y)|^2 + |a(x,y)|^2 + 2A(x,y)a(x,y)\cos[\psi(x,y) - \phi(x,y)] \tag{A.2-6}$$

In its simplest description, the grating pattern of the hologram is proportional to the interference pattern $I(x,y)$.

A.3 Reconstruction Phase

From the theory of holography [GOOD71], the desired wavefront can be reconstructed by illuminating the hologram with the reference wave:

$$U_C(x,y) = I(x,y)U_R(x,y) \tag{A.3-1}$$

where U_C is the field distribution of the reconstructed wave. The reconstruction process is illustrated in Figure A.3-1, in which the reconstructed wavefront is represented by the virtual image.

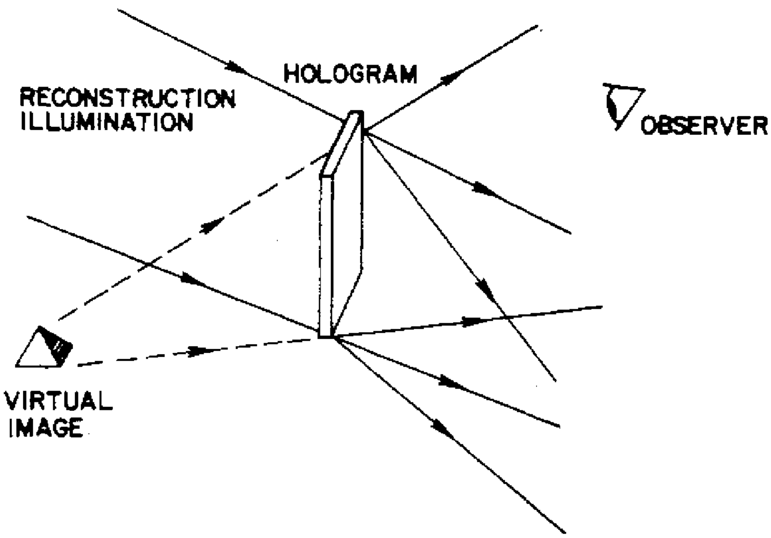

Figure A.3-1: The reconstruction process of a hologram, with an observer on the right seeing the reconstructed virtual image. Reprinted with permission from [GOOD71]. © 1971 IEEE.

APPENDIX B Lens Antenna Theory

B.1 Introduction

In this appendix, a general theory for lens antennas, as well as different types of lens antennas, are presented.

B.2 Basic Theory and Dielectric Plano-Hyperbolic Lens Antenna (DPHLA)

The most common transformation that a microwave, millimetre wave or sub-millimetre wave lens has to perform is to focus electromagnetic plane waves into a single point at a given location, or inversely to transform the electromagnetic waves propagating spherically from a point source into a plane wave. Traditional lenses are made of dielectric material, and the simplest version has a curved surface on one side and a flat surface on the other side. These lenses are often called single-surface lenses [GOLD97]. Considering Figure B.2-1, it is desired that the total electrical length of any path through the lens is the same as any other path. It is assumed that spherical (or circular, in a two-dimensional problem) wavefronts radiate from the focal point P. Two paths are considered, which are sufficient for obtaining the profile of the lens. The first path is PM' through M, while the second path is PC' through C. For the lens to operate properly, it is desired to have the same phase at every location on the output surface of the lens. First, the segments of the paths are defined:

$$\overline{PM} = F \tag{B.2-1a}$$

$$\overline{MM'} = t \tag{B.2-1b}$$

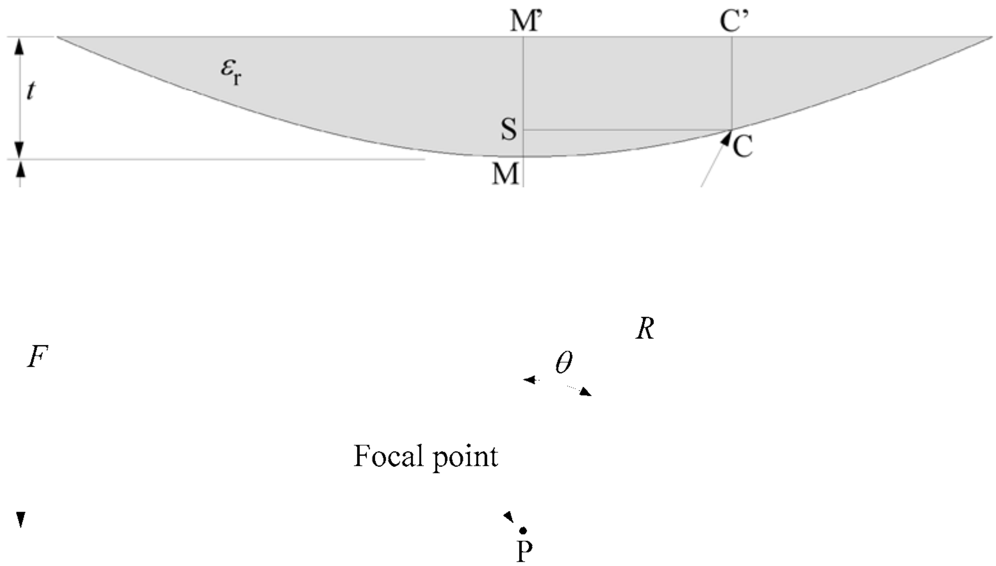

Figure B.2-1: Cross-sectional view of a single-surface lens; the arrangement is also called dielectric plano-hyperbolic lens antenna (DPHLA).

$$\overline{PC} = R \tag{B.2-1c}$$

$$\overline{CC'} = F + t - R\cos\theta \tag{B.2-1d}$$

Equating the electrical length along each of the above ray paths:

$$\frac{2\pi}{\lambda_0}F + \frac{2\pi}{\lambda_g}t = \frac{2\pi}{\lambda_0}R + \frac{2\pi}{\lambda_g}\left(F + t - R\cos\theta\right) \tag{B.2-2}$$

where λ_0 is the free-space wavelength and λ_g is the wavelength in the dielectric material,

$$\lambda_g = \frac{\lambda_0}{\sqrt{\varepsilon_r}} \tag{B.2-3}$$

where ε_r is the relative permittivity. Inserting (B.2-3) in (B.2-2):

$$\frac{2\pi}{\lambda_0}F + \frac{2\pi\sqrt{\varepsilon_r}}{\lambda_0}t = \frac{2\pi}{\lambda_0}R + \frac{2\pi\sqrt{\varepsilon_r}}{\lambda_0}\left(F + t - R\cos\theta\right) \tag{B.2-4}$$

Simplifying (B.2-4):

$$F + \sqrt{\varepsilon_r}\,t = R + \sqrt{\varepsilon_r}\left(F + t - R\cos\theta\right)$$

$$F + \sqrt{\varepsilon_r}\,t = R + \sqrt{\varepsilon_r}\,F + \sqrt{\varepsilon_r}\,t - \sqrt{\varepsilon_r}\,R\cos\theta$$

$$F = R + \sqrt{\varepsilon_r}\,F - \sqrt{\varepsilon_r}\,R\cos\theta$$

$$\sqrt{\varepsilon_r}\,R\cos\theta - R = \sqrt{\varepsilon_r}\,F - F$$

$$R\left(\sqrt{\varepsilon_r}\cos\theta - 1\right) = \left(\sqrt{\varepsilon_r} - 1\right)F$$

$$R = \frac{\left(\sqrt{\varepsilon_r} - 1\right)F}{\sqrt{\varepsilon_r}\cos\theta - 1} \tag{B.2-5}$$

In (B.2-5), R is the distance from the focal point (P) to the lens surface as a function of the radiation angle θ and F is the focal length. Note that t, the thickness of the lens as shown in Figure B.2-1, does not appear in (B.2-5); consequently, the curvature of the lens is independent of the thickness. The curvature of the lens is that of a hyperbola; thus such an arrangement is also called a dielectric plano-hyperbolic lens antenna (DPHLA). Expression (B.2-5) is consistent with the result in [GOLD97].

In this document, full lenses with focal length F of 76.2 mm and diameter D of 152.4 mm (leading to an F/D of 0.5) are used. The single-surface lens is made of Plexiglas, which has a relative permittivity ε_r of 2.56. The calculated lens profile, obtained with (B.2-5), is presented in Figure B.2-2. Other types of lenses are also presented in this figure; these are discussed in Section B.3.

The single-surface lens has the advantage of being frequency independent. Indeed (B.2-5) reveals no dependence on frequency (or wavelength). Consequently, such a lens has no inherent bandwidth limitation. It does not suffer from shadow blockage as for the other types of lens to be discussed in Section B.3. Its major disadvantages are its thickness, weight, and material requirements. It also suffers from a high fabrication cost, requiring machining in prototyping or small production, and moulding for large production.

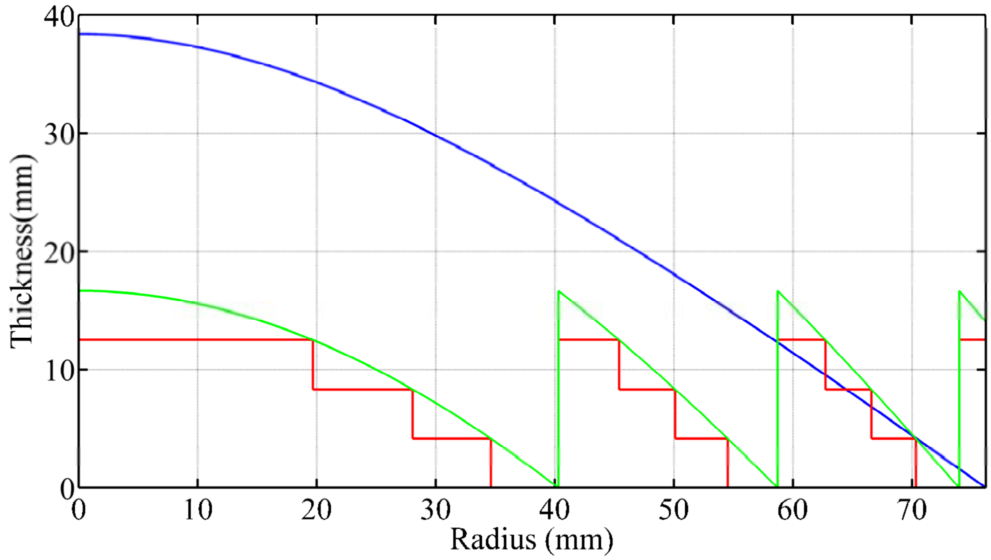

Figure B.2-2: Cross-sectional views of three types of lenses made of Plexiglas (ε_r = 2.56); —— dielectric plano-hyperbolic lens; —— Fresnel lens; —— 90° phase correcting Fresnel zone plate.

B.3 Phase-Correcting Fresnel Zone Plate Antenna (PC-FZPA) and Fresnel Lens Antennas

The dielectric plano-hyperbolic lens presented in section B.2 can lead to an appreciable physical thickness *t*, especially at microwave and millimetre-wave. In fact, it can be seen in Figure B.2-2 that the dielectric plano-hyperbolic lens that is used for reference in this thesis has a thickness of 38.376 mm, even without the extra backing material thickness that is usually present for gain enhancement [GAGN09]. Such a large thickness can be impractical in many designs. Furthermore, it increases the weight of the lens itself and may also result in increased absorptive loss and consequently reduced efficiency.

One way of realising that a thickness reduction can be performed on the dielectric plano-hyperbolic lens is by examining the thickness profile. If the lens thickness results in a phase correction range that is greater than 360° or 2π radians, then the lens thickness can be reduced by substituting the phase correction greater than 360° or 2π radians by an equivalent value less than 360° or 2π radians (modulo). In order to verify if the thickness of the lens results in such a case, it must be verified if the difference between a path in the dielectric material from which the lens is made and a path in free-space results in a 360° or 2π radians phase difference. This can be stated in an equation as follows:

$$\frac{2\pi}{\lambda_g}t - \frac{2\pi}{\lambda_0}t = 2\pi \tag{B.3-1}$$

where in this case t corresponds to a maximum lens thickness for 360° or 2π radians phase correction. Simplifying (B.3-1):

$$\frac{2\pi\sqrt{\varepsilon_r}}{\lambda_0}t - \frac{2\pi}{\lambda_0}t = 2\pi$$

$$\frac{\sqrt{\varepsilon_r}}{\lambda_0}t - \frac{1}{\lambda_0}t = 1$$

$$\left(\frac{\sqrt{\varepsilon_r}}{\lambda_0} - \frac{1}{\lambda_0}\right)t = 1$$

$$\left(\frac{\sqrt{\varepsilon_r} - 1}{\lambda_0}\right)t = 1$$

$$t = \frac{\lambda_0}{\sqrt{\varepsilon_r} - 1} \tag{B.3-2}$$

In the current case, (B.3-2) leads us to a thickness of 16.67 mm, which is less than half the thickness of the current lens. Consequently, the maximum lens thickness when implementing a maximum phase correction of 360° or 2π radians is given by (B.3-2), without considering the thickness of backing support.

A phase-correcting zone plate allows for correcting the phase by predetermined steps of 360°/P or $2\pi/P$, where P corresponds to the number of corrections within 360° or 2π radians. (For example, for 90° phase correction, P = 4; for 180° phase correction, P = 2.) The thickness of the steps, denoted s, is obtained by proceeding in a similar way as in (B.3-1):

$$\frac{2\pi}{\lambda_g}s-\frac{2\pi}{\lambda_0}s=\frac{2\pi}{P} \tag{B.3-3}$$

Solving as in (B.3-2) leads to:

$$s=\frac{\lambda_0}{P\left(\sqrt{\varepsilon_r}-1\right)} \tag{B.3-4}$$

The maximum thickness for the phase-correcting FZP is given by

$$t=\frac{(P-1)\lambda_0}{P\left(\sqrt{\varepsilon_r}-1\right)} \tag{B.3-5}$$

Consequently, the fewer steps used, the thinner the FZP; however, this also corresponds to the highest phase error, which translates to the lowest efficiency. For a 90° phase-correcting FZP (P = 4), the phase efficiency is 81%; for 180° (P = 2), it is 41% [GUO02]. Therefore, there is a tradeoff between the thickness and the efficiency for an FZP.

A phase-correcting Fresnel zone plate is made of concentric rings of given thicknesses obtained from (B.3-5). The radius r of each region i, called *zone*, is obtained from the following equation [GOLD97]:

$$r_i=\sqrt{\frac{2iF\lambda_0}{P}+\left(\frac{i\lambda_0}{P}\right)^2} \tag{B.3-6}$$

Figure B.2-2 shows the profile of a 90° phase-correcting lens made of Plexiglas, which is the same dielectric material as the dielectric plano-hyperbolic lens. The thickness reduction is appreciable when compared to a dielectric plano-hyperbolic lens. The radii are calculated using (B.3-6) and the thickness of each step is calculated using (B.3-4).

When the number of corrections is increased up to $P \rightarrow \infty$, the lens is characterised by a smooth curved variation, similar to the dielectric plano-hyperbolic lens, except at the locations where the phase changes by 360°. This special case is called a Fresnel lens. The profile of a Fresnel lens is shown in Figure B.2-2. This case has the advantage of having a very good phase correction (phase efficiency of 100%); however, it corresponds to a higher thickness than phase-correcting FZPs, which typically have $P = 2$ or $P = 4$. Note that when $P \rightarrow \infty$ in (B.3-5), the result from (B.3-2) is obtained, corresponding to the maximum thickness of a phase-correcting lens with maximum phase correction of 360° or 2π radians.

Phase-correcting Fresnel zone plates and Fresnel lenses result in a smaller thickness, volume and material requirement than a dielectric plano-hyperbolic lens; however, they are frequency dependent (see B.3-4 and B.3-6) so their bandwidth performance will be limited compared to a dielectric plano-hyperbolic lens. Another problem arising with these types of lenses is the spurious diffraction occurring at the step discontinuities; this phenomenon is called *shadow blockage* [PETO03a]. These lenses are also more difficult to machine than a traditional dielectric plano-hyperbolic lens because of the requirement of machining in tight spaces, especially for the Fresnel lens.

B.4 Fresnel Zone Plate Antenna (FZPA)

Although the phase-correcting Fresnel zone plate and the Fresnel lens result in thinner structures, the thickness remains of the same order as that of a dielectric plano-hyperbolic lens for most cases. Therefore the size and volume reduction is not a very impressive improvement, especially when one considers that it comes at the expense of increased fabrication difficulty and reduced performance.

One way to obtain a significant improvement in terms of fabrication complexity, cost and volume is through a Fresnel zone plate [HRIS00]. Instead of correcting the phase, like other types of lens antennas do, a Fresnel zone plate blocks the destructively adding radiation and keeps only the constructively-adding radiation. The destructively adding radiation is blocked by opaque rings, generally made of conductive material; the constructively adding radiation is made to propagate through transparent rings, usually constituting of a thin dielectric sheet or membrane. The rings are obtained from (B.3-6) with $P = 2$. There are no grooves present, and the Fresnel zone plate can be fabricated using conventional photolithographic (wet chemical) etching, which is much cheaper than machining or moulding. The result is a binary lensing structure that is extremely thin. However, the performance is poor; the aperture efficiency of such lens is typically between 10% and 15% [HRIS00].

REFERENCES

[ABEL93] C. Abella et al., "Artificial Dielectric Lens Antennas: Assessment of their Potential for Space Applications," in *23rd European Microwave Conference*, Madrid, Spain, pp. 896-898, September 1993.

[ADS06] Advanced Design System (ADS™) 2006A, Agilent Technologies Inc., California, USA.

[ALJO10a] M.A. Al-Joumayly, N. Behdad, "Design of Conformal, High-Resolution Microwave Lenses Using Sub-Wavelength Periodic Structures," in *CNC/USNC/URSI Radio Science Meeting*, Toronto, Canada, July 2010 *(digital format)*.

[ALJO10b] M.A. Al-Joumayly, N. Behdad, "A Generalized Method for Synthesizing Miniaturized Element Band-Pass Frequency Selective Surfaces," in *IEEE AP-S International Symposium*, Toronto, Canada, July 2010 *(digital format)*.

[BAGG93] L.C.J. Baggen, C.J.J. Jeronimus, M.H.A.J. Herben, "The Scan Performance of the Fresnel-Zone Plate Antenna: A Comparison with the Parabolic Reflector Antenna," *Microwave and Optical Technology Letters*, vol. 6, no. 13, pp. 769-774, Oct. 1993.

[BIRB08] F. Birbir, J. Shaker, Y.M.M. Antar, "Chebishev Bandpass Spatial Filter Composed of Strip Gratings," *IEEE Transactions on Antennas and Propagation*, vol. 56, no. 12, pp. 3707-3713, December 2008.

[BODE45] H.W. Bode, *Network Analysis and Feedback Amplifier Design*, Van Nostrand, 1945, New York, NY.

[BROW55] J. Brown, W. Jackson, "The Relative Permittivity of Tetragonal Arrays of Perfectly Conducting Thin Disks," *Proceedings of the IEE - Part B: Radio and Electronic Engineering*, vol. 102, no. 1, pp. 37-42, January 1955.

[BROW66] B.R. Brown, A.W. Lohmann, "Complex Spatial Filtering with Binary Masks," *Applied Optics*, vol. 5, no. 6, pp. 967-969, June 1966.

[BROW69] B.R. Brown, A.W. Lohmann, "Computer-Generated Binary Holograms," *IBM Journal of Research and Development*, vol. 13, no. 2, pp. 160-168, March 1969.

[CHAH06] M.R. Chaharmir, A. Ittipiboon, J. Shaker, "Single-Band and Dual-Band Transmitarray," in *12th International Symposium on Antenna Technology and Applied Electromagnetics (ANTEM 2006)*, Montréal, Canada, pp. 491-494, July 2006.

[CHAH07] M.R. Chaharmir, et al., "Cylindrical Multilayer Transmitarray Antennas," in *URSI Electromagnetic Theory Symposium (EMTS-2007)*, Ottawa, Canada, July 2007 (CD-ROM).

[COHN54] S.B. Cohn, "Artificial Dielectrics for Microwaves," in *Proceedings of the Symposium on Modern Advances in Microwave Technique*, New York, NY, November 1954.

[COHN61] S.B. Cohn, "Lens-Type Radiators," in *Antenna Engineering Handbook*, H. Jasik, Ed., McGraw-Hill, New York, NY, 1961, ch. 14.

[COLL91] R.E. Collin, *Field Theory of Guided Waves*, 2nd Ed., IEEE Press, New York, NY, 1991.

[COLL92] R.E. Collin, *Foundations for Microwave Engineering*, McGraw-Hill, New York, NY, 1992.

[CWIK08] T. Cwik, "Frequency-Selective Screens," in *Modern Antenna Handbook*, C.A. Balanis, Ed., Wiley, Hoboken, NJ, 2008, ch. 16.

[ELLI88] R.S. Elliott, G.J. Stern, "Shaped Patterns from a Continuous Planar Aperture Distribution," *IEE Proceedings H – Microwaves, Antennas and Propagation*, vol. 135, no. 6, pp. 366-370, December 1988.

[ELSH04] M. Elsherbiny, et al., "Holographic Antenna Concept, Analysis, and Parameters," *IEEE Transactions on Antennas and Propagation*, vol. 52, no. 3, pp. 830-839, March 2004.

[EMPI07] EMPIRE XCcel 5.30 by IMST GmbH, Germany, www.empire.de.

[GAGN02] N. Gagnon, *Design and Study of a Free-Space Quasi-Optical Measurement System*, Master's thesis, School of Information Technology and Engineering, University of Ottawa, Ottawa, Canada, May 2002.

[GAGN03] N. Gagnon, et al., "Material Characterization Using a Quasi-Optical Measurement System," *IEEE Transactions on Instrumentation and Measurement*, vol. 52, no. 2, pp. 333-336, April 2003.

[GAGN05] N. Gagnon, J. Shaker, "Accurate Phase Measurement of Passive Non-Reciprocal Quasi-Optical Components," *IEE Proceedings on Microwaves, Antennas and Propagation*, vol. 152, no. 2, pp. 111-116, April 2005.

[GAGN08] N. Gagnon, A. Petosa, D. McNamara, "Phase Hologram Composed of Square Patches on a Thin Dielectric Sheet," in *Proceedings of the International Symposium on Antennas and Propagation (ISAP 2008)*, Taipei, Taiwan, pp. 678-681, October 2008 *(digital format)*.

[GAGN09] N. Gagnon, A. Petosa, D.A. McNamara, "Comparison between Conventional Lenses and an Electrically Thin Lens Made Using a Phase Shifting Surface (PSS) at Ka Band," in *Loughborough Antennas & Propagation Conference (LAPC 2009)*, Loughborough, UK, pp. 117-120, November 2009.

[GAGN10a] N. Gagnon, A. Petosa, D.A. McNamara, “Thin Microwave Phase-Shifting Surface (PSS) Lens Antenna Made of Square Elements,” *IET Electronics Letters*, vol. 46, no. 5, pp. 327-329, March 2010.

[GAGN10b] N. Gagnon, A. Petosa, D.A. McNamara, “Thin Microwave Quasi-Transparent Phase-Shifting Surface (PSS),” *IEEE Transactions on Antennas and Propagation*, vol. 58, no. 4, pp. 1193-1201, April 2010.

[GAGN10c] N. Gagnon, A. Petosa, D.A. McNamara, “Thin Phase-Correcting Lens Antennas Made Using a Three-Layer Phase Shifting Surface (PSS) at Ka Band,” in *14th International Symposium on Antenna Technology and Applied Electromagnetics (ANTEM 2010)*, Ottawa, Canada, July 2010 *(digital format)*.

[GAGN10d] N. Gagnon, D.A. McNamara, A. Petosa, “Performance Comparison of Lens Antennas Realized Using a Thin Free-Standing Transmissive Phase-Shifting Surface (PSS),” in *IEEE AP-S International Symposium*, Toronto, Canada, July 2010 *(digital format)*.

[GOLD97] P.F. Goldsmith, *Quasioptical Systems*, IEEE Press, New York, NY, 1998.

[GOOD71] J.W. Goodman, “An Introduction to the Principles and Applications of Holography,” *Proceedings of the IEEE*, vol. 59, no. 9, pp. 1292-1304, September 1971.

[GOOD96] J.W. Goodman, *Introduction to Fourier Optics*, 2nd Ed., McGraw-Hill, New York, NY, 1996.

[GOUK92] M.A. Gouker, G.S. Smith, “A Millimeter-Wave Integrated-Circuit Antenna Based on the Fresnel Zone Plate,” *IEEE Transactions on Microwave Theory and Techniques*, vol. 40, no. 5, pp. 968-977, May 1992.

[GRAY02] D. Gray, “How to Choose an Antenna Range Configuration,” in *24th Antenna Measurement Techniques Association Symposium (AMTA 2002)*, Cleveland, OH, pp. 347-352, October 2002.

[GUO02] Y.J. Guo, S.K. Barton, *Fresnel Zone Antennas*, Kluwer Academic Publishers, Boston, MA, 2002.

[HFSS07] HFSS (High Frequency Structural Simulator) 11.0 by Ansoft Corporation, USA, http://www.ansoft.com/products/hf/hfss/.

[HIRV97] T. Hirvonen, et al., "A Compact Antenna Test Range Based on a Hologram," *IEEE Transactions on Antennas and Propagation*, vol. 45, no. 8, pp. 1270-1276, Aug. 1997.

[HRIS00] H. D. Hristov, *Fresnel Zones in Wireless Links, Zone Plate Lenses and Antennas*, Artech House, Boston, MA, 2000.

[HUAN07] J. Huang, J.A. Encinar, *Reflectarray Antennas*, Wiley-IEEE Press, Hoboken, NJ, 2007.

[IIZU75] K. Iizuka, et al., "Volume-Type Holographic Antenna," *IEEE Transactions on Antennas and Propagation*, vol. 23, no. 6, pp. 807-810, November 1975.

[KADR05] I. Kadri, A. Petosa, L. Roy, "Ka-Band Fresnel Lens Antenna Fed with an Active Microstrip Patch Array," *IEEE Transactions on Antennas and Propagation*, vol. 53, no. 12, pp. 4175-4178, December 2005.

[KOCK46] W.E. Kock, "Metal-Lens Antennas," *Proceedings of the IRE*, vol. 34, no. 11, pp. 828-838, November 1946.

[KOCK48] W.E. Kock, "Metallic Delay Lenses," *The Bell System Technical Journal*, vol. 27, pp. 58-82, January 1948.

[KOCK68] W.E. Kock, "Microwave Holography," *Microwaves*, vol. 7, no. 11, pp. 46-54, November 1968.

[LEE79] W.-H. Lee, "High Efficiency Multiple Beam Gratings," *Applied Optics*, vol. 18, no. 13, pp. 2152-2158, July 1979.

[LESE69] L.B. Lesem, P.M. Hirsch, J.A. Jordan, "The Kinoform: A New Wavefront Reconstruction Device," *IBM Journal of Research and Development*, vol. 13, no. 2, pp. 150-155, March 1969.

[LÉVI01] K. Lévis, et al., "Ka-Band Dipole Holographic Antennas," *IEE Proceedings on Microwaves, Antennas and Propagation*, vol. 148, no. 2, pp. 129-132, April 2001.

[MATL03] MATLAB 6.5.1 by The MathWorks, Inc., USA, http://www.mathworks.com/

[McGR86] D.T. McGrath, "Planar Three-Dimensional Constrained Lens," *IEEE Transactions on Antennas and Propagation*, vol. 34, no. 1, pp. 46-50, January 1986.

[MUNK00] B.A. Munk, *Frequency Selective Surfaces: Theory and Design*, Wiley, New York, NY, 2000.

[MUNK08] B.A. Munk, *Metamaterials: Critique and Alternatives*, Wiley, New York, NY, 2009.

[PEND99] J. B. Pendry, et al., "Magnetism from Conductors, and Enhanced Non-Linear Phenomena," *IEEE Trans. Microwave Theory Tech.*, vol. 47, no. 11, pp. 2075-2084, November 1999.

[PETO03a] A. Petosa, A. Ittipiboon, S. Thirakoune, "Shadow Blockage Improvement Using a Perforated Dielectric Fresnel Lens," in *IEEE AP-S International Symposium*, Columbus, OH, vol. 4, pp. 514-517, June 2003.

[PETO03b] A. Petosa, A. Ittipiboon, S. Thirakoune, "Design and Performance of a Perforated Dielectric Fresnel Lens," *IEE Proceedings on Microwaves, Antennas and Propagation*, vol. 150, no. 5, pp. 309-314, October 2003.

[PETO06] A. Petosa, N. Gagnon, A. Ittipiboon, "Optimization of Dielectric Fresnel Lens Thickness for Maximizing Gain," in *12th International Symposium on*

Antenna Technology and Applied Electromagnetics (ANTEM 2006), Montréal, Canada, pp. 519-522, July 2006.

[PETO08] A. Petosa, A. Ittipiboon, "Comparison of an Elementary Hologram and Fresnel Zone Plate," *URSI Radio Science Bulletin*, no. 324, pp. 29-36, March 2008.

[PHIL10a] R. Phillion, M. Okoniewski, "An Array Lens for Circular Polarization with Emphasis on Aperture Efficiency," in *4th European Conference on Antennas and Propagation (EuCAP 2010)*, Barcelona, Spain, April 2010 *(digital format)*.

[PHIL10b] R. Phillion, M. Okoniewski, "Using an Array Lens as a Circular Polarization Splitting Prism," in *IEEE AP-S International Symposium*, Toronto, Canada, July 2010 *(digital format)*.

[POZA96] D.M. Pozar, "Flat Lens Antenna Concept Using Aperture Coupled Microstrip Patches," *IEE Electronics Letters*, vol. 32, no. 23, pp. 2109-2110, November 1996.

[POZA98] D.M. Pozar, *Microwave Engineering*, 2nd Ed., Wiley, New York, NY, 1998.

[RYAN10] C.G.M. Ryan, et al., "A Wideband Transmitarray Using Dual-Resonant Double Square Rings," *IEEE Transactions on Antennas and Propagation*, vol. 58, no. 5, pp. 1486-1493, May 2010.

[RORA97] C.B. Rorabaugh, *Digital filter designer's handbook: with C++ algorithms*, McGraw-Hill, New York, NY, 1997.

[SHIB10] R. Shibayama, H. Deguchi, M. Tsuji, "Flat Thin Polarizer-Lens Based on Multiple Resonance Behavior," in *IEEE AP-S International Symposium*, Toronto, Canada, July 2010 *(digital format)*.

[SIEV99] D. Sievenpiper et al., “High-Impedance Electromagnetic Surfaces with a Forbidden Frequency Band,” *IEEE Transactions on Microwave Theory and Techniques,* vol. 47, no. 11, pp. 2059-2074, November 1999.

[SIEV08] D.F. Sievenpiper, “Artificial Impedance Surfaces for Antennas,” in *Modern Antenna Handbook*, C.A. Balanis, Ed., Wiley, Hoboken, NJ, 2008, ch. 15.

[SPIE09] B.E. Spielman et al., “Metamaterials Face-Off,” *IEEE Microwave Magazine*, vol. 10, no. 3, pp. 8-42, May 2009.

[STUT98] W.L. Stutzman, G.A. Thiele, *Antenna Theory and Design*, 2nd Ed., Wiley, Hoboken, NJ, 1998.

[THOU60] L. Thourel, *The Antenna*, Wiley, Hoboken, NJ, 1960.

[TRIC70] G. Tricoles, E.L. Rope, “Binary, Detour Phase, Microwave Holography,” in *G-MTT International Microwave Symposium Digest*, vol. 70, no. 1, pp. 124-125, May 1970.

[VESE68] V. G. Veselago, “The electrodynamics of substances with simultaneously negative values of ε and μ,” *Soviet Physics USPEKHI*, vol. 10, no. 4, pp. 509-514, Jannuary-February 1968.

[WATE66a] W.M. Waters, “An Electronic Half-Tone Image Recording Technique,” *Proceedings of the IEEE*, vol. 54, no. 2, pp. 319-320, February 1966.

[WATE66b] J.P. Waters, “Holographic Image Synthesis Utilizing Theoretical Methods,” *Applied Physics Letters*, vol. 9, no. 11, pp. 405-407, December 1966.

[ZHAN10] Y. Zhang, R. Mittra, W. Hong, “Systematic Design of Planar Lenses Using Artificial Dielectrics,” in *IEEE AP-S International Symposium*, Toronto, Canada, July 2010 *(digital format)*.